Cellular Target Engagement and Selectivity Profiling of Small Molecules for Mechanism-of-Action Studies



Jakub Stefaniak

New College

University of Oxford

Supervised by

Dr. Kilian Huber

Prof. Angela Russell

Submitted: Trinity Term, October 11, 2019

This thesis is submitted to the Department of Chemistry, University of Oxford, as a requirement for the degree of Doctor of Philosophy, Systems Approaches to Biomedical Sciences Centre for Doctoral Training (SABS-CDT)

Declaration

I declare that this thesis is entirely my own work, and except where otherwise stated, describes my own research.

Jakub S. Stefaniak,

New College

Acknowledgements

This thesis would not be possible without the enormous amounts of support I received from my academic supervisors Dr. Kilian Huber and Prof. Angela Russell, as well as my industrial supervisors at AstraZeneca, Dr. Thomas Lundbäck and Dr. M. Paola Castaldi.

In addition, I would like to express enormous gratitude towards my colleagues at the Target Discovery Institute and the Department of Chemistry, in particular Dr. Jennifer Ward, Dr. Andrew Lewis, Dr. Sébastien R.G. Galan, Dr. Carole J.R. Bataille, Dr. Graham M. Wynne, as well as Dr. Darragh O'Brien, Mr. Simon Davis, Ms Emma Kennedy, Dr. Paul Smith, Mr. Adam Thorne, Dr. Felix Feyertag, Dr. Laura Diaz Saez and Mr. Raphael Heilig, as well as the entire proteomics and mass spectrometry facility at the Target Discovery Institute.

Lastly, I would like to thank my family and my wonderful girlfriend Helen, whose support I am very grateful for.

Abstract

A high-quality chemical probe should possess the qualities of being highly specific, potent, and selective against off-target interactions, in order to enable target validation. By contrast, low-quality compounds, which display properties of promiscuity, reactivity and instability can in turn be misleading: such compounds, referred to as Pan-Assay Interference Compounds (PAINS) need to be removed from screening libraries. Target engagement and proteomic studies can often detect undesirable physicochemical properties or polypharmacology within small molecules, as well as help annotate and clean screening libraries and prevent compounds entering biology projects without precautions.

Herein are presented a number of target engagement techniques used to annotate compounds. The introduction summarises currently available techniques and provides a literature review pertaining to the Cellular Thermal Shift Assay (CETSA). The second chapter describes how the use of chemoproteomic techniques, including CETSA, has led to the discovery of a number of undesirable characteristics of a literature compound SJ-172550. The third chapter delves into mass spectrometry (MS)-based CETSA techniques, and describes the development of an algorithm to analyse MS-CETSA output data for target validation, using both open-access datasets as well as the dataset obtained from the analysis of a known protein arginine methyltransferase 5 (PRMT5) inhibitor. The fourth chapter describes the use of Immunoblot-CETSA to investigate cellular target engagement of peroxisome proliferator-activated receptor γ (PPARγ)-targeting compounds in

the context of downstream induction of the uncoupling protein, UCP1. Subsequently, the fifth chapter concerns the development of an AlphaScreen-based target engagement assay with a high-throughput capacity, and the necessary optimisation steps, and provides the link between AlphaScreen-CETSA and MS-CETSA. The sixth chapter pertains to the proteomic analysis of PPARγ-expressing cells, including an MS-CETSA experiment involving a known PPARγ agonist, rosiglitazone, to investigate its off-target interactions. Chapters 5 and 6 together point to the combined use of AlphaScreen-CETSA for hit detection and MS-CETSA for hit follow-up.

Table of Contents

Abstract 3

List of Abbreviations 11

1. Introduction 16

1.1 Chemical probes and chemoproteomics as tools to support drug discovery and improve compounds attrition rate 16

1.1.1 Reasons behind high attrition rate in pharmaceutical industry 16

1.1.2 Chemical probes can support drug discovery 20

1.1.3 Poor quality compounds and the need to validate small molecules 22

1.2 Current non-proteomic methods for profiling compounds 23

1.2.1 Biophysical techniques to study small molecules *in vitro* 23

1.2.2 Fluorescence anisotropy and BRET-based techniques to study cellular target engagement 29

1.2.3 Phenotypic methods are increasingly relevant 31

1.3 Chemoproteomics to enable drug discovery 32

1.3.1 Advances in mass spectrometry and the birth of proteomics 32

1.3.2 Affinity chromatography and ABPP including clickable analogues 34

1.3.3 Cellular Thermal Shift Assay (CETSA) and MS-CETSA 41

1.3.4 Alternative readout methods for CETSA 47

1.3.5 Aims of the project 49

2. SJ-172550, a Putative MDMX Inhibitor: Revealing a Compound's Undesirable Characteristics by a Combination of Cell Biology, Biophysics and Proteomics...52

2.1 Introduction.....52

2.1.1 The p53/MDM2/MDMX Axis.....52

2.1.2 The MDM2/p53 and MDMX/p53 Interaction as a Target 54

2.1.3 SJ-172550 as a first-in-class MDMX inhibitor.....56

2.2 Preliminary cheminformatic, biophysical and phenotypic studies on SJ-172550 58

2.2.1 Cheminformatic analysis of the compounds predicts promiscuity.....58

2.2.2 Inconclusive DSF data on SJ-172550 binding to MDMX.....59

2.2.3 ITC Confirms that SJ-172550 binds MDMX, possibly in a covalent fashion.....60

2.2.4 MS data confirms multiple covalent adduct formation 62

2.2.5 The reduced analogue of SJ-172550 is unable to bind MDMX 64

2.2.6 Cell viability investigations 65

2.3 Evaluating cellular target engagement of SJ-172550 67

2.3.1 CETSA analysis shows SJ-172550 is not stabilising and possibly destabilising MDMX 67

2.3.2 Synthesis and characterisation of a clickable analogue of SJ-172550..69

2.4 Further physicochemical analysis of SJ-172550 and related compounds ...73

2.4.1 Reactions of SJ-172550 with reducing agents 73

2.4.2 Evidence of decomposition of SJ-172550 in aqueous buffers 76

2.4.3 Evidence of decomposition and undesirable reactivity in related molecules 80

2.5 Discussion 82

2.6 Conclusions 83

3. Development and Validation of an Algorithm to Analyse 2D-CETSA Output Data 84

3.1 Introduction 84

3.1.1 Current proteomics workflows and data analysis 84

3.1.2 Quantification strategies using tandem mass tags 88

3.1.3 CETSA/TPP Data Analysis 90

3.2 Development of a MATLAB script for further downstream analysis using the GSK3326595 Data 93

3.2.1 The proteomic analysis of a PRMT5 inhibitor GSK3326595 93

3.2.2 The development of an algorithm for post-processing of the data 94

3.2.3 Results 99

3.2.4 Validation of the algorithm on a public dataset 100

3.3 Discussion 102

3.5 Conclusions 103

4. CETSA-Immunoblot Analysis of UCP1-inducing PPARγ Agonists 104

4.1 Introduction.....104

4.1.1 PPARγ in Health and Disease.....104

4.1.2 PPARγ-targeting compounds in the clinic.....107

4.1.3 Brown adipose tissue and the uncoupling protein 109

4.1.4 The need for proteomic annotation of UCP1-inducers.....112

4.2 CETSA-WB studies.....113

4.2.1 The selection of a suitable cell line for initial CETSA-WB studies ...113

4.2.2 Optimisation of CETSA-WB on the A549 line.....114

4.2.3 Optimisation of CETSA-WB on the SW620 line.....117

4.2.4 Optimisation of CETSA-WB in an adipocyte model 120

4.3 Discussion.....121

4.4 Conclusions.....122

5. Development of AlphaScreen CETSA for PPARγ.....123

5.1 Introduction.....123

5.1.1 The shortcomings of WB and the need for quantitative proteome analysis.....123

5.1.2 ELISA and AlphaLISA-based CETSA quantification techniques 124

5.1.3 AlphaScreen-based application of CETSA to screen and examine PPARγ-targeting compounds.....130

5.2 Assay optimisation.....130

5.2.1 Antibody selection and initial experiments to devise appropriate combinations.....130

5.2.2 The switch to biotin-conjugation and bio-layer-interferometry 137

5.2.3 Proof-of-concept AlphaScreen experiments with recombinant PPARγ 140

5.2.4 Optimisation experiments involving 3T3-L1 lysate 144

5.2.5 Lysate CETSA 149

5.2.6 Optimisation of AlphaScreen-based CETSA in live cells 152

5.2.7 Live-cell CETSA 157

5.3 The development of a high-throughput screen assay to study PPARγ agonists 158

5.3.1 Temperature selection in a 96-well format 158

5.3.2 Temperature selection in a 384-well format 161

5.3.3 Pilot screen in a 384-well format 162

5.4 Discussion 164

5.5 Conclusions.....165

6. Proteomic Analysis of PPARγ Modulators in Cellular Models of UCP1 Induction 166

6.1 Introduction.....166

6.1.1 Proteomic analysis of nuclear hormone receptors and difficulties in their detection by MS 166

6.2 Optimisation of experimental conditions to increase coverage of PPARγ and its related protein complexes 169

6.2.1 Immunoprecipitation methods 169

6.2.2 Analysis of cellular lysates and nuclear extracts 173

6.3 Thermal Profiling of Rosiglitazone in 3T3-L1 cells 179

6.3.1 Design of the experiment 179

6.3.2 Results 181

6.4 Discussion 188

6.5 Conclusions 190

7. Closing Remarks 191

References 196

Appendix A: Materials and Methods 248

Appendix B: Source Code for the MATLAB Algorithm 272

Appendix C: Compound NMR Spectra 275

List of Abbreviations

ABL1	Abelson Murine Leukaemia Viral Oncongene Homolog 1
ABPP	Activity Based Protein Profiling
ACAT	Acyl-coenzyme A:cholestrol acyltransferase
ALK	Anaplastic Lymphoma Kinase
AzTb	Azido-TAMRA-Biotin
BADGE	Bisphenol A Diglycidyl Ether
BCA	Bicinchoninic Acid [Assay]
BET	Bromodomain and extra-terminal
BLI	Bio-layer interferometry assay
BMD	Bone Mineral Density
BRD	Bromodomain
BRET	Bioluminescence Resonance Energy Transfer
BRL49653	Rosiglitazone
BTK	Bruton's Tyrosine Kinase
CAP1	Cyclase Associated Protein 1
CDK19	Cyclin-dependent Kinase 19
CDK8	Cyclin-dependent Kinase 8
CETSA	Cellular Thermal Shift Assay
CID	Collision Induced Degradation
CRAPOME	Contaminant Repository for Affinity Purification
CRBN	Cereblon
CRE	cAMP Response Element
CREB	cAMP Response Element Binding Protein
CREBBP	CREB Binding Protein
CRISPR	Clustered Regularly Interspaced Short Palindromic Repeats
CRKL	CT10 Oncogene Homolog-like Protein
CSP	Chemical Shift Perturbations
CuAAC	Copper-Catalysed Azide-Clkyne Cycloaddition
DBD	DNA-binding Domain

DCC	Dicyclohexylcarbodiimide
DDA	Data Dependant Acquisition
DDB1	Damage Specific DNA Binding Protein 1
DHFR	Dihydrofolate Reductase
DMP	Dimethyl Pimelimidate
DMSO	Dimethyl Sulfoxide
EA	Enzyme Acceptor
EDTA	Ethylenediaminetetraacetic Acid
ELISA	Enzyme Linked Immunosorbent Assay
ERRa	Estrogen-Related Receptor Alpha
ESI	Electrospray Ionisation
FAAH	Fatty Acid Amide Hydrolase
FDA	Food and Drug Administration
FDR	False Discovery Rate
FG	Ferrite-glycidyl Methacrylate
FITC	Fluorescin Isothiocynate
FP	Fluorescence polarisation
FRET	Förster Resonance Energy Transfer
GST	Glutathione S-Transferase
HDAC	Histone Deacytylase
HDM	Human Double Minute
HPLC	High Performance Liquid Chromatography
HSQC	Heteronuclear Single Quantum Coherence
HTS	High-throughput Screening
Iah1	Isoamyl Acetate-Hydrolysing Esterase Homolog 1
IDH1	Isocitrate Dehydrogenase 1
IP	Immunoprecipitation
ITC	Isothermal Titration Calorimetry
ITDR	Isothermal Dose Response
ITDRF	Isothermal Dose Response Fingerprinting
JMJD	Jumonji Domain Containing

K_d	Dissociation constant
LC/MS	Liquid Chromatography/Mass Spectrometry
LOA	Likelihood of Approval
Maged1	Melanoma-associated Antigen D1
MALDI	Matrix Assisted Laser Desorption Ionisation
MAPK	Mitogen-activated Protein Kinase
MDM	Murine Double Minute
MDM2	Murine Double Minute 2
MDMX	Murine Double Minute X
MED	Mediator
MEP50	Methylosome Protein 50
MoA	Mechanism of Action
MS	Mass Spectrometry
MW	Molecular Weight
NCOA2	Nuclear Coactivator 2
NCOR1	Nuclear Corepressor 1
NCOR2	Nuclear Corepressor 2
NHR	Nuclear Hormone Receptor
NHS	N-hydroxysuccinamide
NMEs	Novel Molecular Entities
NMR	Nuclear Magnetic Resonance
NMT1	N-myristoyltransferase 1
NTD	N-terminal Domain
PAH	Phenylalanine Hydroxylase
PAINS	Pan-Assay Interference Compounds
PARP	Poly-ADP Ribose Polymerase
PBS	Phosphate-buffered Saline
PCR	Polymerase Chain Reaction
PEG3	Polyethylene Glycol
PGC1α	Pparg coactivator 1 alpha
PISA	Proteome Integral Stability Alteration

PPARγ	Peroxisome Proliferator-Activated Receptor Gamma
PPI	Protein-Protein Interaction
PPRE	PPAR Response Elements
PRMT5	Protein-Arginine Methyltransferase 5
PTM	Post-translational Modification
R&D	Research and Development
RING	Really Interesting New Gene
RXR	Retinoid-X-Receptor
SAR	Structure-activity relationship
SCCPDH	Saccaropine Dehydrogenase
SDMA	Symmetric Dimethylation
SDS-PAGE	Sodium Dodecyl Sulfate Polyacrylamide Gel Electrophoresis
SGC	Structural Genomics Consortium
siRNA	Small Interfering RNA
SLC25	Solute Carrier 25
SMARCA	SWI/SNF-related, Matrix-associated, Actin-dependant Regulator Chromatin Grp. A
SMYD3	SET and MYND Domain Containing 3
SNP	Single Nucleotide Polymorphisms
SPR	Surface Plasmon Resistance
STD	Saturation Transfer Difference
SWI/SNF	SWItch/Sucrose Non-Fermentable
TAR	Thioxene-Anthracene-Rubrene
TCA	Tricarboxylic Acid [Cycle]
TCEP	Tris(2-carboxyethyl)phosphine
T_m	Melting Temperature
TMT	Tandem Mass Tags
TNFα	Tumour Necrosis Factor Alpha
TPP	Thermal Proteome Profiling
TS	Thymidylate Synthase
TTC38	Tetratricopeptide repeat domain 38
TZD	Thiazolidinedione

UCP1	Uncoupling Protein 1
USP	Ubiquitin-specific proteases
UTX	Ubiquitously Transcribed Tetratricopeptide Repeat, X Chromosome
UV	Ultraviolet
WAT	White Adipose Tissue
WB	Western Blot
WT	Wild-type

1. Introduction

1.1 Chemical probes and chemoproteomics as tools to support drug discovery and improve compounds attrition rate

1.1.1 Reasons behind high attrition rate in pharmaceutical industry

Despite more than a two-fold increase in research and development (R&D) expenditure since the turn of the century, translating to a total pipeline of nearly 15,000 drug development projects, the number of novel molecular entities (NMEs) approved by the Food and Drug Administration (FDA) per year has been largely stagnant. Likewise, 2018 brought with it only 6 novel small molecules with a breakthrough-therapy designation, compared to 10 in 2017[1]. This reveals a glaring weakness within the pharmaceutical industry that is the attrition rate of small molecules. Indeed, it is widely accepted that, depending on factors such as disease area, only between one in 10 and one in 20 drugs that enter Phase I trials will eventually become approved for clinical use; moreover, Phase II is the key driver of attrition, eroding nearly two-thirds of compounds that enter it[2]. In addition, the preclinical stage itself only has a 51% success rate for discovery research and 69% for preclinical development[3].

Excluding issues with commercialisation, clinical trial failures are most likely to be attributed to either safety concerns or lack of efficacy[4,5]. The attrition rate is highly heterogeneous across disease areas. Whilst the likelihood of approval (LOA) for a compound entering clinical trials in the infectious diseases area may be

comparatively high at 15-17%, in oncology the rate drops to 5-7%[2,5], and in areas such as Alzheimer's disease, upwards of 99% of compounds result in a clinical failure[6].

Advances in the field of genomics and screening have resulted in a shift from traditional, pharmacology-based drug discovery where emphasis is placed on the compound and its mechanism of action (MoA) and phenotypic effects, to a target-based one, where knockout or overexpression data drives target selection, followed by high-throughput screening (HTS) and lead optimisation[7]. In general, mathematical modelling shows that it is more desirable to test fewer compounds with a better predictive model (such as patient-derived cells or multicellular tissue modelling vs simple *in vitro* binding of target protein by the molecule) than the other way around[8]. This is backed by historical precedent: the very first compound screen by Gerhard Domagk in the 1930s involved roughly 600 dyes from the Bayer laboratories given to mice infected with *Streptococcus*; the optimisation of the eventual hit that alleviated the infection led to the development of the first antimicrobial agent Prontosil[9]. Compare this to today's screens which pit upwards of millions of compounds with 50-60% rate of lead generation per target[10]. Thus, it can be argued that one way to reverse the negative trends within the pharmaceutical industry is to return to pharmacology-based compound discovery and development[7].

In recent years, pharmaceutical companies have devoted significant time and resources to narrowing down the causes of clinical trial failures in order to minimise the risk in the future[11]. These can be broadly categorised as the wrong choice of target, the right choice of target but inadequate exposure at the site (both contributing to low efficacy), and the right choice of target but insufficient selectivity or incorrect understanding of the mechanism of action of the molecule (responsible for toxicity and side effect problems). As the biology is usually incompletely understood, target choice can be the most problematic.

Wrong choice of target can stem from an incomplete hypothesis regarding the underlying biological processes, particularly where extensive genetic data linking the target to the disease area is incomplete or unavailable. For instance, in a recent analysis of discontinued drug pipelines, out of the top five putative MoAs with the most discontinued projects, four have to do with the β-amyloid hypothesis of Alzheimer's disease[12], totalling over 90 clinical failures and raising concerns over the validity of the target[13]. Similarly, the inhibition of acyl–coenzyme A:cholesterol acyltransferase (ACAT) was once seen as an attractive strategy for targeting atherosclerosis[14]; after nearly two decades and nearly 30 discontinued projects, the ACAT inhibitor pipeline has been largely abandoned[12]. By contrast, there are a number of potential unexplored targets (the human kinome, for instance, contains over 500 different proteins, whereas most of the kinase research is focused on a small fraction of it), however, those tend to lack accurate or complete predictive and translational models, and as such tend not to be pursued[15,16].

Assuming correct choice of target, the compound's pharmacology can often be understood in terms of the interactions it makes with biological macromolecules at the site of exposure. For instance, insufficient target engagement in the given tissue or cell can contribute towards lack of efficacy and thus clinical failure, as was the case with AZD3778, a chemokine receptor antagonist developed by AstraZeneca[11,17]. In the case of iniparib, the more recent putative poly (ADP-ribose) polymerase 1 (PARP1) inhibitor that failed in the clinic, the target has long been validated with a number of compounds receiving FDA-approval, such as olaparib[18]. The reason for iniparib's failure is likely because, as the preclinical data suggests, it does not achieve its cytotoxic effects through PARP1 inhibition, but through other, yet undiscovered, mechanisms[19].

Furthermore, if a compound binds to other proteins than the target, this can bring about undesirable toxicity and ultimately the failure of the small molecule in clinical trials due to side effects – together, clinical safety and non-clinical toxicology account for 48% of primary causes for compound terminations[20]. Out of preclinical safety closures, up to 75% occur due to off-target interactions[11] or otherwise compound-related issues (the remaining compounds fail due to toxicity as a result of modulation of the target, which falls under incorrect target selection). In 2016, the clinical trial of BIA 10-2474, a putative fatty acid amide hydrolase (FAAH) inhibitor resulted in five participants developing irreversible neurological damage and necrosis, causing the death of one[21]. Subsequent analysis revealed significant off-target interactors of the molecule and its metabolites resulting in

major alterations in the lipid and metabolic profiles of the treated tissues[22,23]. On the other hand, a recent analysis demonstrates that a non-insignificant proportion of cancer drugs achieve their cytotoxicity through off-target effects[24], further emphasising the need to validate potential compound targets before clinical development.

1.1.2 Chemical probes can support drug discovery

Chemical probes are small bioactive molecules used to study protein function by binding to and either inhibiting or activating targets via a clearly defined MoA. In this respect, they differ from drugs, which permit greater leniency in terms of MoA, in turn offset by stringent pharmacokinetic and pharmacodynamic requirements and as a result, probes are developed mainly as tools to understand the mechanistic underpinnings of specific target modulation, rather than to modulate the target for clinical reasons.

As mentioned earlier, pursuing an incorrect target often leads to compounds failing in Phase II and III trials due to lack of efficacy. In this context, probes can be excellent tools to help de-validate certain targets in a pre-clinical setting, particularly where genetic manipulation data is unavailable or incomplete, or the target exists in a multi-domain or multi-protein complex. For instance, the probe PFI-3 was developed as an inhibitor of SWI/SNF-related, Matrix-associated, Actin-dependent Regulator Chromatin group A (SMARCA2/SMARCA4) bromodomains, which demonstrated cellular target engagement and high target

affinity. However, it could not reproduce the specific effects that SMARCA2 knockdown elicits on chromatin and it was subsequently shown that it is the ATPase domain, not the bromodomain, that should be targeted[25]. Likewise, chemical probes in conjunction with modern genetic manipulation methods, such as clustered regularly interspaced short palindromic repeats (CRISPR) gene editing, can be used to validate targets early in a drug discovery pipeline, before any compound development progresses from the pre-clinical to the clinical phase (or even begins), thus alleviating potential costs to the industry.

Once a target has successfully been validated with a known MoA usually through a combination of genetic and pharmacological manipulation, chemical probes are primed to become potential leads. Because selectivity and efficacy for a given MoA has already been demonstrated *in vitro*, medicinal chemistry can focus on optimising compounds for a safe and adequate pharmacokinetic/pharmacodynamic profile. This was the case with JQ-1, a sub-micromolar inhibitor of bromodomain and extra-terminal (BET) family members, which include BRD2, BRD3 and BRD4[26]. Despite JQ-1's poor pharmacokinetics, which precluded it from being a drug itself, a number of compounds, some of which have entered clinical trials, were developed from its thienotriazolodiazepine scaffold[27].

1.1.3 Poor quality compounds and the need to validate small molecules

Given that the recent advances in medicinal and synthetic chemistry have brought with them an increase in the number of bioactive small molecules, the Structural Genomics Consortium (SGC) has issued specific requirements for chemical probes[28]. These include evidence of cellular target engagement and clear MoA, as well as <1 μM affinity and potency, with a minimum of 30-fold specificity against structurally-related or similar proteins. If possible, a structurally similar yet inactive at the cognate site analogue should be provided as well.

The primary goal of the above guidelines is reducing the fraction of poor-quality compounds. These can include pan-assay interference compounds, or PAINS, named so due to their propensity to appear as false positives in high-throughput screens[29], even though not every low-quality chemical probe is necessarily a PAINS compound. Typical features of PAINS compounds include promiscuity, lack of evidence of cellular target engagement and physicochemical properties, such as aggregation that can potentially contribute towards cellular perturbation[30]. As a result, although these compounds can certainly produce interesting phenotypes (as is the case with two PAINS compounds that proliferate throughout literature despite evidence to the contrary, namely curcumin[31] and resveratrol[32]), the use of these compounds to investigate or validate targets is not recommended.

Validation of a chemical probe should involve assays that establish cellular MoA, the structure-activity relationship (SAR) and target engagement, as well as

selectivity and appropriate physicochemical properties. Conversely, a simple demonstration of binding in a biophysical assay and cell viability data is not enough and can introduce compounds into the literature that, whilst interesting, achieve their phenotypic effects by mechanisms unrelated to their purported target. This necessitates the demonstration of a more proximal marker of specific cellular target engagement. For example, the compound tris(dba)dipalladium was initially reported to be a >1 μM inhibitor of protein *N*-myristoyltransferase 1 (NMT1), and in cell viability assays it was shown to be capable of halting melanoma proliferation[33]. A more recent analysis has, however, shown that the compound, structurally related to curcumin, is an aggregator and does not influence cellular myristoylation levels[34]. Moreover, poor cell permeability can result in a compound having inadequate cellular target engagement despite binding in a biophysical assay. A vital example to cite here is GSK-J1, a high-affinity inhibitor of the jumonji H3K27 histone demethylases JMJD3 and UTX, whose structure, owing to a carboxyl group, rendered the molecule incapable of crossing the cell membrane. A pro-drug version of the probe, GSK-J4, has subsequently been developed, which rapidly crosses macrophage cell membrane and metabolises to GSK-J1[35].

1.2 Current non-proteomic methods for profiling compounds

1.2.1 Biophysical techniques to study small molecules *in vitro*

In general, any method by which the binding of a small molecule to a protein is measured must meet the following criteria:

- Accurate detection, ideally with a low false discovery rate

- Low protein requirement, as expression and purification of recombinant proteins can be costly in terms of time and resources
- High rate of data acquisition, particularly if the method is to be employed for screening purposes
- Little to no requirement of protein modification to enable the readout

Table 1 presents commonly available techniques for *in vitro* experiments on recombinant proteins.

Method	Amount of Protein Required (per experiment)	Requires Protein Modification?	Notes
Differential Scanning Fluorimetry/Light Scattering (T_m Shift)	0.1-10 µg	No	
Isothermal Titration Calorimetry	0.1-10 mg	No	High amount of protein required; provides K_d as well as stoichiometry and binding thermodynamics
Surface Plasmon Resonance	Sub-microgram	Yes, immobilisation	Provides insights into kinetics of binding
Nuclear Magnetic Resonance	10-500 µg	Some techniques require isotopic labelling	Requires an NMR-compatible buffer system or solvent suppression techniques
Fluorescence Polarisation	0.1-10 µg	No	Requires a fluorescent or fluorescently-labelled ligand
Förster Resonance Energy Transfer	0.1-10 µg	Yes, fluorescent modification	
X-ray Crystallography	10 – 500 µg	Potentially (if the protein does not crystallise)	Does not provide a measure of affinity; requires a much more rigorously-purified protein

Table 1: Commonly used biophysical methods to assay interactions between ligands and proteins.

The thermal (T_m) shift assay, is currently used for high-throughput screens in drug discovery projects[36]. It exploits the biophysical principle of thermal stabilisation of

a macromolecule due to the free energy of binding of a small molecule. In a conventional T_m shift assay, this is exploited by the addition of the SYPRO Orange dye that fluoresces as it interacts with the hydrophobic interior of the protein, thus monitoring protein unfolding. Variations on the experiment include using a thiol-reactive coumarin (CPM) dye that fluoresces as it covalently attaches to cysteines normally buried within the hydrophobic interior of the protein[37], utilising innate tryptophan fluorescence which is quenched by solvent contact[38], combining the technique with circular dichroism[39] or replacing thermofluor dye with light scattering[40]. The assay is arguably the simplest one to perform, requiring only the dye, protein (in µg quantities, in a suitable buffer system) and a real-time polymerase chain reaction (RT-PCR) instrument. On the other hand, reliance on a fluorescent dye means that assay interference from innately-fluorescent compounds can be an issue. Similarly, buffer effects, such as the recently-reported interference from EDTA aggregates, can also produce false positives[41]. Conversely, false negatives are often a product of fluorescence quenching by the molecule[42].

Isothermal titration calorimetry (ITC), by contrast, measures the heat change that occurs as a result of a ligand interacting with the protein. The non-covalent interactions result in an enthalpy change which would change the temperature of the sample relative to the reference cell, unless compensated for by reduced or increased heating to the sample cell (and expressed in J/s as the electrical power needed to maintain a small temperature difference between the cells). Thus, each injection of ligand will produce a heat pulse which can be measured and integrated

over time to generate a titration curve (Jelesarov and Bosshard 1999). The advantage of the method is that it can provide not just the dissociation constant K_d, but also the enthalpy (ΔH) and entropy (ΔS) of the interaction, and the stoichiometry. Conversely, the drawbacks include time of measurement (usually measured in hours) as well as the need for comparatively high quantities of the protein in question.

Surface plasmon resonance (SPR), by contrast, is advantageous in being able to provide data using even submicromolar quantities of the protein. The biophysical phenomenon underpinning SPR is the propagation of plasma waves (plasmons) on the interface of gold and an aqueous buffer with a low refractive index. Depending on whether material has adsorbed on the surface, the surface plasmon resonance will be altered, and the technique is very sensitive to even small perturbations allowing to monitor the interactions between the ligand and the protein in real time[43]. The advantage of SPR, in addition to the aforementioned economy in terms of protein requirement, is the ability to compute the k_{off} and k_{on} rate, as well as the thermodynamic quantities if the experiment is performed at different temperatures[44]. Its primary disadvantage is the need to adsorb the protein onto the surface before the experiment can be performed, thus necessitating optimisation for every protein[45].

Nuclear magnetic resonance (NMR) has also emerged as an assay to measure the interactions between the ligand and a protein. Because the chemical shifts of both

the ligand and proximal residues within the binding site will be perturbed upon interaction, chemical shift perturbations (CSP) can be monitored in both a protein-centric and a ligand-centric NMR experiment. In the former, a heteronuclear single quantum coherence spectroscopy (HSQC) experiment is performed on a $^{13}C/^{15}N$ labelled protein in the presence and absence of an unlabelled ligand – if the protein binds the ligand, the nuclei close to the interaction site will experience a chemical shift perturbation, allowing to pinpoint the binding site if previously unknown[46]. A ligand-centric NMR experiment, called saturation transfer difference (STD), by contrast measures the 1D spectrum of the ligand, either without the target protein, or in large excess of it; the two spectra are then compared and subtracted, and the difference, if any, is an indicator of binding[47]. The downsides of using NMR are the need for a deuterated solvent system, or the use of solvent suppression techniques, such as WATERGATE[48] and, with CSP, the need to isotopically label target protein.

The biophysical phenomenon that underpins fluorescence polarisation (FP) is based on slower rates of rotation of a fluorophore when bound to a large macromolecule, meaning that fluorescently-tagged chemical probes will tumble more slowly when complexed with proteins. As a result, one can monitor the anisotropy of emission following plane-polarised excitation; free molecules (i.e. unbound to the target) will emit in an isotropic fashion, whereas those bound to a molecule will likely exhibit high anisotropy of emission[49]. Thus, by using a fluorescent molecule or covalently attaching a fluorescent dye to one, it is possible to monitor target binding;

conversely unlabelled compounds can be used to monitor the displacement of a fluorescent tracer to measure binding kinetics[50]. The upside of the technique is the ease of applicability to a screening format, its downside is the requirement for fluorescently-modified ligand.

The biophysical principle of fluorescence resonance energy transfer (FRET), where fluorophores within ~80 Å exchange energy, has in the past been exploited to create a proximity assay to monitor ligand-protein interactions applicable for screening[51,52]. Typically, the molecule is directly conjugated to a fluorescent tag (tracer) and the protein is expressed with an epitope tag recognised by a fluorescently-labelled antibody. If the binding occurs between the compound and the protein, FRET will be observed between the two fluorophores. As with FP, the technique can be implemented into a screening format, however, it requires both protein and compound modification.

In contrast to the previously presented techniques, X-ray crystallography provides the full structural picture of the binding mode of the molecule to the protein. The two commonly used approaches for obtaining a protein crystal structure with the compound bound are co-crystallisation and soaking. In a co-crystallisation experiment, the protein is complexed with the compound first and then allowed to crystallise, which on one side may reduce crystal lattice artefacts, on the other hand additional molecules in solution will make crystallisation itself more difficult as well as produce differences in resolution between different crystals with different

ligands[53]. In a soaking experiment, the crystal of the apo- form is obtained first, followed by the addition of the compound to the crystallisation drop; this approach is more consistent between experiments and can be applied for screening of ligands, however, it may yield false negatives if the ligand cannot reach the binding site due to the crystal lattice[54], or if ligand binding induces a conformational change within the protein that results in lattice disruption[55].

1.2.2 Fluorescence anisotropy and BRET-based techniques to study cellular target engagement

Whilst the above-presented techniques are immensely useful in the early stages of drug discovery, they primarily deal with an isolated protein, usually recombinant (and sometimes only a particular domain). This, whilst informative, does not take into account the cellular context of the target, nor does it provide insight into the compound's cellular MoA, which as mentioned before, can contribute to high attrition rates within the pharmaceutical industry[56]. As such, additional biophysics-based methods have been developed to look at protein-target interactions in a physiological context.

Firstly, the above-mentioned fluorescence polarisation assay can be adapted to a cellular environment to monitor probe-target interactions. This requires the attachment of an appropriate (for cellular assays) fluorophore to the probe of choice, with the criteria being permeability and non-polarity to ensure it doesn't interfere with the compound's normal MoA, as well as high quantum yield and extinction

coefficient and the absence of pH-induced spectral shifts. Due to anisotropy, the technique can clearly differentiate between bound and unbound molecules of the probe, and it can also be applied to study compound engagement in tissue or even in live animal studies. However, it can only go so far as demonstrating that the probe has engaged a macromolecule within the cell – it cannot necessarily comment on what exactly the compound has bound, requiring additional experiments for target deconvolution. In other words, unless the probe is highly selective, an ensemble of macromolecules will be probed in parallel. Initial studies from the Weissleder group used BODIPY-labelled olaparib, to study PARP1 target engagement[57]. More recently, the technique has also been used to examine the cellular target engagement of ibrutinib, a Bruton's tyrosine kinase (BTK) inhibitor[58].

As mentioned before, FRET is commonly used as a biophysical technique to study compound binding *in vitro*. By replacing the donor fluorophore with a bioluminescent molecule, such as the NanoLuc luciferase[59], the technique becomes adaptable to in-cell studies, as one overcomes the limitations inherent to FRET, notably the background signal as a consequence of the illumination and potential for photobleaching and UV-induced damage to cellular components[60]. This allows the bioluminescence resonance energy transfer (BRET) to be used to monitor cellular protein-compound interactions. In such an experiment, the protein is transiently expressed in the cells of interest fused to the NanoLuc luciferase, with the cell-permeable fluorescent ligand for the target acting as a tracer. In the absence

of a competitor, the BRET signal is high and diminishes as the competitor's concentration is increased; this approach has successfully been used to profile histone deacetylase (HDAC) and protein kinase inhibitors[61,62].

1.2.3 Phenotypic methods are increasingly relevant

Out of the 50 first-in-class NMEs approved between 1999 and 2008, more than half (28) were discovered via phenotypic screening, in contrast to only 17 from target-based approaches[56]. Although the exact fraction of molecules that are discovered as a result of phenotypic screens has later been disputed[63], the relevance of phenotypic screens to drug discovery is not to be downplayed. On its surface, a phenotypic screen measures the response in terms of cellular behaviour to the presence of the small molecule. In recent years, advances in high-content imaging, as well as image analysis and quantification have vastly broadened the scope of phenotypic screening, resulting in the term 'high-content screening' to describe automated microscopy and image analysis screens[64], usually with the aid of multiplexed dyes and 'cell painting'[65] that allow one to conduct more precise phenotypic screening and understand heterogeneity in response (rather than bulk readouts). High-content screening has made it possible to report on phenotypes as diverse as autophagy[66], neuronal degeneration following injury[67], adipogenesis[68] or even profile drugs for potential hepatotoxicity[69].

One advantage of a phenotypic versus target-based approach on a recombinant protein is that a phenotypic screen will, by default deliver a cell-active compound.

However, the mechanistic and target deconvolution studies will subsequently need to be performed in order to fully annotate the compound in terms of its MoA. The primary method used to examine the cellular effects of compounds in detail is via chemoproteomics.

1.3 Chemoproteomics to enable drug discovery

1.3.1 Advances in mass spectrometry and the birth of proteomics

In 1989, the invention of electrospray ionisation meant that suddenly it became possible to ionise, vaporise and finally analyse large macromolecules, including proteins, by mass spectrometry (MS)[70]. Subsequently, the first report of MS analysis of tryptic digests of proteins separated by sodium dodecyl sulfate polyacrylamide gel electrophoresis (SDS-PAGE) began to appear in the 1990s[71,72]. Simultaneously, algorithms for peptide fingerprinting were developed[73], followed by algorithms for the analysis of MS/MS spectra[74,75], enabling unequivocal identification of proteins from peptides via database search. The subsequent development of a quadrupole ion trap mass spectrometer[76] and data-dependent acquisition methods that select peptides for fragmentation based on abundance[77] allowed for high-resolution, high-throughput identification of proteins from even complex mixtures of peptides. Today, with off-line pre-fractionation, it is possible to obtain the entire proteomes of yeast[78], or even human[79] with concomitant identification of thousands of proteins. Moreover, the development of stable isotope labelling techniques[80] and tandem mass tags[81] have paved the way towards

quantitative proteomics, where relative abundances of peptides between groups can be calculated, allowing to readily track proteome changes.

The first proteomics experiments designed to annotate small molecules (Figure 1) revolved around tracking global changes in the proteome following compound addition to the cells[82]. While immensely useful for elucidating molecule's MoA and giving mechanistic insights, it suffers from two major drawbacks. Firstly, it is limited (usually by the instrument's resolution power) to only the most abundant species within the mixture, thus proteins with low expression level might not be present in the dataset. Secondly, it merely tells us the downstream effects of the compound with only tangential information on what species are actually engaged within the cell.

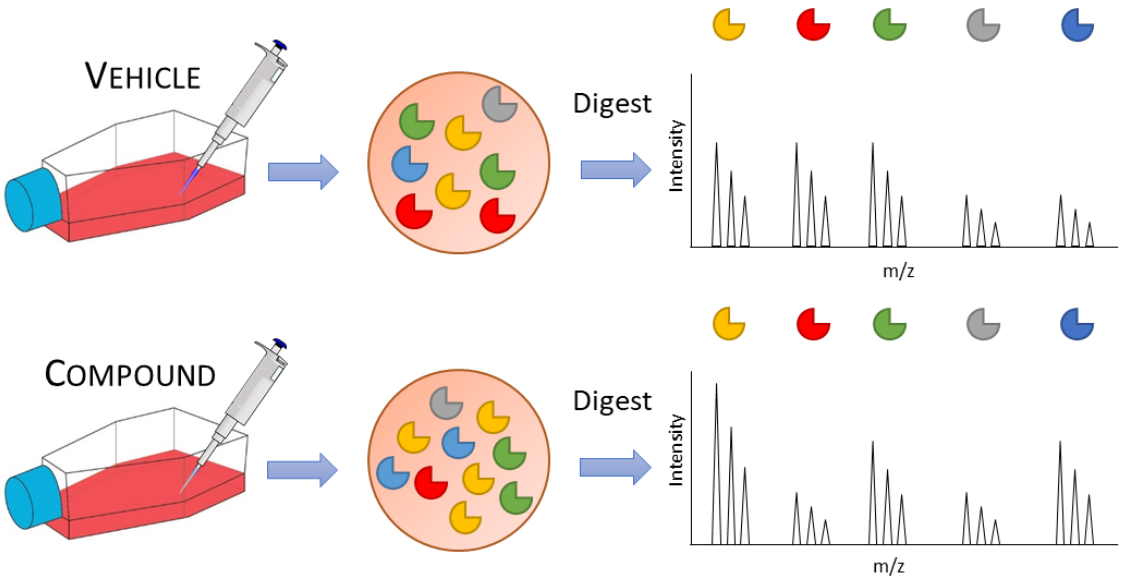


Figure 1: Global proteomic analysis of a compound. The compound is added to the cells, which after an incubation period are then harvested, lysed and analysed by MS to compare proteome changes.

This approach has, for example, been used to compare the proteomes of neuroblastoma cells treated with the two enantiomers of ibuprofen. While most of

the proteome changes detected were of highly abundant proteins, such as the cytoskeleton and the metabolic enzymes, the (*S*)-enantiomer showed upregulated levels of proteins involved in fatty acid synthesis and antioxidant activity, providing mechanistic explanations for ibuprofen's potential neuroprotective role in Alzheimer's disease[83].

1.3.2 Affinity chromatography and ABPP including clickable analogues

Targeted chemoproteomic approaches, in contrast to global proteomics, attempt to directly determine the proteins engaged by a given small molecule. Pulldown methods based on affinity chromatography have been one of the earliest methods of assaying small molecule-target interactions[7]. Typically, the molecule is immobilised on a solid support, which is followed by incubation with the biological analyte (such as cell lysate) and following elution, results in the enrichment for the target protein (as well as off-target interactors). The molecule has to be immobilised in a fashion that does not preclude target binding. If the target is unknown, an understanding of structure-activity-relationships are critical to the design of appropriate active and inactive (negative control) affinity probes, although the SAR in question only applies to the phenotype-driving targets. In order to differentiate between specific and non-specific binders, the analyte can be pre-incubated with an unbound competitor probe. SDS-PAGE followed by Western Blot (WB) is generally used to confirm target engagement via enrichment of the target; conversely target deconvolution usually requires MS analysis (Figure 2).

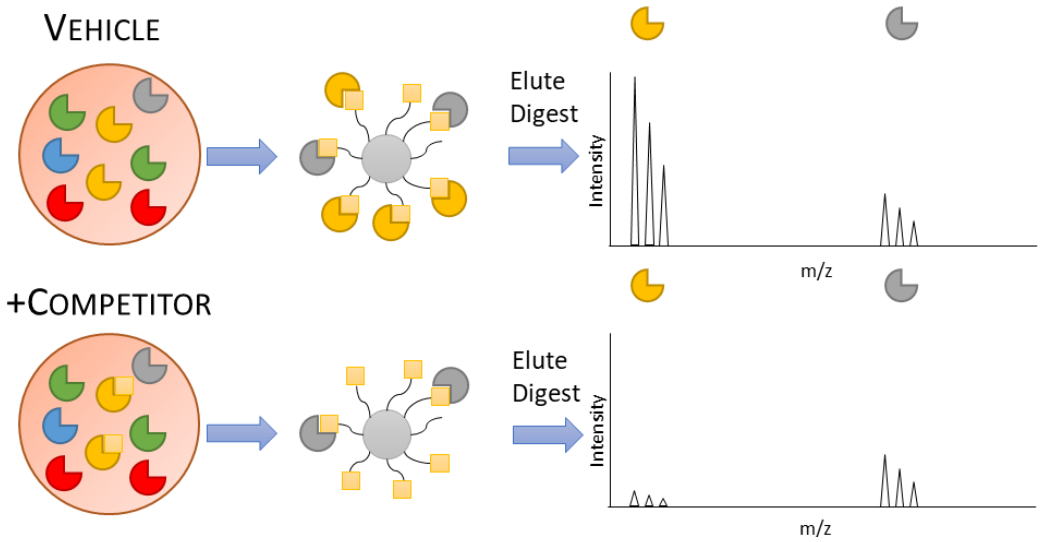


Figure 2: Enrichment for target protein by compound immobilisation on bead. The addition of a pre-incubation step with an unlabelled competitor helps distinguish true targets (yellow) from non-specific interactors (grey)

A number of different supports and capture strategies are summarised in Table 2.

Resin Used	Characteristics
Agarose/Sepharose	Does not readily bind proteins on its own, reducing non-specific interactions; easily functionalised, physically and chemically-resistant, which can be enhanced further by crosslinking
Polyacrylamide	Can be synthesised to have specific physicochemical properties, easily functionalised
Polystyrene Beads	Can be made to incorporate paramagnetic particles, allowing for separation using a magnet without the need for centrifugation steps (Dynabeads ®)
AminoLink Resin	Readily crosslinks with proteins
Capture Chemistry	**Characteristics**
Streptavidin	The covalent attachment of streptavidin allows for enrichment for biotin-containing probes and their targets
N-hydroxysuccinimide (NHS) ester	Readily reacts with free amines to form amides
Tosyl ester	Readily reacts with free amines to form amides
Epoxide	Readily reacts with free amines to form β-hydroxyamines
Azlactone/oxazolone	Readily reacts with free amines to form amides, resin more stable than NHS
Carboxylic acid groups	Less reactive on their own; require activation with carbodiimide compounds EDC and DCC
Iodoacetyl/Maleimide	Readily reacts with thiol groups
Hydrazide	Generally reactive nucleophilic group

Table 2: Commonly used strategies for compound immobilisation on bead.

Rosiglitazone (Avandia) is a thiazolidinedione (TZD)-based PPARγ agonist that was initially approved for the treatment of diabetes[84]. However, following a large meta-analysis of 42 clinical trials involving rosiglitazone, the FDA issued a

restriction on the drug due to an increased risk of myocardial infarction and, albeit borderline insignificant, an increased risk of death from cardiovascular events[85]. Recently, affinity chromatography was used to examine the off-target interactions of rosiglitazone, pioglitazone and the TZD scaffold; each molecule was conjugated to an epoxy resin, and incubated with extracts from rat heart tissue. MS analysis of the captured protein revealed substantial promiscuity of the TZD scaffold, as the three compounds engaged a number of dehydrogenases, ion channels, and mitochondrial enzymes, which could explain the cardiovascular side effects associated with rosiglitazone treatment[86]. A similar approach was used to deconvolute the targets of the teratogenic compound thalidomide; a carboxyl-containing thalidomide derivative was conjugated to ferrite-glycidyl methacrylate (FG) beads via amide coupling. This was followed by incubation with HeLa cell extracts, washing and elution with free thalidomide; proteomic analysis revealed CRBN and DDB1, which together form an E3 ubiquitin ligase complex, as proteins captured by thalidomide[87].

A variant of affinity chromatography utilizes a mixture of immobilised broad spectrum kinase inhibitors in order to capture a large proportion of the kinome. This approach, referred to as 'kinobeads'[88], enables profiling of more specific kinase inhibitors. By outcompeting the resin through the use of an unmodified compound, one obtains the picture of all the kinases engaged by the inhibitor with high affinity, and has been used to profile and re-profile a number of small molecule kinase-targeting compounds[89].

Activity-based protein profiling (ABPP) is an extension of this method. At its core, ABPP involves the use of a probe with a reactive warhead that covalently binds the target proteins, as well as a tag that enables enrichment or visualisation. The development of a bioorthogonal copper-catalysed azide-alkyne cycloaddition (CuAAC) reaction that can be performed *in situ*[90,91] has in addition led to the development of alkyne-tagged probe analogues, where the probe can be incubated with the cells and, following lysis, conjugated to a resin or a fluorophore for visualisation. This can be performed on live cells, making the assay more physiologically relevant. ABPP was recently used in a study of compounds targeting ubiquitin-specific proteases (USPs); an irreversible USP inhibitor was profiled by synthesising an alkyne-containing derivative, which was incubated with U2OS cells. The cells were then lysed and azido-TAMRA-biotin (AzTb) was clicked to the probe, both enabling the visualisation of protein targets by SDS-PAGE in-gel fluorescence but also the capture of the probe on a NeutrAvidin resin. MS analysis revealed that it binds a number of members of the USP family, but also that its covalent warhead could bind a number of oxygenases, dehydrogenases and glutathione transferases[92].

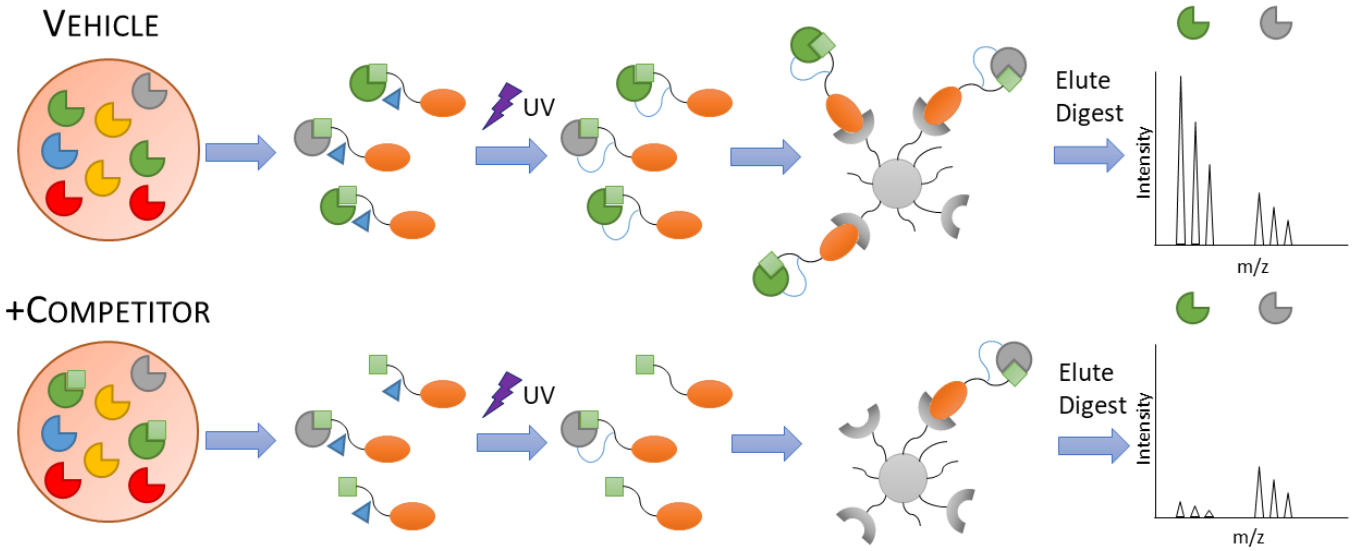


Figure 3: Generalised workflow for an ABPP experiment. An ABPP probe will usually contain the small molecule 'bait' attached to a moiety that facilitates covalent attachment (by photoreactivity, as shown on the diagram, or through the use of covalent warheads or by using an innately covalent 'bait') as well as a species that facilitates attachment to beads, such as biotin for streptavidin capture. As with previous methods, preincubation with an unlabelled competitor allows to distinguish between 'true' hits and non-specific interactions.

It needs to be pointed out that some of the above examples of ABPP make use of an irreversible covalent compound – given that the protein is thus directly conjugated to the molecule, even multiple washing steps or denaturing conditions do not result in the dissociation of one from the other. If non-covalent compounds are used instead and one wants to ensure capture (particularly relevant for compounds with low affinity for their cognate targets), the chemical probe should be modified to feature not only its chemotype (referred to as 'bait'), but also a capturing warhead (such as a reactive sulfonyl fluoride or a diazirine photoreactive moiety capable of covalent modification), alongside the affinity label (Figure 3).

This method was used to profile the cellular targets of staurosporine, a natural product that inhibits kinases with little selectivity. The authors designed a cell-permeable staurosporine derivative with a diazirine warhead and a clickable alkyne tag. The probe was added to HepG2 cells and the cells were ultraviolet (UV) irradiated to induce covalent labelling of staurosporine targets. Following lysis, the alkyne group was initially clicked to rhodamine azide (for in-gel fluorescence scanning readout) and then biotin-azide for pulldowns and MS analysis, the latter indicating 43 different cellular targets engaged by the compound[93]. A similar approach was used to profile dasatinib, a dual Src/Abl inhibitor[94]. Today, synthetic strategies exist for a number of cell-permeable clickable linkers with diazirine warheads[95] or even live-cell imaging tags[96] that can be more readily attached to a given probe to facilitate ABPP.

As mentioned earlier, one of the main reasons for compound failures in clinical trials is toxicity/adverse effects, which is why a strong case can be made for chemoproteomic target identification approaches as de-risking strategies. The previously-described clinical trial of a molecule BIA 10-2474 was abruptly halted after some participants developed life-threatening neurological lesions. Subsequent use of ABPP to examine potential off-target interactors of the molecule and its metabolites revealed that the compound inhibited lipolytic serine hydrolases and disrupted the lipid profile of neuronal cells, whereas its metabolites irreversibly inhibited aldehyde dehydrogenases, likely explaining the observed

neurotoxicity[22,23]. Similarly, C646 is a Michael-acceptor containing p300 inhibitor. Its undesirable promiscuity towards off-target cysteine residues was recently demonstrated by ABPP, with the use of a clickable analogue firstly by in-gel fluorescence and subsequently via MS analysis[97].

Whilst useful for their ability to detect the cellular targets of small molecules and potentially differentiate between on- and off-target interactions, the above listed methods have a disadvantage in the form of the need to chemically modify the molecule in question. First of all, this may not always be possible (not all labs have access to an organic chemistry lab and custom synthesis orders can be prohibitively expensive for some groups). Moreover, even if synthesis is possible, the SAR of the molecule must be sufficiently understood such that the modification does not disrupt the compound's ability to engage its target(s) and several linker conjugating strategies would be needed to more properly cover this aspect. As a result, in recent years, there has been an increased interest in label-free chemoproteomic methods.

1.3.3 Cellular Thermal Shift Assay (CETSA) and MS-CETSA

The cellular thermal shift assay (CETSA) derives from the previously-described thermal (T_m) shift assay. Unlike the conventional thermal shift assay, however, CETSA is applied to complex sample matrices and relies on the removal of unfolded protein aggregates by centrifugation; the proteins engaged by the ligand will be thermally stabilised and thus remain in solution at higher temperatures

relative to vehicle. SDS-PAGE followed by WB is then used to visualise target engagement[98,99].

In a CETSA-WB assay, lysate or live cells are incubated with a small molecule for a period of time to allow compound entry. Following harvesting and aliquoting, the aliquots are subjected to a temperature gradient, cooling and lysis followed by high *g* centrifugation to remove aggregated and unfolded proteins. The samples are then loaded onto SDS-PAGE for later analysis by immunoblot. An increase in signal for the treated group at higher temperatures is indicative of thermal stabilisation and thus target engagement of the native protein (Figure 4).

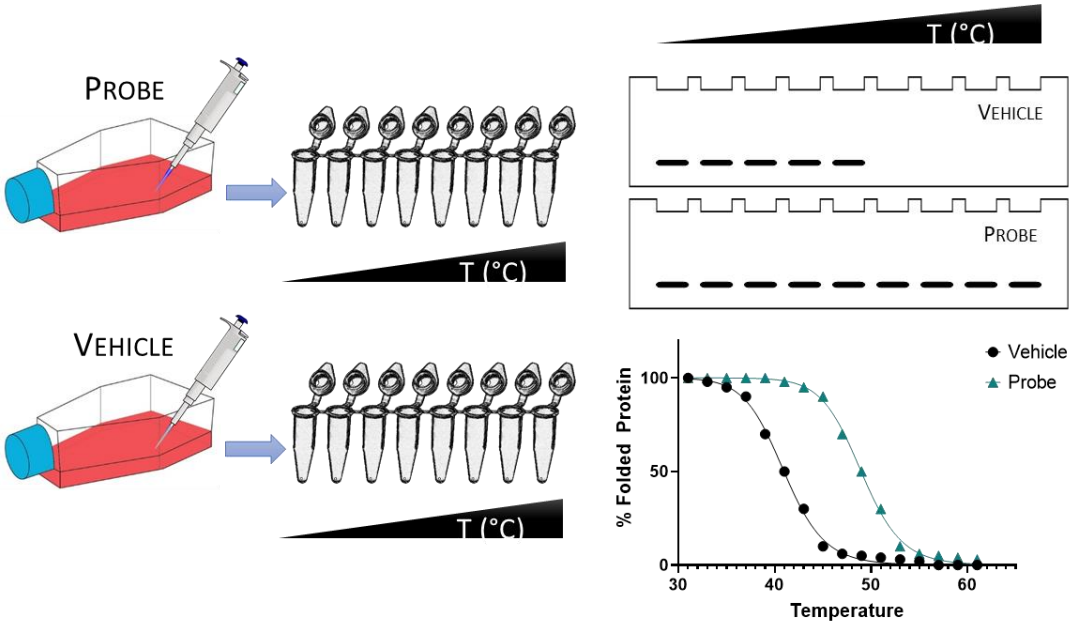


Figure 4: The typical workflow for a CETSA assay in live cells to validate target engagement in a cellular context. Typically, the cells are treated with either the compounds or the vehicle, which is followed by aliquoting and differential heat treatment, which leaves in the treated group a greater amount of the target protein, which can be detected by Western Blot.

In a conventional CETSA experiment, the concentration of the compound is fixed in the treated group, whereas the temperatures are varied to generate a thermal aggregation curve. The thermal aggregation curves for a target protein in the presence and absence of a compound can then be compared. Conversely, it is also possible to apply a heat challenge at a single temperature, usually derived from the CETSA melting curves, in the presence of increasing concentrations of the ligand. This is known as isothermal dose-response fingerprinting (ITDRF) and generates the curve of thermal stabilisation of the target as a function of ligand concentration, as well as an EC_{50} value for each ligand, making ITDRF studies useful for ranking compounds in terms of their affinities as well as SAR studies.

The use of CETSA to validate cellular target engagement was initially demonstrated on existing probes present in the literature, such as p38α targeting compounds[98]; proof-of-concept experiments on lysate and live cells were also performed with dihydrofolate reductase (DHFR) and thymidylate synthase (TS) inhibitors, respectively methotrexate and raltitrexed[99]. Interestingly, disparity between live cell and lysate data is often indicative of poor compound permeability, and was demonstrated on stapled peptide-based MDM2 family inhibitors, many of which exhibited strong thermal shifts in lysate but lack thereof on live cells[100]. Conversely, disparity between data from different cell lines can be indicative of potential mechanisms of resistance by occlusion of the binding site through interacting proteins or cellular efflux – a recent CETSA study measuring the effects of crizotinib in different cell lines found that the resistant cell lines also exhibited

smaller thermal shifts of anaplastic lymphoma kinase (ALK+), which is the target of crizotinib; subsequently it was demonstrated that resistant cells overexpress beta-catenin, which through binding to ALK+ physically prevents crizotinib from reaching the binding site[101].

In recent years, CETSA has established itself as one of the methods for probe candidate validation, as evidenced by an uptick in publications featuring the method in the last 3 years (PubMed). An example of that was the validation of BM-1197, an inhibitor of the anti-apoptotic Bcl family of proteins. Initial, encouraging data exhibiting *in vitro* target binding and cell viability effects was coupled with CETSA-WB to demonstrate cellular target engagement of both Bcl-xL and Bcl-2[102]. Moreover, CETSA can be used to validate hits obtained in other chemoproteomic assays: the profiling of the compounds ABT-199 (venetoclax) and RG7388 (idasanutlin) by affinity chromatography showed a number of putative off-target interactors, such as the mismatch repair member PMS1, which were subsequently validated in a CETSA assay[103].

By multiplexing different antibodies, one can in principle study the target engagement of a probe to a variety of targets. However, if the putative target is unknown, a combination of CETSA and mass spectrometry (MS-CETSA, or thermal proteome profiling, TPP) can be used for target deconvolution and measurable elucidation of the proteome engaged by the small molecule. Initially, the proof-of-concept data came from the analyses of cellular targets of (*S*)-crizotinib

and broad spectrum kinase inhibitors including staurosporine, with successful profiling of over 3000 proteins in each study; moreover, ferrochelatase was established as being an off-target of kinase inhibitors[104]. Conversely, methotrexate was discovered to be a thermal stabiliser of thymidylate synthase (TS), likely as a result of its conversion to a more potent polyglutamate derivative. This means that, in principle CETSA can give more detailed information about the compound's MoA by examining not only its own cellular targets, but also the targets of its metabolites[105]. More recently, MS-CETSA was used to successfully validate two antimalarial drugs pyrimethamine and E64d, as well as establish purine nucleoside phosphorylase as the target of the compounds quinine and mefloquine[106]. Similarly, CETSA can also demonstrate secondary stabilisation effects as a result of protein-protein interactions. Dasatinib, whilst not being an inhibitor of the Abelson murine leukemia viral oncogene homolog 1 (ABL1), was nonetheless found to destabilise the v-crk avian sarcoma virus CT10 oncogene homolog-like protein (CRKL) protein; as ABL1 is a non-receptor tyrosine kinase and CRKL interacts with phosphorylated proteins, it is possible that dasatinib blocks the phosphorylation of CRKL interactors by ABL1, and this lack of interactions is what lowers CRKL's melting temperature[107]. In a more recent example, MS-CETSA was used to gain insight into palbociclib's (a cyclin-dependent kinase 4/6 inhibitor) MoA as a proteasomal activator[108].

MS-CETSA, whilst in principle capable of profiling large portions of the proteome for engagement by the molecule, has got a number of limitations. Firstly, protein

abundance is an issue with holistic MS experiments, as the signal from more abundant, housekeeping proteins can drown out the signal from the less-expressed but perhaps more significant proteins. Secondly, not all proteins are inherently amenable to CETSA, in other words the energy of molecule binding is not always sufficient to manifest itself in a noticeable thermal shift, which can be the case with larger proteins. In addition, secondary thermal effects can play a role – if the ligand disrupts a protein-protein interaction (PPI), this can result in one, or both of the proteins being thermally destabilised; moreover if two proteins are constitutively in a tight complex, the stabilisation of one by a ligand will confer residual stabilisation on the other, which will appear as a hit – on one side this is a critical strength of CETSA, as it expands its purview to potentially elucidating PPIs, however, any potential hits have to be validated to elucidate whether they occur from primary or secondary effects. Lastly, whilst cells tend to be incubated with compounds for the minimum amount of time needed to achieve saturation (usually 30 minutes), there is the possibility of the compound initiating gene expression changes, resulting in concentration-dependent abundance changes that can be detected as hits across all temperatures (including control group, making such false positives comparatively easier to spot) despite not being direct binders of the molecule.

Thermal proteome profiling (TPP) can be performed as a 2-dimensional experiment, where both the temperature effects and the effects of varying compound concentration on proteome stability are taken into account. In conjunction with MS, this can be effectively used to elucidate the off-target

interactions of a small molecule, and was recently used to examine the off-targets of a pan-HDAC inhibitor panobinostat[109] in order to provide a mechanistic explanation for a number of side effects the compound can cause. Both HepG2 live cells and cell lysates were studied, which enables the differentiation between direct and indirect effects of the drug, and four proteins were identified this way; two of them were canonical panobinostat targets, whereas the other two, tetratricopeptide repeat domain 38 (TTC38) and phenylalanine hydroxylase (PAH) were previously unidentified. Subsequent validation confirmed both proteins as binding partners of panobinostat.

1.3.4 Alternative readout methods for CETSA

Conventionally, when examining target engagement of a compound using CETSA, the read-out technique of choice is SDS-PAGE in conjunction with WB. Whilst the technique is relatively simple and allows for fast data acquisition and quantification via densitometry, it has a number of drawbacks, including poor antibody choice leading to spurious WB readouts[110] as well as issues with densitometry itself[111]. In addition, CETSA sample preparation relies on the removal of thermally-denatured proteins via centrifugation following lysis, which can create additional problems if the detergent used for cell lysis has the capacity to resolubilise unfolded aggregates. This has prompted the development of readout methods for quantifying CETSA assays that not only circumvent the need for WB, but also discriminate between the folded and the unfolded versions of the target protein *in situ* without the need for separation.

Analogously, one can transfect the cell with a constitutively-expressed gene encoding a target of choice fused with a split reporter and thus combine CETSA with a complementation assay, whereby thermal stabilisation of the target by the probe will result in subsequent signal following enzyme complementation. Note that, whilst this assay bypasses the common issues associated with CETSA-WB, careful optimisation must be performed to ensure that a number of factors don't confound the results, namely that the tag has no stabilising effects on the protein, the compound of choice does not stabilise the tag instead of the target, and that the unfolding of the protein also results in the concomitant unfolding of the tag. Such an approach was recently used with a galactosidase tag (ProLabel ®) to examine the binders of the histone lysinemethyltransferase SMYD3[112], as well as with a split luciferase (NanoLuc®) to examine the binders of a mutant isocitrate dehydrogenase variant IDH1-R123H[113]. It must be stressed, however, that this CETSA application, by necessitating modification of the protein and transfection of cells, is no longer strictly 'label-free'.

A separate method involves the use of two AlphaScreen ® proximity assay[114] beads coupled to enzyme-linked immunosorbent assay (ELISA)-compatible antibodies that recognise the protein only in the folded state. In this way, the mixture of the beads and antibodies is added following the heat pulse and lysis of the cell pellet; because the antibodies discriminate between the folded and the unfolded forms of the protein, there is in principle no need for centrifugation steps. The mixture is then transferred to an appropriate microplate and allowed for the target-antibody-

bead complex to develop. Subsequent imaging of the plate provides a quantitative measure of the signal without having to resort to densitometry and image analysis. With the use of liquid handling and compound dispensing aperture, the assay has thus been adapted to a high-throughput format to profile agonists of p38α and thymidylate synthase, as well as the androgen receptor[98,115,116].

1.3.5 Aims of the project

The aims of the project were to explore and further develop some of the proteomics techniques presented in the introduction to annotate a number of small molecules that showed interesting phenotypes.

Chapter 2 concerns the analysis of the compound SJ-172550. Originally discovered as a binder of the murine double-minute family member MDMX and thus an inhibitor of the interaction between MDMX and p53, subsequent evidence has emerged that put the compound's specificity into doubt. SJ-172550 was thus profiled using a combination of biophysical (ITC, thermal shift) and chemoproteomics (in-gel fluorescence, CETSA-WB) techniques to reveal highly undesirable issues with promiscuity. Subsequent analysis also shows that the compound is inherently unstable.

Chapter 3 describes the development of an algorithm to validate MS-CETSA output data. Using the dataset obtained from performing a 2D-CETSA-MS experiment with a protein-arginine methyltransferase 5 (PRMT5) inhibitor GSK3326595, a

MATLAB script was written to analyse the dataset of 5926 proteins and select potential hits based on both the magnitude and the goodness-of-fit based on representing the data as a 3D surface model. The algorithm manages to identify a second protein thermally stabilised by the compound in the assay.

Chapter 4 introduces the work on peroxisome proliferator-activated receptor gamma (PPARγ) targeting compounds. Some of them produce interesting effects in adipose tissue, most notable amongst them is the morphological switch from white to beige adipose. The compounds are examined using CETSA-WB, initially on immortalised cell lines, and subsequently on the 3T3-L1 adipose cell line. The limitations of the immunoblot readout are discussed.

Chapter 5 describes the development of an AlphaScreen-based readout method for CETSA assays for studying the intracellular target engagement of PPARγ-targeting compounds. The assay involves the AlphaScreen proximity assay with a dual antibody recognition that overcomes the immunoblot limitations and presents an opportunity for a microplate-based CETSA screen in a cellular context. The optimisation steps of the assay are described, detailing the antibody selection process, assays on recombinant PPARγ, lysate and finally live cells. The development of a CETSA-based screen is also described, with preliminary results.

Chapter 6 reports on the use of the TPP assay to annotate a known PPARγ agonist rosiglitazone, in terms of its MoA and potential off-target interactions. Given that

PPARγ is not a highly-abundant protein, a number of optimisation steps are outlined, designed to maximise the detection of PPARγ. The results of the TPP assay are described in the larger context of PPARγ signalling and gene expression. Overall, the combination of biophysical, cell-based and chemoproteomics methods can and should be used for small molecule appraisal in early stages of compound development. On one side, the methods presented aim to detect undesirable properties within compounds that potentially disqualify them from being pursued further. On the flipside, they can also provide more detail on the compound mechanism of action and the underlying biology, as well as detect putative interactions necessary to achieve the desired phenotype, which may prove to be useful in future strategies for compound or therapy design.

2. SJ-172550, a Putative MDMX Inhibitor: Revealing a Compound's Undesirable Characteristics by a Combination of Cell Biology, Biophysics and Proteomics

2.1 Introduction

2.1.1 The p53/MDM2/MDMX Axis

P53 is a tumour suppressor protein that was discovered simultaneously by two groups in the late 1970s as the protein sequestered by the SV40 tumour-virus oncoprotein, which induced cell transformation[117,118]. Since then, research into the protein has elucidated a number of functions the protein performs to safeguard genome stability, arrest cell cycle and stimulate apoptosis, giving it the nickname 'the guardian of the genome'[119]. Whilst normally present at low levels[120], in response to stimuli, such as DNA damage[121], ribosomal stress[122], hypoxia[123] or metabolic stress[124], p53 levels increase as the protein accumulates in the cell. The tumour-suppressive effects of p53 are subsequently mediated by interactions with the p53-response element on the DNA[125] where p53 acts as a transcription factor[126], resulting in the expression of a number of genes, such as p21, which mediates cell cycle arrest[127,128] or the pro-apoptotic members of the Bcl-2 family[129]. Other proteins regulated by p53 include factors responsible for cellular senescence[130], DNA repair[131], protection from oxidative stress[132] and metabolic shift away from glycolysis[133,134].

Wild-type p53 binds DNA as a tetramer, and many of the mutation 'hot spots' for p53 are in the region of the DNA binding site[125,135]. Interestingly, the majority of p53 mutations are missense, rather than null[136], as mutant p53 can act as an oncogene, enhancing the cell's tumorigenic potential[137]. This is partially due to the fact that mutant p53 can oligomerise with wild-type (WT) p53, inactivating the entire oligomer in a dominant negative fashion[138] and partially due to mutant p53 potentially recognising and regulating transcription of novel DNA elements, perhaps in tandem with other transcription factors[139,140]. As a result, it is of little wonder that 50% of tumours harbour p53 mutations[136].

In the remaining 50% of tumours, p53 has to be inactivated in a different fashion for tumorigenesis to proceed, as the presence of uninhibited, wild-type p53 will likely result in tumour regression[130]. As mentioned earlier, basal levels of wild-type p53 in untransformed cells are low. This is because the levels and transcriptional activity of p53 are kept in check by the murine double minute (MDM; human isoforms are sometimes referred to as human double minute, HDM) family of proteins. The first one, MDM2, was discovered in the 1990s to be an oncogenic protein that binds to and inhibits transcription from p53 response elements[141]. In addition, through its zinc-finger type RING (Really Interesting New Gene) domain, MDM2 ubiquitinates and signals p53 for degradation[120,142,143], explaining the low p53 levels under basal conditions. MDM2 is amplified in about 7% of human cancers[144], with sarcomas, including the human U2OS cell line, being a prominent example[145]. In other cases, suppression of p53 by overexpression of MDM2 is

achieved without an increase in copy number, either via mutations within the promoter region of its gene[146] or by aberrant upstream signalling[147].

The second MDM family member discovered was MDMX, also known as MDM4, and it was found to have similar characteristics[148]. Indeed, the two proteins share a 31% sequence similarity[149] and whilst the RING domain in MDMX lacks E3 ligase activity and can't ubiquitinate p53 on its own, the two proteins oligomerise via their RING domains[150] and MDMX enhances MDM2 ubiquitination[151]. As is the case with MDM2, amplification and/or overexpression of MDMX is often present in malignant cell lines[152,153].

2.1.2 The MDM2/p53 and MDMX/p53 Interaction as a Target

Due to the highest sequence similarity between MDM2 and MDMX occurring within the p53 binding site, the two proteins bind the same N-terminal (NTD) region of p53[154]. The region is intrinsically disordered, however, adopts an amphipathic α-helical structure upon binding[155], and p53 mutants with increased residual helicity tend to bind MDM2 more strongly, mimicking the phenotype of p53 suppression[156]. Three residues within the p53 NTD play a key role, namely Phe19, Trp23 and Leu26. In the case of MDM2, the residues make key contacts with the MDM2 binding site (Figure 5). In addition, the interaction site forms a deep, hydrophobic cleft, structurally akin to a binding site, and as a result, the idea of pharmacologically blocking it to free p53 is not novel, beginning with peptides mimicking the p53 NTD[157,158]. To date, a number of potent MDM2 inhibitors have

been identified[159–161], with the canonical MDM2 inhibitor being the cis-imidazoline nutlin-3a[162].

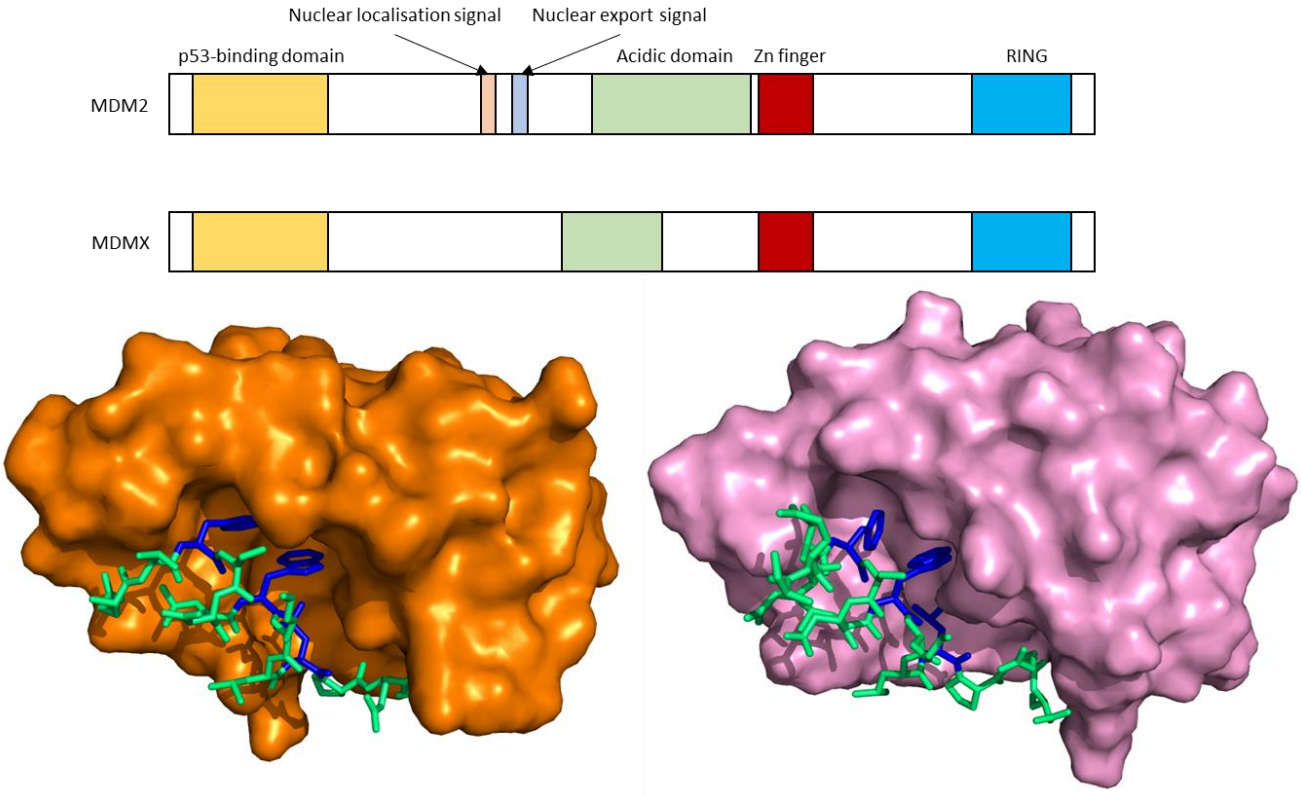


Figure 5: Domain comparison between MDM2 and MDMX. Top: sequence map of MDM2 and MDMX. Bottom: comparison between MDM2 (left) and MDMX (right) p53-binding sites in complex with the short p53 region (represented as sticks); the 3 key residues that make contacts (Phe19, Trp23 and Leu26) are highlighted in blue.

By contrast, despite the sequence similarity, the p53-binding site on MDMX differs structurally from that of MDM2. Crystallographic data indicates that the binding groove on MDMX is shallower and differently-shaped[163], and modelling studies show that MDMX, owing to greater rigidity, has lower affinity for p53 and an even lower affinity for MDM2 inhibitors mimicking p53, such as nutlin-3a[164]. As a result, there are comparatively few compounds that target the MDMX-p53 interaction[165]. This is particularly troubling given the mounting evidence that the

two proteins can compensate for one another, with siRNA knockdown of MDMX being shown to act in a synergistic manner with nutlin-3a[166,167]. This has created a demand in recent years to develop MDMX-targeting compounds, not only for a therapeutic reasons, but also to help understand the complex interplay between MDM2, MDMX and p53 (Figure 6).

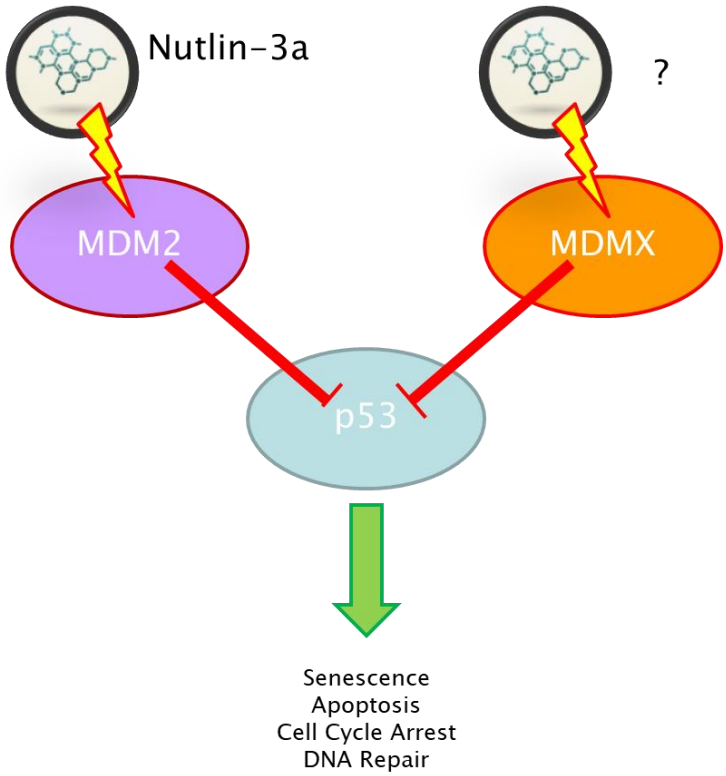


Figure 6: Summary of the p53-MDM2-MDMX axis. The tumour suppressor p53 governs the cellular processes that bring about cell cycle arrest, apoptosis and senescence, as well as genome repair, however it is sequestered and degraded by the oncogenes MDM2 and MDMX. Nutlin-3a inhibits MDM2, however the MDMX inhibitor landscape is less-well explored.

2.1.3 SJ-172550 as a first-in-class MDMX inhibitor

A recent development in the field of MDMX-p53 inhibition has been the discovery of SJ-172550, a small molecule capable of specifically blocking said interaction[168].

SJ-172550 was discovered in an *in vitro* HTS based on an FP assay looking at the displacement of a fluorescein isothiocyanate (FITC) labelled p53 NTD from a recombinant MDMX construct comprised of GST-MDMX(1-185), with an EC_{50} value of 0.84 µM. Structurally, the compound's benzylidene-5-pyrazolone scaffold (Figure 7) was postulated to mimic the three key residues by which p53 engages MDMX, and despite the presence of an electrophilic Michael acceptor, SJ-172550 was originally purported to be a non-covalent inhibitor. Furthermore, SJ-172550 was shown to potentiate the cytotoxic effects of nutlin-3a in two cell lines with elevated levels of MDMX, Weri1 (retinoblastoma) and transgenic SJSA-X cells stably overexpressing MDMX, however, the phenomenon only occurred at concentrations of SJ-172550 exceeding 20 µM.

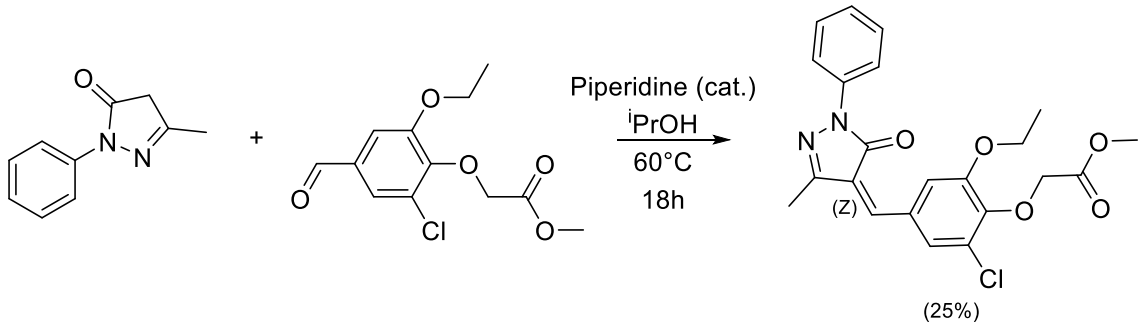


Figure 7: Structure and synthesis of SJ-1 72550. The synthesis proceeds via a Knoevenagel condensation to produce a Michael acceptor containing product, SJ-172550. The compound's vibrant orange coloration (see below for photos) suggests the presence of a conjugated π-bond system chromophore.

A subsequent analysis of the compound revealed some interesting features. Whilst originally thought to be a competitive inhibitor of MDMX, subsequent MS data indicated that SJ-172550 interacts with its target in a covalent manner, binding cysteine thiols via conjugate addition[169]. The formation of SJ-172550 adducts was

demonstrated by MS despite the cysteine residue being present at a significant distance away from the active site and buried within the interior of the recombinant MDMX construct, which suggested SJ-172550 could potentially partially unfold its target. In addition, the presence of reducing agents strongly attenuated SJ-172550's capacity to bind MDMX, and an analogue with the benzylidene moiety reduced, thus incapable of functioning as a Michael acceptor, could not engage MDMX at all. These inconsistencies and an overall lack of cellular target engagement data raised questions about SJ-172550 usefulness as a tool compound to study MDMX. Nonetheless, due to its 'first-in-class' status, it finds frequent use in literature[170–172], which unfortunately is often the case with potentially low-quality probes and underscores the importance of appropriate early-stage compound assessment. As a result, SJ-172550 was synthesised (Figure 7) and analysed using a combination of cell biology, biochemical, biophysical and proteomic methods.

2.2 Preliminary cheminformatic, biophysical and phenotypic studies on SJ-172550

2.2.1 Cheminformatic analysis of the compounds predicts promiscuity

Initial analysis of the compound via a number of commonly-available algorithms for small molecule appraisal has raised a number of concerns. These algorithms can be useful tools for biologists, as they predict aggregative or promiscuous properties based on the structure of the molecule, and as a result their use is often advised in

drug discovery projects[173]. Firstly, the Shoichet Aggregator Advisor scipt[174] revealed that, whilst not sharing any structural features, the compound's calculated LogP of 3.5 makes it a potential aggregator compound. Secondly, two separate analyses with algorithms that predict compound promiscuity, Badapple[175] and cAPP[176], revealed that the compound's structure is predictive of promiscuity (Figure 8), containing a 5-membered heterocyclic alkylidene – this motif, similarly to alkylidene rhodanines, exhibits PAINS-like behaviour as it can react with free nucleophiles such as cysteines[177]. Reduction of the Michael acceptor group removes the warning (see below for further analysis of the reduced analogue).

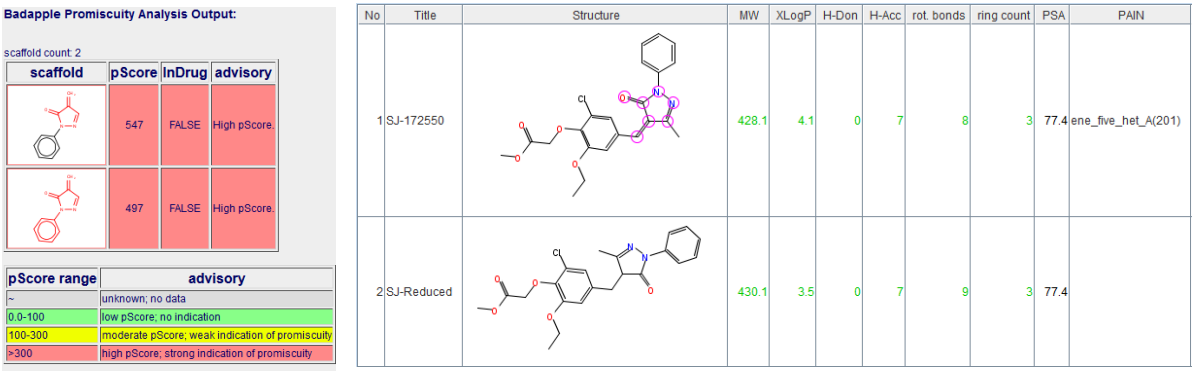


Figure 8: Cheminformatic analysis of SJ-172550 for potential promiscuity. Left: Analysis with Badapple indicates that the compound's scaffold has a high promiscuity score. Right: Analysis with cApp shows that the compound's scaffold falls into the category of PAINS, unlike an analogue with the Michael acceptor reduced, dubbed SJ-Reduced (see below).

2.2.2 Inconclusive DSF data on SJ-172550 binding to MDMX

Initially, SJ-172550's ability to bind MDMX in a thermal shift assay was examined. To this end, recombinant GST-MDMX(1-120) was expressed in *E. coli* and purified, with the removal of the GST tag (for full sequence, refer to the experimental section). Afterwards, the protein was assayed via differential scanning

fluorimetry in accordance with previously-established protocols[36] using SYPRO Orange as the dye. The experiment produced inconclusive data (Figure 9); whilst the T_m for the DMSO-containing vehicle is 67 °C and that with SJ-172550 present is 71 °C, with an apparent ΔT_m of 4 °C, this data is confounded by high initial fluorescence of the protein, making curve-fitting difficult, and an overall reduction of SYPRO Orange fluorescence by SJ-172550. Note that reduction in fluorescence can be indicative of quenching of SYPRO Orange by the compound, or the compound inducing protein aggregation which reduces the overall surface for the dye to bind to.

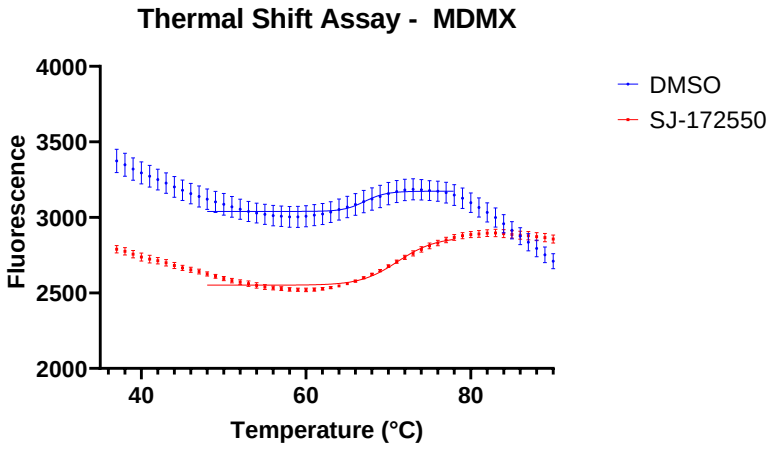


Figure 9: Differential scanning fluorimetry data for MDMX using SJ-172550. The curve was fitted between the onset and endpoint of unfolding and the melting temperature (T_m) was calculated as the mid-point on the sigmoidal curve.

2.2.3 ITC Confirms that SJ-172550 binds MDMX, possibly in a covalent fashion

Isothermal titration calorimetry experiments in HEPES-NaCl and non-reducing conditions subsequently confirmed that SJ-172550 binds the MDMX construct *in*

vitro, however, saturation on the curve was not achieved (Figure 10), despite high concentration of protein in the cell, which is indicative of low affinity (K_d >13 µM). As the area under each peak reflects the heat evolved during each ligand injection[178], the broad nature of peaks was suggestive of a slow event such as the formation of a covalent interaction[179]. Interestingly, analysis of the data also predicted a 1.3 binding stoichiometry, rather than 1, as would be anticipated, suggesting that the mode of binding might be more complex than originally speculated. As a result, it was decided to assay the binding of SJ-172550 to MDMX via mass spectrometry.

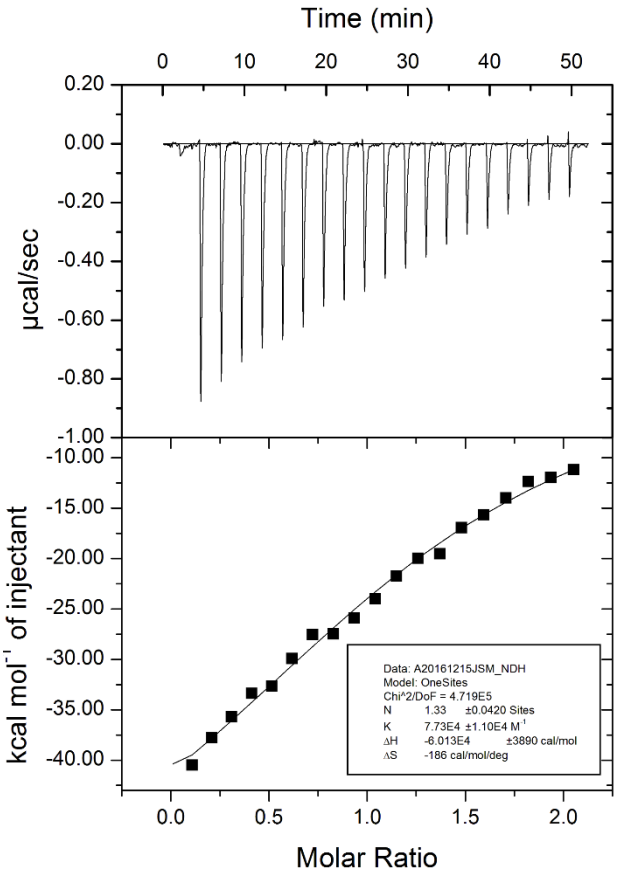


Figure 10: Isothermal titration calorimetry data for MDMX using SJ-172550. The top panel shows exothermic peaks as a result of each injection and the bottom panel shows normalised integrated heats as a function of molar ratio of SJ-172550 to MDMX.

2.2.4 MS data confirms multiple covalent adduct formation

We assessed the binding of SJ-172550 to MDMX by mass spectrometry; to this end, the untagged recombinant MDMX (1–120) protein was incubated with a slight excess (1:1.4) of SJ-172550 in HEPES-NaCl buffer (pH 7.5) at room temperature for one hour, and the presence of three adducts indicated that the compound potentially binds three cysteines present within the MDMX construct (Figure 11, top). Of note is the fact that, upon repetition with different incubation times, the cysteines are engaged in differing amounts (Figure 11, bottom), suggesting different accessibility of the cysteines and perhaps hinting at potential unfolding or destabilising of the protein by the compound. Indeed, following long incubations of four or more hours, no unlabelled MDMX remains in solution.

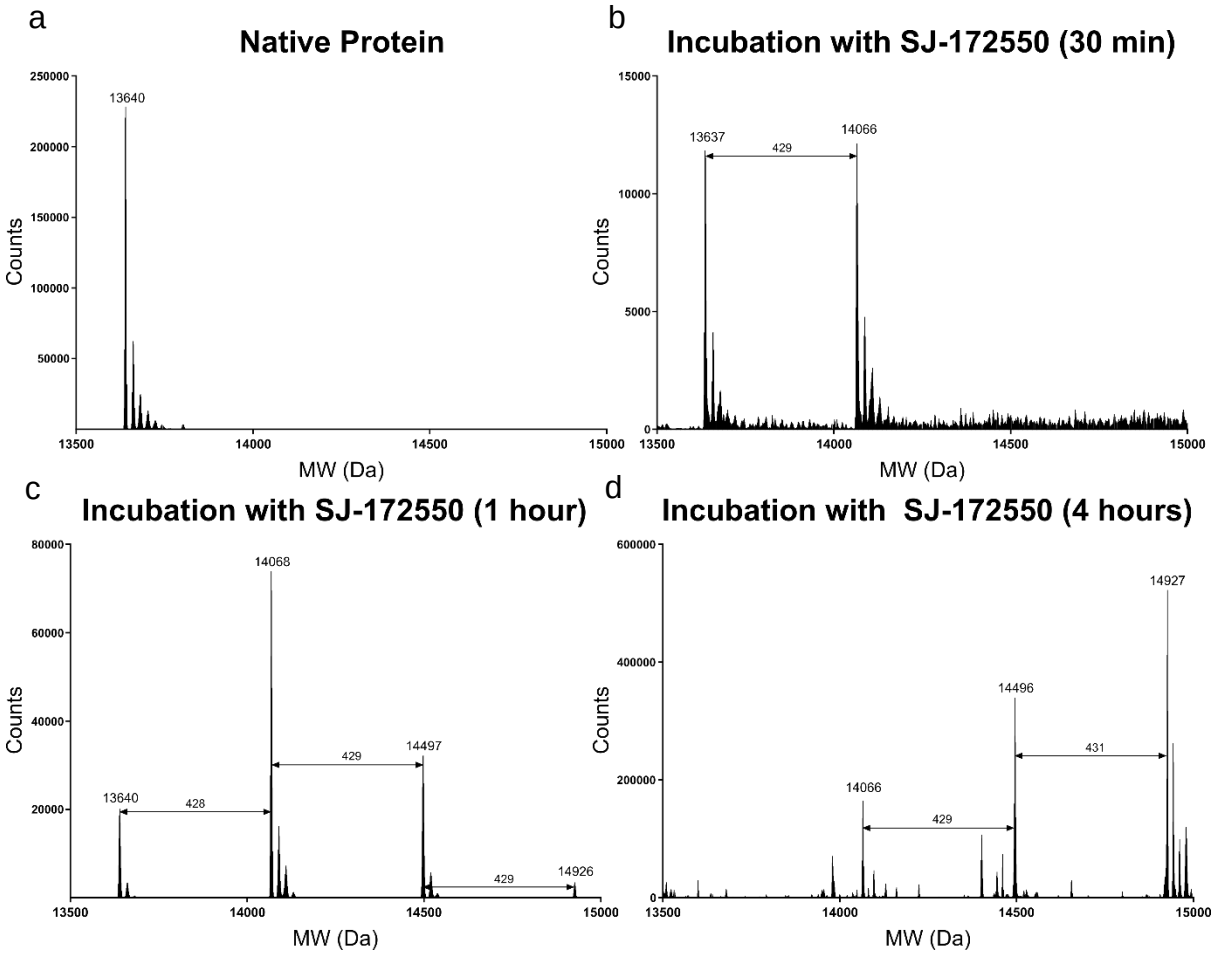


Figure 11: The results of the incubation of the native MDMX(1-120) construct with SJ-172550 for varying amounts of time. Recombinant MDMX construct (a) was incubated with SJ-172550 for 30 minute (b), 1 hour (c) and 4 hours (d), and the mixture was analysed by MS for the presence of adducts. The construct's predicted MW from sequence is 13639.70. SJ-172550's MW is 428.87.

Interestingly, earlier reports suggested that only the closest cysteine to the p53-binding pocket is engaged by SJ-172550, however, the MDMX construct used in the study was shorter (residues 23–111) than the construct used in this experiment and as a result had no other cysteines[169], raising concerns about the compound's potentially indiscriminate reactivity towards cysteines.

2.2.5 The reduced analogue of SJ-172550 is unable to bind MDMX

In order to test the hypothesis that the Michael acceptor within SJ-172550 is responsible for binding the cysteines within the MDMX construct, the compound was reduced with sodium borohydride, to produce the reduced analogue, dubbed SJ-Reduced (Figure 12):

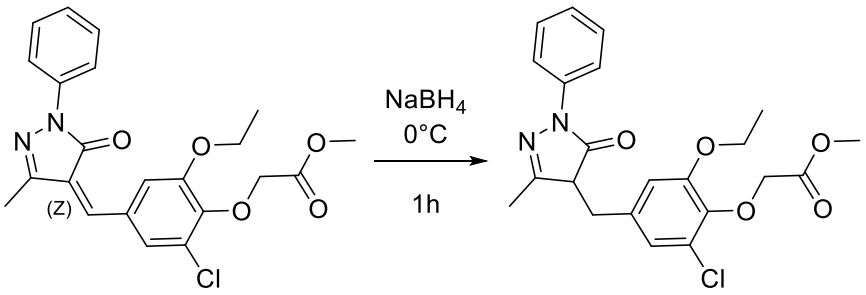


Figure 12: Synthesis and structure of SJ-Reduced. SJ-Reduced has the Michael acceptor reduced and is thus unable to undergo conjugate addition with thiols and other nucleophiles.

The compound was then assayed for its ability to bind MDMX, through a combination of ITC and MS (Figure 13). Neither method detected any measurable binding to the recombinant protein, suggesting SJ-172550 primarily exhibits its function by covalently binding MDMX via its Michael acceptor moiety.

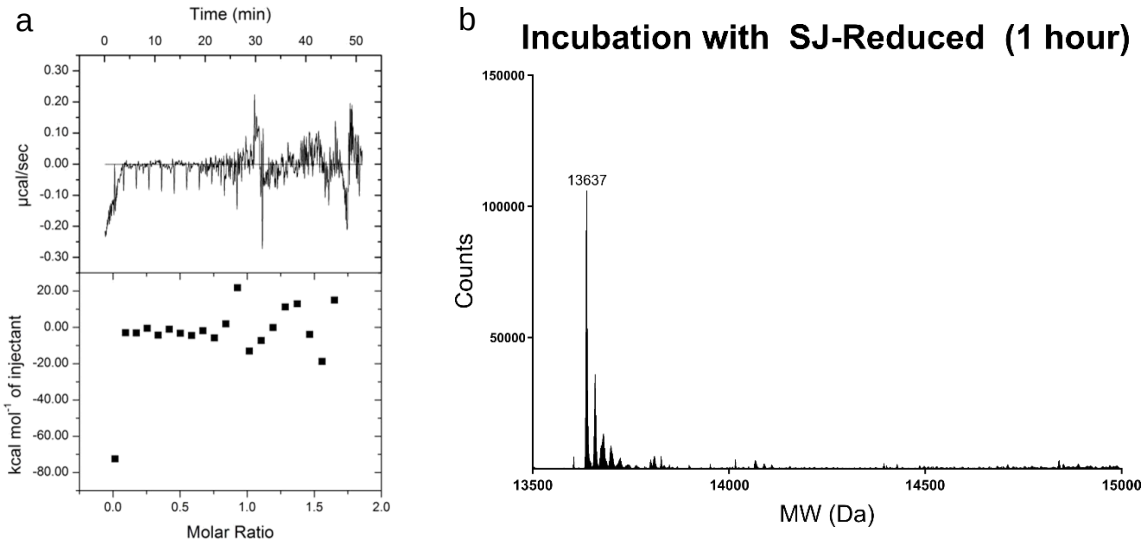


Figure 13: SJ-Reduced is unable to bind MDMX. Isothermal titration calorimetry data (a) show no changes in enthalpy associated with binding when SJ-Reduced is injected to MDMX. Mass spectrometry data (b) indicate that even after an hour of incubation, no adducts form between the protein and the compound.

2.2.6 Cell viability investigations

In light of the data showing SJ-172550 to be an MDMX binder with potential specificity issues, the compound's ability to induce cell death in a suitable cell line was validated. As mentioned before, U2OS cells are p53-wild type osteosarcoma cells, and previous data show that they are less sensitive to MDM2-only targeting strategies, such as nutlin-3a, and thus require dual inhibition of both MDMX and MDM2, with siRNA knockdown of MDMX lowering the EC_{50} of nutlin-3a by about an order of magnitude[167]. On its own, SJ-172550 was only mildly cytotoxic, with an EC_{50} value of 47 µM (Figure 14), consistent with previous data obtained for Weri1 cells[168]. Conversely, SJ-Reduced exhibited very little toxicity, even at high concentrations. Moreover, nutlin-3a had an EC_{50} value of 14.8 µM, also consistent with previous data[167]. As a result, the rationale was that a sub-EC_{50} dose

of SJ-172550 would, analogously to the aforementioned siRNA knockdown of MDMX, lower nutlin-3a's EC_{50} in a cooperative cell-viability assay, assuming that the compounds were highly synergistic. Thus, it was decided to perform the Nutlin-3a cytotoxicity study with the addition of 10 µM SJ-172550. The EC_{50} for Nutlin-3a remained at 14.8 µM despite the presence of the MDMX inhibitor, casting doubt on whether the compound's cellular MoA occurs via inhibition of MDMX and prompting the need to validate the compound's cellular target engagement.

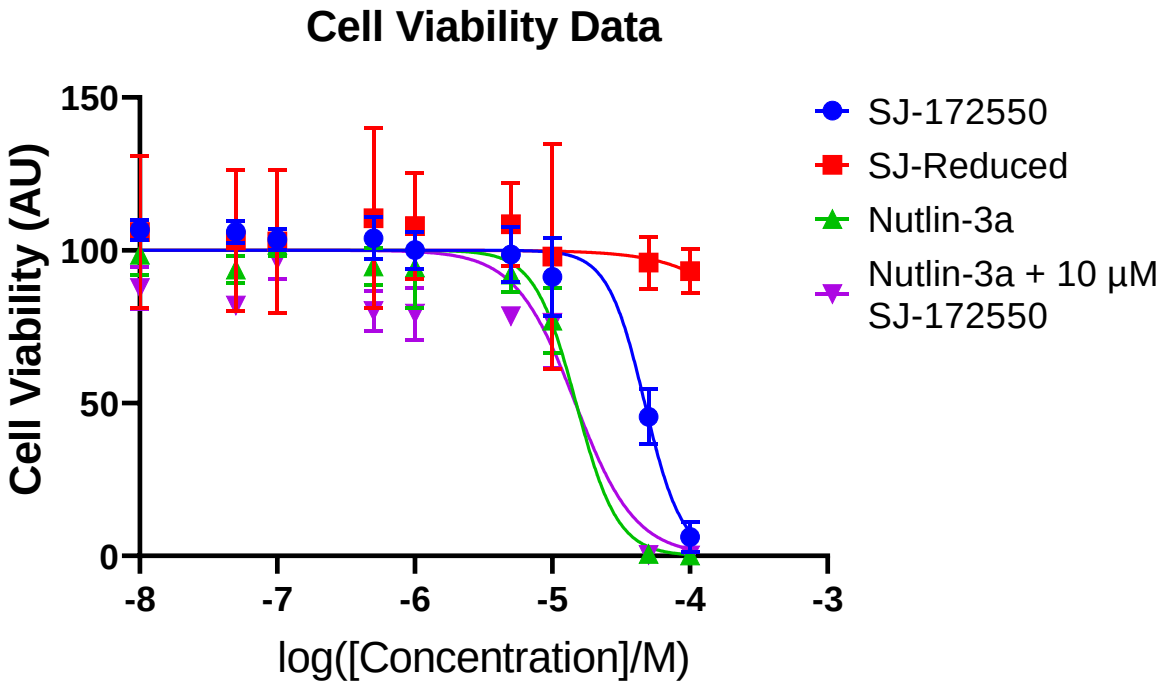


Figure 14: Cell viability data for SJ-172550, Nutlin-3a and the two compounds in combination. Following 72 h of incubation, the cells were assayed for viability with the Cell-Titer Glo cell assay. EC_{50} values: SJ-172550 (blue): 47 µM, Nutlin-3a (green): 14.8 µM, Nutlin-3a with 10 µM SJ-172550 in the medium (purple): 14.8 µM. The data were normalised to the DMSO value.

2.3 Evaluating cellular target engagement of SJ-172550

2.3.1 CETSA analysis shows SJ-172550 is not stabilising and possibly destabilising MDMX

Despite the evidence of SJ-172550 engaging MDMX *in vitro*, cellular engagement of its cognate target has not been validated in a relevant physiological model. As a result, it was decided to perform a CETSA-Immunoblot assay, using the aforementioned U2OS cells and test if SJ-172550 can stabilise MDMX in a cellular environment. Previous studies have shown that MDMX is amenable to CETSA, that is, exhibits cellular thermal shifts when cells are treated with p53-mimicking stapled peptides[100], and a similar protocol was followed.

Initially, using the same antibody as the one used in the aforementioned study, CETSA-WB showed no stabilisation of MDMX in the environment of U2OS cells, and perhaps even mild destabilisation (Figure 15), however, there were a number of additional bands present on the blot, which were attributed to non-specific interactions of the antibody. Lower MDMX signal for the SJ-172550 treated group, even at low temperatures, could indicate that the compound causes a proportion of it to aggregate and precipitate during the centrifugation steps. Nevertheless, it was decided to optimise the experiment to reduce the non-specific bands on the immunoblot.

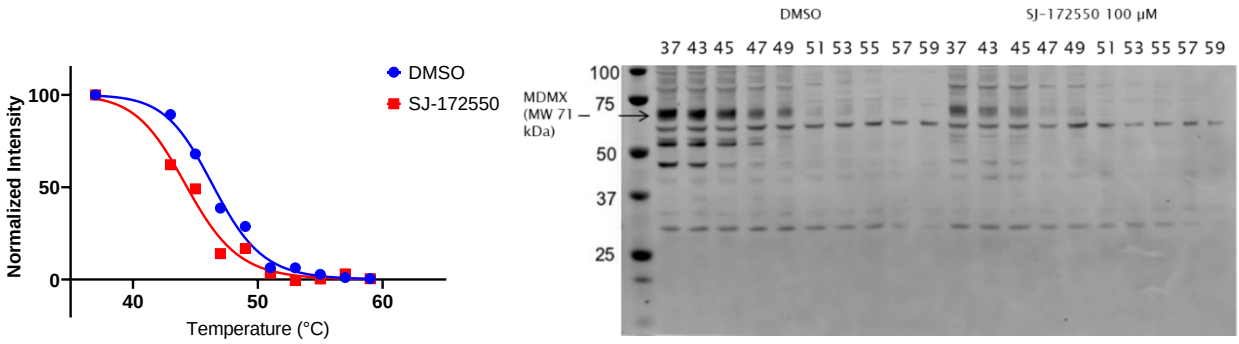


Figure 15: CETSA-WB Data for SJ-172550 in U2OS cells. The cells were incubated with either 100 µM SJ-172550, or equivalent volume of DMSO, for one hour, followed by aliquoting, heat pulse and centrifugation. The samples were visualised by SDS-PAGE followed by WB (right), and quantified by densitometry to produce the melting curves (left). The T_m values are as follows: DMSO: 46.5 °C, SJ-172550 44.3 °C, indicating a destabilisation by 2.2 °C. The data were normalised to the DMSO value.

Subsequently, the experiment was carried out with the same cells and SJ-172550 dosage (Figure 16), however, the blotting technique was changed. This time, no significant stabilisation or destabilisation was exhibited by SJ-172550. With the negative results of CETSA-WB, it would appear that the compound might not engage MDMX within a cellular environment.

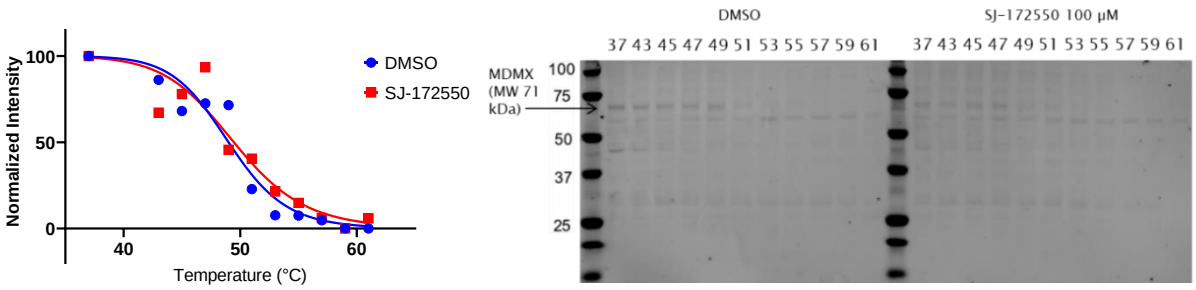


Figure 16: CETSA-WB Data for SJ-172550 in U2OS cells following optimisation. The cells were incubated with either 100 µM SJ-172550, or equivalent volume of DMSO, for one hour, followed by aliquoting, heat pulse and centrifugation. The samples were visualised by SDS-PAGE followed by WB (right), and quantified by densitometry to produce the melting curves (left). The T_m values are as follows: DMSO: 49.0 °C, SJ-172550 49.4 °C. The data were normalised to the DMSO value.

2.3.2 Synthesis and characterisation of a clickable analogue of SJ-172550

SAR data on SJ-172550 from molecular dynamics studies has previously shown that structural modifications at C4 of the benzylidene moiety do not preclude target binding due to the tail of the molecule pointing out of the binding site[168]. With this in mind, a structural analogue of SJ-172550 containing an alkyne moiety, called SJ-Alkyne was synthesised (Figure 17). The alkyne tail made the molecule clickable via the bioorthogonal copper-catalysed alkyne-azide cycloaddition (CuAAC) reaction[90], thus paving the way towards ABPP and enabling the clicking of biotin azide, for streptavidin-based matrix pulldown, or fluorescent dyes, for in-gel fluorescence studies.

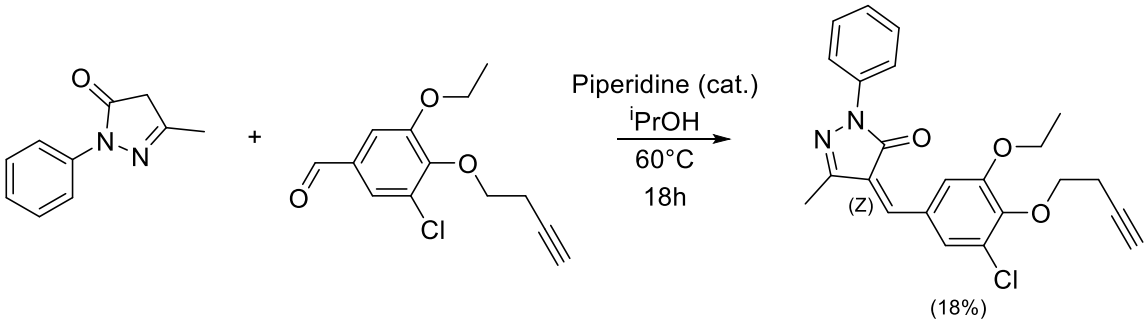


Figure 17: Structure and synthesis of SJ-Alkyne. Z isomerism was assigned by analogy to SJ-172550

The compound's ability to bind MDMX was validated, by MS, and indeed, the formation of covalent adducts with the recombinant protein was demonstrated (Figure 18).

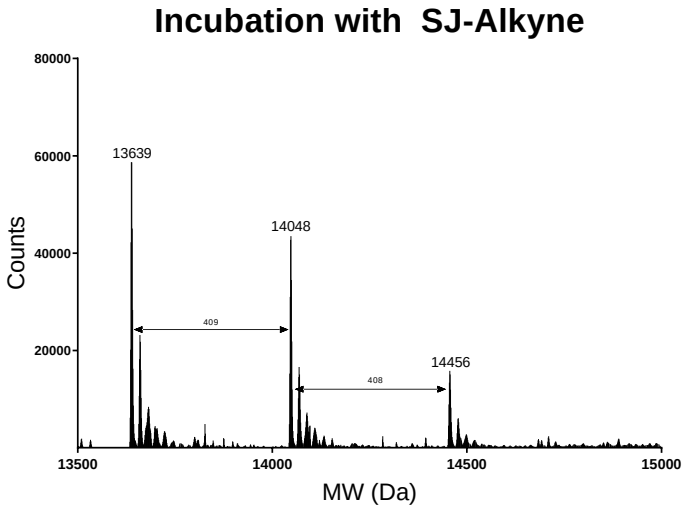


Figure 18: SJ-Alkyne can covalently bind to MDMX. Mass spectrometry data indicate that after an hour of incubation adducts form between the protein and the SJ-Alkyne. The compound's molecular weight is 408.88

In order to assay the compound's target engagement, initially SJ-Alkyne (or DMSO in the control group) was added to U2OS lysate, and incubated for 1 hour at 4 °C. This was followed by in-lysate click reaction with biotin-azide, and enrichment on a streptavidin resin. The experiment was performed twice, however, it yielded inconclusive results, as no protein was visibly enriched for (Figure 19), prompting speculation that the compound itself has certain physicochemical properties, such as aggregation or instability, which abrogate the pull-down assay.

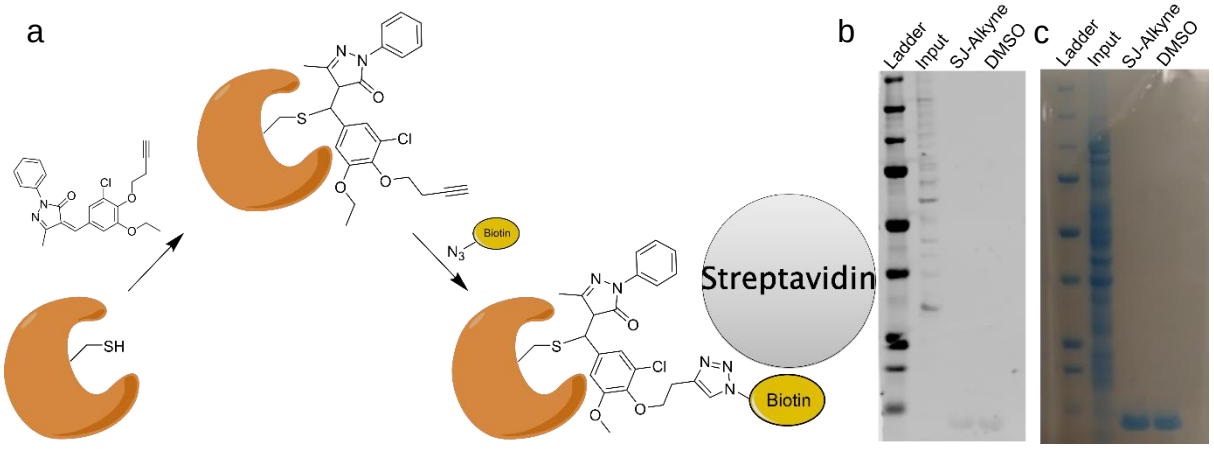


Figure 19: ABPP affinity pulldown assay. (a) The simplified scheme for the biotin-click pulldown assay using streptavidin resin. Briefly, the compound is incubated with SJ-Alkyne, and via click reaction covalently attached to biotin, followed by enrichment on streptavidin beads. (b) The results of the WB and (c) SDS-PAGE of the pulldown, where SJ-Alkyne and DMSO indicate what compound was initially incubated with the U2OS lysate. The experiment was performed twice without prior optimisation, representative blots shown.

In a follow-up experiment, instead of clicking biotin azide, cyanine-5.5-azide (a fluorescent dye) was conjugated. The resulting mixture was then loaded onto polyacrylamide gel and, following SDS-PAGE and separation, visualised on an imaging system to display the bands that correspond to the cognate target and perhaps some off-target interactors[92,97]. Interestingly, SJ-Alkyne was shown to label a significant portion of the proteome in a concentration-dependent manner (Figure 20), raising questions about the compound's specificity.

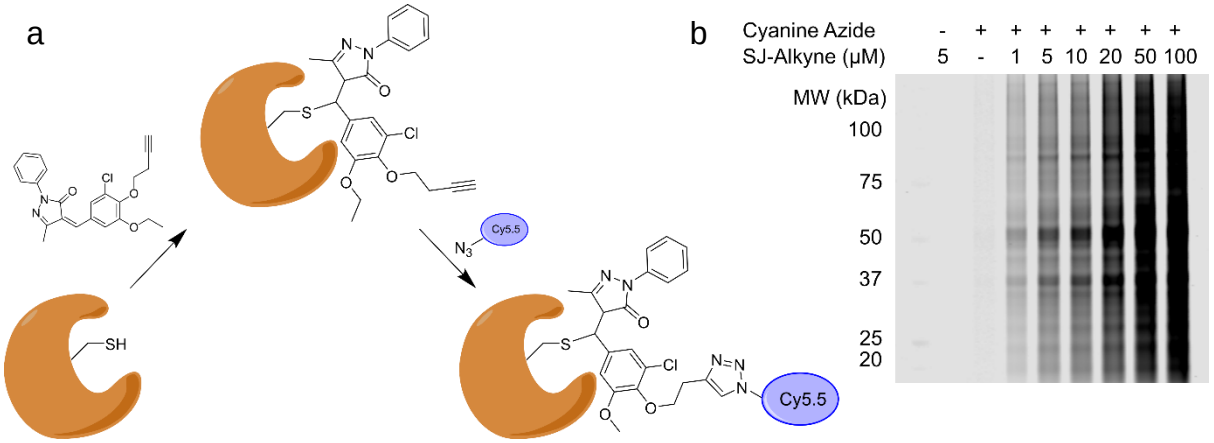


Figure 20: ABPP in-gel fluorescence assay. (a) The simplified scheme for the biotin-click in-gel fluorescence assay. Briefly, U2OS lysate is incubated with SJ-Alkyne, and via click reaction protein targets are covalently attached to a fluorescent dye, followed by in-gel fluorescence. (b) The results of the SDS-PAGE imaging, showing concentration-dependent labelling of the proteome by the compound.

In order to validate those results, a subsequent experiment was performed in the presence of a competitor as U2OS lysate was preincubated with increasing concentrations of SJ-172550. The presence of SJ-172550 reduced the labelling of the probe, whereas the presence of SJ-Reduced had no significant effect on labelling (Figure 21), increasing the amount of evidence that the compound exhibits its MoA via non-specific Michael acceptor conjugate addition to free thiols.

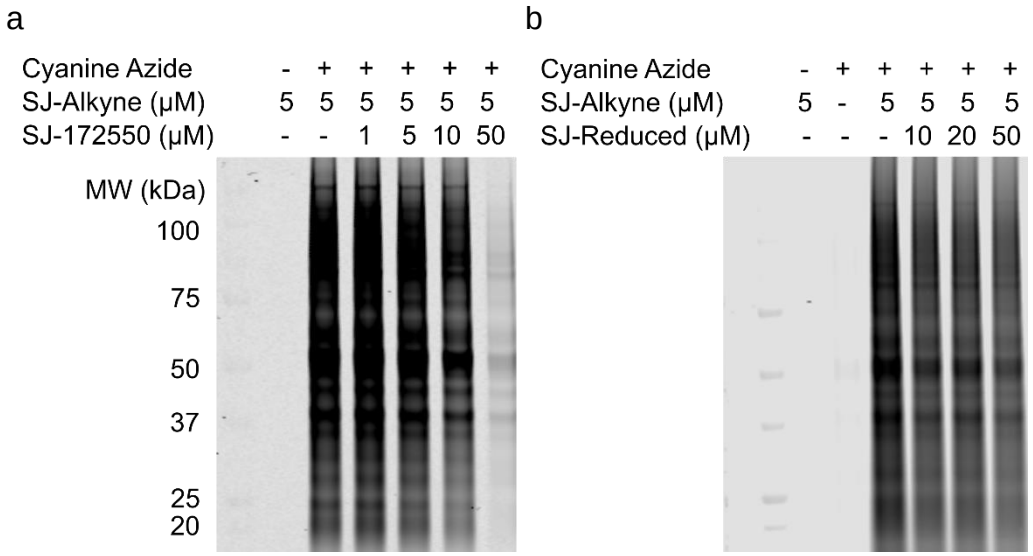


Figure 21: Competitive ABPP in-gel fluorescence assay. In-gel fluorescence was performed as before with SJ-Alkyne, however the lysates were pre-incubated with increasing concentrations of SJ-172550 (a), or SJ-Reduced (b). SJ-172550, but not SJ-Reduced significantly reduces SJ-Alkyne signal in the experiment.

2.4 Further physicochemical analysis of SJ-172550 and related compounds

2.4.1 Reactions of SJ-172550 with reducing agents

Following from the previous data that indicate SJ-172550 can non-specifically and covalently bind proteins through its electrophilic Michael acceptor moiety, the compound was incubated with two reducing agents, glutathione (cysteine-containing peptide) and TCEP (reducing agent not containing thiols) to assay for adduct formation. Incubation with equimolar amounts of glutathione followed by LC/MS analysis resulted in the appearance of a peak on the chromatogram, whose molecular weight corresponded to a covalent adduct between glutathione and SJ-172550 (Figure 22), demonstrating that SJ-172550, in addition to non-specifically binding cysteine residues can also bind nucleophiles on other small molecules, including the cysteine residue on the tripeptide glutathione, which is potentially

worrying given that the intracellular glutathione concentration is in the millimolar range[180].

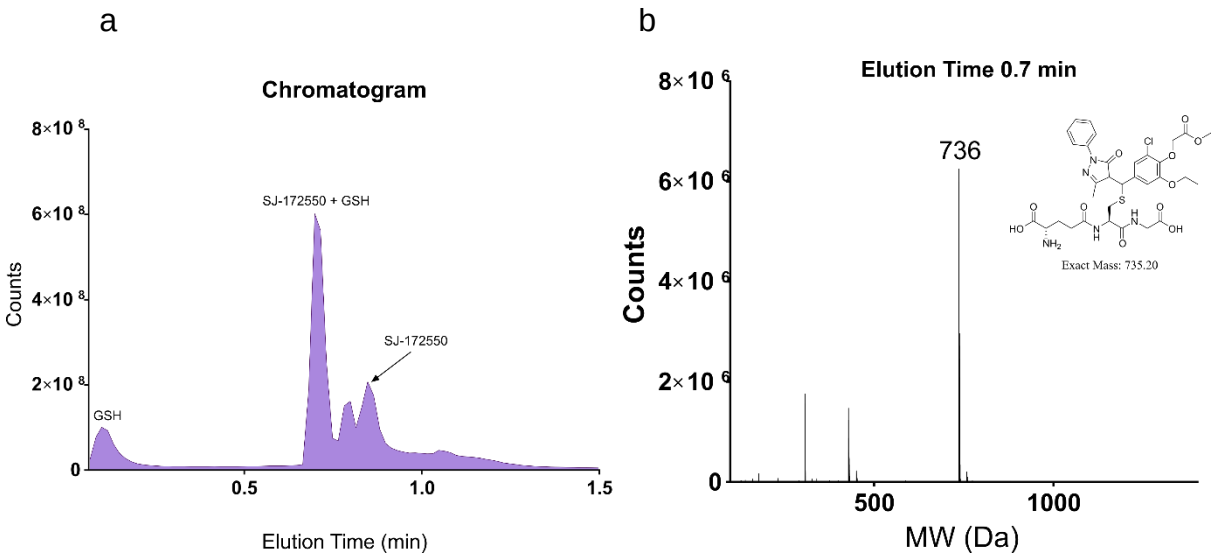
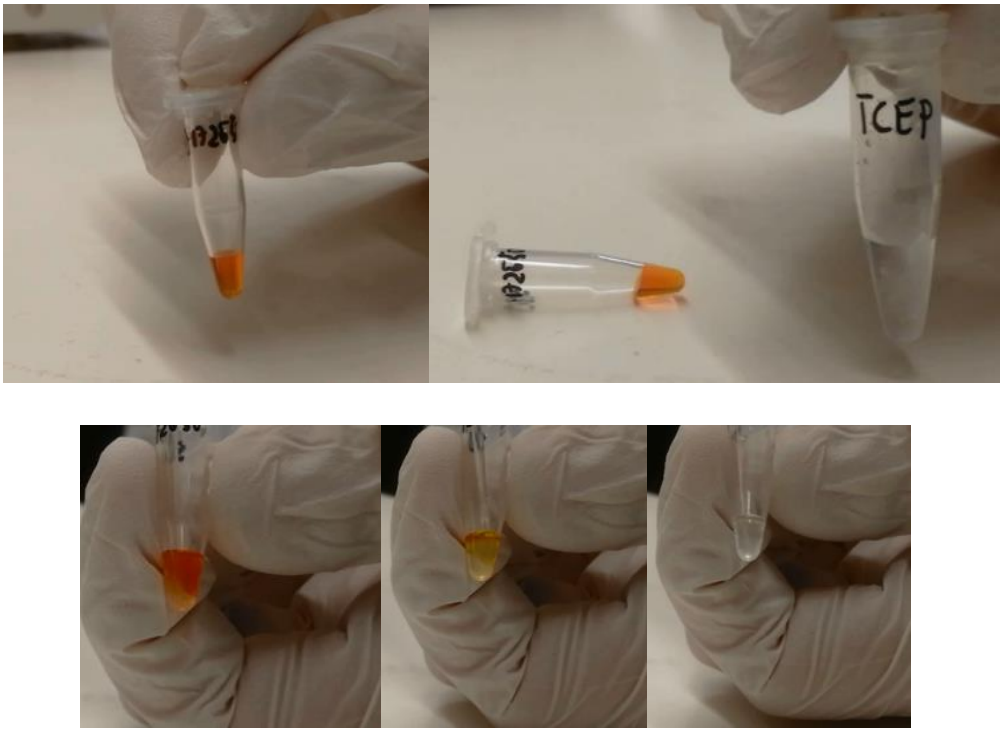


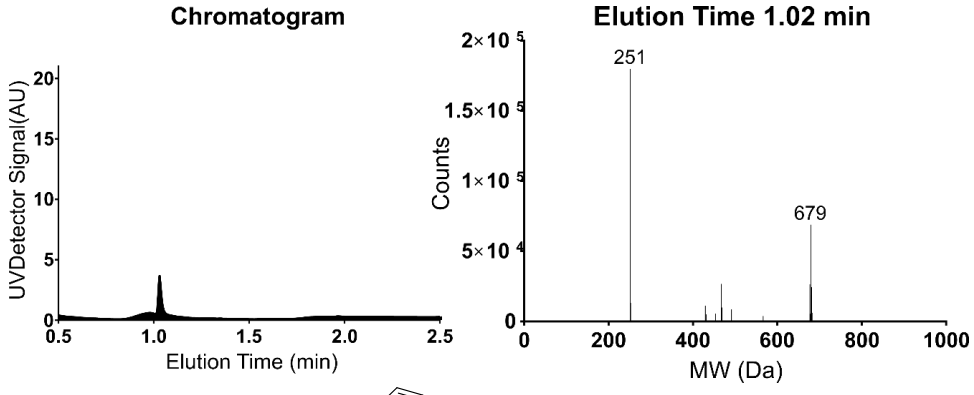
Figure 22: Demonstration of SJ-172550 reactivity towards glutathione. When SJ-172550 is added to glutathione, its orange colour disappears instantly (see text). Analysis of the mixture by LC/MS confirms the existence of a novel peak on the chromatogram (a) that elutes around 0.7 min. Analysis of the peak (b) reveals it contains a novel species, whose MW corresponds to a glutathione-SJ-172550 adduct.

Incubation of SJ-172550 with TCEP also resulted in adduct formation, likely via the phospha-Michael addition[181]. This is significant, as previous reports have also suggested that, being non-nucleophilic, TCEP is unable to react with SJ-172550[169]. However, there is perfunctory evidence that reaction proceeds extremely fast, as the orange colour of SJ-172550 solutions, presumably arising from the extended chromophore, disappears almost instantly upon the addition of TCEP, with LC/MS confirming the formation of a novel compound (Figure 23).

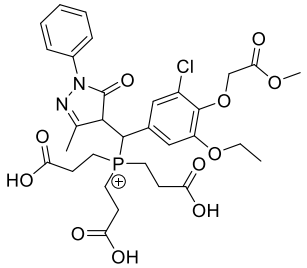
a



b



c



Exact Mass: 679.18

Figure 23: Demonstration of SJ-172550 reactivity towards TCEP. (a) The bleaching of SJ-172550 upon the addition of TCEP occurs instantly, indicating a reaction has proceeded. (b) Subsequent analysis by LC/MS indicates the presence of a new species (c), whose MW corresponds to the product of a phospha-Michael addition between SJ-172550 and TCEP.

2.4.2 Evidence of decomposition of SJ-172550 in aqueous buffers

A closer examination of the various chromatograms from the MS analyses of reactions involving SJ-172550, such as Figure 22, above, revealed the presence of an additional, previously uncharacterised peak. Analysis of the peak revealed the presence of a novel species that was not present originally, but appeared over time following the incubation of the compound in aqueous buffers, as evidenced by experiments with fresh SJ-172550 aliquots.

This previously unnoted reactivity of the compound manifests itself in a reverse Knoevenagel condensation, followed by conjugate addition of one of the degradation products to another SJ-172550 molecule, resulting in the formation of a new, bispyrazolinone compound, named SJ-Bis. This was unambiguously established by comparison with an authentic sample of SJ-Bis produced via a de novo synthesis (Figure 24).

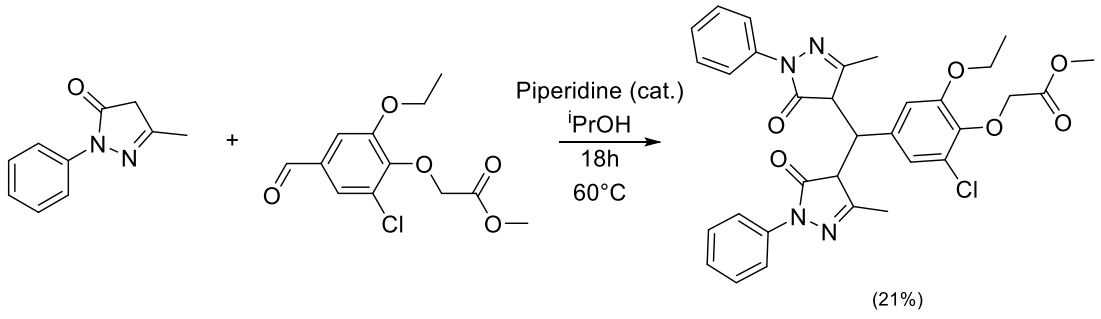


Figure 24: Structure and synthesis of SJ-Bis. The reaction follows the same scheme as the original synthesis of SJ-172550. However, by doubling the molar equivalent of the pyrazole, one can steer it towards the formation of SJ-Bis instead.

A literature search revealed that this behaviour is not uncommon to arylmethylidenepyrazolinones[182,183]. We further assayed the rate of SJ-172550 decomposition and concomitant formation of SJ-Bis by LC/MS and found that, at 37 °C in mildly alkaline aqueous buffers such as HEPES-NaCl pH 7.5 (or any physiologically-relevant buffer system), SJ-Bis begins to appear within minutes, and within 4 hours, nearly 50% of SJ-172550 is gone (Figure 25).

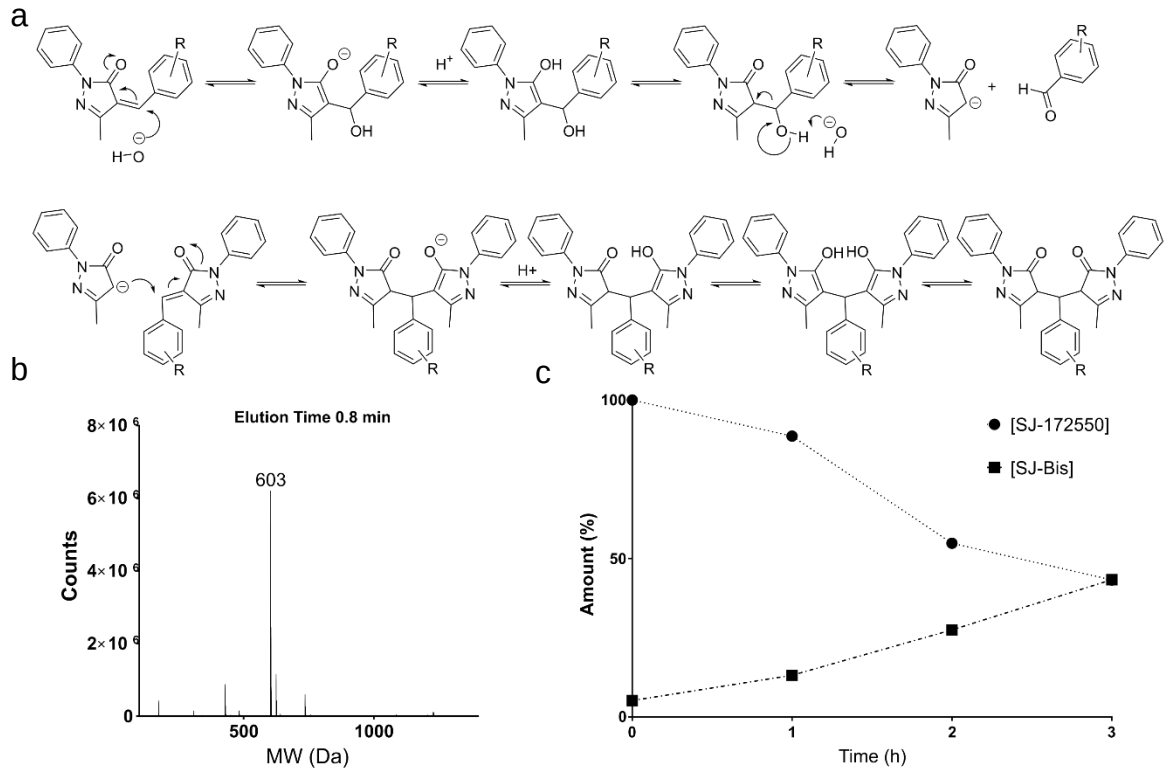


Figure 25: The formation of arylmethylidenebispyrazolinones. (a) The generalised mechanism for the degradation of arylmethylidenepyrazolinones via reverse Knoevenagel, followed by the nucleophilic attack by the enol π electrons on the Michael acceptor in a second molecule, which leads to the formation of an arylmethylidenebispyrazolinone product. (b) Analysis by LC/MS of a solution of SJ-172550 in HEPES-NaCl buffer, pH 7.5 confirms the formation of a new compound; the MW of SJ-Bis is 602.19 g/mol. (c) The kinetics of degradation measured by LC/MS indicate that the compound degrades on a timescale measured in hours (n=1).

As it was possible that the cellular effects of SJ-172550 were in fact attributable to SJ-Bis, its ability to bind MDMX was assayed, via both ITC and MS (Figure 26). Whilst no binding was detected via ITC, MS analysis produced an interesting result, namely the formation of an adduct with the molecular weight corresponding to SJ-172550, rather than SJ-Bis. This has prompted further investigations into whether SJ-Bis can decompose back into SJ-17255. Firstly, LC/MS analysis of an SJ-Bis sample in solution following 4h incubation revealed the presence of SJ-172550 in it. Moreover, long-term incubation of a sample of SJ-Bis on a benchtop results in the normally colourless sample acquiring an orange hue, indicative of SJ-172550 formation. Lastly, in an ABPP competition assay, SJ-Bis appears to be able to outcompete SJ-Alkyne at 50 μM more than an equivalent concentration of SJ-Reduced (Figure 27).

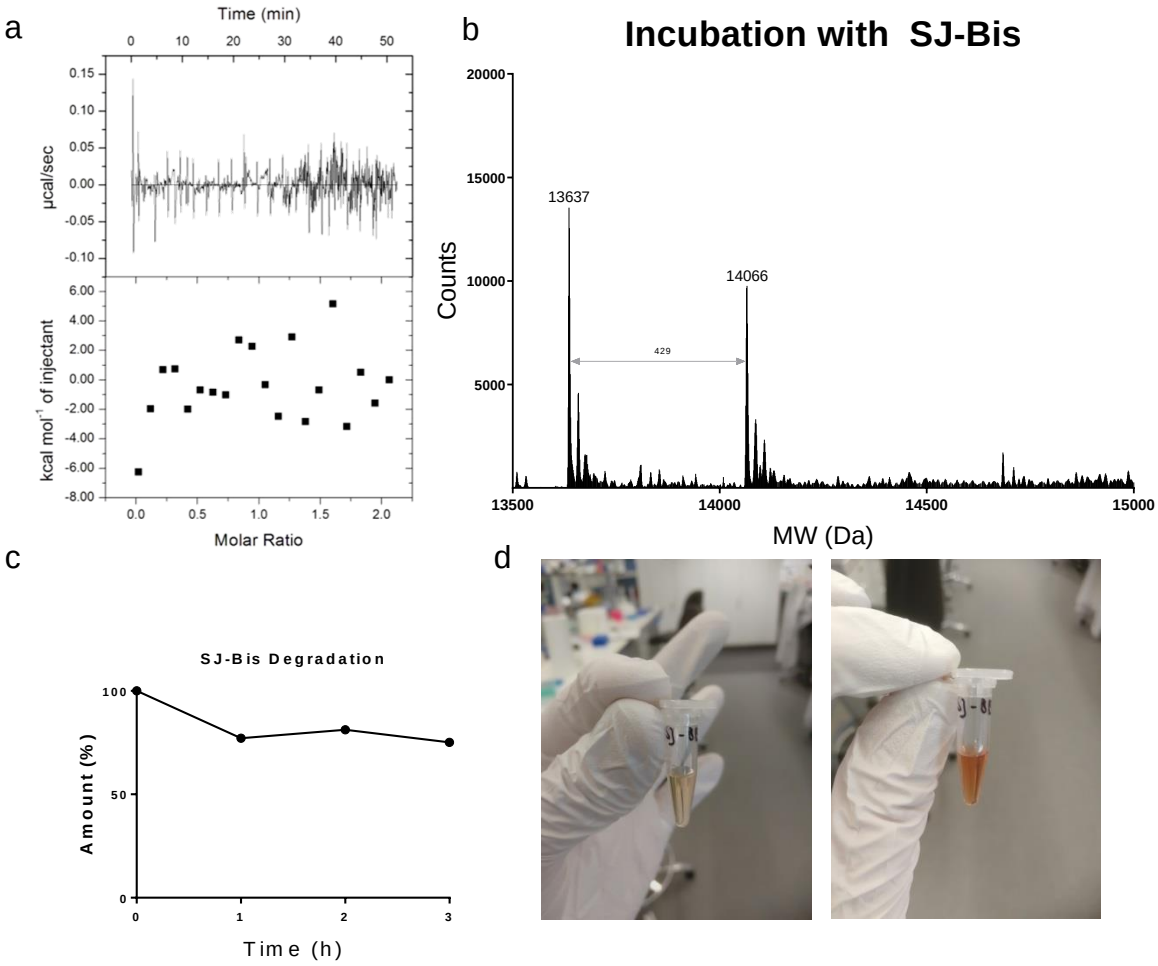


Figure 26: SJ-Bis is unable to bind MDMX, however, it decomposes to SJ-172550. (a) In an ITC experiments, SJ-Bis does not appear to bind MDMX. (b) MS analysis of the mixture following incubation of MDMX with SJ-Bis for 1 hour indicates the presence of an adduct with the MW of SJ-172550. (c) Time-resolved LC/MS data indicates slow degradation of SJ-Bis over time. (d) Visual inspection shows SJ-Bis can convert back to SJ-172550 over extended periods of time.

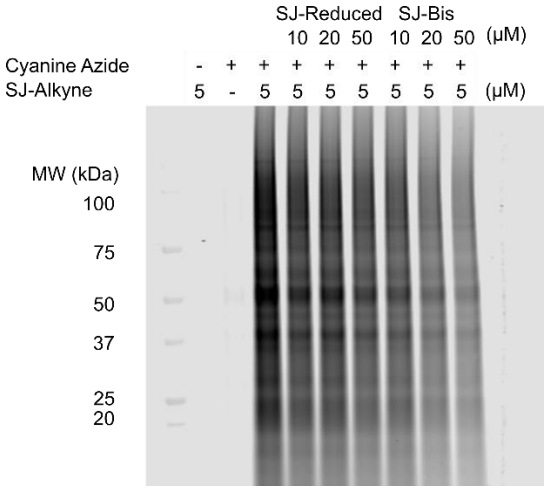


Figure 27: Competitive ABPP data indicates that SJ-Bis can outcompete SJ-Alkyne to a greater extent than SJ-Reduced. In-gel fluorescence was performed as before with SJ-Alkyne, however the lysates were pre-incubated with increasing concentrations of SJ-Reduced and SJ-Bis. At very high concentrations, SJ-Bis can outcompete SJ-Alkyne, likely due to its conversion back to SJ-172550.

2.4.3 Evidence of decomposition and undesirable reactivity in related molecules

C646 is a structurally-related compound to SJ-172550, that was, using proteomic methods, also shown to be a promiscuous binder[97]. As a result, it was postulated that, similarly to SJ-172550, C646 could exhibit undesirable reactivity and instability. Indeed, incubation of C646 at 37 °C in HEPES-NaCl using the same protocol as for SJ-172550, shows an appearance of a very small peak on the chromatogram that appears to have the MW corresponding to the decomposition product (Figure 28).

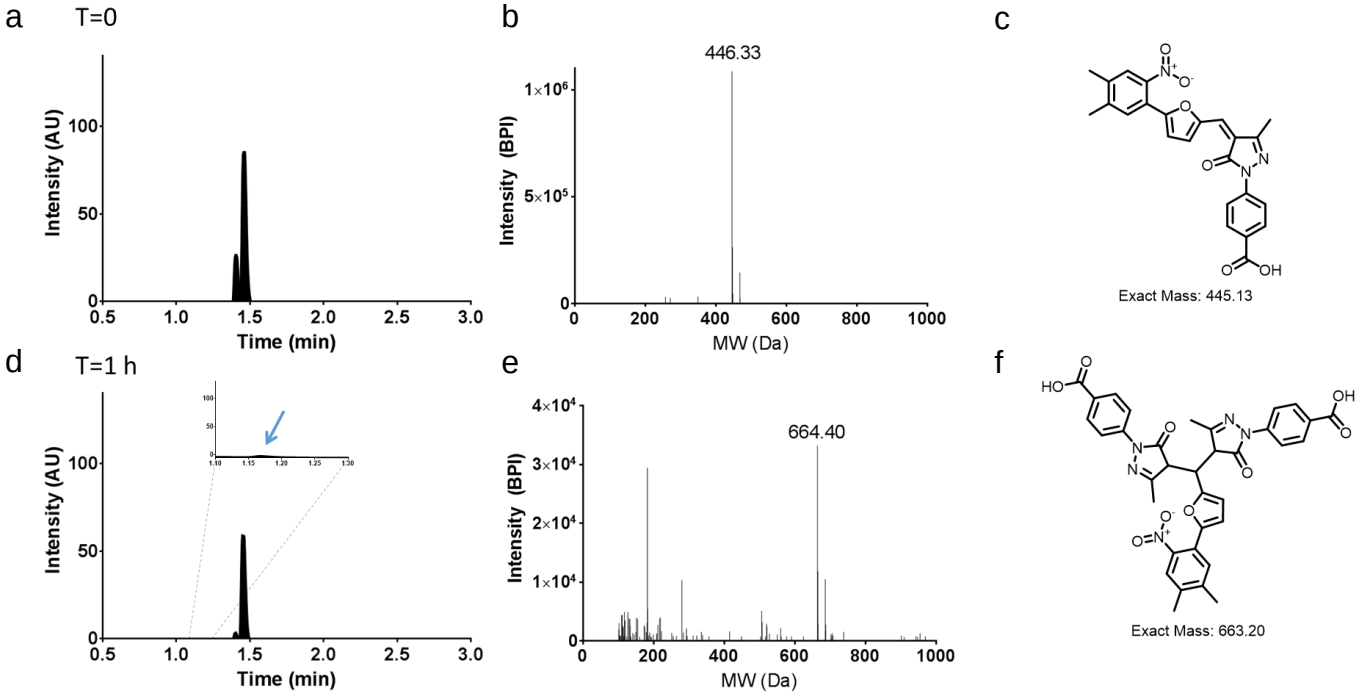


Figure 28: C646 also decomposes to a bis product, however the rate of decomposition appears to not be as rapid as SJ-172550. (a) Initial chromatogram of C646 in an alkaline buffer solution. (d) MS analysis of the major peak on the chromatogram reveals a compound whose MW (c) corresponds to C646. (d) After 1 hour of incubation, a novel peak appears on the chromatogram, albeit with a comparatively miniscule area. MS analysis of the peak indicates the presence of a compound (e) whose MW (f) corresponds to a bispyrazolinone product of C646 decomposition.

Secondly, the addition of TCEP to the orange-coloured C646 solution likewise caused an instant colour disappearance, later on validated by MS to have the phospha-Michael adduct (Figure 29).

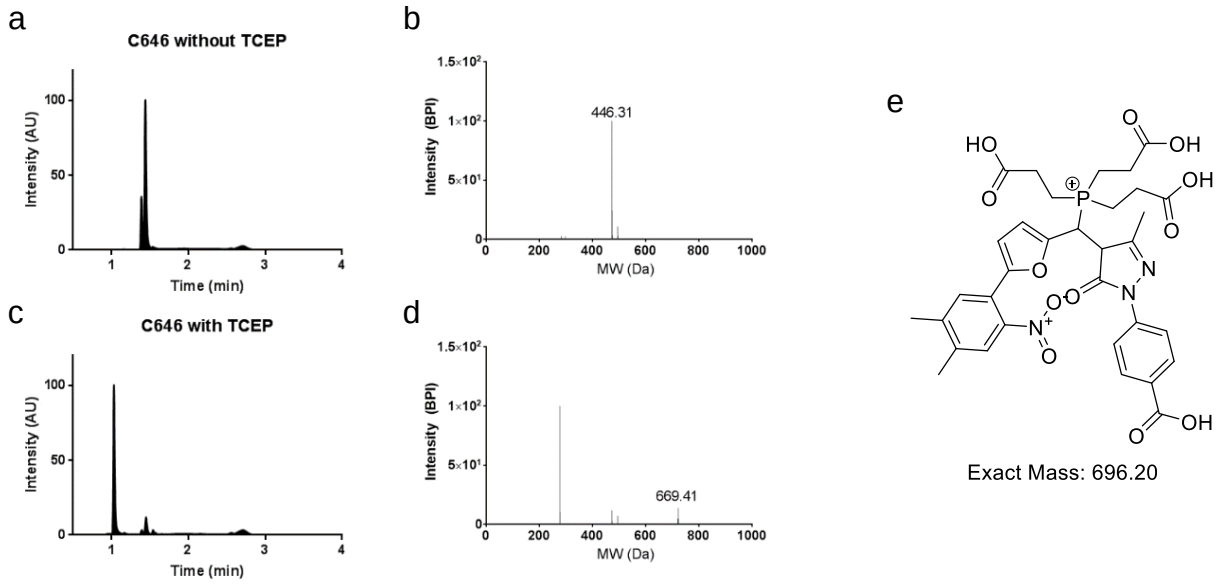


Figure 29: C646 also covalently reacts with TCEP. (a) The chromatogram of C646 without TCEP, indicating the presence of C646 (b). Following the addition of TCEP, the orange solution went immediately colourless. Analysis of the solution by LC/MS indicates almost complete disappearance of the peak corresponding to C646 (c) – instead, a novel compound is present (d), whose MW corresponds to the phospha-Michael adduct between C646 and TCEP.

2.5 Discussion

The analysis of SJ-172550 has proven to be more challenging than initially anticipated. The compound's physicochemical characteristics, namely potential to aggregate, autoreactivity in aqueous buffers and undesirable proclivity to bind to free thiols and even the thiol-lacking reducing agent TCEP make it a difficult compound to work with. In addition, despite showing initial promise in the ITC assay in being able to bind recombinant MDMX, in cellular assays the compound does not show signs of direct engagement of MDMX. This is further complicated by the molecule's overall low synergy with nutlin-3a, an inhibitor for MDM2 in a genetically-validated cell line.

2.6 Conclusions

Taken together, the data suggests SJ-172550's MoA is not via MDMX-mediated activation of p53, and the cytotoxic effects are more likely attributed to non-specific labelling of proteins and potential propensity to aggregate and destabilise them[184]. Further analysis indicates that this behaviour is not exclusive to SJ-172550, as a structurally similar compound C646 exhibits some of SJ-172550's problematic traits as well, as demonstrated in the decomposition and TCEP adduct assay.

3. Development and Validation of an Algorithm to Analyse 2D-CETSA Output Data

3.1 Introduction

3.1.1 Current proteomics workflows and data analysis

As mentioned before, advances in modern MS techniques have enabled even complex solutions of peptides to be analysed, with today's technology allowing for the identification of potentially thousands of proteins to be identified in a relatively short space of time[78]. In a typical bottom-up proteomics experiment, the proteome is extracted from the organism of study (this can be homogenised tissue, or cell culture, for example), followed by digestion with a specific protease. The peptides can be further enriched by affinity chromatography, or be separated by HPLC, followed by mass/charge ratio measurement of the digested proteins in a high-resolution mass spectrometer. Ionisation usually proceeds via electrospray ionisation (ESI)[185] or matrix assisted laser desorption ionisation (MALDI)[186]. The MS1 spectra containing peptide isotope patterns are obtained, whilst subsequently the peptides are further fragmented by collision-induced degradation (CID), followed by the recording of fragment (MS2) spectra. The peptides selected for fragmentation are usually done so on the basis of intensity, with the exclusion of masses already selected, in a process termed data-dependent acquisition (DDA). The MS1 and MS2 spectra are saved and analysed (Figure 30). Due to advances in isotopic fine structure MS, at the ultrahigh resolution one can be confident that each peak corresponds to a species with the same elemental composition, as well as

potentially even resolve different $^{13}C/^{15}N$ isotopic masses of the same fragment[187], followed by reduction (or 'deisotoping') of the spectrum[188].

The reason for the use of tandem mass spectrometry is that it allows for the introduction of an additional level of fingerprinting – just as proteins can be fingerprinted by the peptides they generate during digestion, the peptides themselves can be fingerprinted by the fragments they generate during CID, as the fragmentation usually proceeds alongside the peptide backbone (Figure 30, bottom), generating specific prefix and suffix molecules ($a_1 \ldots c_3$ and $x_3 \ldots z_1$, albeit virtually all breakages occur to generate b and y suffix molecules). Moreover, just as the protein can be identified via fingerprinting from the peptide spectra it generates, and thus the comparison of the experimental to a theoretical spectrum can be used to assign proteins to spectra in a probabilistic fashion, each individual peptide can be further identified by the comparison of a theoretical and experimental MS/MS spectra during a database search. This offers a significant advantage over only using MS spectra, as it no longer becomes necessary for all peptides from a single protein to be present on one MS spectrum and as a result one is free to perform deep fractionation of the samples in order to identify as many peptides as possible, potentially bypassing the issues of low abundance.

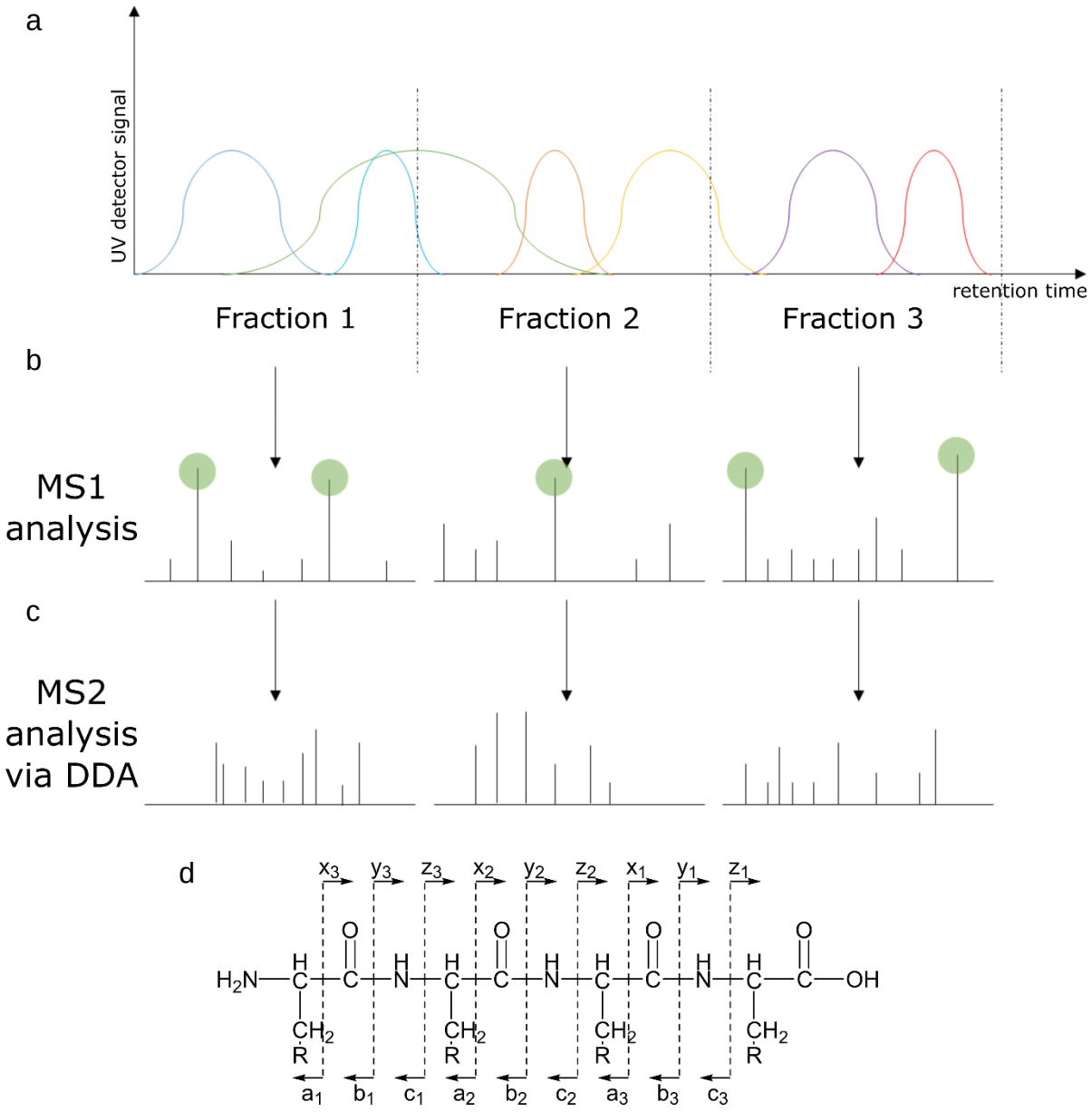


Figure 30: The bottom-up shotgun proteomics workflow. (a) Initially, the peptides are fractionated, as MS/MS analysis removes the requirement for peptides from the same protein to be present in the same fraction. (b) The mass spectrometer first performs a "scans" in the MS mode, where the mass/charge spectra of the peptides are obtained; (c) in a data-dependent acquisition mode, the instrument selects the ions with the highest intensities for fragmentation and further analysis in MS/MS mode. (d) Because the peptides fragment in predefined ways, this enables peptide identification via fingerprinting from theoretical MS/MS spectra.

If the complete genomic data for a given organism is known, a theoretical protein sequence database can be constructed, with concomitant theoretical peptides formed as a result of *in silico* protease cleavage. Analogously, a theoretical MS/MS fragments list can be generated for each peptide, which has led to the development of a number of algorithms for peptide and thus protein identification, such as Mascot or OMSSA[189,190]. The basic principle of these algorithms is that for a given peptide, theoretical fragmentation spectra are drawn for all theoretical peptides within said peptide's mass range, and that peptide's subsequent fragmentation spectrum is compared to the theoretical fragmentation spectra. In order to safeguard against false positives, the fragmentation spectrum can also be compared against a 'decoy' database fragmentation spectra, allowing for the calculation of posterior error probabilities and thus control over the false discovery rate (FDR). Modern algorithms, such as MaxQuant also allow for taking post-translational modifications (PTMs) into account by including MS/MS spectra for modified peptides and even pinpointing modification, such as phosphorylation sites, by scoring against different phosphorylation variants[191,192].

Due to the fact that a single peptide can originate from more than one protein, it is imperative for database algorithm to also correctly assemble proteins from peptides without generating false positives as a result of nonunique peptides. Consider the following: assuming only canonical amino acids, there are 3,200,000 different peptide combinations with length of 5 amino acids; given that the human uniprot database contains nearly 40,000,000 amino acids' worth of protein sequences, each

pentapeptide will appear on average ~12 times in the proteome, meaning by random assignment one is less than 10% likely to correctly assign it. Only peptides of length of 7 amino acids and over can be reasonably expected to be unique[193], however, that may also depend on sequence homology or the presence of conserved domains. Most protein assembly algorithms work by attempting to find the smallest possible dataset of proteins that explains the experimental data[194,195]. It is worth noting that the user can usually specify the FDR (for instance in MaxQuant), with lower FDR corresponding to fewer false positives but also more proteins missing, and higher FDR finding more proteins at the cost of a lower confidence in the dataset.

3.1.2 Quantification strategies using tandem mass tags

In chemoproteomics experiments, such as CETSA, the proteome needs to be analysed quantitatively, in order to correctly measure the aggregation and removal of each individual protein due to the heat pulse. As such, one usually employs relative quantification methods, to calculate ratios of particular peptides at different temperatures.

In theory, it would be possible to employ relative label-free quantification based on signal intensities of MS1 peptides as input, however, in practice this is not feasible due to issues with LC/MS alignment and normalisation[196]. More commonly, isobaric mass tags are used [197], whereby peptides from different groups are labelled with isobaric tags, which have the same mass but fragment differently, which allows sample multiplexing (Figure 31). The tandem mass tags (TMT,

ThermoFisher) allow for ease of labelling by featuring an amine-reactive NHS group that reacts with free amines, usually on the N-terminus of a peptide, however, conjugation to a lysine residue is also possible, and algorithms assigning MS/MS spectra to peptides usually account for the possibility of double/multiple TMT adducts[198].

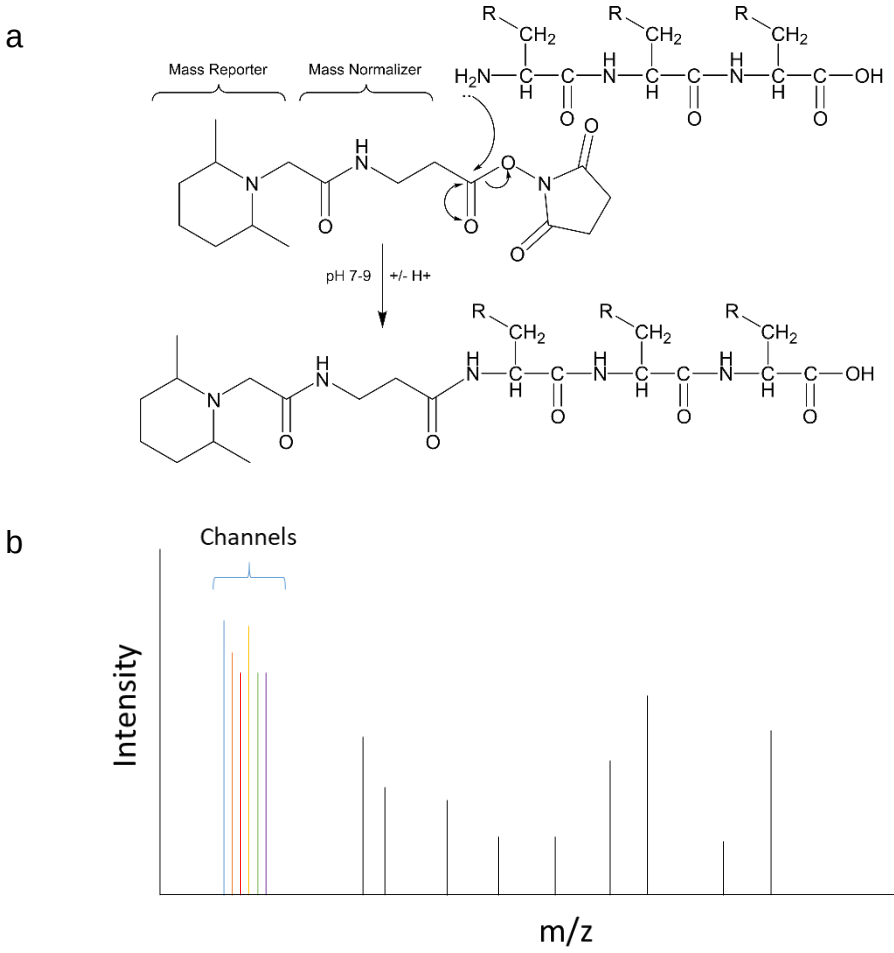


Figure 31: The TMT strategy for quantitative proteomics. (a) Each TMT tag (in this example, TMTzero shown) contains a mass reporter which will appear in the low mass end of the MS/MS spectrum and a mass normaliser, allowing direct comparison between TMT channels intensity for quantification during tandem mass spectrometry (b).

3.1.3 CETSA/TPP Data Analysis

As mentioned previously, the cellular thermal shift assay (CETSA) and its MS counterpart, thermal proteome profiling (TPP) are chemoproteomics techniques for target deconvolution based on the principle of cellular protein engagement inducing thermal stabilisation against a denaturing heat pulse[107]. In a 2D experiment, the cells are treated with 4 different concentrations of the compound or equivalent DMSO, and due to isothermal dose-response (ITDR) effect, stabilisation of the protein can be observed at a single temperature point by increasing concentrations of the ligand. Following the heat pulse (usually 12 temperatures are used) and sample processing, including TMT labelling, the peptides are pooled and analysed by MS, followed by processing of the spectra with the use of a protein assembly tool, such as Thermo Proteome Discoverer. This produces an output in the form of a data file that describes each detected protein's sequence coverage, score and number of peptides identified, as well as quantitative ratios between groups based on the TMT-labelling data. The quantification data is subsequently normalised with the use of the TPP R Package[107], which outputs the data for every protein in the form of a 12x5 (ordinarily) matrix that describes the relative protein abundance (fold change) at every combination of temperature and compound concentration, and can also use this to ascertain whether stabilisation occurs at each temperature, by fitting a sigmoidal dose-response curve. The abundance data is normalised at each temperature to the DMSO value, thus in principle, if the protein is stabilised by the compound, it will result in fold change >1 as the temperature and concentration increases (Figure 32), and vice versa. Typically, stabilisation at two adjacent

temperatures is indicative of the protein being a 'hit'. In practice, however, false positives may arise, necessitating the development of techniques that can efficiently differentiate between them and true positives out of datasets containing thousands of different proteins.

	DMSO	0.02 µM	0.143 µM	1 µM	5 µM
42 °C	1	1.1	1.12	0.99	1.01
44.1 °C	1	1.05	1.06	1.15	1.05
46.2 °C	1	1.25	1.33	1.3	1.29
48.1 °C	1	1.67	1.92	1.89	1.64
50.4 °C	1	3.27	4.09	4.58	4.62
51.9 °C	1	4.18	5.66	7.04	7.27
54 °C	1	2.65	3.88	5.16	7.5
56.1 °C	1	2.78	4.16	7.13	10.14
58.2 °C	1	1.93	2.72	6.05	13.09
60.1 °C	1	1.2	1.64	3	9.88
62.4 °C	1	1.16	1.06	2.13	10.36
63.9 °C	1	1.03	1.07	1.14	3.98

Figure 32: Heat map shown relative protein abundance of HDAC1 at different temperatures and concentrations of HDAC1 inhibitor panobinostat. Representative data from the TPP dataset obtained by Becher et al[109].

Because the dataset size approaches 10^6 datapoints (for an experiment involving 4 different compound concentrations and 12 temperatures that detects 5000 different proteins, for instance, 300,000 datapoints be generated), this makes visual inspection highly inefficient. Moreover, whilst potential hits can be validated by CETSA-WB or biophysical techniques, it is vital to reduce the dataset as much as possible to minimise the need for purchasing antibodies and time commitment necessary for WB validation. To this end, it was decided to develop a MATLAB algorithm that processes 2D TPP datasets and, for every protein, can obtain the magnitude of (de)stabilisation by the compound, as well as a measure of confidence

in that magnitude, in order to rank the proteins in order of likelihood that they are true hits from the assay.

The dataset used for the development of the algorithm was decided to be the TPP experiment profiling the protein arginine methyltransferase 5 (PRMT5) inhibitor GSK3326595. PRMT5 is an enzyme belonging to the family of arginine methyltransferases that generate various arginine methylation products (monomethylation as well dimethylation, symmetric or asymmetric) on target proteins, with PRMT5 largely processing symmetric dimethylation, or SDMA[199]. PRMT5 is an oncoprotein, originally discovered to alter the activity of p53 by methylation[200]. It was subsequently discovered that PRMT5 overexpression can result in the transformation of cells[201], whilst knockdown in cancer cell lines has growth-attenuating properties[202], making PRMT5 a potentially-viable target in oncotherapy. Recently, a small-molecule inhibitor of the protein has been developed, called GSK3326595, shown to inhibit PRMT5, resulting in cell death due to a transcriptional switch that results in the expression of an MDMX isoform incapable of inhibiting p53, and thus p53-mediated cell death[203]. The validation of the MoA was largely confirmed by p53 knockout studies, which rendered most cells invulnerable to PRMT5 inhibition; however, some cell lines were still affected by GSK3326595, suggesting possible polypharmacology or the involvement of other biological pathways. As such, it was decided to perform proteome-wide profiling of GSK3326595 interactions, and use the dataset to develop and refine the MATLAB algorithm.

3.2 Development of a MATLAB script for further downstream analysis using the GSK3326595 Data

3.2.1 The proteomic analysis of a PRMT5 inhibitor GSK3326595

Initially, CETSA-WB was performed, in order to test whether the primary target can be detected via CETSA, in other words whether it will respond to thermal stabilisation by the compound. Indeed, there was a strong significant thermal shift of PRMT5 when KMS11 cells were incubated with GSK3326595 for 1 hour, followed by a temperature pulse (Figure 33).

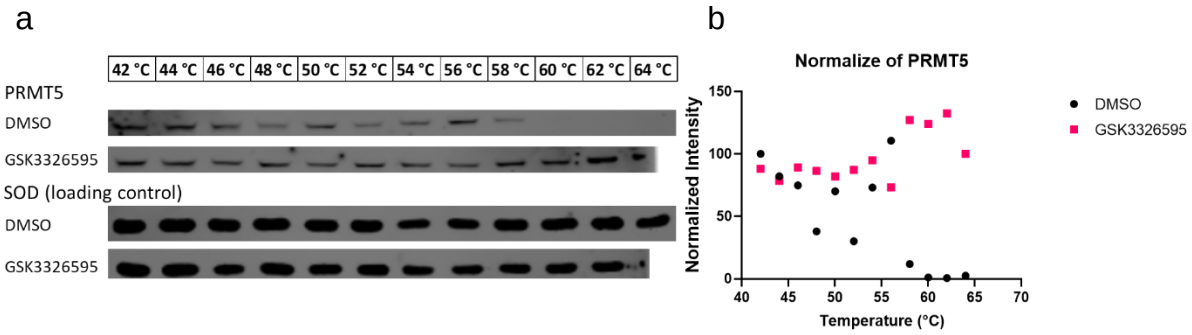


Figure 33: CETSA-WB results for KMS11 cells treated with GSK3326595. The cells were incubated with either GSK3326595, or equivalent volume of DMSO, for one hour, followed by aliquoting, heat pulse and centrifugation. The samples were visualised by SDS-PAGE followed by WB (a), and quantified by densitometry to produce the melting plot (b). The membrane was slightly truncated, resulting in a slightly reduced band for the treated group at 64 °C. GSK3326595 by inspection appears to be stabilising for PRMT5. The datapoints are normalised to the DMSO value at 42 °C.

Subsequently, MS-CETSA was performed according to the above-mentioned protocol, using the following temperature-concentration layout for the purposes of TMT-labelling (Figure 34). The dataset was analysed in Proteome Discoverer, followed by processing with the TPP R script.

Temp (°C)	126	127L	127H	128L	128H	129L	129H	130L	130H	131	RefCol	
42	5	1	0.2	0.04	0	-	-	-	-	-	128H	F1
62	-	-	-	-	-	5	1	0.2	0.04	0	131	
44	5	1	0.2	0.04	0	-	-	-	-	-	128H	F2
64	-	-	-	-	-	5	1	0.2	0.04	0	131	
46	5	1	0.2	0.04	0	-	-	-	-	-	128H	F3
58	-	-	-	-	-	5	1	0.2	0.04	0	131	
48	5	1	0.2	0.04	0	-	-	-	-	-	128H	F4
60	-	-	-	-	-	5	1	0.2	0.04	0	131	
50	5	1	0.2	0.04	0	-	-	-	-	-	128H	F5
54	-	-	-	-	-	5	1	0.2	0.04	0	131	
52	5	1	0.2	0.04	0	-	-	-	-	-	128H	F6
56	-	-	-	-	-	5	1	0.2	0.04	0	131	

Figure 34: The TMT labelling layout for the quantitative proteomics of the GSK3326595 dataset. F1-F6 denote the pooled fractions of TMT-labelled samples.

Overall, 5926 proteins were identified in the dataset. Out of those, 5434 proteins were found to have high FDR confidence (and 5773 had at least medium FDR confidence), and the number of proteins with sequence coverage greater than 10% was 3930. Moreover, the number of proteins with complete quantitation data without missing responses in any of the TMT channels was 3362. TMT labelling efficiency was 95 %.

3.2.2 The development of an algorithm for post-processing of the data

Given that for each protein we are given a 2D dataset of protein abundance relative to the DMSO value at a particular temperature (Figure 35), a tempting notion would be to imagine it as a surface and simply integrate the volume underneath, followed by ranking of the dataset by the volumes. Within the broader context of the literature, the idea of obtaining a measure of integral thermal stabilisation across the entire temperature range by adding the total relative (compound vs DMSO)

protein amounts is not entirely novel, and has been recently explored in what is called Proteome Integral Stability Alteration (PISA) assay[204]. In contrast to CETSA, PISA pools together fractions within the treated and untreated groups, across a temperature range where protein melting occurs, and integration of the thermal aggregation curve is a feature of the experimental set-up, allowing for the use of relative abundance between vehicle and compound to serve as proxy for T_m.

a

PRMT5 Dataset

Temperature	DMSO	0.04 µM	0.2 µM	1 µM	5 µM
42 °C	1.00	1.00	0.96	1.01	0.99
44 °C	1.00	0.97	0.94	0.96	0.96
46 °C	1.00	1.01	0.97	0.98	0.96
48 °C	1.00	0.99	1.01	0.99	0.99
50 °C	1.00	0.95	0.93	0.98	0.94
52 °C	1.00	1.01	0.98	0.99	0.99
54 °C	1.00	0.99	1.04	1.02	1.01
56 °C	1.00	1.31	1.36	1.27	1.26
58 °C	1.00	2.00	2.06	2.04	1.79
60 °C	1.00	2.65	2.85	2.47	1.85
62 °C	1.00	2.28	2.54	2.27	2.44
64 °C	1.00	2.21	3.03	2.93	3.24

Baseline Removed

PRMT5 Dataset

Temperature	DMSO	0.04 µM	0.2 µM	1 µM	5 µM
42 °C	0.00	0.00	-0.04	0.01	-0.01
44 °C	0.00	-0.03	-0.06	-0.04	-0.04
46 °C	0.00	0.01	-0.03	-0.02	-0.04
48 °C	0.00	-0.01	0.01	-0.01	-0.01
50 °C	0.00	-0.05	-0.07	-0.02	-0.06
52 °C	0.00	0.01	-0.02	-0.01	-0.01
54 °C	0.00	-0.01	0.04	0.02	0.01
56 °C	0.00	0.31	0.36	0.27	0.26
58 °C	0.00	1.00	1.06	1.04	0.79
60 °C	0.00	1.65	1.85	1.47	0.85
62 °C	0.00	1.28	1.54	1.27	1.44
64 °C	0.00	1.21	2.03	1.93	2.24

b

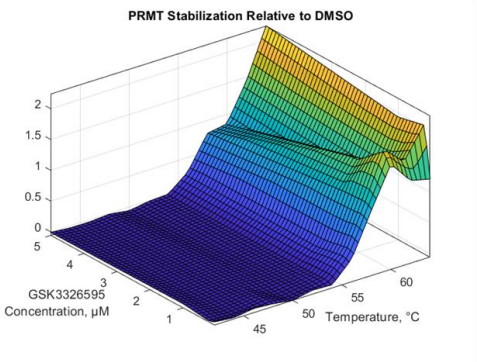


Figure 35: Input data and surface plot for PRMT5. (a) The input is the 2D fold change data for each protein, normalised to the DMSO value at each temperature. By baseline removal, one can obtain relative stabilisation over DMSO, and plot a 3D surface plot (b) to visualise the stabilisation, where the amount of PRMT5 relative to control increases with temperature and compound concentration.

Thus, the initial approach was to use MATLAB's interpolation functionality to convert the surface to a 3D mesh and calculate its volume (Figure 35). Whilst this

approach can be thought of as, in essence, the sum total of all stabilisation by all the compound concentrations at all temperatures, it is flawed for a number of reasons. Firstly, it is prone to false positives, as outliers in the experimental data, rather than being sufficiently accounted for, simply increase or decrease the protein's score. Secondly, the approach does not make an effort to look at the data as a two-dimensional relationship between temperature, compound concentration and protein abundance.

Accession	Name	Integral Stability
Q01518	Adenylyl cyclase-associated protein 1 OS=Homo sapiens GN=CAP1 PE=1 SV=5	97.86
P06899	Histone H2B type 1-J OS=Homo sapiens GN=HIST1H2BJ PE=1 SV=3	66.65
Q15120-2	Isoform 2 of [Pyruvate dehydrogenase (acetyl-transferring)] kinase isozyme 3, mitochondrial OS=Homo sapiens GN=PDK3	63.46
Q13112	Chromatin assembly factor 1 subunit B OS=Homo sapiens GN=CHAF1B PE=1 SV=1	57.19
Q13813	Spectrin alpha chain, non-erythrocytic 1 OS=Homo sapiens GN=SPTAN1 PE=1 SV=3	54.80
Q15366-3	Isoform 3 of Poly(rC)-binding protein 2 OS=Homo sapiens GN=PCBP2	48.48
O14744	Protein arginine N-methyltransferase 5 OS=Homo sapiens GN=PRMT5 PE=1 SV=4	46.89
Q9Y248	DNA replication complex GINS protein PSF2 OS=Homo sapiens GN=GINS2 PE=1 SV=1	44.78
Q8WWW0	Ras association domain-containing protein 5 OS=Homo sapiens GN=RASSF5 PE=1 SV=1	42.56
O75531	Barrier-to-autointegration factor OS=Homo sapiens GN=BANF1 PE=1 SV=1	37.69
Q9Y2Z4	Tyrosine--tRNA ligase, mitochondrial OS=Homo sapiens GN=YARS2 PE=1 SV=2	33.88
P51692	Signal transducer and activator of transcription 5B OS=Homo sapiens GN=STAT5B PE=1 SV=2	33.67
Q9BQA1	Methylosome protein 50 OS=Homo sapiens GN=WDR77 PE=1 SV=1	33.08
K7ELC2	40S ribosomal protein S15 OS=Homo sapiens GN=RPS15 PE=1 SV=1	32.37
Q8NEC7	Glutathione S-transferase C-terminal domain-containing protein OS=Homo sapiens GN=GSTCD PE=1 SV=2	31.99
Q9BV20	Methylthioribose-1-phosphate isomerase OS=Homo sapiens GN=MRI1 PE=1 SV=1	31.64
Q96ER3	Protein SAAL1 OS=Homo sapiens GN=SAAL1 PE=1 SV=2	31.61
P52429	Diacylglycerol kinase epsilon OS=Homo sapiens GN=DGKE PE=1 SV=1	30.81
Q96F07	Cytoplasmic FMR1-interacting protein 2 OS=Homo sapiens GN=CYFIP2 PE=1 SV=2	30.52
P35908	Keratin, type II cytoskeletal 2 epidermal OS=Homo sapiens GN=KRT2 PE=1 SV=2	30.46

Figure 36: Top 20 hits, by integral surface volume. PRMT5 is present amongst the hits (highlighted in green), however some proteins are present that are commonly identified as contaminants, such as keratin (highlighted in red)

Returning to the PRMT5 data set, the following top twenty hits by volume under the surface are presented (Figure 36). Reassuringly, PRMT5 is present amongst the hits. By inspection we can also identify a number of false positives, such as Type II Keratin, a fibrous protein commonly identified by the Contaminant Repository for Affinity Purification (CRAPOME), a repository for frequently-observed false positives in MS proteomics experiments[205], as a contaminant. Examination of the

plots of the data reveals that indeed, for these false positives, the surface does not resemble the hit-like shape of that of PRMT5 (Figure 37), and instead is largely a flat surface with single datapoint inflating the integral, signifying both the need to visually inspect the hits, as well as improve the analysis pipeline downstream of the algorithm to eliminate such false positives.

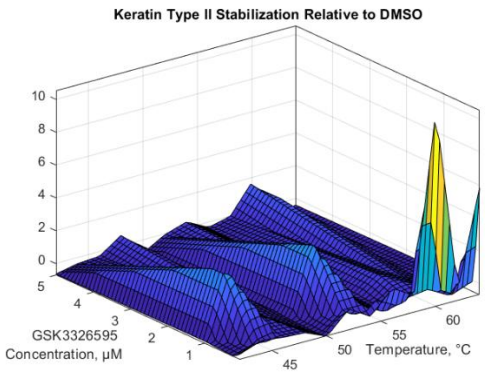


Figure 37: Surface plot for Keratin, type II. As can be observed, despite a high integrated signal, the protein appears to be a false positive.

Following these results it was decided to make further improvements to the algorithm, as it was discovered that MATLAB's poly31 model could fit a surface equation to the stabilisation data with a least-squares model, resulting in a fitted surface with an R-squared value that gave a measure of the goodness-of-fit of the model, as well as the relative integral volume under the fitted surface, giving a measure of the magnitude of stabilisation that is, in principle, corrected for outliers. With that in mind, by -log transforming ($1-R^2$) and plotting the data, one obtains a plot akin to a volcano plot, depicting both the magnitude and a measure of goodness of model fit. By setting the cut-off at R^2 of 0.8, two proteins appear as hits from the

assay, methylosome protein 50 (WDR77/MEP50) and, as mentioned above, PRMT5, with another protein, adenylyl cyclase associated protein 1 (CAP1) being a possible hit, although its goodness-of-fit is far below the cut-off, suggesting the high magnitude could be a false positive (Figure 38).

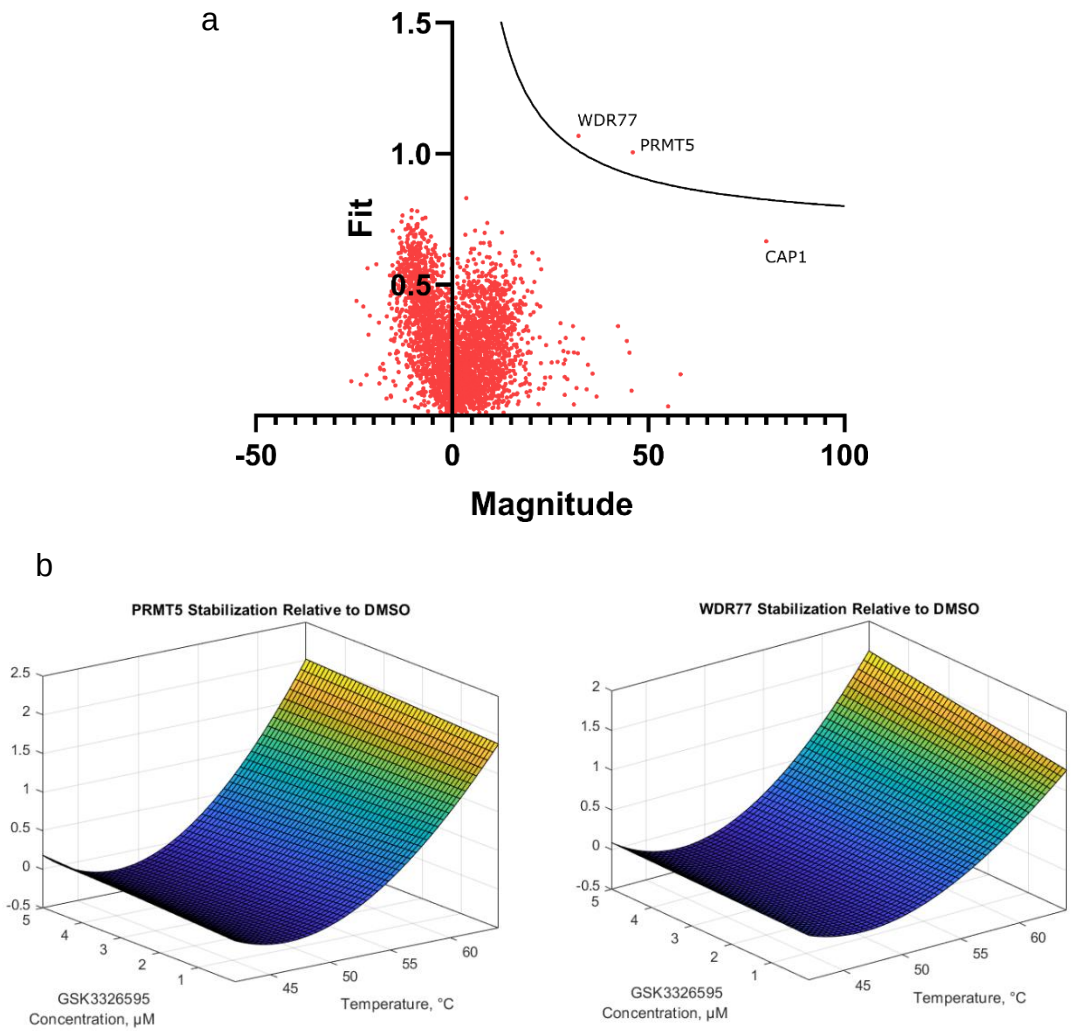


Figure 38: Application of the algorithm to investigate possible hits from the assay. (a) The pseudo-volcano plot, y-axis: -log(1-R^2), giving a measure of the goodness-of-fit of the model; x-axis: the magnitude of stabilisation, measured by the volume under the surface. The hits identified as above the R^2 cut-off are identified. (b) The surface plots for the two hits, PRMT5 and WDR77.

Given that PRMT5 has already been validated, the focus was on validation of WDR77/MEP50 and CAP1. The two hits were to be validated by CETSA-WB, using the same protocol that was used to initially profile the cellular thermal stabilisation of PRMT5 by GSK3326595. Interestingly, the immunoblot data confirms WDR77 is thermally stabilised by GSK3326595, whereas CAP1 is not (Figure 39).

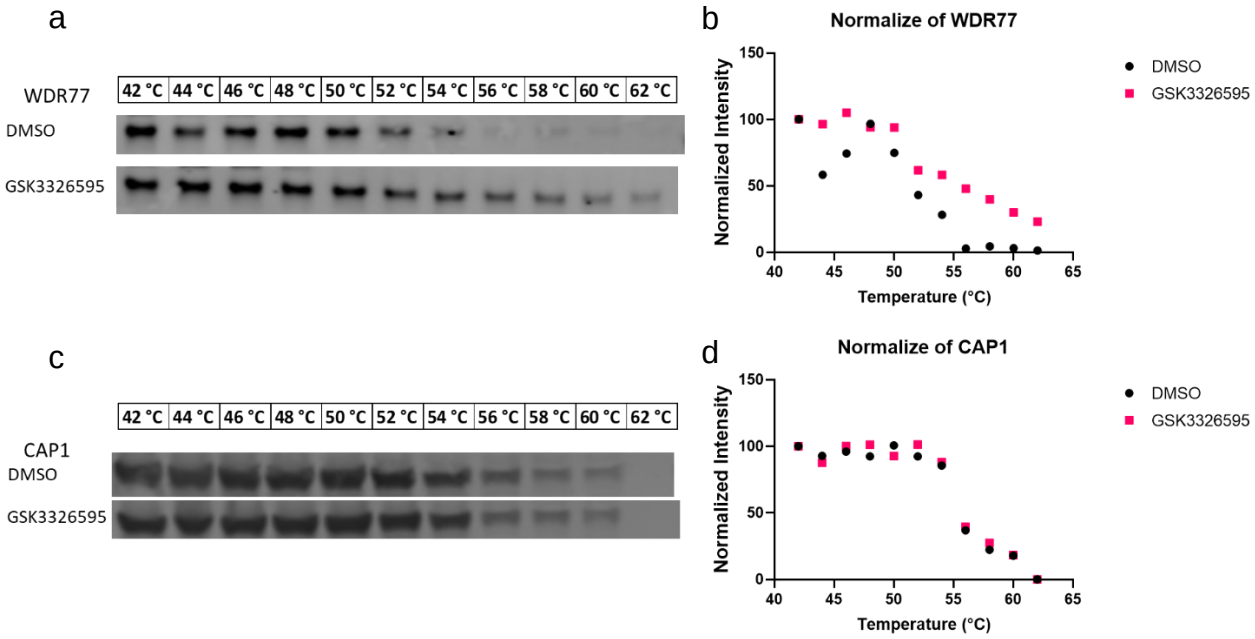


Figure 39: Validation of the hits obtained by the use of the algorithm by CETSA-WB. The cells were incubated with either GSK3326595, or equivalent volume of DMSO, for one hour, followed by aliquoting, heat pulse and centrifugation. The samples were visualised by SDS-PAGE followed by WB (a,c), and quantified by densitometry to produce the melting plots (b,d). WDR77 is stabilised by GSK3326595. CAP1, whose measure of fit was below the cut-off, is not stabilised by GSK3326595. The datapoints are normalised to the DMSO value at 42 °C.

3.2.3 Results

Methylosome Protein 50 (MEP50/WDR77) is a 50-kDa protein that, together with PRMT5 forms what is termed the methylosome complex; within the complex, WDR77 serves to mediate the interaction between PRMT5 and methylation targets,

thus facilitating the function of the methylosome[206]. The crystal structure of the PRMT5-WDR77 complex shows a number of key contacts between the proteins, as well as the residues involved in methylosome substrate recognition[207].

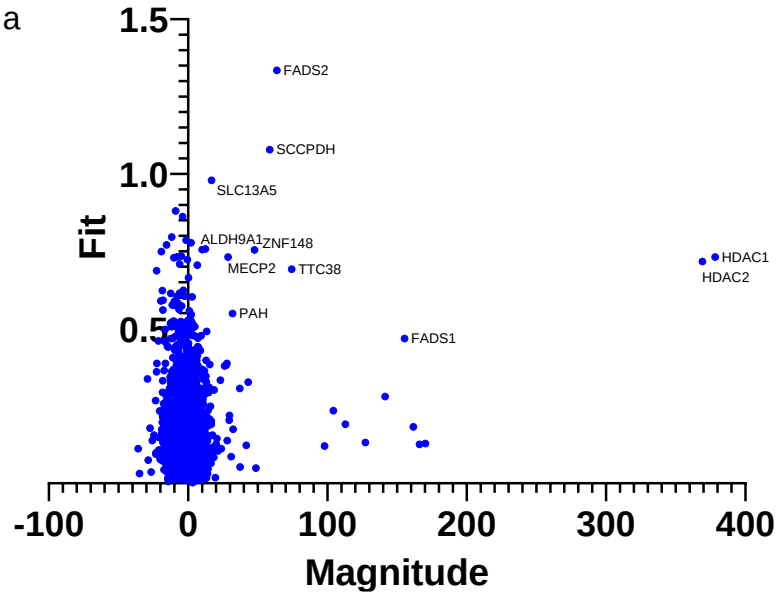
Whilst the data indicates strong thermal stabilisation of WDR77 by GSK3326595, it has to be noted that this does not necessarily have to be via direct interactions between the protein and the compound. Indirect CETSA effects have been previous demonstrated[208] and for proteins that constitutively form a tight complex, stabilisation of the cognate target will often confer residual stabilisation on its interaction partners. As a result, a biophysical assay to measure binding (or lack thereof) of recombinant WDR77 to GSK3326595 would be justified. Interestingly, the regulation of alternative splicing by the methylosome complex occurs through the zinc finger protein ZKSCAN1/ZNF36 protein[209], however, the ZNF36 protein was not detected in the dataset. As the experiment was performed in KMS11 cells, and the PRMT5/WDR77 complex is particularly active in breast cancers, it would be interesting to repeat the experiment in such a cell line, for instance MCF-7, where ectopic expression of PRMT5 has in the past shown to promote growth and survival by reduction of the transcription of the pro-apoptotic protein Bax[210].

3.2.4 Validation of the algorithm on a public dataset

The algorithm was subsequently used on the publicly-available 2D TPP dataset that explored the cellular targets of the histone deacetylase (HDAC) inhibitor panobinostat[109]. The original study found that, in addition to being a HDAC

inhibitor, panobinostat also targets phenylalanine hydroxylase (PAH), and has been shown to thermally stabilise a number of other proteins, such as tetratricopeptide repeat family member TTC38 or saccharopine dehydrogenase (SCCPDH).

a



b

2D-TPP in cells: 15 stabilized >1 peptide, >1.5fold twice	
clustername	**IPI number**
ALDH9A1	IPI00479877
BAT5	IPI00791049
EPHX2	IPI00104341
FADS1	**IPI00784651**
FADS2	**IPI00183786**
FMO5	IPI00215760
HDAC1	**IPI00013774**
HDAC2	**IPI00289601**
HDAC6	**IPI00005711**
MIER1	IPI00477825
PAH	**IPI00017579**
SCCPDH	IPI00329600
TBP	IPI00022831
TTC38	**IPI00550644**
ZNF148	IPI00010833

Figure 40: Validation of the algorithm using the panobinostat 2D TPP dataset obtained by Becher et al[109]. (a) The volcano plot showing the hits from the MATLAB algorithm analysis. (b) The hits from the analysis by the original authors of the study using the TPP R script. There is significant overlap between the two, with the MATLAB algorithm correctly identifying 9 of the 15 stabilized proteins.

Interestingly, following the analysis, there appears to be an overlap between the hits originally discovered by the authors, and the proteins that stand out following the analysis (Figure 40). The greatest magnitude, indicating the greatest thermal shift, is by far exhibited by the original cognate targets of panobinostat, namely HDAC1 and HDAC2. HDAC6, whilst identified as a hit in the original dataset, was rejected by the algorithm due to the presence of missing values in the heat map. In addition,

the algorithm also identifies the fatty acid desaturase members FADS1 and FADS2, as well a number of other proteins, such as the zinc finger protein ZNF148.

3.3 Discussion

The surface fitting algorithm is a relatively simplistic approximation of the stabilisation elicited by the compound on the protein over a temperature range. In fact, the algorithm has a bias towards heat maps with large fold changes across the final two temperatures, albeit of note is the fact that this means they will usually tend to pass the standard criterion of compound stabilisation observed across two adjacent temperatures[109]. The other shortcoming of the algorithm is the fact that it tends to impose harsh R^2 penalties on heatmaps containing outliers and missing data. This means that, in practice, the algorithm should be used as a complement to the TPP R script, and not used as a standalone analysis tool. The TPP R script fits an ITDRF dose-response sigmoidal curve at each temperature point and thus the number of temperature points at which stabilisation occurs is taken for the overall measure of stabilisation, with pEC_{50} values at the temperature closest to the protein's T_m being a closer measure of the compound's potency (which can potentially give pEC_{50} values orders of magnitude away from what would be expected, necessitating further validation). Whilst this approach tends to produce more 'hits', by inspection it also includes the heat maps arising from gene expression events and issues with protein extraction/quantification[109], which are excised by the MATLAB script; on the other hand, the aforementioned harsh

penalties on R^2 that the surface fitting function assigns for the presence of outliers and missing data mean that the false negative rate suffers.

3.5 Conclusions

Overall, a relatively simple algorithm has been developed for the purpose of analysing the output of 2D-CETSA experimental data. The approach it uses is fitting a surface equation over the 2-dimensional area, followed by integration of the volume under the surface, which gives a measure of the stabilisation by the compound; the goodness-of-fit measure is an indicator of confidence in the hit and, as the CAP1 data shows, the goodness-of-fit appears to be the more important factor in deciding which proteins to follow-up.

4. CETSA-Immunoblot Analysis of UCP1-inducing PPARγ Agonists

4.1 Introduction

4.1.1 PPARγ in Health and Disease

Peroxisome proliferator-activated receptor gamma (PPARγ) is a member of the PPAR subfamily of the nuclear hormone receptor (NHR) family, which are cell-soluble proteins that, in response to a cell-permeable fatty agonist dimerise, translocate to the nucleus and act as transcription factors, stimulating gene expression from promoters featuring the appropriate response element. The NHR family also includes the androgen receptor, estradiol receptor, vitamin D receptor and others[211]. PPARγ was discovered in the 1990s as a protein sharing homology with the earlier-discovered PPARa, a nuclear hormone receptor capable of stimulating peroxisome proliferator in response to fibrates[212].

Structurally, PPARγ has the same modular domain organisation as other members of the NHR superfamily: the N-terminal domain governs transcription activation and serves as a phosphorylation hub for upstream signalling; this is followed by the DNA-binding domain, and a large C-terminal ligand-binding and dimerisation domain[213]. PPARγ achieves its transcriptional activity via heterodimerisation with the retinoid-X-receptor (RXR) family members and of note is the fact that two alternative promoters for PPARγ exist, resulting in two isoforms, PPARγ1 and PPARγ2, the latter having an additional 30 amino acids at its N-terminal domain[214].

Whilst PPARγ1 is more ubiquitously-expressed across the body, PPARγ2 is more confined to the adipose tissue, as well as, to a much smaller degree, lung and skeletal muscle[215].

Since its discovery, the functions of PPARγ have been studied in detail, revealing some of its more important functions. First of all, PPARγ has been shown to promote differentiation of pre-adipocytes, by altering the expression of a number of key genes that halt cell proliferation (downregulation of beta-catenin or platelet-derived growth factor receptor, upregulation of growth arrest-specific protein) and reduce extracellular matrix remodelling and promote attachment (downregulation of matrix metalloproteinases and upregulation of extracellular matrix proteins), resulting in the cells adopting a mature adipocyte phenotype[216]. The phenotypic changes observed during differentiation can be observed, using the preadipocyte cell line 3T3-L1 as an example (Figure 41). Interestingly, PPARγ-/- embryonic stem cells are unable to undergo differentiation in a mouse model[217], nor are 3T3-L1 with PPARγ knockdown via RNAi[218]. By contrast, ectopic expression of PPARγ induces adipogenic differentiation of cultured fibroblasts[213].

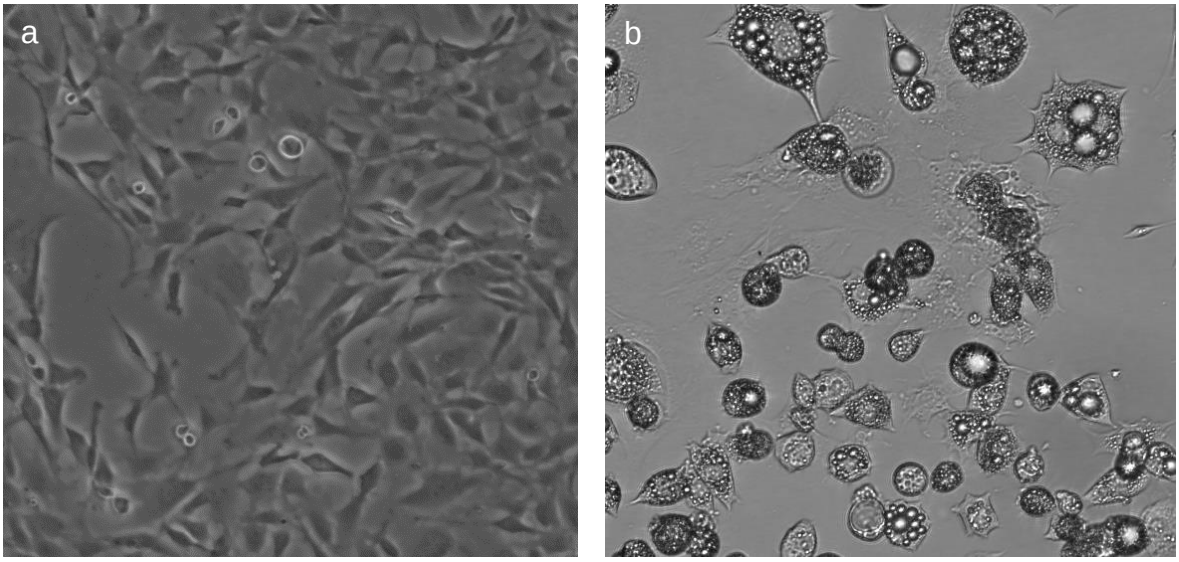


Figure 41: Undifferentiated (a) and differentiated (b) 3T3-L1 adipocytes. The preadipocytes have a more fibroblast-like phenotype. By contrast, the differentiated adipocytes adopt a round phenotype with a prominence of lipid droplets.

Moreover, PPARγ is responsible for large-scale metabolic alterations, which prime the cell towards fatty acid metabolism (upregulation of glycerol-3-phosphate acyltransferase), adipose storage (upregulation of heart-type fatty acid binding protein) and lipogenesis (upregulation of long-chain-enoyl-CoA hydratase)[219]. In addition, PPARγ promotes lipoprotein lipase[220] and fatty acid translocase CD36[221] expression, explaining why PPARγ agonism results in fat uptake by subcutaneous adipose depots[222]. The upregulation of perilipin by PPARγ stimulation results in the formation of lipid droplets[223], contributing to the differentiated adipocyte phenotype.

The RXR-PPARγ heterodimers achieve this transcriptional regulation by binding to PPAR response elements, PPREs[224], which are usually present in the enhancer

region of the gene[225]. Of interest is the fact that deletion of the N-terminal region upstream of the DNA-binding domain (DBD) on PPARγ results in increased transcription[213], suggesting that there is an inhibitory element within that region. Indeed, serine 112 within the region is a phosphorylation site for mitogen-associated protein (MAP) kinase, and phosphorylation of that residue results in reduced rate of transcription from PPREs[226]. Moreover, proline to glutamine missense mutations neighbouring that serine that prohibit serine phosphorylation result in a constitutively activated PPARγ with an elevated rate of adipocyte differentiation, as well as increased fat accumulation, manifesting itself in obesity in humans carrying the mutation[227]. However, S112A mutant mice, which abrogates phosphorylation, don't bear these hallmarks of increased fat mass; on the other hand they remain insulin-sensitive even on a high-fat diet[228].

4.1.2 PPARγ-targeting compounds in the clinic

Given that gain-of-function PPARγ mutations produce an obese phenotype, it would perhaps seem counterintuitive to try to devise PPARγ-targeting agonists for a therapeutic purpose. However, in the 1980s, before the discovery of PPARγ, a number of compounds belonging to the thiazolidinedione (TZD) class emerged that produced very interesting phenotypes, namely stimulation of adipocyte differentiation[229] and reduction of insulin resistance in an obese mouse model[230]. In the 1990s, the connection between the two was made, as the TZD compound BRL49653 (rosiglitazone) was shown to be a PPARγ agonist with a nanomolar affinity in radiolabelling assay[231] and capable of inducing stem cell differentiation

to adipocytes. As mentioned before, the PPARγ-induced expression of genes responsible for increased fat uptake is indeed a hallmark of TZD treatment, where rosiglitazone-treated rats display increased fatty acid uptake into the adipose tissue and reduced fatty acid uptake into liver and muscle, concomitantly reducing insulin resistance[232]. This has important ramifications for Type 2 diabetes therapy, where rosiglitazone was associated with lower blood glucose and free fatty acids, as well as increased rate of fat oxidation[233]. This is likely achieved via decreased expression of pro-insulin resistance proteins, such as tumour necrosis factor alpha (TNFα) and resistin[234]. Nonetheless, TZD treatment is associated with weight gain, fluid retention and cardiovascular side effects[235], partially as a result of off-target interactions mentioned in Chapter 1, and as a result they are no longer used in the clinic for the treatment of diabetes and metabolic syndrome.

Since PPARγ agonists increase fat mass, it would perhaps make sense to develop PPARγ antagonists with the aim of reducing fat mass to combat diet-induced obesity. The hypothesis is supported by genetic data, where PPARγ+/- mutant mice with PPARγ deficiency are protected against high-fat diet-induced insulin resistance and fat gain[236]. On the other hand, loss-of-function mutations within the ligand-binding domain of PPARγ result in lipodystrophy and severe insulin resistance[237], suggesting the interplay between PPARγ (ant)agonism and insulin signalling is complex. The nanomolar affinity (measured by radioligand binding) PPARγ antagonist GW9662 (capable of reducing 3T3-L1 adipogenesis by nearly 50% at submicromolar doses), confers resistance to diet-induced obesity in mice,

however, has no effect on insulin resistance[238]. By comparison, another antagonist SR202 protects from not only fat mass increase but also insulin resistance[239]. Inhibition of PPARγ by the relatively weak affinity (100 μM, radioligand binding) antagonist bisphenol A diacylycidyl ether (BADGE) *in vitro* causes inhibition of differentiation[240] and in wild-type mice has effects similar to SR202. Perhaps confoundingly, however, in PPARγ heterozygous mice, BADGE causes an increase in insulin resistance and depletion of white adipose mass[241], suggesting that the compounds have additional off-target effects, or conversely that effects of PPARγ antagonism or depletion can have a deleterious effect, if done in excess.

4.1.3 Brown adipose tissue and the uncoupling protein

Being a transcription factor, PPARγ binds and engages a wide variety of nuclear coactivators[242] and corepressors[243], including nuclear coactivator family members, sirtuins, the mediator complex and CREB-binding protein (Figure 42). One of the most interesting ones, however, is PGC1α. Discovered as a transcriptional coactivator whose levels increase in response to low temperature, PGC1α was shown to increase the transcriptional activity of PPARγ; in addition, it was demonstrated to cause the expression of the uncoupling protein, which is the hallmark of brown adipose tissue[244].

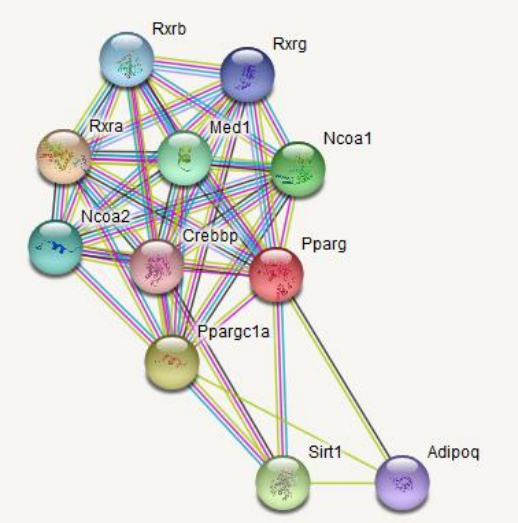


Figure 42: The functional protein association network of PPARγ interactome in mouse. Figure generated using the STRING Database (string-db.org). A number of nuclear transcriptional coactivators and mediators are shown as interaction partners. Pppargc1a is the mouse homolog of PGC1α.

Brown adipose tissue, in contrast to white adipose tissue, is primed more towards energy expenditure; brown adipocytes tend to be richer in mitochondria and have a higher metabolic rate, moreover their expression of the uncoupling protein (UCP1) enables them to dissipate energy as heat[245]. UCP1 itself is a member of the solute carrier 25 (SLC25) family member that's expressed within the inner mitochondrial membrane – by shuttling protons down the electrochemical gradient, it works to essentially short-circuit the mitochondrial electron transport chain and dissipate the energy from the TCA cycle in the form of heat[246]. UCP1-null mice are more cold-sensitive[247], however, they are more resistant to diet-induced obesity[248] despite the fact that ectopic expression of UCP1 in mice causes a reduction in fat stores[249].

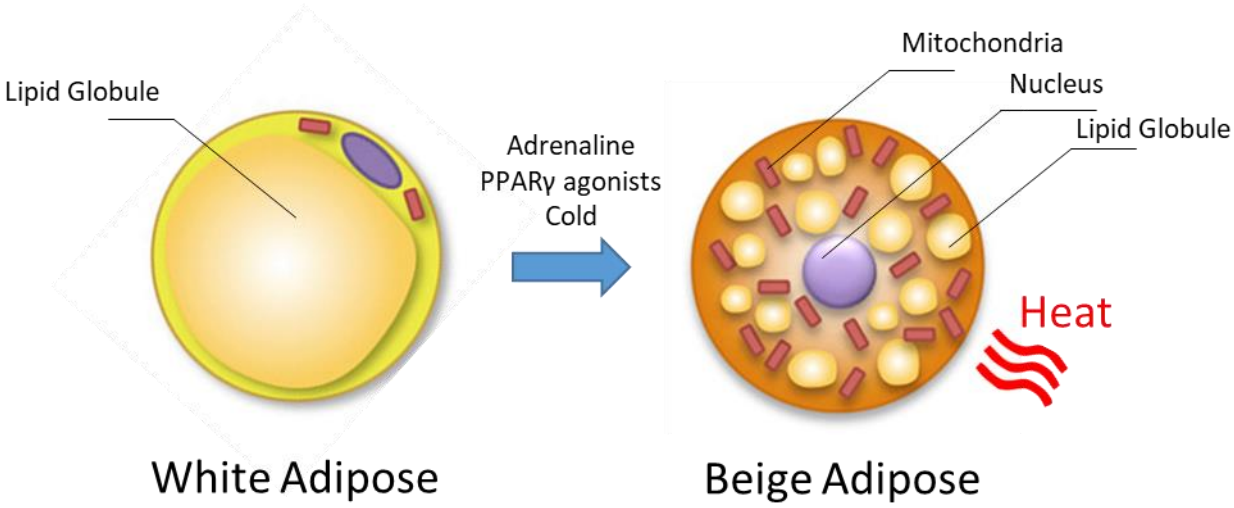


Figure 43: Conversion of white adipose tissue (WAT) to beige adipose tissue. The beige adipose has phenotypic features similar to brown adipose, namely increased energy expenditure and expression of UCP1.

Initially, brown fat adipose tissue was thought to be mostly present in infancy, and largely gone by the age of adulthood, with the possible exception of people chronically exposed to low temperatures[250]. However, recent data shows that, to a certain extent, adipose remodelling is possible, and brown features can appear in otherwise white adipose, termed 'beige adipose' (Figure 43). CRE (cAMP Response Element) signalling can turn on brown phenotype features and UCP1 expression, as demonstrated by overexpression of β-1 adrenergic receptors in adipose tissue[251], or knockouts of protein kinase A regulatory subunits, which leaves the catalytic subunits constitutively active[252]. This is because the *Ucp1* gene has, in addition to a PPRE, a CRE motif upstream within an enhancer region[253]. As mentioned before, PPARγ signalling in tandem with the coactivator PGC1α, can also contribute to UCP1 expression[244,254]. For instance, the canonical PPARγ agonist, rosiglitazone, can induce UCP1 expression in white adipose cells in a

PGC1α-dependent manner[255]. Perhaps surprisingly, though, it appears the link between potency of PPARγ agonism and UCP1 induction isn't well established, as comparably 'weak' in terms of potency PPARγ agonists, such as NC2100 (achieves 80% of maximal PPARγ activation in a luciferase reporter gene assay at 100 μM) were also capable of inducing UCP1 expression in a mouse model[256]. In fact, in a recent study, Imatinib (Gleevec) was shown to act as a PPARγ antagonist *in vitro*, while increasing UCP1 expression and browning of adipose in a mouse model[257].

4.1.4 The need for proteomic annotation of UCP1-inducers

Given the wide interaction network between PPARγ and various nuclear corepressors and coactivators, as well as the unclear link between PPARγ agonism potency and UCP1 induction, and taken together with the known and established polypharmacology of some of the known UCP1 inducers, such as rosiglitazone, it was decided that it is necessary to profile some of these compounds via chemoproteomic methods. The goal of using chemoproteomics on compounds, such as rosiglitazone, would be to potentially elucidate some of the mechanistic pathways involved in UCP1 induction. As was shown previously, MS-CETSA can detect binding partners to a particular target, and it can also detect compound off-target interactions.

Thus, it was decided to first develop CETSA-WB in suitable cellular models, followed by the establishment of a more robust AlphaLISA-based platform for detecting cellular PPARγ agonists (Chapter 5), which would ultimately guide the

MS-CETSA experiment to annotate the small molecules under study using proteomics (Chapter 6).

4.2 CETSA-WB studies

4.2.1 The selection of a suitable cell line for initial CETSA-WB studies

Initially, the focus was to establish that PPARγ is amenable to CETSA. To this end, a number of suitable immortalised cell lines, shown by the Protein Atlas to have high mRNA levels of PPARγ (in addition, for one of the cell lines, A549, the ProteomicsDB database also reports high PPARγ protein levels), were analysed for PPARγ expression levels. The cell lines were compared by Western Blot for PPARγ expression (Figure 44). Two of the cell lines were selected, SW620 and A549. SW620 is a colon cancer line, where PPARγ activation coincided with cancer stem cell suppression[258]. A549 is a lung cancer cell line, where PPARγ activation has been shown to directly inhibit tumour progression[259].

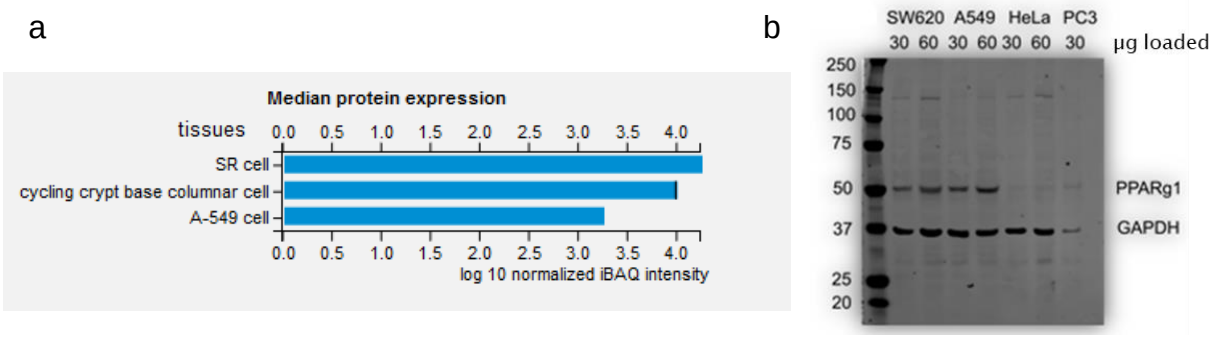


Figure 44: PPARγ expression levels in selected cell lines. (a) Protein expression levels as indicated on ProteomicsDB (proteomicsdb.org) database. (b) Direct comparison of expression levels between different cell lines by WB.

4.2.2 Optimisation of CETSA-WB on the A549 line

The initial CETSA-WB experiments would seek to establish the optimal temperature range for performing the experiment in the future. The starting compound was a well-established TZD-class PPARγ agonist pioglitazone, shown to have a Kd of 630 nM against PPARγ via scintillation proximity assay[260], which initially prompted the use of 100 μM final concentration. Unfortunately, PPARγ appeared to be much less thermostable than predicted, and thus the first experiment, which increased temperature in 4 °C increments did not provide meaningful data (Figure 45). Subsequently, it was decided to change the temperature steps to 1 °C, as well as decrease the pioglitazone concentration to 20 μM, in the unlikely event that the drop in signal is due to cell death as a result of overstimulation. The experiment showed that, fundamentally, pioglitazone is capable of stabilising PPARγ in a cellular context, however, the melting curve never plateaus on either side as a result of the small increment. Thus, it was decided to use 2 °C increments.

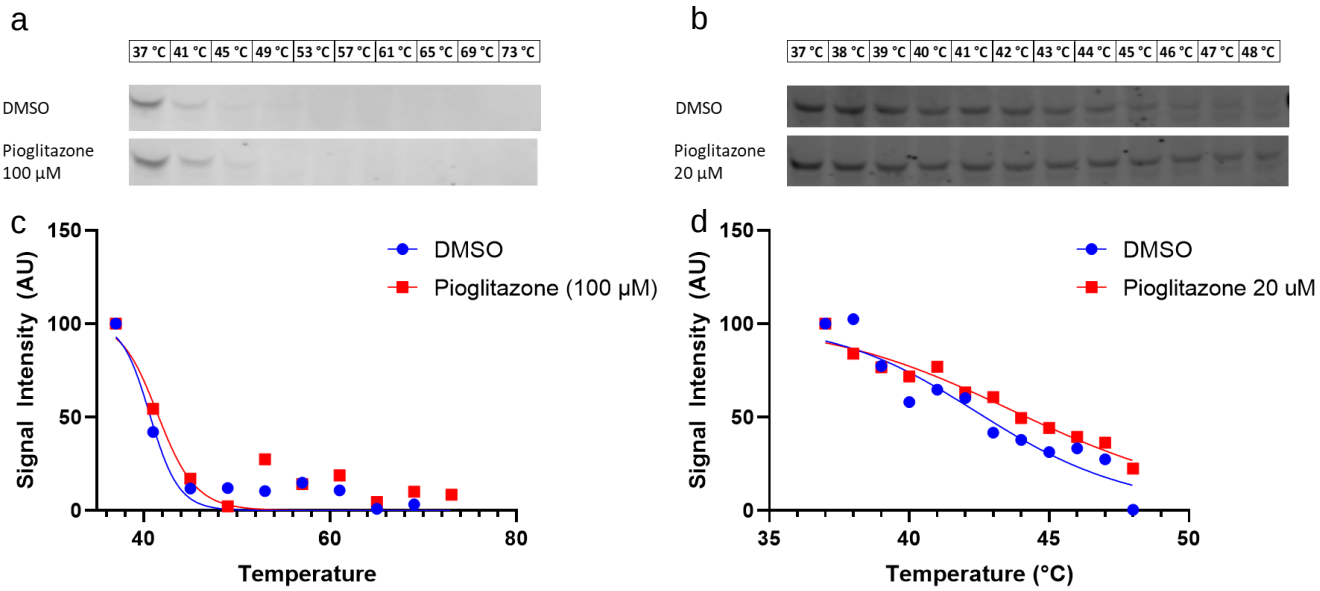


Figure 45: Initial optimisation experiments. The cells were incubated with either pioglitazone, or equivalent volume of DMSO, for one hour, followed by aliquoting, heat pulse and centrifugation. The samples were visualised by SDS-PAGE followed by WB (a,b), and quantified by densitometry to produce the melting plots (c,d). Left: CETSA-WB at 4 °C intervals. Right: CETSA-WB at 1 °C intervals. Melting temperature: DMSO: 42.7 °C; Pioglitazone 44.2 °C. The data is normalised to the 37 °C value.

Subsequently, pioglitazone and another two compounds were tested in A549 cells (Figure 46). These were the aforementioned antagonist GW9662 and a more potent agonist S26948[261].

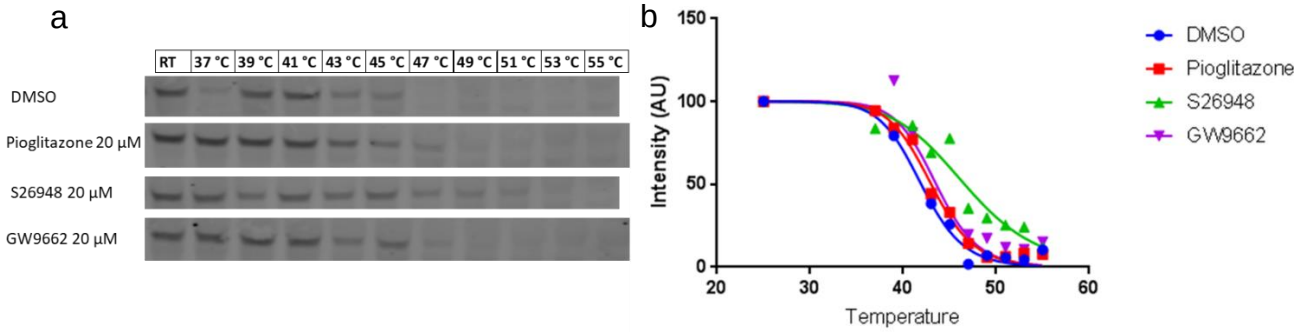


Figure 46: First CETSA experiment on A549 cells. The cells were incubated with the compounds, or equivalent volume of DMSO, for one hour, followed by aliquoting, heat pulse and centrifugation. The samples were visualised by SDS-PAGE followed by WB (a), and quantified by densitometry to produce the melting plots (b). Tm: DMSO: 41.9 °C; Pioglitazone: 43.1 °C (ΔTm = 1.2 °C) S26946: 46.6 °C (ΔTm = 4.7 °C) GW9662: 43.6 °C (ΔTm = 1.7 °C). The data is normalised to the 37 °C value.

Of note is the observation that pioglitazone was markedly less stabilising than in the initial assay. Meanwhile, S26948, which binds to PPARγ with a K_d of 43 nM in a radioligand assay[262], stabilised PPARγ by 4.7 °C. The antagonist, GW9662, was comparable to pioglitazone.

In addition to the number of PPARγ-targeting compound, an additional compound, LG100268 was investigated in this assay. Instead of targeting PPARγ, LG100268 targets the RXR receptor with a Kd of 3 nM, by radioligand assay[263], and thus promotes the dimerisation between PPARγ and RXR. The rationale was that the dimerisation itself would thermally stabilise PPARγ, resulting in an apparent ΔTm following LG100268 treatment. Perhaps contrary to expectations, RXR agonism did not result in PPARγ stabilisation (Figure 47).

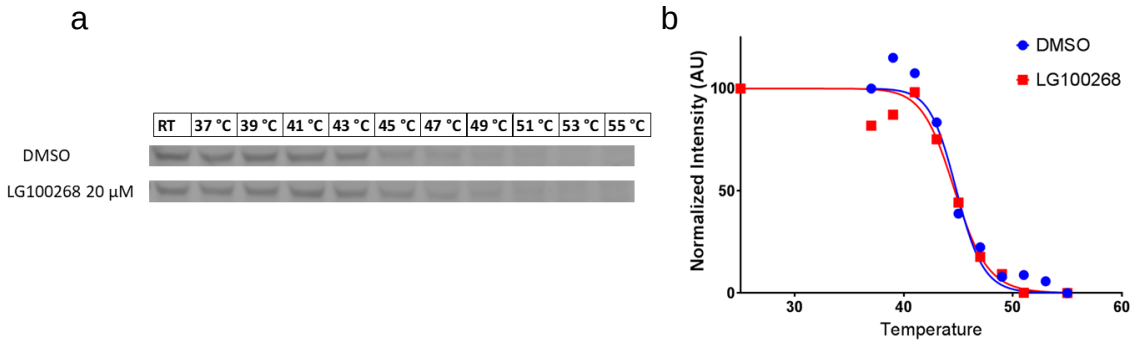


Figure 47: LG100268 does not stabilise PPARγ. The cells were incubated with LG100268, or equivalent volume of DMSO, for one hour, followed by aliquoting, heat pulse and centrifugation. The samples were visualised by SDS-PAGE followed by WB (a), and quantified by densitometry to produce the melting plot (b). Tm: DMSO: 44.8 °C; LG100268: 44.7 °C. The data is normalised to the 37 °C value.

Finally, a dual PPARγ/PPARα agonist Saroglitazar was tested. In light of its strong thermal stabilisation of PPARγ, it was decided to test it in tandem with the antagonist, GW9662. Previous CETSA studies on a related receptor, androgen receptor, show that NHR antagonists can decrease the thermal stabilisation elicited by agonists[116]. This was not shown to be the case with PPARγ; instead, an additive effect was observed, as the melting temperature for the two compounds in combination was greater than either one individually (Figure 48).

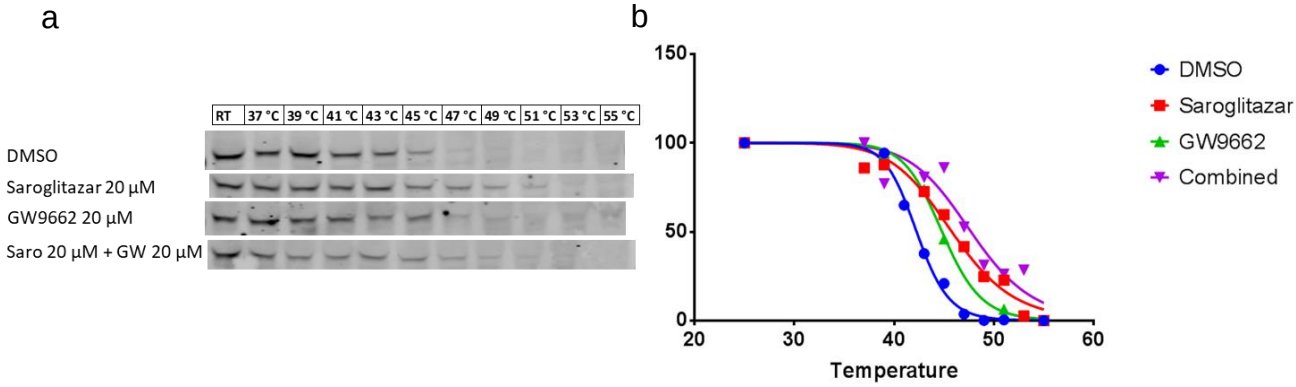


Figure 48: The additive effect of saroglitazar and GW9662 on thermal stabilisation. The cells were incubated with the compounds, or equivalent volume of DMSO, for one hour, followed by aliquoting, heat pulse and centrifugation. The samples were visualised by SDS-PAGE followed by WB (a), and quantified by densitometry to produce the melting plot (b). Tm: DMSO: 42.3 °C Saroglitazar: 45.8 °C (ΔTm = 3.5 °C) GW9662: 44.8 °C (ΔTm = 2.5 °C) Combined: 47.7 °C (ΔTm = 5.4 °C). The data is normalised to the 37 °C value.

4.2.3 Optimisation of CETSA-WB on the SW620 line

As previously, the first optimisation experiment involved looking at the stabilisation of PPARγ in SW620 cells using a canonical TZD agonist pioglitazone and a non-canonical one, S26948 (Figure 49). Interestingly, while the thermal stabilisation for pioglitazone was similar to that observed in A549 cells, in range of 1 °C, the overall thermal stability for both DMSO and pioglitazone groups has

shifted right by about 3.5 °C. The stabilisation by S26948 is also comparatively lower for SW620 cells than for A549.

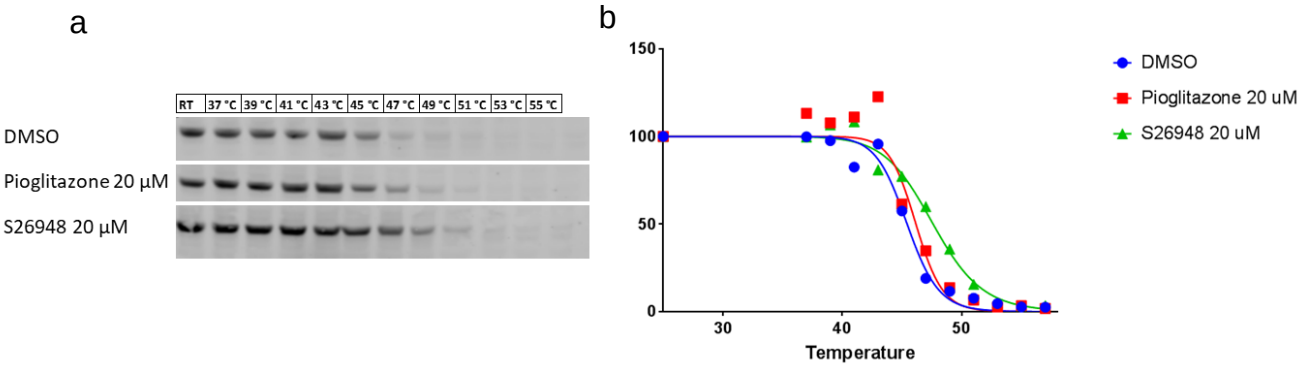


Figure 49: First CETSA experiment on SW620 cells. The cells were incubated with the compounds, or equivalent volume of DMSO, for one hour, followed by aliquoting, heat pulse and centrifugation. The samples were visualised by SDS-PAGE followed by WB (a), and quantified by densitometry to produce the melting plot (b). Tm: DMSO: 45.4 °C; Pioglitazone: 46.8 °C (ΔTm = 1.4 °C) S26946: 47.6 °C (ΔTm = 2.2 °C) GW9662: 43.6 °C (ΔTm = 1.7 °C). The data is normalised to the 37 °C value.

In light of the relatively-weak stabilisation by pioglitazone, it was also decided to replace it with the related, albeit stronger rosiglitazone. Indeed, compared to pioglitazone, rosiglitazone is more strongly stabilising (Figure 50).

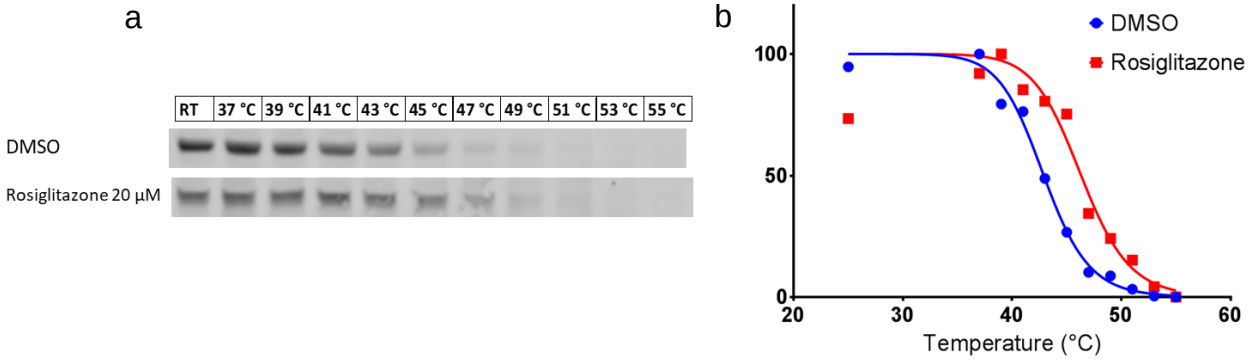


Figure 50: Rosiglitazone is a PPARγ stabiliser. The cells were incubated with rosiglitazone, or equivalent volume of DMSO, for one hour, followed by aliquoting, heat pulse and centrifugation. The samples were visualised by SDS-PAGE followed by WB (a), and quantified by densitometry to produce the melting plot (b). Tm: DMSO: 42.9 °C; Rosiglitazone: 46.3 °C (ΔTm = 3.4 °C). The data is normalised to the 37 °C value.

Saroglitazar, similarly to its behaviour in A549 cells, was also shown to be strongly stabilising in SW620 cells (Figure 51).

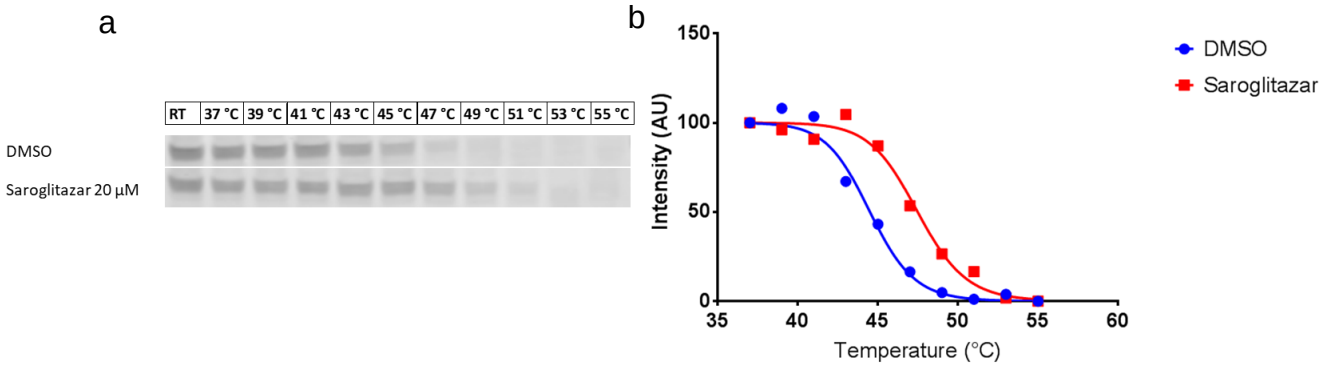


Figure 51: Saroglitazar is a potent PPARγ stabiliser. The cells were incubated with saroglitazar, or equivalent volume of DMSO, for one hour, followed by aliquoting, heat pulse and centrifugation. The samples were visualised by SDS-PAGE followed by WB (a), and quantified by densitometry to produce the melting plot (b). Tm: DMSO: 44.5 °C; Saroglitazar: 47.5 °C (ΔTm = 3 °C). The data is normalised to the 37 °C value.

Given that rosiglitazone was shown to be a potent stabiliser in a cellular context, it was decided to pursue the compound further. Initially, the compound was tested in an ITDRF assay at 49 °C, where the apparent EC_{50} was 6.4 µM (Figure 52), however, it has to be stressed that complete rescue of rosiglitazone does not occur, as the compound isn't sufficiently stabilising under these conditions.

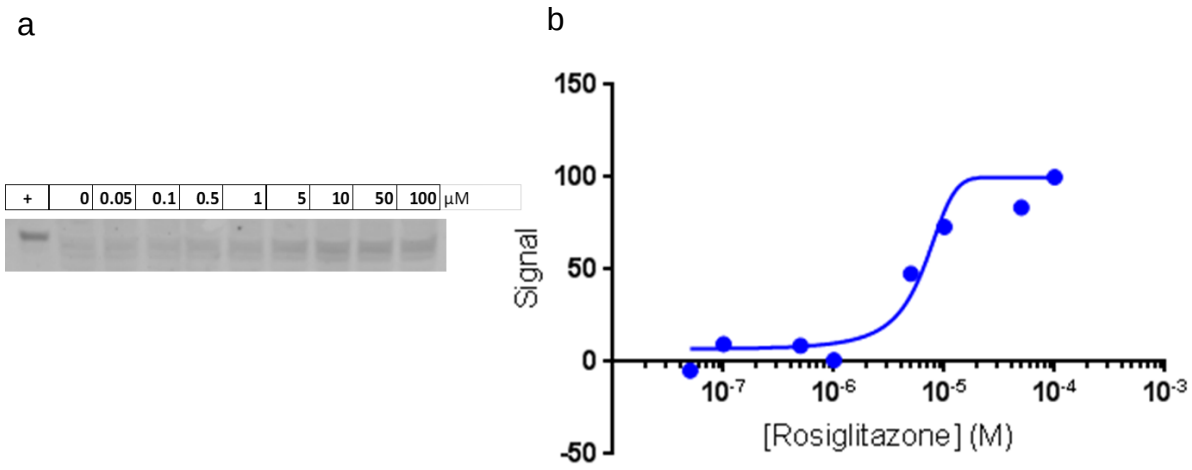


Figure 52: Isothermal dose-response fingerprinting experiment with rosiglitazone in SW620 cells. The cells were incubated with increasing doses of rosiglitazone, or equivalent volume of DMSO, for one hour, followed by aliquoting, isothermal heat pulse at 49 °C and centrifugation. The samples were visualised by SDS-PAGE followed by WB (a), and quantified by densitometry to produce the melting plot (b). The apparent EC_{50} is 6.4 µM. The data is normalised between the DMSO and the 100 µM value. The positive control was heated to 37 °C.

4.2.4 Optimisation of CETSA-WB in an adipocyte model

Now that the proof-of-concept CETSA has been achieved in two different immortalised cell lines, it was decided to perform CETSA-WB in the aforementioned differentiated 3T3-L1 adipocytes, as a more biologically-relevant cell line, using rosiglitazone. Moreover, as ITDRF has demonstrated a concentration-dependent stabilisation effect, it was decided to increase the dimensionality of the experiment to 2D-CETSA, with 3 different concentrations of rosiglitazone, from 1 µM, which is the minimum concentration required to trigger differentiation, to 20 and 100 µM, which are saturating concentrations, as well as the DMSO control. The change in thermal aggregation temperatures varies from 0.9 °C for 1 µM rosiglitazone, to 3.5 °C at 100 µM (Figure 53).

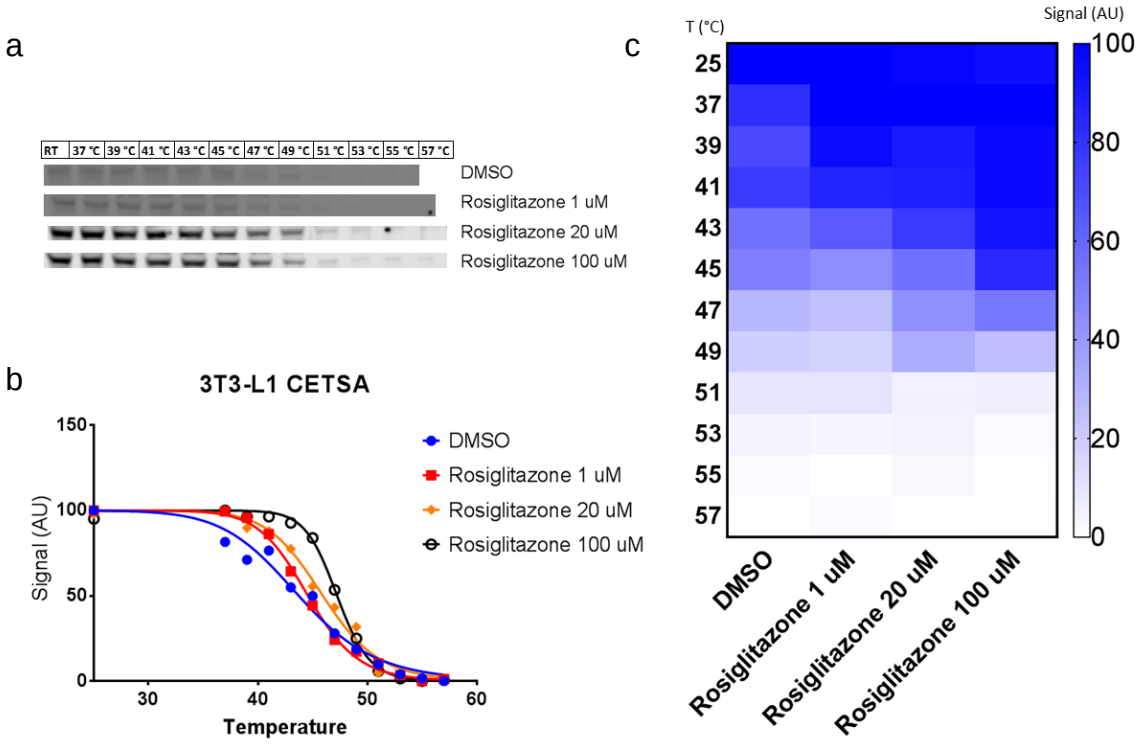


Figure 53: 2D CETSA on 3T3-L1 adipocytes with varying concentrations of rosiglitazone. The cells were incubated with increasing doses of rosiglitazone, or equivalent volume of DMSO, for one hour, followed by aliquoting, heat pulse and centrifugation. The samples were visualised by SDS-PAGE followed by WB (a), and quantified by densitometry to produce the melting plot (b), as well as a 2D heat map (c). Melting temperatures: DMSO: 43.7; 1 µM: 44.6 (ΔTm = 0.9 °C); 20 µM: 45.9 (ΔTm = 2.2 °C); 100 µM: 47.2 (ΔTm = 3.5 °C). The data is normalised to the 37 °C value.

4.3 Discussion

As can be seen, CETSA-WB experiments demonstrated that PPARγ in the context of three different cells is amenable towards thermal stabilisation, with some compounds being noticeably stronger stabilisers than others. However, the experiments also demonstrated an urgent need to shift from the immunoblot method of readout. Between untreated samples, the melting temperature can vary by as much as 3 °C, making it difficult to draw accurate conclusions about relative thermal stabilisation across different experiments, which is further compounded by

issues with image quantification and occasionally high background. In addition, if one were to make enough replicates to have more confidence in the results, it would not be feasible in the long term, thus further necessitating alternate readout methods.

4.4 Conclusions

In conclusion, the Western Blot readout of CETSA is inadequate for long-term and high-throughput thermal profiling of small molecule PPARγ inibitors. The problems resulting from attempting to quantify the blots via densitometry, as well as the inherently low-throughput methodology meant that the approach had to be abandoned in favour of the development of a quantitative, AlphaScreen-based readout for CETSA experiments.

5. Development of AlphaScreen CETSA for PPARγ

5.1 Introduction

5.1.1 The shortcomings of WB and the need for quantitative proteome analysis

As mentioned before, WB as a technique for protein quantification has a number of significant drawbacks; issues with signal saturation due to inappropriate loading, antibody non-specific binding and target misidentification, nonlinear protein quantification with respect to densitometry data and normalisation errors are the most common problems associated with it[111]. Moreover, WB is limited in its throughput by the relatively slow SDS-PAGE mediated separation and blotting procedure, which, depending on the instrument, usually precludes more than 30 samples being run at once.

As a result, in recent years efforts have been undertaken in order to improve the quantification of CETSA target engagement assays and reduce the overreliance on densitometry. Such a technique has to possess the following qualities:

- Accuracy of quantification without the need to resort to densitometry or image analysis – ideally spectrophotometric/luminescence data readable with the use of a microplate reader that scales linearly with the amount of protein (requiring the optimisation via construction of appropriate standard curves)

- Specificity for the target, without the risk of quantifying a different protein
- Recognition of folded versus unfolded protein, ideally without the need for centrifugation, thus ensuring that there are no issues with cell lysis technique (detergent) resolubilising unfolded protein, which may lead to false positives
- As little genetic manipulation of cells as possible, ideally none – the more the cells are manipulated, the more the assay deviates from being physiologically-relevant
- High-throughput with microplate compatibility, allowing for multiple replicates to run on one plate and paving the way towards a CETSA screening platform

5.1.2 ELISA and AlphaLISA-based CETSA quantification techniques

As mentioned in the introduction, one potential avenue towards high quality CETSA data acquisition that is not WB reliant is, as mentioned in the introduction, the use of AlphaScreen/AlphaLISA technology. In brief, an Alpha assay involves the use of two beads: one containing a phthalocyanine photosensitiser that, upon irradiation at 680 nm, generates singlet oxygen molecules (the ‘donor’ bead) and one containing three olefins (Thioxene-Anthracene-Rubrene, or TAR) capable of resonance energy transfer between one another; as the singlet oxygen reacts with thioxene, light is emitted and transferred to anthracene and further to rubrene, resulting in broad spectrum emission in the range of 520-620 nm – this bead is

known as the ‘acceptor’ bead[264]. Because the lifetime of singlet oxygen in aqueous media is only about 4 µs, the distance at which this reaction can occur is inherently constrained to less than 250 nm, as modelling shows the steady state concentration of singlet oxygen at that distance from the donor bead to be less than 1% [114]. This, coupled with the fact that the singlet oxygen tends to diffuse in all directions from the bead, converts the reaction into a *bona fide* proximity assay. In AlphaLISA, the acceptor bead contains europium instead of anthracene and rubrene; reaction of thioxene with singlet oxygen thus results in the formation of a dioxetane intermediate, which fragments and excites the europium, resulting in chemiluminescence at a specifically defined wavelength of emission at 610 nm[265]. If the donor and acceptor beads are within the aforementioned proximity, the singlet oxygen from the donor bead will be able to reach the acceptor bead in sufficient quantities to stimulate emission that is detectable by the use of the plate reader. Thus, by attaching the beads to two ELISA-compatible antibodies that recognise only the folded form of the protein, the two antibodies can be added to the lysed cells following the heat shock, and in principle provide CETSA signal on the amount of folded (stabilised) protein in the crude lysate. An added benefit is that the procedure requires very few experimental steps between the heat pulse and the generation of the data, and, if done in a microplate format, allows for high-throughput applications. In principle, it would be possible to directly attach the beads to the antibodies; however, due to the bulk of the beads this is generally not advised, as the slow kinetics of the complex formation would result in a long time to develop the signal. The convention is to utilise anti-species capturing antibodies

that are in turn covalently attached to the beads, as well as two target antibodies from different animals that recognise different epitopes (Figure 54) – this approach has the advantage of one capturing antibody being compatible with numerous primary ones, as long as they are all from the same animal. However, this is also one of its key limitations – one cannot use two primary antibodies from the same animal. In a similar approach, a protein A-conjugated secondary antibody can be used, however, in this case it is paramount that the other capturing antibody has no cross-reactivity with protein A.

As mentioned before, it is absolutely crucial that the two antibodies selected are ELISA-compatible and, ideally, recognise only the folded form of the protein (though this is not necessary, as aggregates can be separated from native protein, for instance by centrifugation). Moreover, the two antibodies need to bind separate epitopes that are ideally on opposite sides of the protein to prevent steric clashes between the antibodies. Typically, as part of the optimisation process, a number of primary antibodies are selected and tested on lysates and recombinant target protein. This is done on both heat-denatured and unheated analyte to look for optimal signal-to-background ratio and high (>10) fold change between the two. Once suitable pairs are chosen, the antibodies are tested in a live cell environment, to determine the optimal amount of starting protein and, for the experiments on live cells, the optimal number of cells per well.

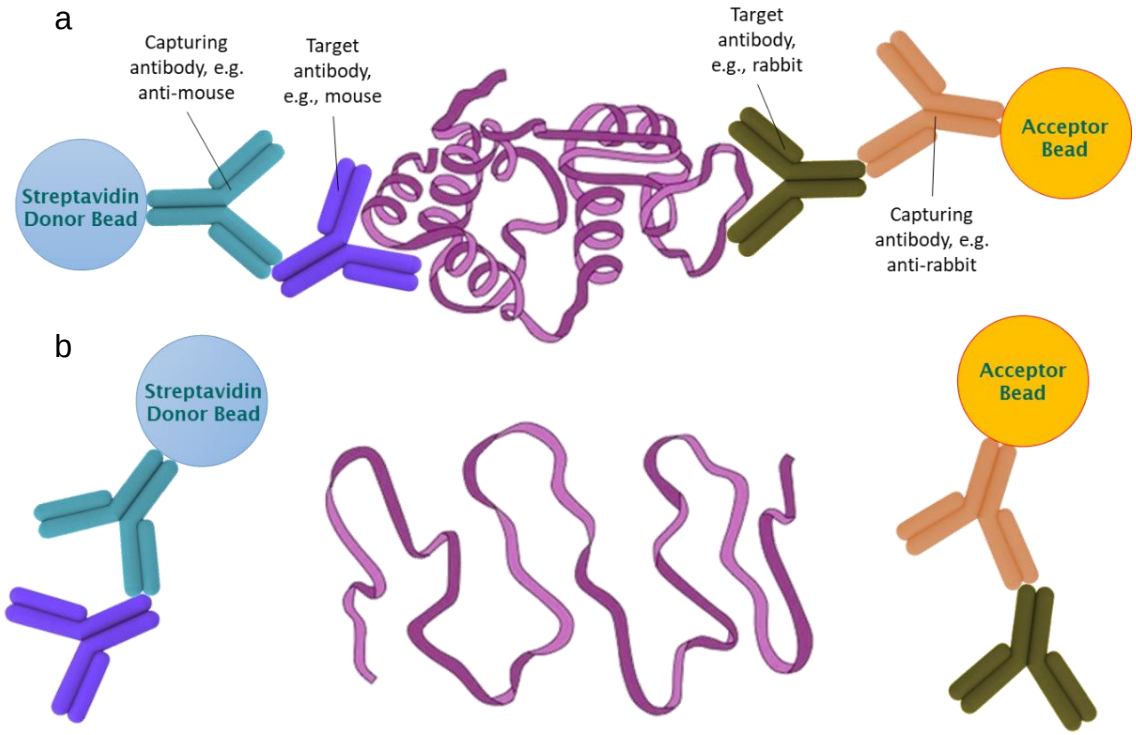


Figure 54: The experimental set-up for a typical CETSA experiment with an AlphaScreen set-up. The illustration of the scheme using two primary antibodies from different species, and suitable secondary antibodies directly conjugated to beads. (a) If the protein is folded, the ELISA-exclusive antibodies will recognise it, thus forming a complex with the secondary antibodies where the beads are in proximity, resulting in signal. (b) If the protein is heat-denatured and aggregated, the antibodies won't recognise the aggregates, thus resulting in no signal.

When optimising for antibody selection, there are two primary criteria that need to be obeyed, namely the above mentioned steric effects that occur when two antibodies bind the same, or very close epitopes on the protein, and epiturbance, which is broadly defined as a change in protein tertiary structure as a result of ligand binding that results in epitope masking, and can also result in a signal drop (Figure 55). Thus, any potential antibody combinations have to be tested with and without the presence of an agonist or even better a selection of representative modulators.

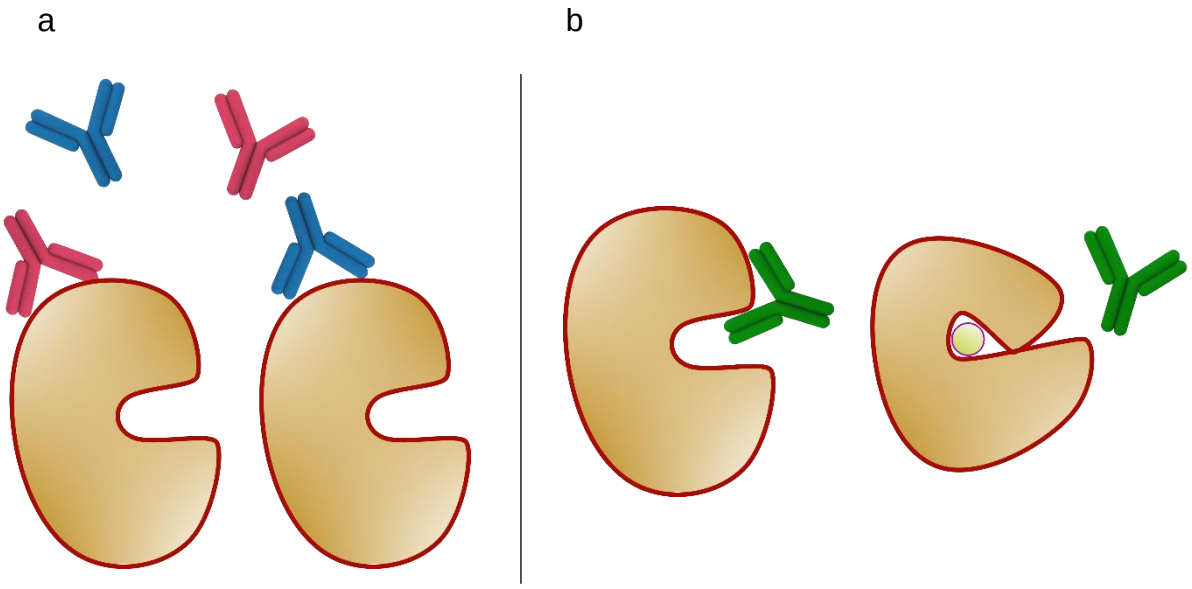


Figure 55: Two potential antibody-related issues that may interfere with AlphaScreen signal. (a) Antibody steric issues occur as a result of the antibodies recognising epitopes that are too close and typically manifest themselves as little to no signal. (b) Epiturbance occurs when structural rearrangements in the protein as a result of ligand binding result in epitope masking, resulting in no signal when the target is incubated with the ligand. Note that because different ligands bind different sites and thus elicit different conformational changes, it may not be possible to optimise for every single ligand, thus usually only the canonical ones are used.

The experimental set-up is adaptable to a microplate environment, requiring a microplate-compatible PCR instrument. If the instrument is capable of a spatial heat gradient, a classic CETSA experiment can be performed in high throughput; conversely, in the case of instruments, such as the Roche Lightcycler, where the entire plate is heated to one temperature, an ITDRF experiment can be performed instead. Moreover, once the melting temperature of the protein has been elucidated, entire libraries can be potentially screened for their ability to stabilise the protein, turning the assay into a high-throughput screen that can complement conventional screening campaigns[98].

An alternative approach, recently described, utilises only one antibody combined with cell fixation, making it more geared towards adherent, rather than suspended cells[266]. With this method, cells are seeded onto a treated microplate and allowed to attach. Afterwards, the compounds are added onto the microplate and, following a period of incubation, the microplate is heated. The cells are then fixed and permeabilised, which is followed by blocking with albumin and incubation with the primary antibody; subsequently the plate is washed and a secondary, fluorophore-conjugated antibody is added. Data is acquired by imaging the microplate.

The above approaches, whilst useful, requires the use of highly-specific, ELISA or immunofluorescence compatible antibodies. If such antibodies are unavailable, a third method makes use of an enzyme complementation assay[112,113]. The approach, dubbed InCELL Pulse, involves transfecting the cell with the gene encoding the recombinant target linked to a short sequence that complements the enzyme acceptor (EA) to form a competent enzyme, such as beta-galactosidase, capable of generating chemiluminescence. Following the microplate heat pulse, the cells are lysed and the EA is added alongside substrate, after which the microplate is read. Whilst an interesting alternative to the antibody-based readout, this approach requires genetic manipulation of cells, therefore making it less physiologically-relevant.

5.1.3 AlphaScreen-based application of CETSA to screen and examine PPARγ-targeting compounds

With the above in mind, it was decided to move from a WB-based approach, to an AlphaScreen-based approach for the purpose of CETSA target engagement assay, with the later possibility of developing a microplate-based screen. The AlphaScreen-based method was chosen, as this technique is well-established, with a number of publications detailing its use and a clear optimisation pathway[115,116,266]. Moreover, the amount of available ELISA-compatible antibodies against PPARγ was found to be sufficient for a variety of permutations and combinations, making it unnecessary to have to employ cell fixation. The requirement for 3T3-L1 cell differentiation and limited passages of the cell line also potentially complicates the generation of stable transfects, thus favouring AlphaScreen over InCELL Pulse.

The following sections describe the various optimisation steps undertaken for the purpose of antibody selection and bead conjugation, followed by the use of the technique for CETSA readout and a potential screening application for the purpose of detecting potential PPARγ agonists.

5.2 Assay optimisation

5.2.1 Antibody selection and initial experiments to devise appropriate combinations

A number of potential antibodies with ELISA-specificity were selected and purchased (Table 3). The selection criteria for the antibodies included recognising

different portions of the full-length protein, demonstrated application in ELISA and derived from either mouse or rabbit to fit the bead conjugation strategy.

Name	Animal/Type	Epitope/Immunogen
ab45036	Rabbit/Polyclonal	PPARγ2 aa 1-16
ab59256	Rabbit/Polyclonal	All PPARγ near Ser112
ab66343	Rabbit/Polyclonal	All PPARγ, aa 38-87
ab41928	Mouse/Monoclonal	All PPARγ, aa 3-105
CS81B8	Rabbit/Monoclonal	All PPARγ, near His494
ProteinTech 16643	Mouse/Monoclonal	PPARγ fusion protein Ag10005
ProteinTech 60127	Mouse/Monoclonal	PPARγ fusion protein Ag10005
sc-7273	Mouse/Monoclonal	All PPARγ, aa 486-505

Table 3: The selection of antibodies against PPARγ. All antibodies are ELISA-compatible according to the various manufacturers' websites; however, only some are ELISA-exclusive, necessitating care with optimisation.

As mentioned before, the initial steps in antibody optimisation involve selecting the antibody pairs capable of binding the protein in tandem, in other words those pairs where there are no steric issues. To this end, a number of possible assays were investigated, the first one being the double-antibody pulldown. The rationale behind the experiment was that, since conventional immunoprecipitation (IP) can enrich for the target protein, the addition of another primary antibody following the incubation and washing step will result in that antibody also being enriched for, but only if it can bind PPARγ alongside the 'bait' antibody immobilised on the resin (Figure 56).

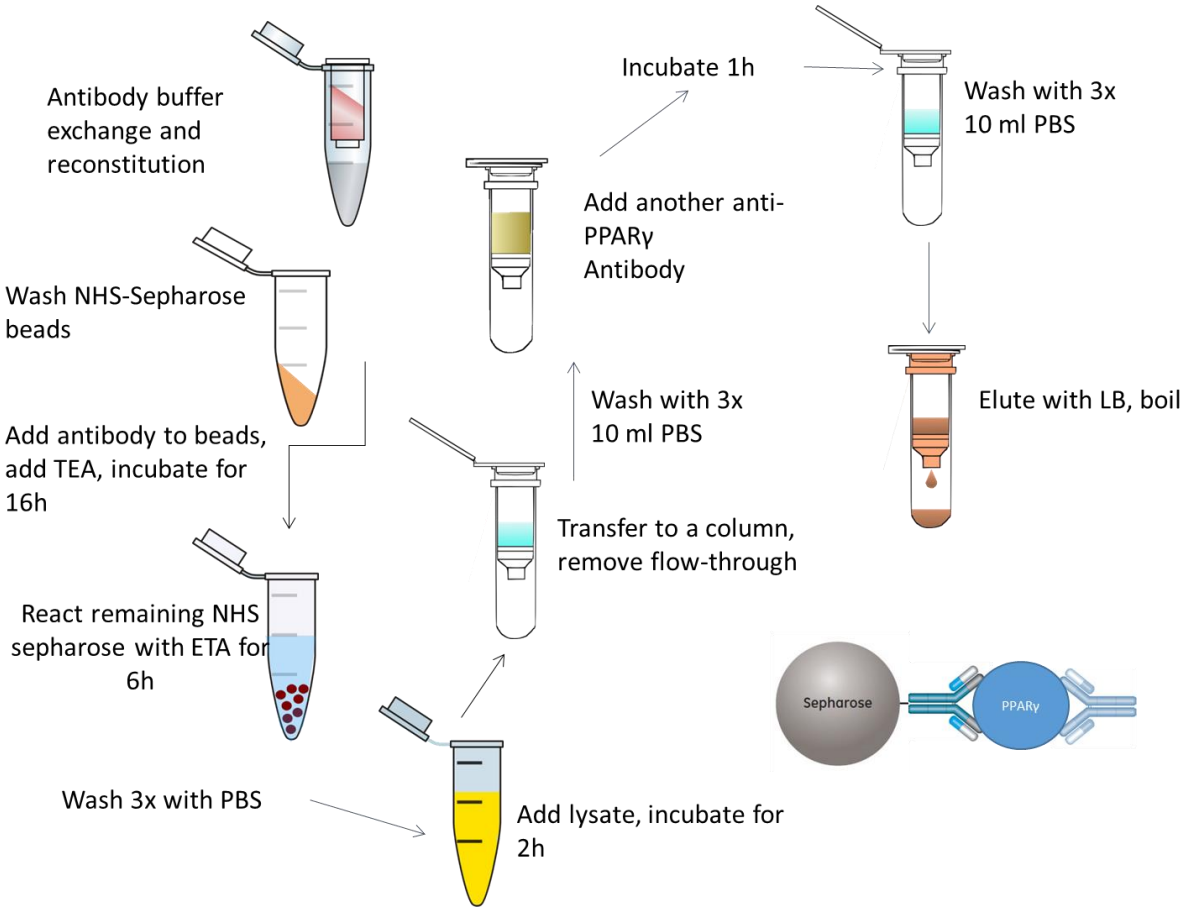


Figure 56: The double-antibody pulldown experimental set-up. The 'bait' antibody is immobilised on a sepharose resin, which is followed by the addition of lysate and capture of PPARγ. A second antibody is then incubated with the resin, and if the two antibodies are compatible, it will get captured via PPARγ. Note that all antibodies are ELISA-compatible according to the various manufacturers' websites; however, only some are ELISA-exclusive, necessitating care with optimisation.

Initially, the CS81B8 antibody was chosen as the 'bait' antibody. According to the manufacturer's website, this antibody has been previously used for WB and validated for IP/ELISA on the manufacturer's website and, out of the PPARγ antibodies, it has the highest number of citations. Another 4 antibodies (ab45036, ab59256, ab66343, ab41928) were chosen in the proof-of-concept experiment. Following the experimental protocol as outlined above, the primary antibodies were eluted off the column and transferred by WB. The membrane was blocked and probed using secondary antibodies alone, for the presence of both light chain (MW ~25 kDa) and heavy chain (MW ~50 kDa). Interestingly, all four antibodies were found to have been pulled, albeit at different amounts (Figure 57). This potentially suggests that the antibodies have different affinities for PPARγ, or that they also recognise other proteins and thus perturb the antibody amount available for binding PPARγ.

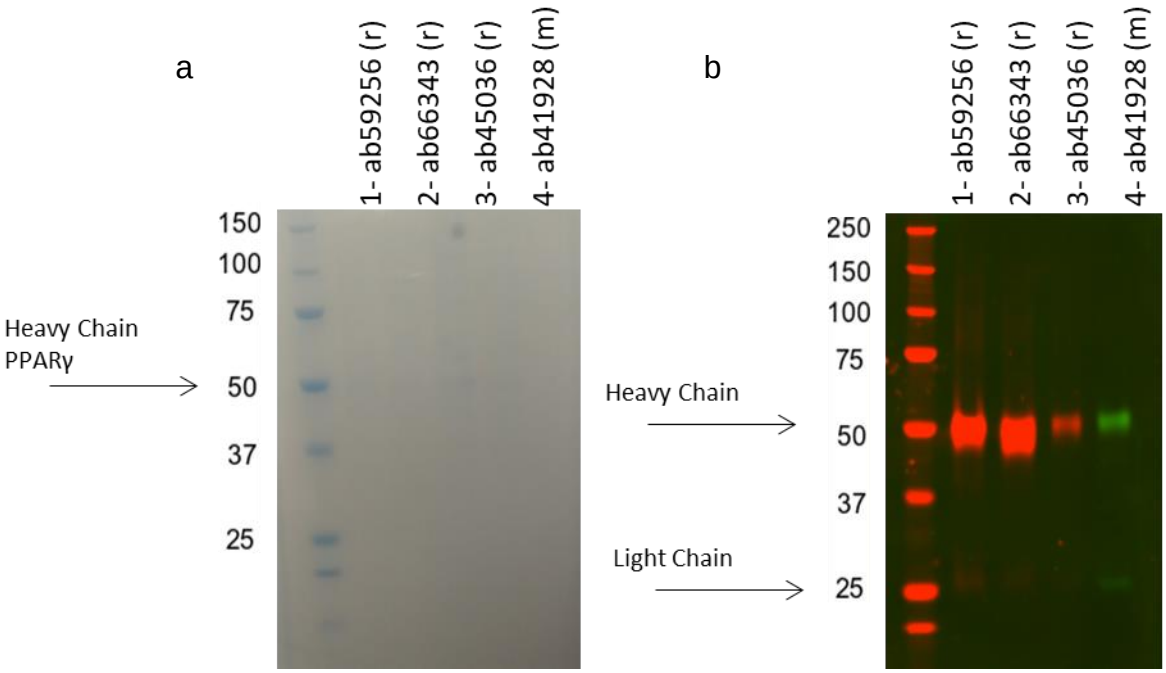


Figure 57: The results of the double antibody pulldown. Antibody heavy chain elutes at ~50 kDa, in the same region as PPARγ, potentially complicating the interpretation of the results. Antibody light chain elutes at ~25 kDa. (a) SDS-PAGE output, stained with Coomassie. (b) WB output, probed with anti-primary antibodies; the fluorophores attached to the secondary antibodies emit at different wavelengths. False colouring is used to distinguish between the anti-mouse and anti-rabbit antibodies. As the bait antibody was covalently linked to the resin, the bands are likely derived from the antibodies precipitated together with PPARγ, rather than the bait antibody itself.

Whilst encouraging, the protocol involved extensive washing of the beads following PPARγ binding to the antibody – this makes the experiment potentially less relevant to the eventual AlphaScreen experiment, as the two antibodies will have to bind PPARγ in the presence of the lysate, alongside all the potential interfering factors. The washing steps were therefore omitted by including the antibody to be enriched for in the lysate (Figure 58). Moreover, it was also discovered that shortening the 'bait' antibody conjugation time from 16 hours to 1 hour did not negatively impact the output. Notably, the signals for some of the

antibodies is significantly reduced, for instance ab59256, suggesting that in a lysate environment, the formation of the complex between the antibodies and PPARγ can be affected by the presence of other proteins.

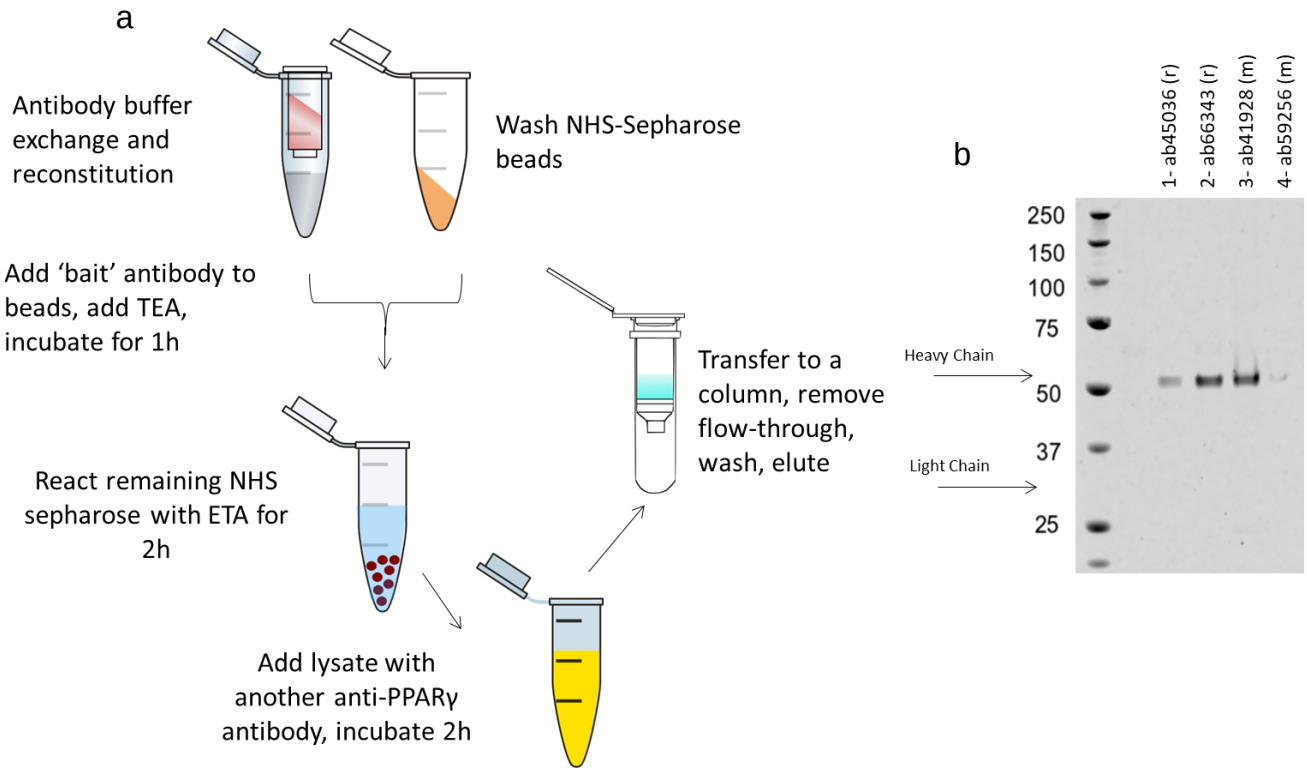


Figure 58: The set-up and results of the double antibody pulldown without washing steps. (a) The 'bait' antibody is immobilised on a sepharose resin, which is followed by the addition of lysate and capture of PPARγ. A second antibody is then incubated with the resin, and if the two antibodies are compatible, it will get captured via PPARγ. Note that this time, the resin is not washed between the incubation steps. (b) The WB output without false colouring shows that the amount of antibodies differ from each other and from the previous experiment.

With the complex formation established between some of the antibody combinations, it was also necessary to ensure that epiturbance does not reduce signal. To test for epiturbance, the experiment was performed with the two best antibodies (ab41928 and ab66343), in the presence of 100 µM rosiglitazone in the lysate or equivalent volume of DMSO (Figure 59). Notably, the signal for either antibody was not significantly reduced in the presence of rosiglitazone, as demonstrated by densitometry, suggesting that the two antibody combinations could be taken for further optimisation.

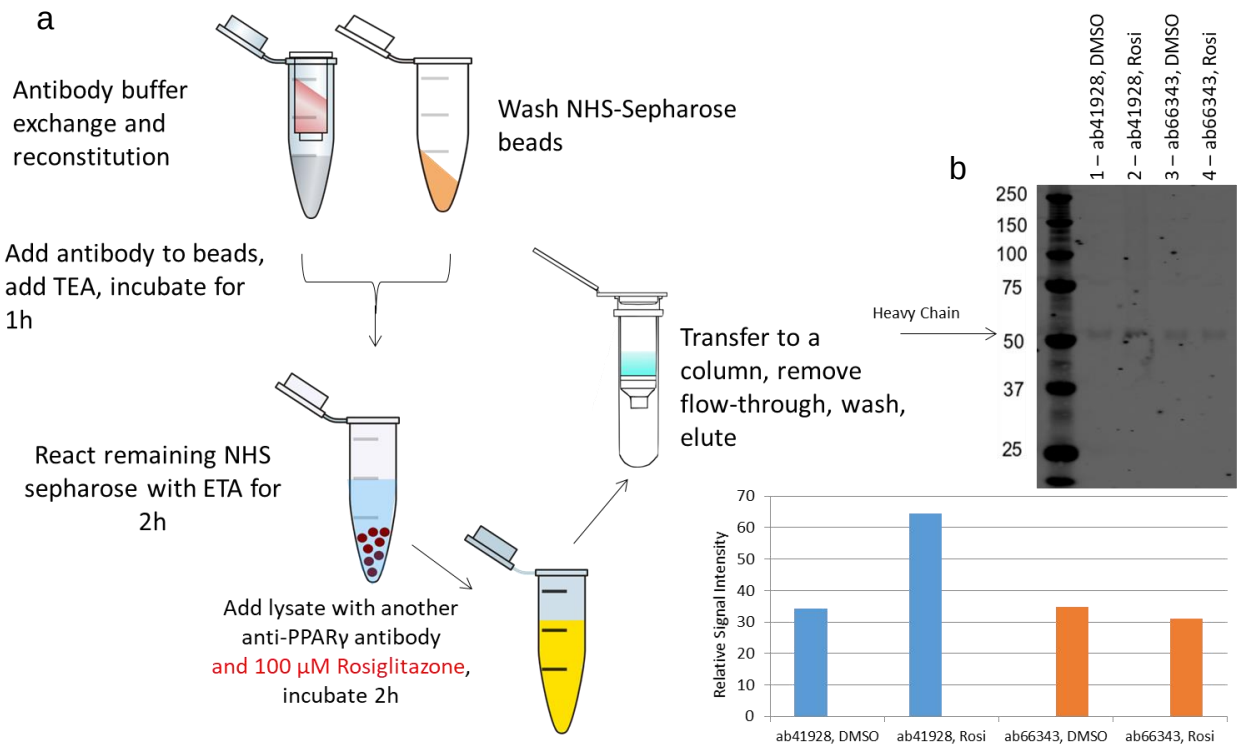


Figure 59: The set-up and results of the double antibody pulldown including rosiglitazone to account for potential epiturbance. (a) The 'bait' antibody is immobilised on a sepharose resin, which is followed by the addition of lysate and capture of PPARγ. A second antibody is then incubated with the resin, and if the two antibodies are compatible, it will get captured via PPARγ. Note that this time, the resin contains saturating amounts of rosiglitazone, such that epiturbance can be assayed.. (b) The WB output without false colouring shows that the binding of either antibody to PPARγ does not appear to be inhibited by the presence of PPARγ agonist rosiglitazone.

The results, while encouraging, did not lead to the double antibody pulldown being pursued further. Unfortunately, out of the potential hits to be taken to the next phase of optimisation, ab66343 was discontinued by the manufacturer and ab45036, due to being PPARγ2-specific, was also rejected, as initial experiments were to revolve around total PPARγ, rather than focusing on specific isoforms. Moreover, the need to perform antibody-resin conjugation for every antibody meant that ultimately the procedure was very resource-intensive. In addition, the fact that both immunoglobulin (Ig) heavy chains and PPARγ appear at the same MW band creates further complications, ultimately necessitating the pursuit of other methods that allow for the study of potential antibody-PPARγ complex permutations, ideally all (or most) in one go and with minimal resource investment.

5.2.2 The switch to biotin-conjugation and bio-layer-interferometry

Out of the 6 antibodies left, 4 were of mouse and 2 were of rabbit origin. Assuming the experimental set up reliant on secondary capture antibodies covalently attached to beads, this allows for only 8 possible combinations out of the original 15. Moreover, one of the antibodies is polyclonal – such antibodies, due to their nature, can potentially be used in combination with themselves, as there is a possibility that different clonalities bind the epitope in a way that permits two different antibodies binding simultaneously. As a result, it was decided to pursue a novel approach. Instead of using secondary capture antibodies, each antibody would be covalently conjugated to biotin, and then a second lot would be directly conjugated to an

AlphaScreen acceptor bead. With the use of a streptavidin-conjugated donor bead, complex formation would be achieved that is completely independent of the species of the antibody used, allowing for many more combinations to be assayed during the optimisation steps (Figure 60).

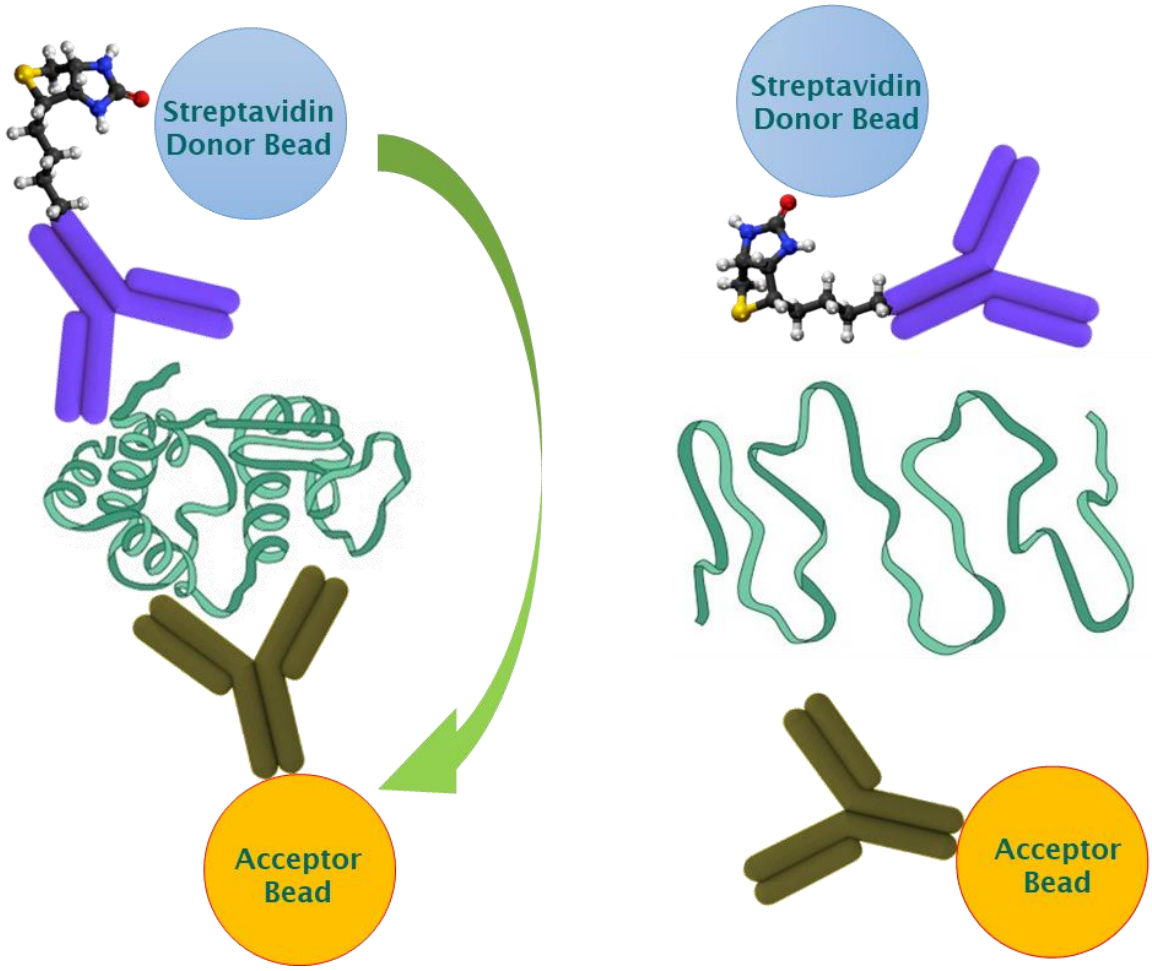


Figure 60: The novel approach towards the AlphaScreen readout for CETSA. Instead of using specie-dependent capture antibodies, the donor antibody is conjugated to biotin (NB diagram not to scale) and captured via streptavidin to the donor bead. The acceptor antibody is directly conjugated to its bead.

The first step involved the conjugation of the antibodies to biotin. This was performed using the ChromaLink kit – the Chromalink biotin contains a long chain PEG3 linker, as well as a chromophore that absorbs in the region of 354 nm and a NHS ester handle for conjugation in basic conditions, including most buffer systems (Figure 61). The presence of the chromophore allows for detection and relative quantification of the stoichiometry of the amount of biotins conjugated per antibody.

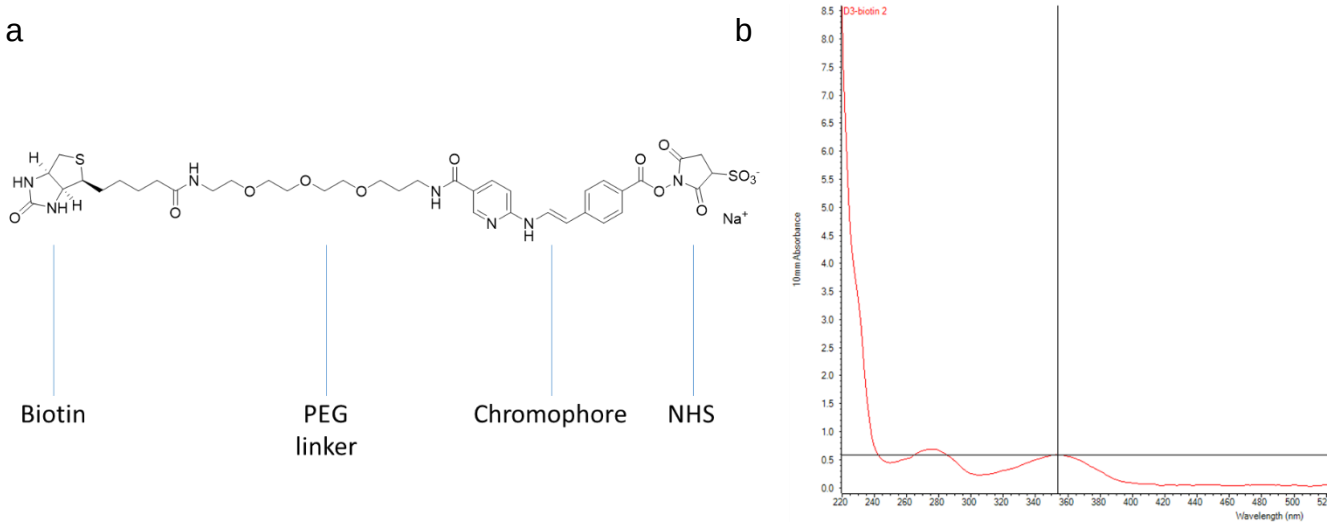


Figure 61: The Chromalink biotin kit. (a) The structure of the biotin-containing reagent, including a PEG linker and a chromophore, as well as the reactive NHS warhead, which conjugates to free amines, such as lysine resides, at basic pH. (b) A representative Nanodrop UV/vis spectrum of a biotinylated antibody – notice the peak at 354 nm signifying that the conjugation was successful.

Subsequently, the 6 labelled antibodies were tested for their ability to bind full-length recombinant PPARγ in a bio-layer interferometry assay (BLI) using a streptavidin matrix. Whilst all antibodies loaded onto the matrix, only a number

showed satisfactory binding to PPARγ (Figure 62), and notably, the SantaCruz antibody (sc7237) exhibited no binding at all relative to control (buffer only). All binding events were associated with relatively slow off-rates, with D3 and D4 ranking as the most stable.

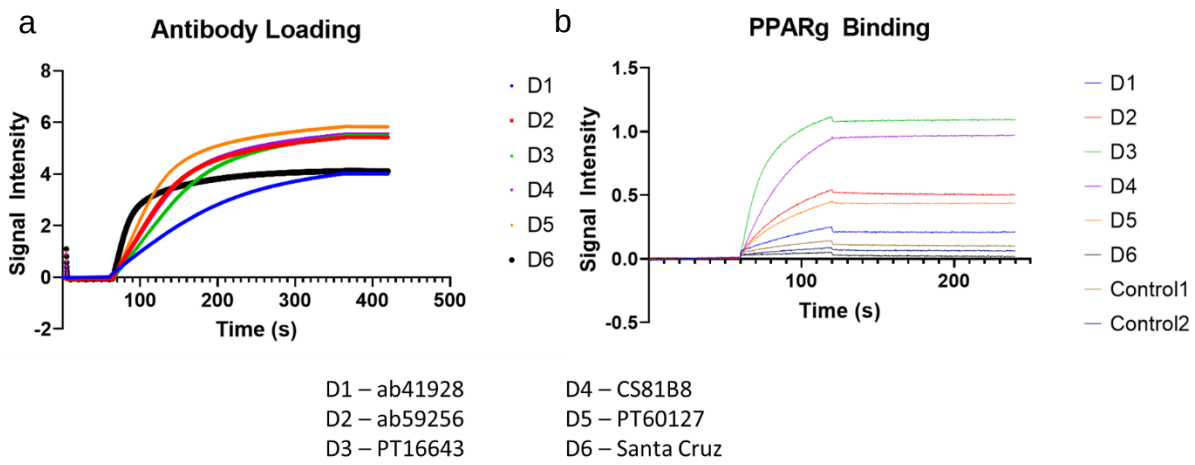


Figure 62: Biolayer interferometry. In a BLI experiment, the biotinylated antibody is first immobilized onto the streptavidin resin, which is followed by incubation with recombinant PPARγ to assay binding. (a) Antibody loading. All antibodies load onto the matrix.(b) Antibody-PPARγ binding. All antibodies with the exception of sc7237 (SantaCruz) appear to bind PPARγ, although with different binding capacities and off-rates.

5.2.3 Proof-of-concept AlphaScreen experiments with recombinant PPARγ

Initially, ab41928 and ab59256 were chosen to be conjugated to the acceptor beads. Despite displaying a lower binding capacity in the BLI assay, ab41928 (A1) has signalled that it can potentially form a full complex with CS81B8 in the double-antibody pulldown assay shown earlier. The second antibody was ab59256 (A2), having the third highest PPARγ binding capacity. The two binders with the highest binding capacity and also slow off-rates, CS81B8 (D4) and PT16643 (D3), were

initially designated to function in the donor configuration. The resultant combinations of antibodies were tested using AlphaScreen for their ability to produce signal in the presence of recombinant PPARγ (Figure 63), with or without rosiglitazone to ensure there is no epiturbance.

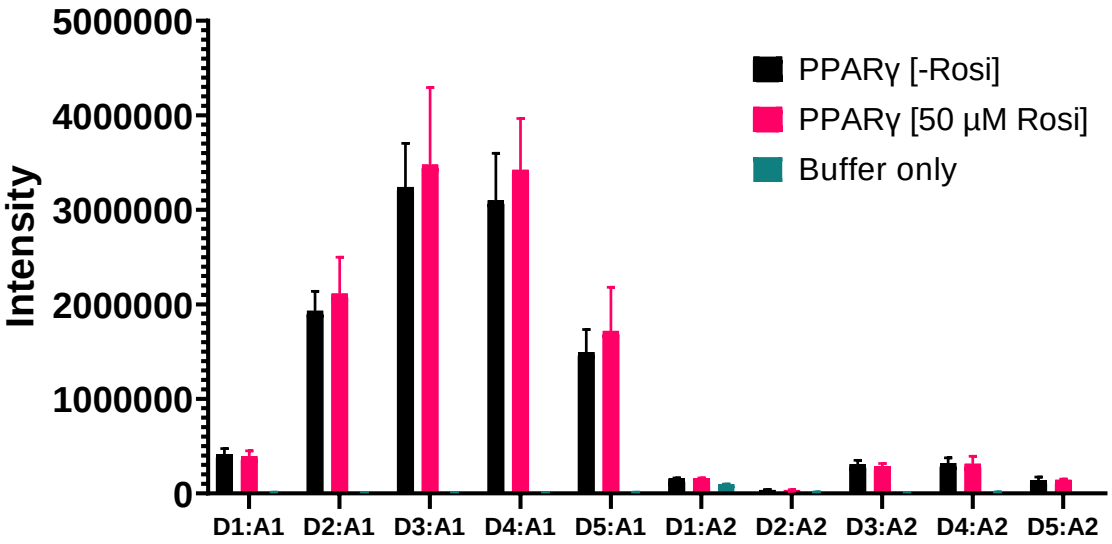


Figure 63: Results of the first optimisation screen. Overall, ten combinations of antibodies were tested with and without rosiglitazone, to check for epiturbance, with two different antibodies in the acceptor configuration and five in the donor configuration. Antibody nomenclature: A1 and D1: ab41928, A2 and D2: ab59256. D3: PT16643, D4: CS81B8 D5: PT60127

Perhaps unsurprisingly, the two donor antibodies that bound most strongly to PPARγ in the BLI assay also produced the greatest signal-to-noise ratio in the initial optimisation assay, and, interestingly, the CS81B8-ab41928 combination (D4:A1), came out as one of the top combinations. No epiturbance was detected. Of note is the fact that, the polyclonal antibody ab59256 is unable to produce signal with itself (D2:A2) but the monoclonal antibody ab41928 is (D1:A1). Given that the combination produces no signal when PPARγ is replaced with buffer only, it is

unlikely that this is due to autoreactivity. Perhaps the contact it makes with its PPARγ epitope is very small relative to the immunogen size (residues 3-105 were used as the immunogen), not only potentially allowing two antibodies to bind the same immunogen, but also explaining why the antibody readily forms high-signal complexes with the other 4 antibodies.

Subsequently, it was decided to follow-up three of the combinations in an assay comparing the signal of native vs heat-denatured recombinant PPARγ (Figure 64). Since many of the antibodies used were WB-compatible, there was indeed a possibility that they would recognise unfolded and aggregated PPARγ as well, giving poor assay window in subsequent assays.

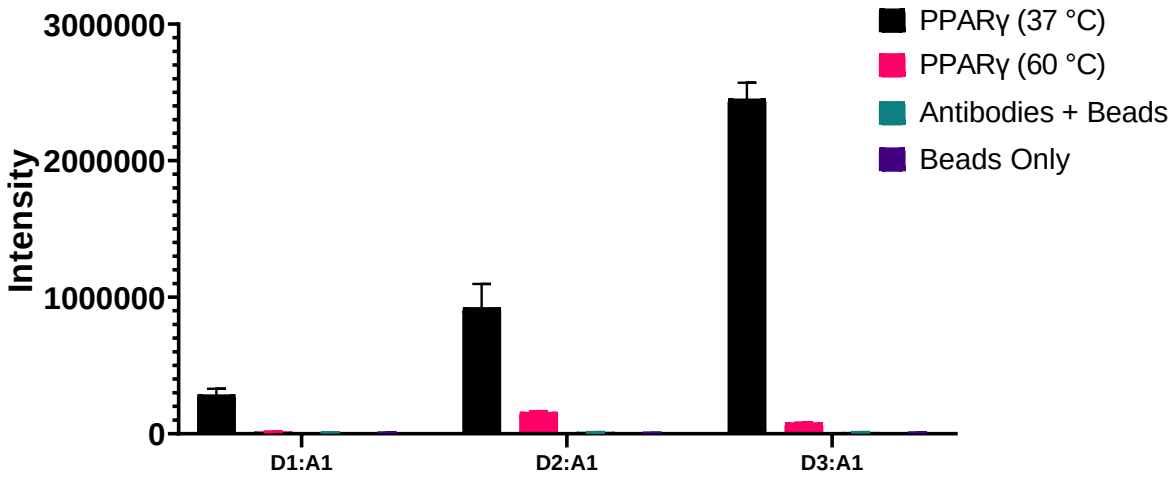


Figure 64: Assay window optimisation. The antibody pair has to, on one side, detect folded PPARγ (black) with high intensity, on the other hand, give low signal for denatured PPARγ (magenta). Out of the three combinations tested, D3:A1 gave more than 10-fold ratio of native to denatured PPARγ. The antibodies and beads on their own produce negligible signal, as the ternary complex is not formed without PPARγ.

Notably, for the D3:A1 combination, there was more than 10-fold change from unheated to heated protein, which was promising with respect to the potential assay

window. The combination was then taken forth to perform a full titration test to determine optimal reagent concentration for subsequent assays. Since it is not recommended to alter the concentration of donor and acceptor beads beyond a certain range, it was decided to keep the bead concentration fixed, and instead titrate PPARγ and the biotinylated antibody (Figure 65).

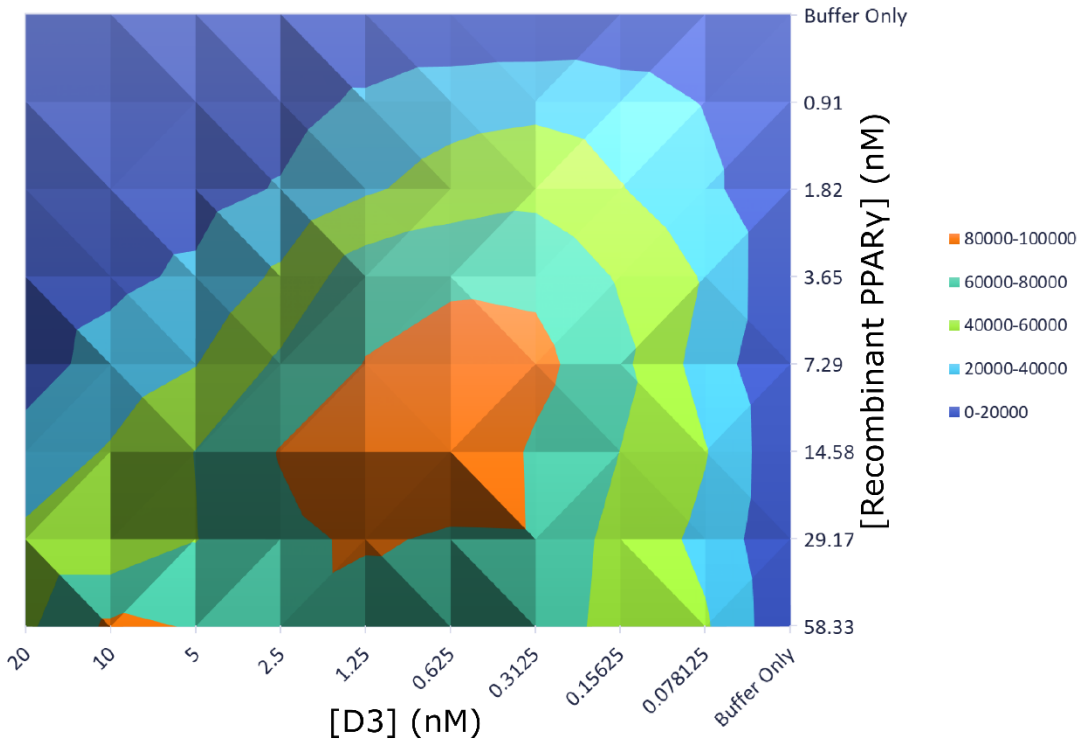


Figure 65: Titration experiment, investigating signal as a function of the concentration of PPARγ and the biotinylated antibody. The concentration of the antibody and recombinant PPARγ is varied in order to obtain maximum signal, represented as a 3D surface plot. Note that, due to the hook effect, increasing the concentration of either beyond a certain point is counterproductive.

It is interesting to point out that signal does not increase indefinitely with the increase in reagent concentration. This phenomenon is known as the hook effect – if we have a fixed amount of PPARγ and the two beads, increasing the amount of the biotinylated donor antibody will initially result in an increase in signal;

however, at a certain point, the surplus of the antibody results in one molecule binding PPARγ, another molecule binding streptavidin-donor bead, and in consequence no productive complex forming. The same holds true for PPARγ when there is a fixed concentration of the donor antibody. With this proof-of-concept established for at least one antibody concentration (D3:A1), it was decided to move to optimisation in lysate.

5.2.4 Optimisation experiments involving 3T3-L1 lysate

As the double-antibody pulldown experiments have demonstrated, the PPARγ-antibody complex formation in the absence of lysate does not guarantee formation of the same complex in the presence of it. Cell lysates contain numerous proteins that interact not only with the target, but also the antibody; less-specific antibodies may well get sequestered by the proteins in the lysate they cross-react with, and interactions between the target and its interactome may mask the epitopes necessary for antibody binding. In addition, there is a small possibility that two antibodies both recognise the same off-target, resulting in the tracking of a completely different protein. As a result, extensive lysate optimisation experiments have to be performed.

The first experiment involved taking the nuclear extract from 3T3-L1 cells. As PPARγ localises primarily to the nucleus[267], the nuclear extract is particularly enriched in PPARγ (Figure 66). Thus, the rationale behind using a nuclear extract

was that, due to its high PPARγ content, less of it would be needed thus minimising potential antibody cross-reactivity issues.

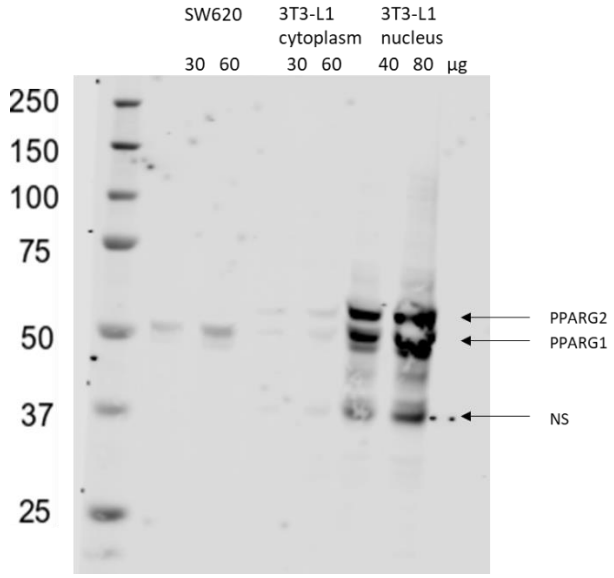


Figure 66: Distribution of PPARγ in 3T3-L1 cells. Two different concentrations of cytoplasmic and nuclear fractions from 3T3-L1 cells were loaded onto SDS-PAGE and subsequently analysed by WB. SW620 lysate loaded for comparison. As can be seen, the adipocytes are rich in PPARγ, most of which is localised to the nucleus. NS: non-specific antibody binding.

Unfortunately, incubation of the nuclear extract with the beads and the antibodies resulted in a drastic drop of signal compared to the recombinant PPARγ (Figure 67). This low signal persisted, even if the extract was kept with the antibodies for 8 hours. Moreover, a third antibody (CS81B8 – A3) was directly conjugated to the acceptor bead and assayed with different donor antibodies in the presence of nuclear extract – the signal remained low.

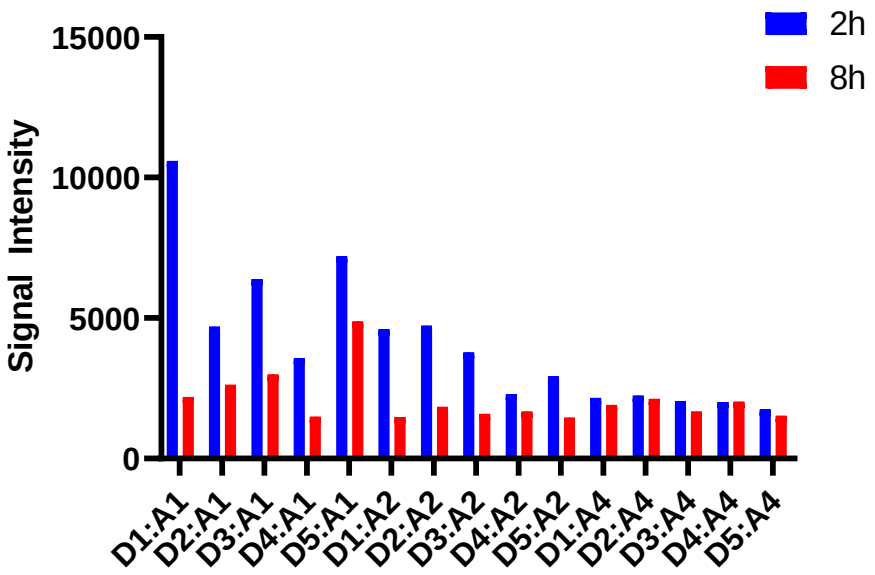


Figure 67: Nuclear extract optimisation. Nuclear extract from 3T3-L1 cells was incubated with the beads and various combinations of donor and acceptor antibodies. Signal is persistently low for all the combinations tested, regardless of incubation time.

Upon further investigation, it was revealed that the nuclear extraction buffer contains a different detergent composition to the buffer systems commonly used in AlphaScreen experiments. The experiment was therefore performed following standard lysis of 3T3-L1 cells using an appropriate pre-formulated buffer compatible with AlphaScreen experiments. Initially, just one antibody combination (D3:A1) was used. The signal intensity was much greater than in the previous experiment. Perhaps equally important, heat-denatured lysate gave no signal (Figure 68).

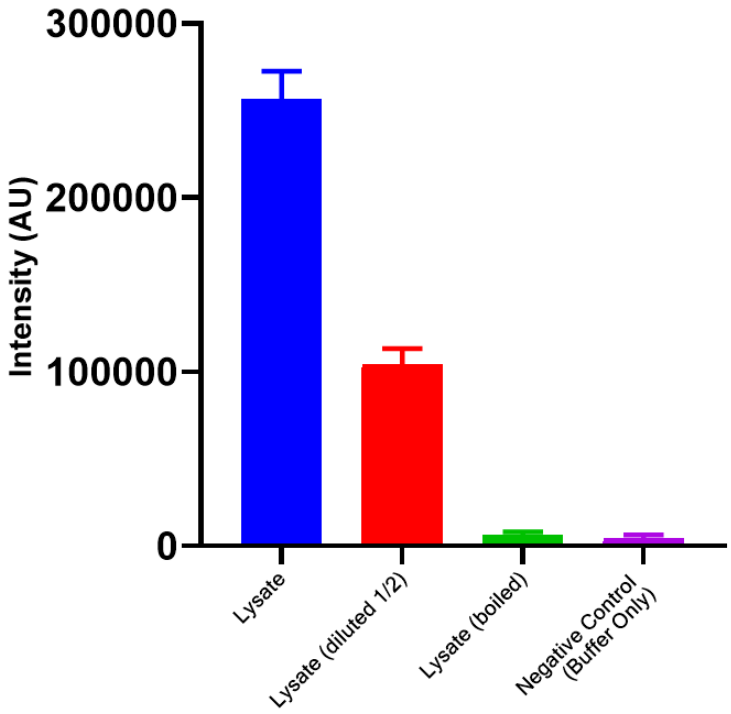


Figure 68: Lysate optimisation. Lysate from 3T3-L1 cells was incubated with the beads and one combination of donor and acceptor antibodies. The antibody combination used was D3:A1. In case of hook effect, diluted lysate was tested alongside the rest of the samples. The lysate was incubated for 2 hours.

Analogously to the optimisation with regards to the recombinant protein, the subsequent step was the titration of both the appropriate lysate and antibody concentrations while keeping the bead concentration constant using the combination D3:A1. In addition, a second repeat of the 2D titration was incubated overnight, rather than for 2 hours, in order to ascertain whether longer incubation will result in a higher signal owing to slower kinetics of association in a lysate environment (Figure 69). This was indeed shown to be the case, with samples incubated overnight showing approximately 5-fold more signal than those that only had 2 hours to develop. Thus it was decided to always incubate for longer.

Incubation time: 2 hours

Antibody Conc (nM)	Lysate (mg/ml)								
	3	1.5	0.75	0.375	0.1875	0.09375	0.046875	0.023438	Buffer Only
25	29317	15865	4959	5301	5472	4275	3648	5510	3496
12.5	53979	24168	11552	7296	5776	4750	3534	4351	3667
6.25	86108	29507	13205	8569	5510	5263	3952	4921	4180
3.125	61104	48336	21926	10355	3971	6783	5852	5586	4807
1.5625	38969	27360	14649	9538	7334	6802	5928	6612	4541
0.78125	19152	12426	6403	6783	4541	4294	4902	5187	5035
Buffer Only	3002	1672	1634	1387	3230	3420	1881	5016	2299

Incubation time: Overnight

Antibody Conc (nM)	Lysate (mg/ml)								
	3	1.5	0.75	0.375	0.1875	0.09375	0.046875	0.023438	Buffer Only
25	44365	22154	9101	6023	5814	3933	3705	7011	3819
12.5	197068	23674	12616	6802	6270	3401	4674	4313	2299
6.25	431205	38057	17822	5890	7125	3933	4921	4864	3325
3.125	244397	71972	20501	12939	6707	4902	5567	6346	4161
1.5625	154679	53086	14953	8778	8645	5225	3268	5928	5871
0.78125	79952	31103	9557	4712	4465	5016	3914	3819	3629
Buffer Only	1558	2185	2983	1159	4199	3192	4123	4218	3724

Figure 69: Titration experiment, investigating signal as a function of the lysate concentration and the biotinylated antibody (D3). Lysate from 3T3-L1 cells was incubated with the beads using the D3:A1 antibody combination, however both the lysate concentration and antibody concentration were varied, as well as incubation period. Incubating the components overnight results in stronger signal. Interestingly, the hook effect is not reached with respect to the lysate concentration, suggesting more concentrated lysate can be added.

In order to ensure that the two antibodies are indeed tracking the correct protein, rather than getting sequestered by other proteins or binding the wrong target, it was decided to perform a spike-in experiment, where additional recombinant PPARγ would be added to the lysate. As can be seen from the titration experiment, the hook effect is not quite reached despite increasing concentrations, indicating that the system has not reached saturation with respect to PPARγ. Indeed, for two of the antibody combinations (D3:A1 and D4:A1), the lysate was able to take much more recombinant PPARγ before saturation was reached, with signal linearity persisting until PPARγ concentration reached 5 nM, and saturation with concomitant signal decline beginning only after 15 nM (Figure 70). Unfortunately, for the other two antibody combinations (D2:A1 and D5:A1), the signal diminished early, followed

by erratic behaviour, indicating that they were unsuitable for further optimisation and should be discarded. Out of the two best ones, D3:A1 performed marginally better, and thus it was the antibody combination selected for further experiments, with D4:A1 to be used as back-up.

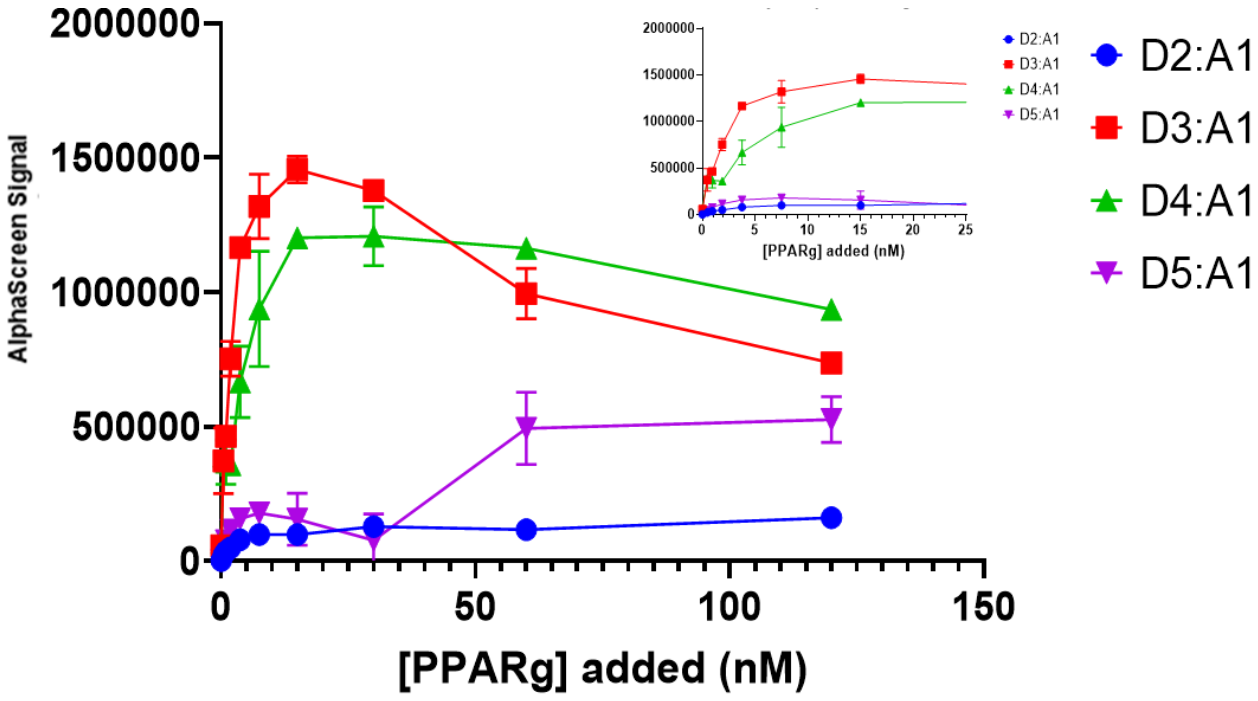


Figure 70: Titrating additional recombinant PPARγ to investigate signal linearity and assay robustness. Lysate from 3T3-L1 cells was incubated with the beads using a number of antibody combinations at the optimal lysate and antibody concentrations obtained earlier, with additional spiked in PPARγ. The small insert shows the same data, but restricted to maximum 15 nM PPARγ added. For two of the antibody combinations tested, signal linearity persists up 5 nM.

5.2.5 Lysate CETSA

Given that the proof-of-concept has now been established in a lysate environment, it was decided to attempt a lysate CETSA experiment. Thus, the lysate was incubated with 250 µM rosiglitazone, which is a maximal rosiglitazone dose – the

reason for using such a dosage is due to the inherent loss of sensitivity in a CETSA given the rearrangements of equilibria that occur upon heating. After 30 minutes, the lysate was aliquoted and aliquots heated to different temperatures. Following cooling, the antibodies and beads were added and transferred into a suitable microplate, and after overnight incubation, the microplate was imaged (Figure 71). Despite such a high dose of rosiglitazone, no stabilisation was observed compared to the control group. Moreover, compared to live cell CETSA, the melting temperature shifted to >50 °C, raising questions about the validity of performing lysate CETSA instead of live cell.

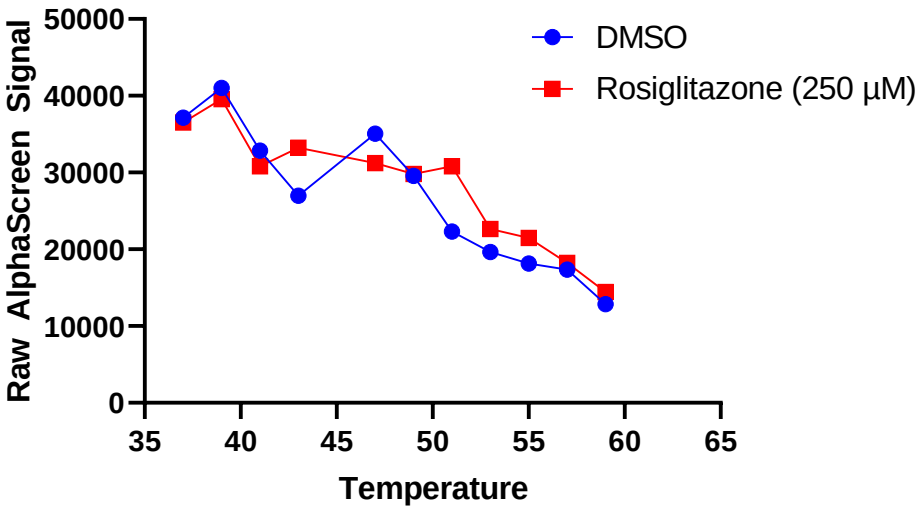


Figure 71: Lysate CETSA using AlphaScreen readout. 3T3-L1 lysate was incubated with either rosiglitazone, or equivalent volume of DMSO, for 30 minutes, followed by aliquoting, heat pulse and centrifugation. The samples were transferred to a microplate and the beads and antibodies were added to afterwards for microplate readout. No stabilisation is observed. In addition, the melting temperature appears to be shifted. No curve fitting was performed to avoid bias.

Subsequently, CETSA was performed with lysate that was spiked-in with recombinant PPARγ, in order to increase the assay window. In addition, the

experiment was expanded to be 2-dimensional, with concentrations of rosiglitazone ranging from 100 µM to 1.7 nM. Likewise, no significant stabilisation was observed at higher temperatures, even at the maximal concentrations of rosiglitazone, relative to DMSO (Figure 72).

a

°C	DMSO	0.001694	0.005081	0.015242	0.045725	0.137174	0.411523	1.234568	3.703704	11.11111	33.33333	100	µM
61	272536	304171	299022	284648.5	278939	316188.5	366044.5	77833.5	314070	342760	317794	325470	
60.5	258143.5	289778.5	266579.5	270066	266161.5	302233	325641	145454.5	258533	253507.5	269192	269923.5	
59.8	295440.5	327522	277419	270626.5	304750.5	377881.5	360439.5	314155.5	269154	283356.5	344622	339492	
58.7	340347	342836	350018	302138	322344.5	419349	403968.5	345192	356829.5	326401	358625	354692	
57	336471	355205	341658	338418.5	393452	370395.5	453843.5	389139	404272.5	418950	423614.5	411036.5	
55.3	486799	495672	496916.5	541528.5	587527.5	675431	663328	558790	542383.5	538868.5	541281.5	513275.5	
52.9	766897	765766.5	794561	852131	876042.5	899327	804745	941583	763591	876270.5	830281	804526.5	
50.5	1307742	1389014	1336935	1420089	1483796	1491291	1478409	1556651	1282918	1513854	1423138	1371154	
47.5	1972400	1950322	1920558	2036734	2021467	2003142	1982365	1976304	1915599	1992264	2025951	2004880	
45	2461992	2307949	2394789	2453204	2010286	2370022	2428979	2320204	2165174	2346605	2314647	2379332	
43	2689460	2560402	2765526	2888257	2516892	2872629	2862113	2952125	2818213	2472698	2809711	2719451	
41.1	2606610	2583136	2629391	2650918	2493798	2783567	2566615	2666489	2510214	2439553	2664247	2786284	
39.5	3059247	3031707	3041226	3033569	3226381	2987465	3015737	3104705	2936802	3583932	3948324	2899381	
38.3	2867528	2741966	2842932	2843778	2795176	2726101	2810024	2721617	2758515	2617269	2819049	2805901	
37.4	2909052	2744332	2677271	2244622	2705781	2998267	2813596	2717561	2661378	2303190	2699150	3069184	
37	2324384	2368246	2268610	2360152	2473031	2400907	2458429	1275993	2293433	2256697	2722083	2586204	

b

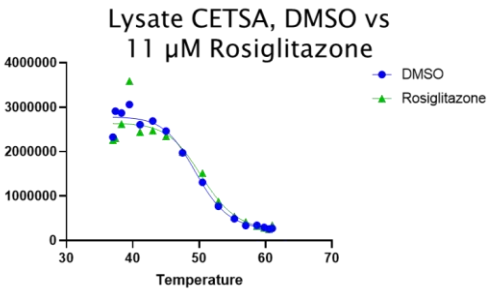


Figure 72: 2D CETSA in a lysate format with protein spike-in. 3T3-L1 lysate with additional PPARγ spiked in was incubated with varying concentrations of rosiglitazone, for 30 minutes, followed by aliquoting, heat pulse and centrifugation. (a) The full 2D lysate CETSA heat map. (b) A representative melting curve of 11 µM Rosiglitazone vs DMSO taken from the heat map. Curve fitting shows melting temperatures: DMSO: 49.6 °C, Rosiglitazone: 50.5 °C (ΔTm = 0.9 °C).

It is plausible that the detergents present in the lysis buffer confer thermal stabilisation upon PPARγ that is far greater than the stabilisation elicited by rosiglitazone, thus explaining the supposed lack of stabilisation. Conversely, a different explanation is that cell lysis disrupts the natural confinement of PPARγ to the nucleus and hence may create new stabilising interactions with endogenous lipids in the lysate that are less prominent in live cells. As a result, the idea of performing CETSA in a lysate format was ultimately abandoned.

5.2.6 Optimisation of AlphaScreen-based CETSA in live cells

Subsequently, the focus was shifted to optimising the experiment in live cells, which would pave the way towards live-cell CETSA experiment. The first step would involve optimising the experimental set-up to maximise the amount of signal in a microplate with respect to the number of cells per well. Note that, whilst it is possible to calculate the protein concentration in a well using a BCA assay and then use the previous optimisation steps to deduce appropriate reagent amounts, in practice this approach is cumbersome and introduces unnecessary variability into the set-up. Instead, the experiment should be optimised top-down with respect to cell number. The potential experimental set-up is below (Figure 73).

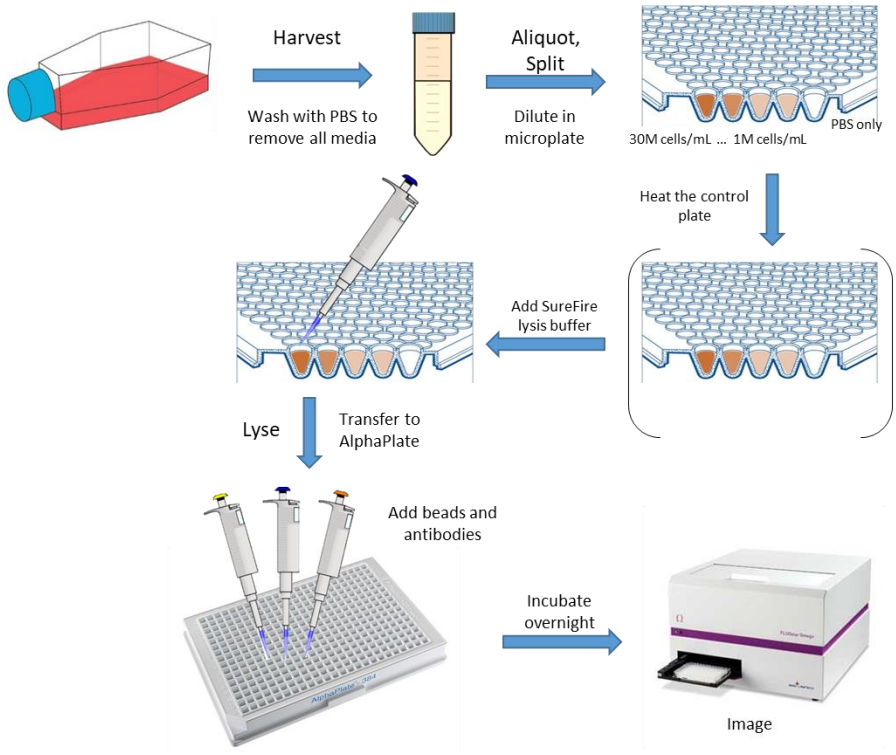


Figure 73: Experimental set-up for a microplate-based AlphaScreen CETSA. The cells are harvested, washed with PBS and aliquoted into two microplate at varying concentrations. One microplate (control) is given a denaturing heat pulse, whereas the other is kept at RT. The cells are lysed, transferred to an AlphaScreen plate, followed by bead and antibody addition and plate readout following overnight incubation.

Typically, in order to reduce the number of experimental steps to a minimum, the cells and reagents would be added to the microplate in the cell culture medium without washing. However, in the planning stages of the experiment, it was discovered that the cells need to be washed in PBS in order to remove the medium, as the presence of medium drastically reduces the signal. Upon probing with WB, the presence of a new band was confirmed, which was absent when cells were washed with PBS (Figure 74). Given that the medium is supplemented with 10% FBS, it would not be outside the realm of plausibility that albumin or a related protein present in the serum is interfering with the signal, thus driving the need for complete medium removal:

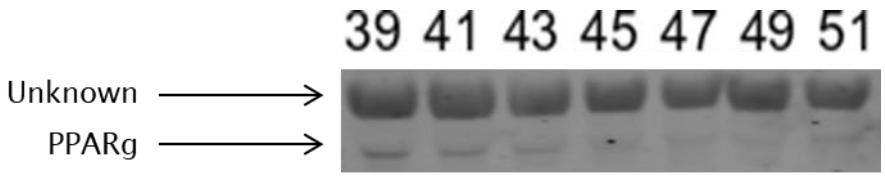


Figure 74: The presence of a novel, unknown band on a WB, when medium is left in the cells. The band disappears if medium is removed from cells prior to compound incubation. The protein appears to bind a large portion of the anti-PPARγ antibody.

With the signal problems stemming from the presence of medium solved, the cell number optimisation experiment was performed again, this time including the necessary washing steps. Whilst definitely demonstrating a linear relationship between cell number and signal, the signal itself remains low. One possible reason for that is the absence of the centrifugation steps. Not only is the volume per well high, as medium is never removed, lowering the effective concentration of reagents,

the absence of a high *g* spin step before the addition of the beads and antibodies could result in the cellular debris interfering with the components, although in principle the assay should be robust enough to resist such hindrance.

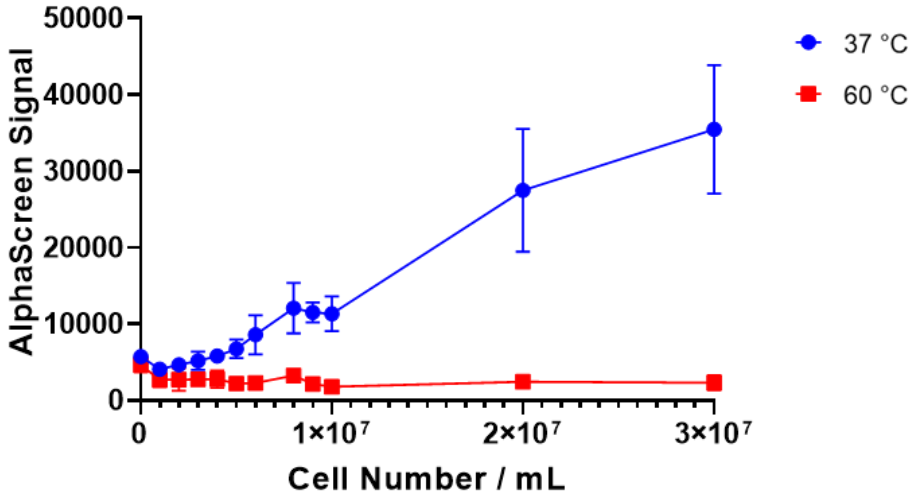


Figure 75: The initial cell number optimisation in a 96 well format. The experiment was performed according to the protocol outlined above. Whilst the signal is indeed linear, it is lower than expected, which could stem from overdilution of the sample or interference from cellular debris.

In order to test the hypothesis that spin steps result in increased signal, the experiment was performed in a PCR-tube environment, where more control can be exercised over the samples with respect to spin steps and medium/buffer removal, although it has to be stressed that, ideally, the assay should work in a microplate environment for screening capability. The set-up was as follows (Figure 76).

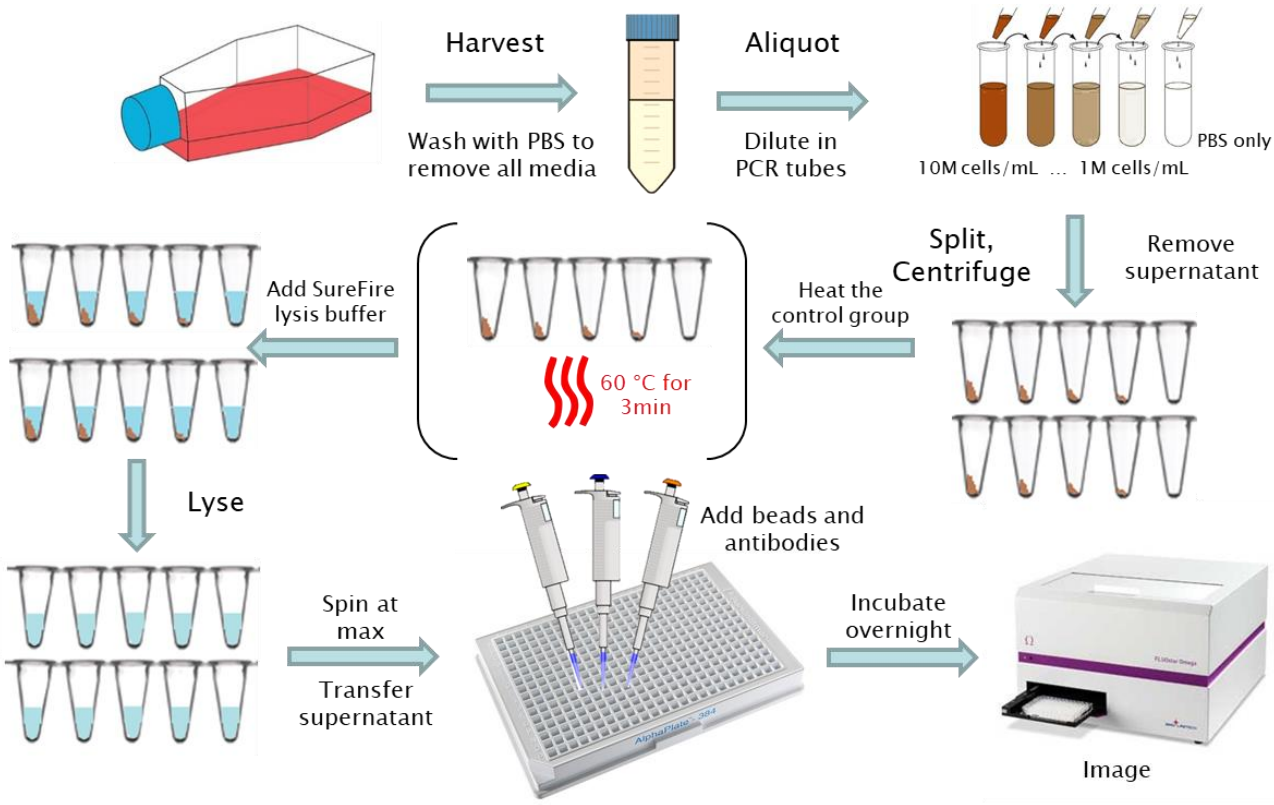


Figure 76: Experimental set-up for a microplate-based AlphaScreen CETSA including spin steps. The cells are harvested, washed with PBS and aliquoted into two sets of PCR tubes at varying concentrations. PBS is removed via centrifugation, leaving only cell pellets. One set of PCR tubes (control) is given a denaturing heat pulse, whereas the other is kept at RT. The cells are lysed, and denatured proteins are pelleted by centrifugation. The supernatants are transferred to an AlphaScreen plate, followed by bead and antibody addition and plate readout following overnight incubation.

Indeed, it appears that the inclusion of spin steps results in an increase in signal by an order of magnitude (Figure 77). Signal linearity persists until ~400,000 cells per PCR tube – this is quite a large number, as it means that 96 data points (a microplate) will require over 38 million cells, which is more than one confluent T-175 cell culture flask. In practice, the assay would likely be run with fewer cells than that and ultimately, it would be preferable to run the assay in a 384 or higher well format.

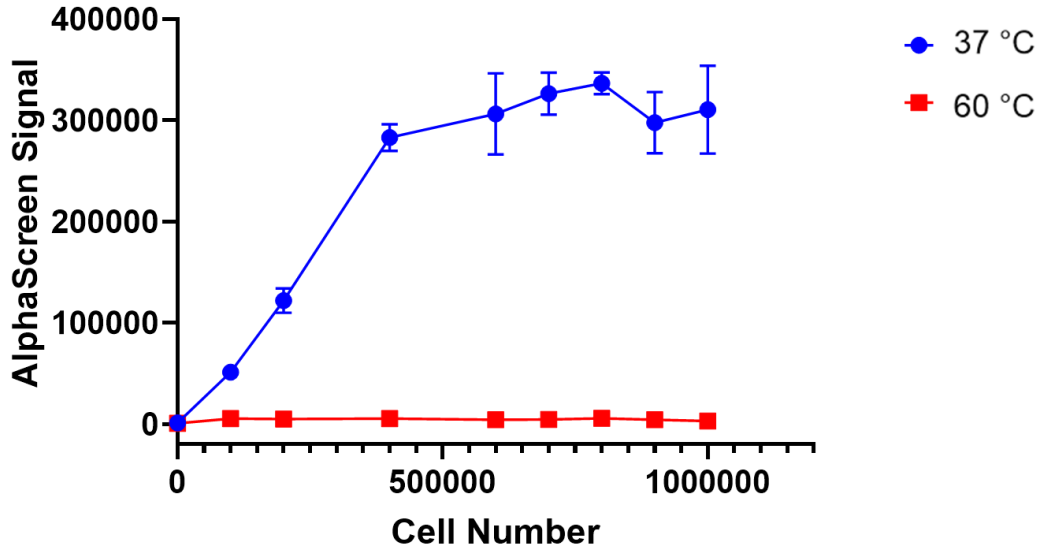


Figure 77: Signal vs cell number optimisation in a PCR tube format. The experiment was performed according to the protocol outlined above. Signal linearity persists up to about 400,000 cells.

Subsequently, it was decided to combine the spin approach from the PCR optimisation experiment with the microplate assay. The experimental set-up was the same as initially, however, the necessary centrifugation steps were included. This has resulted in a marked signal increase relative to the optimisation assay (Figure 78). Signal linearity now persists up to nearly 1 million cells, however, as mentioned before, in practice a much smaller number of cells will be used, both in order to conserve resources, and to ensure that the signal falls on the steep part of the curve without the risk of potential plateauing, but nonetheless with an appropriate assay window.

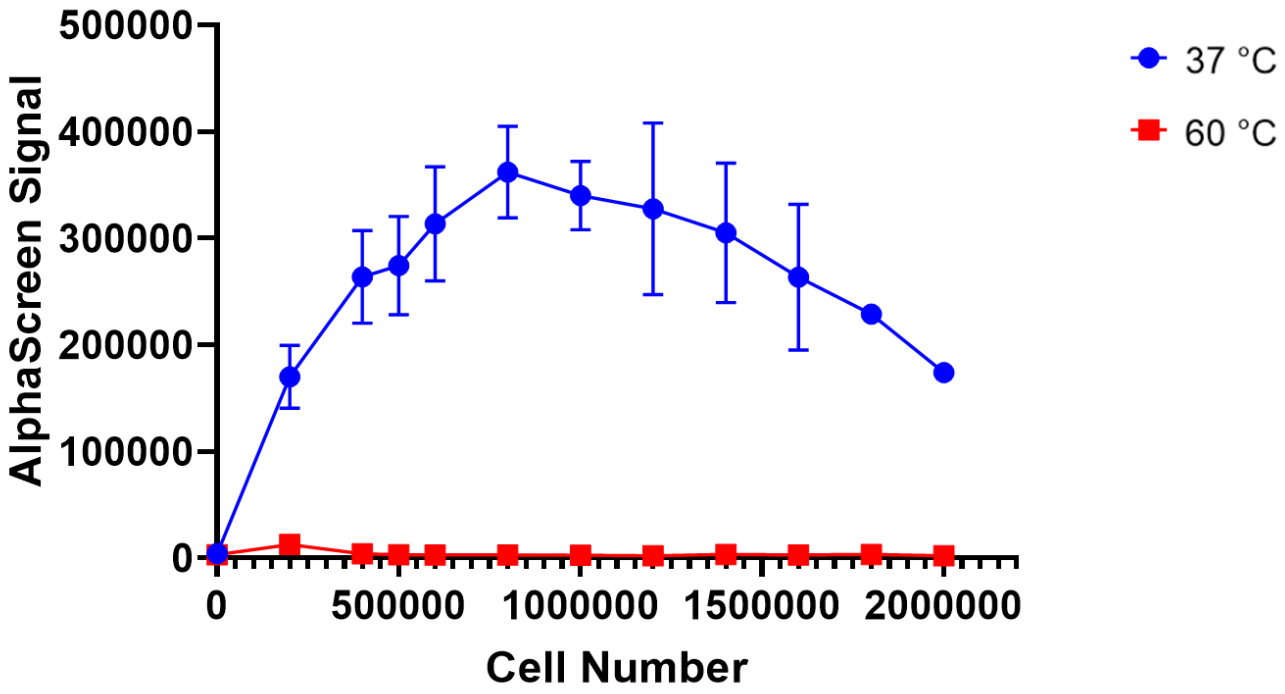


Figure 78: The final optimisation of signal vs cell number in a 96-well format. In this experiment, the cells were harvested, washed with PBS and aliquoted into two microplates at varying concentrations as earlier, however PBS was removed via centrifugation, leaving only cell pellets. One plate was given a denaturing heat pulse, whereas the other was kept at RT. The cells were lysed, and denatured proteins pelleted by centrifugation. The supernatants were then transferred to an AlphaScreen plate, followed by bead and antibody addition and plate readout following overnight incubation.

5.2.7 Live-cell CETSA

Following the cell number optimisation, a proof-of-concept CETSA experiment was performed with the AlphaScreen readout in a 96-well format. As mentioned before, due to cell number constraints, 200,000 cells were used per well. The concentration of rosiglitazone was kept at 50 µM and the initial compound incubation lasted 30 minutes. As can be seen (Figure 79), rosiglitazone induced a modest shift of 2.3 °C, in line with previous data using a WB readout.

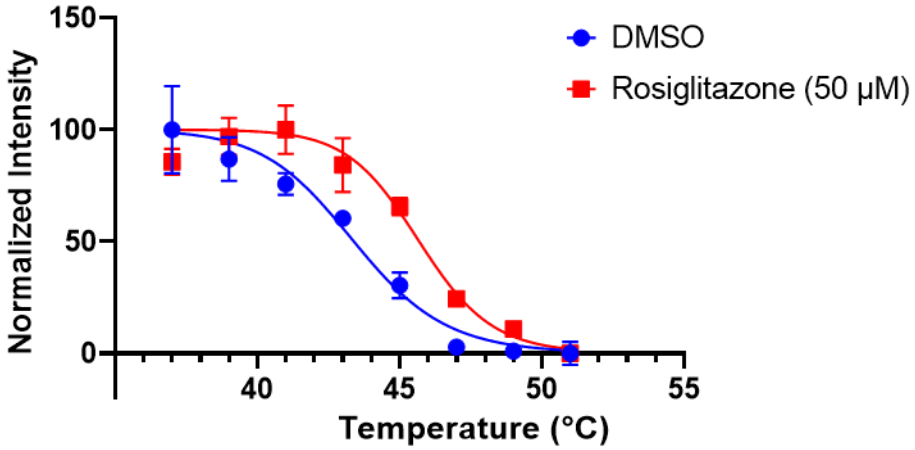


Figure 79: CETSA in a 96-well format using AlphaScreen readout. The cells were incubated with rosiglitazone, or equivalent volume of DMSO, for 30 minutes, followed by aliquoting in a microplate, removal of PBS by centrifugation and heat pulse. The cells were lysed and the microplate was centrifuged again to pellet the heat-denatured proteins. The supernatants were transferred to an AlphaScreen plate and the beads and antibodies added for overnight incubation, followed by measuring the signal in a plate reader. The melting temperatures are as follows: DMSO: 43.4 °C, Rosiglitazone 45.7 °C (ΔTm = 2.3 °C).

5.3 The development of a high-throughput screen assay to study PPARγ agonists

5.3.1 Temperature selection in a 96-well format

As mentioned earlier, the microplate CETSA assay using AlphaScreen readout technology allows for a potential development of a screening platform. In such an adaptation of the assay, the microplate is heated to a single temperature, at which normally a significant portion of protein heat-denatures, and the ability of different compounds to 'rescue' the signal is thus a measure of their thermal stabilisation and thus cellular target engagement. In order for the assay to perform properly, however, the temperature selection is key. From the melting curves above, it was speculated that 45 °C (reduction of protein signal for the untreated group by ~75%)

and 47 °C (the untreated protein signal is nearly completely gone) might be good starting temperatures for such an assay. To test this hypothesis, a proof-of-concept ITDRF experiment was performed at those 2 temperatures, using 2 concentrations of rosiglitazone and DMSO (Figure 80). Indeed, rosiglitazone elicited a partial rescue of PPARγ signal in a concentration-dependent manner, however, 250 µM induced complete detachment of cells after even a short incubation of 30 minutes, suggesting toxicity and cell death.

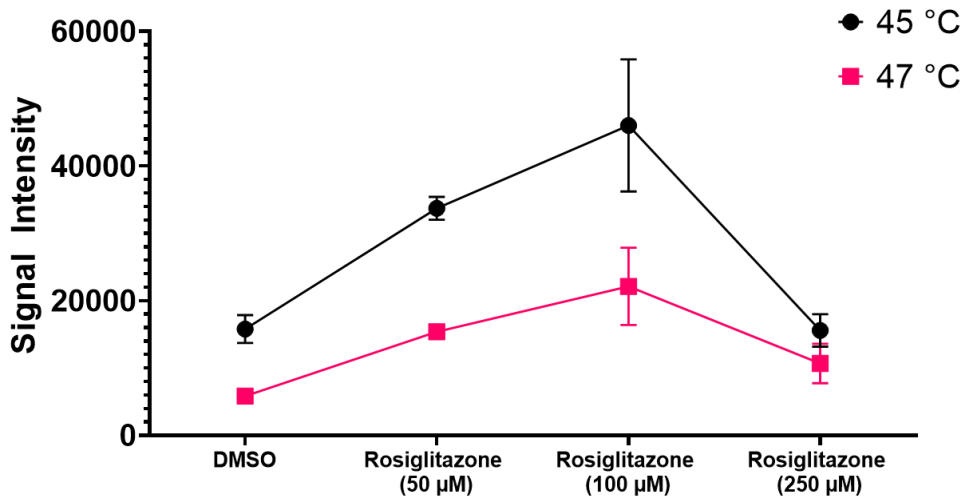


Figure 80: Proof-of-concept ITDRF experiment in a 96-well format. The cells were incubated with different concentrations of rosiglitazone, or equivalent volume of DMSO, for 30 minutes, followed by aliquoting in a microplate, removal of PBS by centrifugation and heat pulse. The cells were lysed and the microplate was centrifuged again to pellet the heat-denatured proteins. The supernatants were transferred to an AlphaScreen plate and the beads and antibodies added for overnight incubation, followed by measuring the signal in a plate reader.

Subsequently, a full ITDRF curve was constructed for rosiglitazone, in a 96-well format. Previous ITDRF-WB studies have shown that rosiglitazone, due to its modest stabilisation, can only partially rescue PPARγ, therefore it was decided to,

in tandem, include a second compound, S26948, which previously was shown to be a stronger stabiliser (Figure 81). The ITDRF data appears to validate those results, as S26948 produces 1.5-fold times the signal of rosiglitazone at maximal concentration. When performed at 47 °C, the signal increase in the presence of these ligands is proportionally lower, which would increase the risk of false negative in the screening assay and results in a larger uncertainty in the data because of a poor assay window. As a result, it was decided that lower temperature might be more conducive towards a greater assay window despite incomplete denaturation.

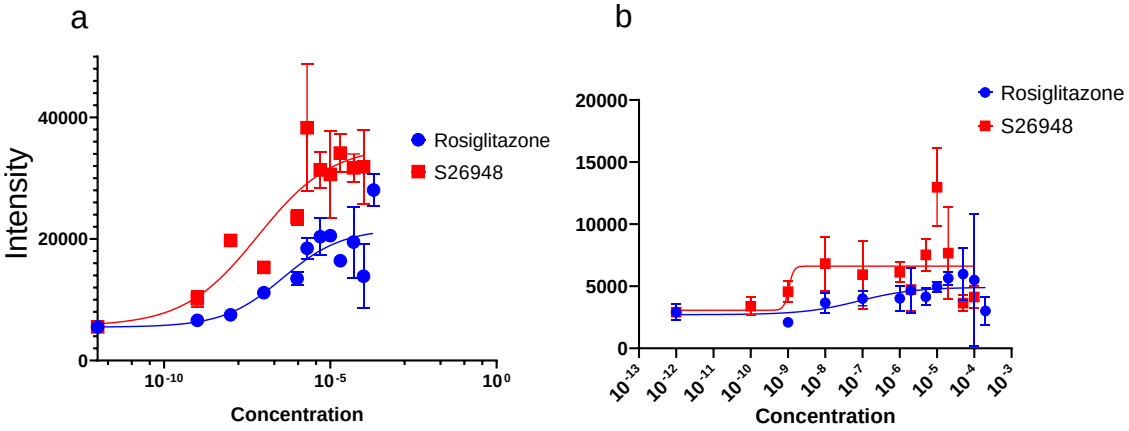


Figure 81: Comparison of ITDRF at 45 °C and 47 °C. The cells were incubated with different concentrations of rosiglitazone, or equivalent volume of DMSO, for 30 minutes, followed by aliquoting in a microplate, removal of PBS by centrifugation and heat pulse at 45 °C (a) or 47 °C (b). The cells were lysed and the microplate was centrifuged again to pellet the heat-denatured proteins. The supernatants were transferred to an AlphaScreen plate and the beads and antibodies added for overnight incubation, followed by measuring the signal in a plate reader. The greater signal increase at 45 °C points towards the use of this temperature in assays. The IC_{50} values are rosiglitazone: 371 nM; S26948 67 nM at 45 °C (a) and rosiglitazone: 80 nM; S26948: 1 nM at 47 °C, however, the data at 47 °C are associated with larger uncertainties (b).

5.3.2 Temperature selection in a 384-well format

As mentioned before, whilst the assay was initially optimised to work in a 96-well format, the high demand for cells meant that, subsequently it would have to be miniaturised to a 384-well format, to reduce the strain on the cell culture. To this end, the experiment was performed in a 384-well format, with a 2D-CETSA configuration: rosiglitazone was used as the compound at concentrations ranging from 200 µM to 1 nM, and the temperature range spanned 37 °C to 60.5 °C (Figure 82). Interestingly, it appears that at 43 °C, there is a small concentration-dependent stabilisation of PPARγ, which is absent at 45 °C and 47 °C, suggesting that in this arrangement, the protein is inherently less thermally-stable, although the experiment did not yield a sufficient signal to background to draw any solid conclusions. A potential reason for that could be due to the fact that 96-well microplate wells are generally thicker than 384-well ones, resulting in a higher apparent melting temperature (T_{app}) inside the wells of a 384-well microplate despite the same heat pulse.

a

D	1 nM	10 nM	50 nM	100 nM	500 nM	1 µM	5 µM	10 µM	50 µM	100 µM	200 µM
60.5	10184	9253	6887.5	7970.5	7267.5	6355.5	7609.5	7875.5	7970.5	10165	8901.5	8920.5
59.8	9861	9139	8350.5	8673.5	7505	7913.5	6108.5	9148.5	8227	9424	8578.5	8873
58.7	8692.5	6916	7543	6526.5	6982.5	5548	5937.5	7030	6431.5	7362.5	8132	10222
57	9006	7267.5	5852	4873.5	7115.5	6707	5358	6080	6764	7771	7552.5	9129.5
55.3	6602.5	6346	6270	7049	5434	5947	5054	6821	7191.5	6517	10887	9025
52.9	6260.5	5814	5795	7628.5	4959	6621.5	5196.5	8569	5063.5	6260.5	6156	6422
50.5	5567	5823.5	5681	6868.5	5909	5728.5	4446	5538.5	5453	6963.5	5614.5	6403
47.5	7552.5	5120.5	5234.5	6298.5	6317.5	8037	6963.5	6944.5	6906.5	6916	6460	6422
45	6868.5	7343.5	7581	7305.5	7638	9044	9785	7628.5	8189	8027.5	7524	8597.5
43	8958.5	8816	6963.5	8673.5	8151	9642.5	9272	11447.5	10801.5	11476	10307.5	9832.5
41.1	12483	11409.5	11058	11856	12274	11314.5	11134	9272	9984.5	10402.5	7448	9243.5
39.5	13708.5	11732.5	10934.5	12207.5	12188.5	13024.5	12160	14373.5	14098	13832	15456.5	11618.5
38.3	12901	12540	15513.5	13537.5	13024.5	13480.5	15608.5	11267	14573	15627.5	14487.5	14003
37.4	15950.5	13718	14953	13518.5	14259.5	13062.5	13556.5	15456.5	17993	17366	12739.5	15694
37	20178	18990.5	18620	20244.5	16691.5	14915	16235.5	22116	16995.5	18496.5	16625	16102.5

b

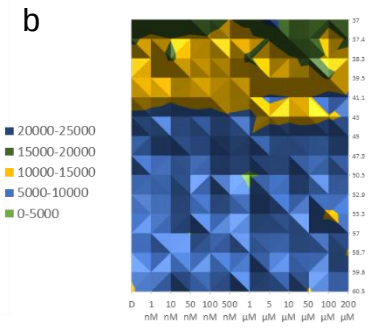


Figure 82: 2D-CETSA in a 384-well format. The cells were incubated with different concentrations of rosiglitazone, or equivalent volume of DMSO, for 30 minutes, followed by aliquoting in a microplate, removal of PBS by centrifugation and heat pulse. The cells were lysed and the microplate was centrifuged again to pellet the heat-denatured proteins. The supernatants were transferred to an AlphaScreen plate and the beads and antibodies added for overnight incubation, followed by measuring the signal in a plate reader. (a) The heat map of the 2D-CETSA, showing temperature-dependent denaturation of PPARγ. (b) The same data represented as a surface plot.

This was subsequently validated in standalone ITDRF experiments performed at 45 °C, 43 °C, 41 °C and 37 °C, where the concentration-dependent thermal shift was most pronounced at 43 °C (Figure 83), for both S26948 and rosiglitazone. Thus, 43 °C was selected as the temperature at which to perform the screen.

Rosiglitazone	DMSO	0.002	0.005	0.015	0.046	0.137	0.412	1.235	3.704	11.111	33.333	100.000
45	11020.000	11941.500	12331.000	7609.500	9072.500	9481.000	10459.500	8046.500	11903.500	13461.500	12350.000	12692.000
43	24006.500	20966.500	24795.000	30951.000	33193.000	33193.000	43548.000	37012.000	33687.000	25042.000	26153.500	22629.000
41	67469.000	67991.500	73473.000	89813.000	83856.500	89176.500	88834.500	79011.500	80408.000	67640.000	66101.000	53827.000
37	139574.000	170753.000	161367.000	175655.000	183008.000	171760.000	166354.500	182457.000	154451.000	135717.000	143716.000	114950.000
S26948	DMSO	0.002	0.005	0.015	0.046	0.137	0.412	1.235	3.704	11.111	33.333	100.000
45	6517.000	8483.500	8483.500	9519.000	12198.000	12863.000	11742.000	12407.000	12122.000	11941.500	10602.000	11001.000
43	21584.000	31112.500	33658.500	30371.500	30533.000	32908.000	34703.500	29250.500	30666.000	32775.000	31293.000	24690.500
41	93090.500	100567.000	102989.500	99170.500	91694.000	103740.000	100662.000	97422.500	69008.000	78850.000	75363.500	73805.500
37	169793.500	178286.500	148523.000	169632.000	165366.500	157462.500	179075.000	154926.000	123842.000	105630.500	125276.500	139640.500

Figure 83: ITDRF in a 384-well format at four different temperatures. The cells were incubated with different concentrations of rosiglitazone, or equivalent volume of DMSO, for 30 minutes, followed by aliquoting in a microplate, removal of PBS by centrifugation and heat pulse. The cells were lysed and the microplate was centrifuged again to pellet the heat-denatured proteins. The supernatants were transferred to an AlphaScreen plate and the beads and antibodies added for overnight incubation, followed by measuring the signal in a plate reader. At 43 °C there appears to be concentration-dependent stabilisation.

5.3.3 Pilot screen in a 384-well format

Initially, a small selection of compounds were selected for the pilot assay, which included both commercial molecules and proprietary compounds from the collaborator. Amongst in-house molecules, there were two canonical TZD-scaffold PPARγ agonists (rosiglitazone and pioglitazone), a dual PPARα and PPARγ agonist (saroglitazar), a non-canonical PPARγ agonist (S26948), a PPARγ antagonist (GW9662), an RXR agonist (LG100268), two natural products with potential PPARγ-targeting properties[268] (honokiol and magnolol), a PPARα agonist (GW7647), a non-PPARγ targeting compound that has been shown to stimulate brown fat differentiation[269] (metformin), as well as two potential PAINS

compounds (SJ-172550 and C646), to validate the assay's robustness against false positive compounds.

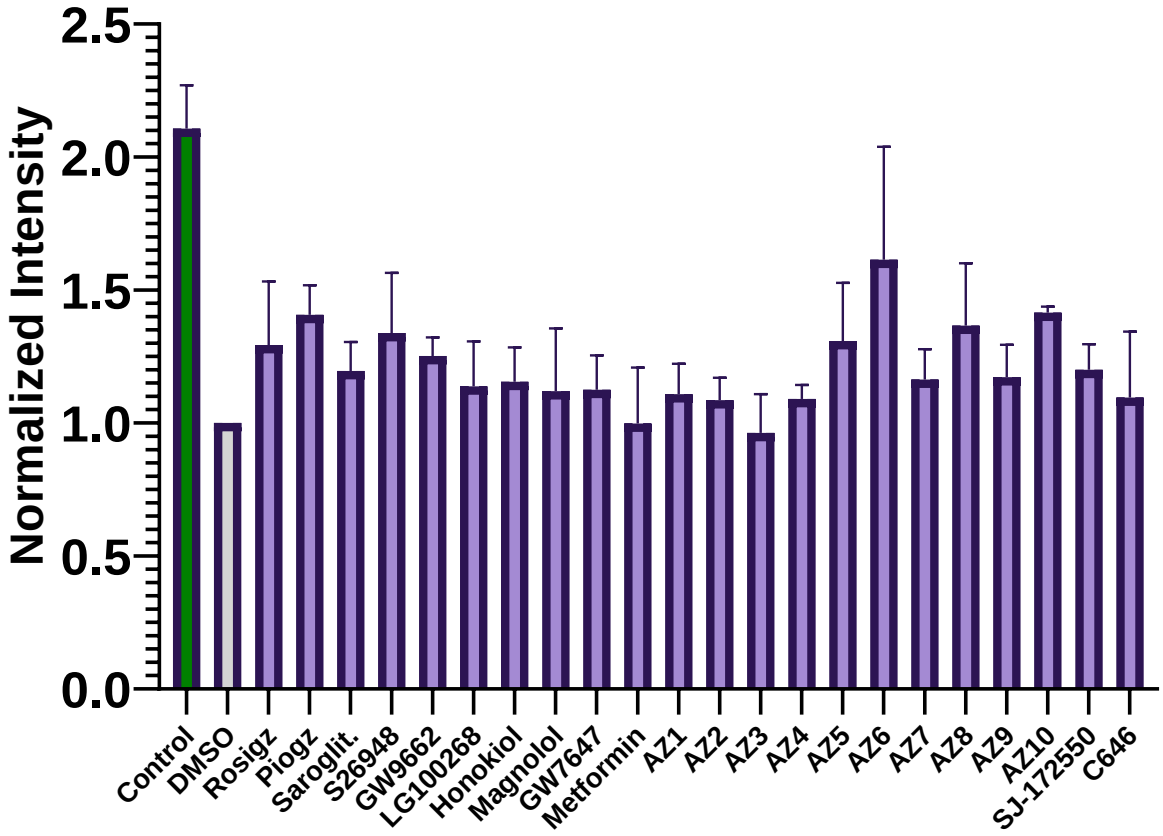


Figure 84: Results from the pilot screen at 43 °C. The cells were incubated with different concentrations of the compounds, or equivalent volume of DMSO, for 30 minutes, followed by aliquoting in a microplate, removal of PBS by centrifugation and heat pulse. The cells were lysed and the microplate was centrifuged again to pellet the heat-denatured proteins. The supernatants were transferred to an AlphaScreen plate and the beads and antibodies added for overnight incubation, followed by measuring the signal in a plate reader. The concentration of in-house compounds was 50 µM. AstraZeneca proprietary compounds were diluted 100-fold. DMSO was kept constant at 1%. The control group was not subjected to a non-denaturing heat pulse at 37 °C. The number of biological replicates is 3.

The assay was performed at 43 °C, the temperature selected from previous optimisation in a 384-well format. The control group was heated to 37 °C instead.

As can be seen (Figure 84), the assay window is noticeably small, and most compounds produce only modest stabilisations, with none completely rescuing PPARγ. This is somewhat understandable – as most compounds were only shown to stabilise the protein by a few degrees in both AlphaScreen and WB format, this means that there is usually significant melting curve overlap between the untreated and treated samples, which results in incomplete rescue in ITDRF assays and, concomitantly, only a small increase in signal vs DMSO. Perhaps reassuring is the fact that metformin, a compound that, whilst capable of producing interesting brown-fat-related phenotypes, does not appear to affect the assay. Out of proprietary AstraZeneca compounds, AZ-6 appears to be a very strong stabiliser. Unfortunately, the error on most datapoints is too great to make definitive conclusions.

5.4 Discussion

The AlphaScreen-based readout of CETSA appears to be a significant improvement over the WB approach. Despite the relatively long optimization period, during which suitable antibody pairs were selected for their ability to detect folded PPARγ only with a high signal-to-background ratio, the technique is fully quantitative due to the fluorometric, plate reader-based detection, as well as high-throughput if performed in a microplate format. This creates a possibility for an isothermal screening experiment, where possibly entire compound libraries are tested for their ability to engage the target in a cellular environment.

The results of the pilot screen appear promising. Indeed, despite the small assay window, and relatively small thermal shifts elicited by the compounds tested, it is not implausible that the assay can be developed further – with the use of appropriate liquid handling platforms, human error will be reduced and the number of replicates performed at once can substantially increase, as can the number of compounds screened, increasing the reliability of the results.

5.5 Conclusions

Detection of folded and unfolded protein via AlphaScreen presents a viable alternative towards the conventional CETSA readout via WB. However, it must be stressed that, due to a long optimization period, such an approach should be reserved for projects involving a significant number of compounds engaging a single target, particularly where the differences between compounds in terms of their abilities to elicit thermal stabilisation are to be considered. As a result, it was well-suited for analysing PPARγ-targeting small molecules. On the other, if the number of compounds is small, while the number of targets substantial, the need for robust optimization for each protein outlined in the chapter would normally preclude AlphaScreen from routine usage.

6. Proteomic Analysis of PPARγ Modulators in Cellular Models of UCP1 Induction

6.1 Introduction

6.1.1 Proteomic analysis of nuclear hormone receptors and difficulties in their detection by MS

About 13% of current drugs on the market[270] target nuclear hormone receptors (NHRs), a long established target class that has been in the focus of scientific research for decades. However, when it comes to omics approaches, NHRs are notoriously difficult to detect via mass spectrometry and proteomic techniques[271]. Many experiments specifically designed to examine NHR pharmacology have failed to identify the actual receptors themselves; the recent proteomic analysis of natural (estradiol) and artificial (bisphenol A, phthalates, polychlorinated biphenyls) NHR ligands, whilst showing proteome changes attributable to compound treatment, failed to detect the NHRs the compounds in question are supposed to bind, i.e. members of the estrogen receptor, androgen receptor, or thyroid receptor families[272].

PPARγ, in particular, appears a challenging target: in 2014, a draft map of the human proteome showed PPARγ to be in the bottom quarter of all proteins by the total number of unique peptides identified (6) and in the bottom third of all proteins by maximum MaxQuant score[79]. In a complementary study[273], which used protein separation by SDS-PAGE, PPARγ was detected in only one of the 30 different

tissues/cells under study, namely adult retina, with only one peptide and 3% sequence coverage; notably, the other family member PPARα was not detected at all (Figure 85).

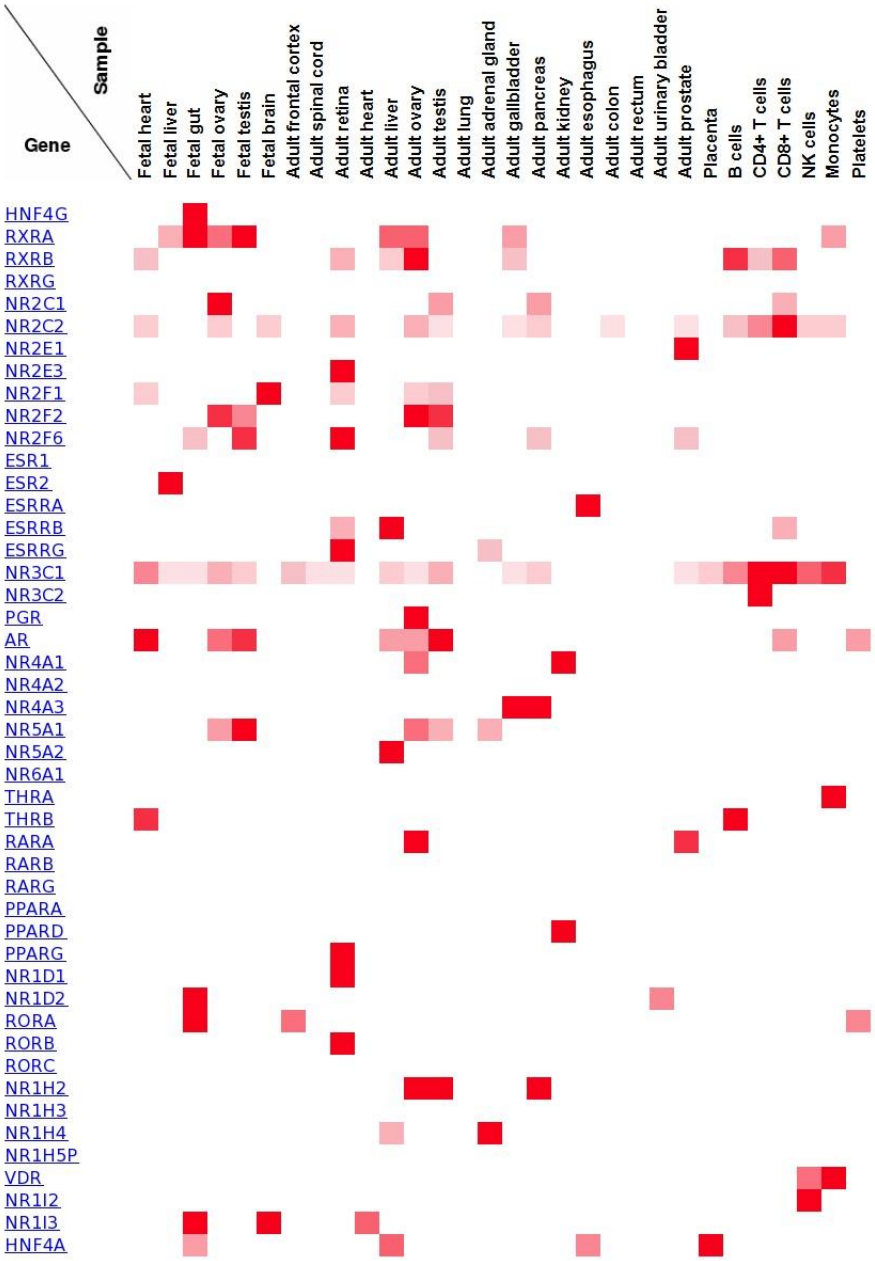


Figure 85: Proteomic detection of NHRs by MS using the Human Proteome Atlas (humanproteomemap.org).

So far the best results for MS analyses of NHR receptors involved either immunoprecipitation, protein separation, affinity enrichment, cell fractionation, or a combination thereof. Firstly, a recent analysis of the breast cancer tumour proteome utilised peptide isoelectric focusing, and detected not only the estrogen receptor family members, but also the androgen receptor, retinoid acid receptor family members and one member of PPAR family, namely PPARδ[274]. Earlier, nuclear extraction was coupled with immunoprecipitation to generate a dataset containing many of the NHRs, including estrogen receptor, PPARα, PPARγ, and retinoid receptor family, as well as their coactivators[275]. To date, the most complete study, using a combination of nuclear extraction and affinity enrichment using immobilised DNA hormone receptor response elements, detected 35 NHRs in mouse liver tissue out of 41 that are expressed on mRNA level[271].

In order to enable thermal profiling or other chemoproteomic experiments to examine NHR modulators, a number of assays were selected to explore the detection of PPARγ. These included immunoprecipitation from relevant cell lines using specific antibodies such as the ones identified in the AlphaScreen experiments described in previous chapters, as well as subcellular fractionation techniques and chromatography methods.

6.2 Optimisation of experimental conditions to increase coverage of PPARγ and its related protein complexes

6.2.1 Immunoprecipitation methods

During the antibody selection step for the development of the AlphaScreen assay, a number of the antibodies were tested for their ability to enrich native PPARγ from lysate, and, to evaluate possible off-target specificities of the antibodies. In all, 5 of the antibodies were tested (Figure 86), on lysates initially originating from A549 and SW620 cells. (These cell lines were chosen due to the amount of cells needed to obtain the amounts of lysate sufficient for all the immunoprecipitation experiments).

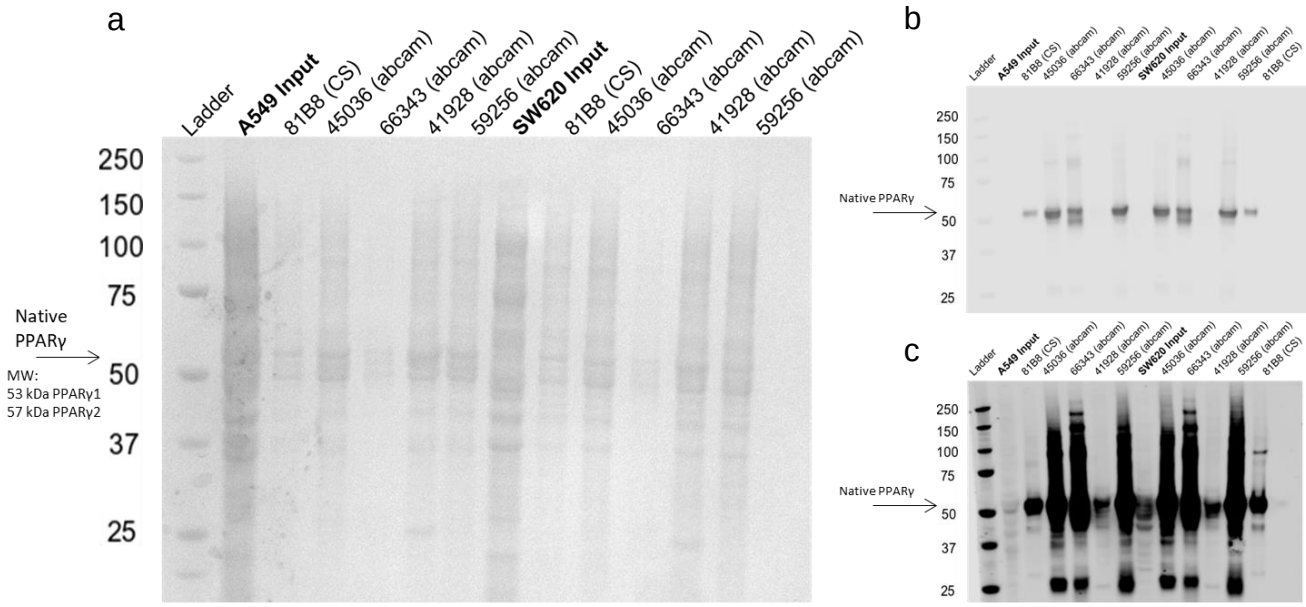
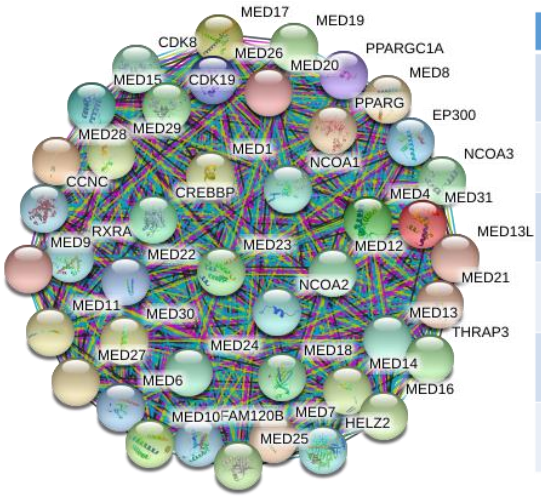


Figure 86: Results of PPARγ immunoprecipitation from A549 and SW620 cellular lysate. SW620 and A549 lysates were immunoprecipitated with a panel of anti- PPARγ antibodies. (a) Results visualised on SDS-PAGE, under UV light. (b) Results visualised on a WB probing for PPARγ (CS81B8, 1:1000) with low exposure and (c) high exposure. 'Native' PPARγ describes endogenous PPARγ.

As can be seen, the antibodies indeed appear to bind PPARγ, however, there are a number of other important observations. Firstly, the antibodies enrich for differing amounts of PPARγ; interestingly ab41928 (a weak PPARγ binder from the BLI assay) enriches for comparatively little while CS81B8 (the second strongest PPARγ binder from the BLI assay) not only enriches for PPARγ, it also appears to be highly specific given the lack of additional bands on both the SDS-PAGE and the high-exposure immunoblot.

Subsequently, it was decided to analyse the entire eluates by MS, initially without prior protein separation by SDS-PAGE. Thus, the eluents were precipitated, digested with trypsin, peptides desalted and analysed. Given the presence of additional bands with other antibodies, it was expected that other proteins would be present in the MS dataset; moreover, a simple demonstration of the protein's presence via WB is no guarantee that it will show up in MS, even if the band is intense[276]. Indeed, PPARγ was not found in the dataset, in any of the eluents tested. It must be stressed, however, that PPARγ mediates transcription from PPARγ-response elements (PREs) usually in complex with mediators, corepressors and coactivators[277,278]. Out of the PPARγ interactome (Figure 87), a number were found (most notably nuclear coactivator NCOA2, nuclear corepressors NCOR2 and NCOR1, 6 MED family members, CDK8/CDK19), however, their sequence coverage did not surpass 10% in any of the samples. The most abundant proteins in the sample appeared to be structural proteins, such as actin, likely from non-specific interactions with the antibody or the resin.

a



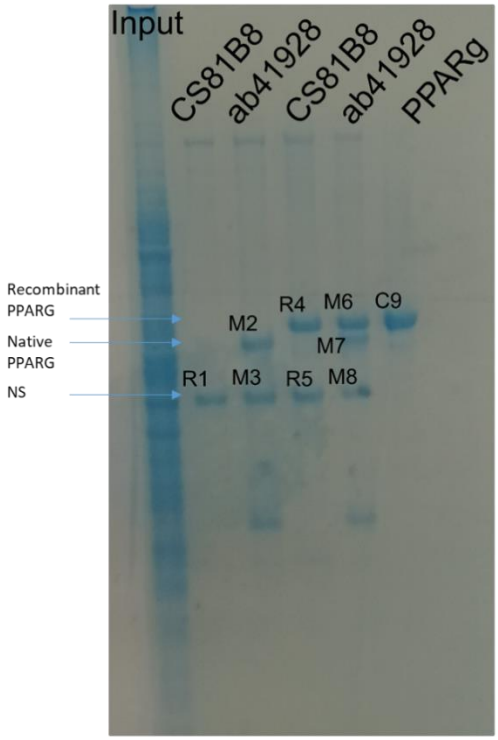
b

Protein ID	Name	Function
XRCC1,5,6	X-ray repair cross complementing	DNA repair
CROCC	Rootletin	Centrosome positioning
ERR1	Steroid hormone receptor ERR1	Nuclear hormone receptor
HLTF	Helicase-like transcription factor	Transcription
MOGS	Mannosyl-oligosaccharide glucosidase	Enzyme
RD23B	UV excision repair protein RAD23 homolog B	DNA repair

Figure 87: PPARγ interactome involved in DNA binding and transcription. (a) STRING analysis of PPARγ reveals a number of nuclear mediators, receptors and coactivators involved in gene expression. (b) Additional proteins that coelute with PPARγ following pulldown using immobilised DNA sequences corresponding to PPARγ response elements in the presence of PPARγ agonists performed by the Griffin group, putatively involved in PPARγ transcriptional activity[278].

In order to investigate the lack of MS detection of cellular PPARγ despite satisfactory WB results, the experiment was repeated, albeit this time with only two antibodies (the rabbit antibody CS81B8 and the mouse antibody ab41928). A549 cellular lysate was used and, as a positive control, recombinant PPARγ was included in a separate lane, as well as lysate spiked with recombinant PPARγ. Moreover, this time instead of analysing the entire eluent, proteins were separated on a gel and the respective bands excised, followed by extraction and digestion for MS analysis (Figure 88). Actin was found to be present in all the IP eluates, which could have masked the presence of PPARγ in the previous experiment.

a



b

Band	Mascot Rank	Mascot Score	Accession Code	Gene Name
R1	1	165	P53470	ACT1
M2	1	226	P01863	GCAA_MOUSE
M3	1	220	P53470	ACT1
R4	1	385	P37231	PPARG_HUMAN
R5	1	243	P53470	Actin-1
M6	1	419	P37231	PPARG_HUMAN
M7	1	206	P01863	GCAA_MOUSE
	2	160	Q4U3Q4	PPARG_CANLF
M8	1	200	P53470	ACT1
M9	1	574	P37231	PPARG_HUMAN

Figure 88: Results of PPARγ immunoprecipitation from A549 cellular lysate, using 2 antibodies and including spike-in control. (a) Results visualised on SDS-PAGE, using Coomassie staining. The first two lanes following the input lane are without recombinant PPARγ added to the lysate; the second two lanes have spiked-in lysate; the final lane is pure recombinant PPARγ. Because the recombinant PPARγ is FLAG-tagged, it appears slightly higher than expected for the endogenous ('native') protein. (b) The results following tryptic digest and MS analysis of the bands (NB: Band M7 appears to be identified as dog PPARγ; the sequence similarity is 99.0%).

Moreover, as mentioned before, immunoglobulin heavy chain and PPARγ both have a molecular weight of ~50 kDa, and as a result, it is challenging to distinguish them on SDS-PAGE. As can be seen from the image of the gel and the analysis, in the lysate precipitated with ab41928, the expected PPARγ band contains mostly IgG peptides and is identified as such; in the lysate precipitated with CS81B8, the band was too faint to excise and analyse. This is despite the fact that recombinant PPARγ, when spiked into the lysate, is precipitated, and suggests that the abundance

of PPARγ in the cell lines tested is too low (despite using concentrated lysate) to be efficiently enriched for, with the major constituents being non-specific contaminants, such as actin, and denatured antibody. With regards to the latter, the experiment was repeated with the antibody covalently cross-linked to the resin via reaction with dimethyl pimelimidate (DMP)[279] – this ensures that the antibody stays attached to the resin despite the denaturing Laemmli Buffer elution conditions, nevertheless, PPARγ was not detected. With that in mind, attention was shifted towards analysing cell lysates and extracts, and improving PPARγ detection via fractionation.

6.2.2 Analysis of cellular lysates and nuclear extracts

Given that immunoprecipitation was unable to detect cellular PPARγ via MS, the strategy was shifted, initially, to whole cell lysate analysis. As the previous two immortalised cell lines express less PPARγ than the 3T3-L1 adipocyte cell line, and much less lysate was required (µg instead of mg quantities that were needed for IP), it was decided to switch to the adipocyte cell line. Lysate from fully differentiated cells was precipitated, digested and de-salted, which was followed by high-pH fractionation of the lysate into 4 separate fractions, which were analysed by mass spectrometry. Whilst a total of 4,887 proteins were identified, no specific peptides for PPARγ could be detected. Out of the proteins potentially involved in nuclear receptor transcription from PPARγ response elements, RXRα was identified, as well as 6 members of the mediator complex and NCOA5 and NCOR2; unfortunately, none of the proteins had a greater sequence coverage than 10%. In

parallel, a solution of recombinant PPARγ was also analysed the same way. Reassuringly, PPARγ was detected, with a sequence coverage of 62% (Figure 89).

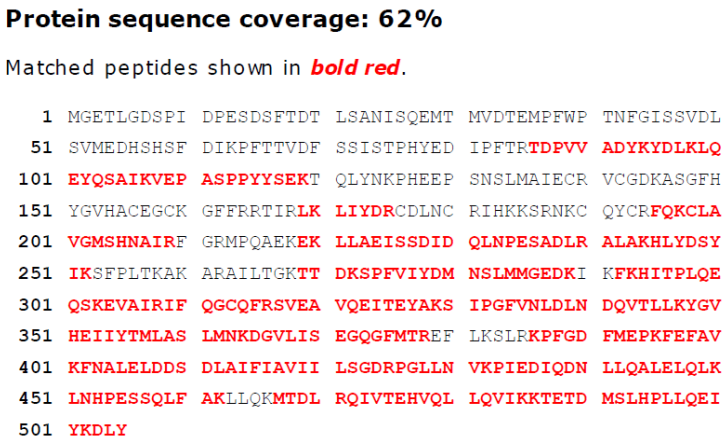


Figure 89: MS analysis of the tryptic digest of recombinant PPARγ.

Subsequently, it was decided to perform nuclear extraction using 3T3-L1 cells. Since PPARγ performs its major functions in the nucleus and the vast majority of it is localised there, it was reasoned that not only would nuclear extraction maximise the chances of detecting PPARγ, it would also increase the chances of detecting the major coactivators and binders of PPARγ. In addition, given that, as explained earlier, digestion with trypsin can result in missed cleavages and lower sequence coverage, it was decided to also include an additional experiment, where trypsin is combined with LysC. Live differentiated 3T3-L1 adipocytes were thus harvested, pelleted, and nuclear extraction was performed using an appropriate kit (Merck) according to manufacturer's protocols. Afterwards, the proteins were precipitated using the standard chloroform-methanol extraction procedure, and digested with either trypsin only or in combination with LysC. The peptides were then

fractionated via high pH reversed-phase chromatography[280] to generate 4 fractions. The peptides were then separated via HPLC and injected for MS. Fortuitously, not only was PPARγ identified, most of the major proteins involved in transcription from nuclear hormone receptors were also detected, oftentimes with sequence coverage exceeding 10% (Table 4).

Unique peptides Trp N	Unique peptides Trp_Lys_C N	Sequence coverage Trp [%] N	Sequence coverage Trp_Lys_C [%] N	Protein names T	Gene names T
5	6	4.8	4.2	Mediator of RNA polymerase II transcription subunit 14	Med14
4	6	2.8	3.1	Mediator of RNA polymerase II transcription subunit 12	Med12
2	2	1.8	2	Mediator of RNA polymerase II transcription subunit 13	Med13
0	2	0	11.5	Mediator of RNA polymerase II transcription subunit 22	Med22
3	2	3.5	2.2	Mediator of RNA polymerase II transcription subunit 16	Med16
3	3	2.5	2.3	Mediator of RNA polymerase II transcription subunit 23	Med23
0	2	0	20.5	Mediator of RNA polymerase II transcription subunit 19	Med19
1	1	2.8	2.8	Mediator of RNA polymerase II transcription subunit 25	Med25
3	3	8.3	3.9	Mediator of RNA polymerase II transcription subunit 17	Med17
2	3	8.5	12.2	Mediator of RNA polymerase II transcription subunit 6	Med6
2	2	3	3	Mediator of RNA polymerase II transcription subunit 15	Med15
4	9	4.1	8.4	Mediator of RNA polymerase II transcription subunit 1	Med1
9	7	12.4	8.2	Mediator of RNA polymerase II transcription subunit 24	Med24
1	1	7.6	7.6	Mediator of RNA polymerase II transcription subunit 21	Med21
4	6	17	24.8	Mediator of RNA polymerase II transcription subunit 4	Med4
1	1	7.1	5.2	Mediator of RNA polymerase II transcription subunit 8	Med8
1	2	15.4	31.6	Mediator of RNA polymerase II transcription subunit 11	Med11
1	0	8.5	0	Mediator of RNA polymerase II transcription subunit 29	Med29
2	4	5	9.9	Peroxisome proliferator-activated receptor gamma	Pparg
1	0	3.9	0	NAD-dependent protein deacetylase sirtuin-6	Sirt6
1	1	3.3	3.3	NAD-dependent protein deacetylase sirtuin-3	Sirt3
2	2	6.3	6.3	NAD-dependent protein deacetylase sirtuin-4	Sirt4
5	5	19.5	17	NAD-dependent protein deacetylase sirtuin-2	Sirt2
0	1	0	1.1	Nuclear receptor coactivator 3	Ncoa3
5	8	4.4	8.8	Nuclear receptor coactivator 1	Ncoa1
2	6	3.1	7.6	Nuclear receptor coactivator 2	Ncoa2
8	9	15.2	16.2	Nuclear receptor coactivator 5	Ncoa5
3	4	2.8	2.8	Nuclear receptor corepressor 1	Ncor1
6	6	4.5	4.2	Nuclear receptor corepressor 2	Ncor2
5	6	5.7	5.7	CREB-binding protein	Crebbp
3	3	14.7	14.7	Cyclic AMP-responsive element-binding protein 1	Creb1
2	3	3.7	8	Cyclin-dependent kinase 8;Cyclin-dependent kinase 19	Cdk8;Cdk19
1	1	4.5	8.7	Retinoic acid receptor alpha	Rara
0	2	0	10.5	Retinoic acid receptor gamma	Rarg
3	3	25.3	25.3	Retinoic acid receptor RXR-alpha	Rxra
1	1	13.1	12.7	Retinoic acid receptor RXR-beta	Rxrb
8	5	32.5	19.2	Steroid hormone receptor ERR1	Esrra
0	1	0	2.8	Vitamin D3 receptor	Vdr

Table 4: MS analysis of the tryptic and LysC digest of 3T3-L1 nuclear extract, repeat 1. The different protein subgroups are highlighted: green: the mediator complex, blue: sirtuins, orange: nuclear receptor corepressors and coactivators, purple: CREB and CREBBP, blue: retinoic acid receptor and related, grey: other nuclear hormone receptors

Following the initial success, the experiment was repeated using a new batch of differentiated 3T3-L1 cells, keeping conditions the same. Despite a strong overlap between the samples in the proteins detected, and in some cases increased sequence coverage for some of the nuclear proteins, PPARγ itself was not detected (Table 5).

N: Unique peptides LysC_2	N: Unique peptides Trp_2	N: Sequence coverage LysC_2 [%]	N: Sequence coverage Trp_2 [%]	T: Protein names	T: Gene names
2	1	2.7	1.6	Mediator of RNA polymerase II transcription subunit 13-like	Med13l
3	4	10.5	15	Mediator of RNA polymerase II transcription subunit 25	Med25
4	4	72.3	72.3	Mediator of RNA polymerase II transcription subunit 10	Med10
11	11	24.7	30.4	Mediator of RNA polymerase II transcription subunit 15	Med15
14	18	16.2	19.9	Mediator of RNA polymerase II transcription subunit 14	Med14
20	22	13.2	15.6	Mediator of RNA polymerase II transcription subunit 12	Med12
4	4	31	31	Mediator of RNA polymerase II transcription subunit 22	Med22
13	14	15.1	14.8	Mediator of RNA polymerase II transcription subunit 23	Med23
7	7	12	12	Mediator of RNA polymerase II transcription subunit 16	Med16
0	1	0	4	Mesenteric estrogen-dependent adipogenesis protein	Medag
2	3	2.1	2.3	Mediator of RNA polymerase II transcription subunit 13	Med13
1	2	2.2	4.6	Mediator of RNA polymerase II transcription subunit 26	Med26
4	3	35.7	30.7	Mediator of RNA polymerase II transcription subunit 19	Med19
11	11	20.2	26.2	Mediator of RNA polymerase II transcription subunit 17	Med17
1	2	10.6	26.8	Mediator of RNA polymerase II transcription subunit 9	Med9
3	3	19.1	29.2	Mediator of RNA polymerase II transcription subunit 28	Med28
4	4	11.8	11.8	Mediator of RNA polymerase II transcription subunit 6	Med6
18	17	17.4	18.4	Mediator of RNA polymerase II transcription subunit 1	Med1
9	8	14.6	11.2	Mediator of RNA polymerase II transcription subunit 24	Med24
4	4	48.6	48.6	Mediator of RNA polymerase II transcription subunit 21	Med21
7	7	39.6	39.6	Mediator of RNA polymerase II transcription subunit 4	Med4
2	2	12.4	12.4	Mediator of RNA polymerase II transcription subunit 30	Med30
3	3	29.8	29.8	Mediator of RNA polymerase II transcription subunit 31	Med31
4	4	19.2	16.3	Mediator of RNA polymerase II transcription subunit 18	Med18
2	3	21	27.9	Mediator of RNA polymerase II transcription subunit 7	Med7
6	6	37.2	37.2	Mediator of RNA polymerase II transcription subunit 8	Med8
2	2	31.6	31.6	Mediator of RNA polymerase II transcription subunit 11	Med11
7	6	40.5	31.5	Mediator of RNA polymerase II transcription subunit 27	Med27
5	6	40.2	44.2	Mediator of RNA polymerase II transcription subunit 29	Med29
1	0	9.4	0	Mediator of RNA polymerase II transcription subunit 20	Med20
6	6	23.9	25.1	NAD-dependent protein deacetylase sirtuin-2	Sirt2
1	1	12.4	12.4	NAD-dependent protein deacetylase sirtuin-7	Sirt7
2	1	5.2	3.6	NAD-dependent protein deacetylase sirtuin-1;SirtT1 75 kDa fragment	Sirt1
1	0	7.8	0	NAD-dependent protein deacetylase sirtuin-6	Sirt6
2	1	6.6	3.3	NAD-dependent protein deacetylase sirtuin-3	Sirt3
2	2	7.5	7.5	NAD-dependent protein deacetylase sirtuin-4	Sirt4
5	3	6.7	4.4	Nuclear receptor coactivator 3	Ncoa3
4	5	6.5	7.4	Nuclear receptor coactivator 2	Ncoa2
0	0	29.6	23.9	Nuclear receptor coactivator 5	Ncoa5
0	0	9.1	6.5	Nuclear receptor corepressor 1	Ncor1
0	0	13.1	10.4	Nuclear receptor corepressor 1	Ncor1
1	2	2.1	2.7	Nuclear receptor coactivator 6	Ncoa6;Rap250
28	30	20.2	19.5	Nuclear receptor corepressor 2	Ncor2
2	2	2.2	2.2	Nuclear receptor coactivator 1	Ncoa1
1	1	2.9	2.9	Nuclear receptor coactivator 4	Ncoa4
2	2	27.5	23.5	Nuclear receptor coactivator 5	Ncoa5
10	11	12.8	12.2	CREB-binding protein	Crebbp
2	3	12.6	15.5	Cyclic AMP-responsive element-binding protein 1	Creb1;CREB
0	0	14.3	5.3	Cyclin-dependent kinase 8	Cdk8
4	4	26.8	26.8	Retinoic acid receptor RXR-beta	Rxrb
2	2	17.8	17.8	Retinoic acid receptor RXR-alpha;Retinoic acid receptor RXR-gamma	Rxra;Rxrg
4	3	13.8	13.1	Retinoic acid receptor gamma	Rarg
1	2	5.2	9	Steroid hormone receptor ERR1	Esrra

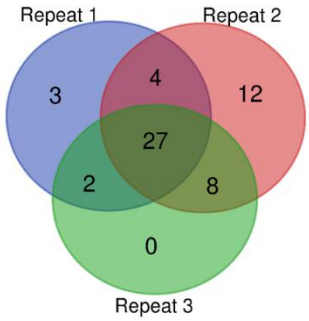
Table 5: MS analysis of the tryptic and LysC digest of 3T3-L1 nuclear extract, repeat 2. The different protein subgroups are highlighted: green: the mediator complex, blue: sirtuins, orange: nuclear receptor corepressors and coactivators, purple: CREB and CREBBP, blue: retinoic acid receptor and related, grey: other nuclear hormone receptors. Of note is the fact that two mouse proteins with different UniProt accession codes and sequences, E9Q9Y2 and E9Q2B2, both appear to be called Ncor1.

On the other hand, the coverage of other nuclear transcription components in the sample was found to be noticeably greater, and average sequence coverage for these selected nuclear proteins went from 7.31% (tryptic digest) and 8.90% (tryptic + LysC digest) to 17.96% (tryptic digest) and 17.88% (tryptic + LysC digest). Due to the great variability between the two nuclear extracts and the lack of PPARγ detection, the experiment was repeated with only trypsin and LysC combination as it produced a greater average sequence coverage in the first experiment, and marginally the same average sequence coverage in the second (Table 6).

N: Unique peptides	N: Sequence coverage [%]	T: Protein names	T: Gene names
1	3.5	Mediator of RNA polymerase II transcription subunit 25	Med25
1	24.1	Mediator of RNA polymerase II transcription subunit 10	Med10
3	5.2	Mediator of RNA polymerase II transcription subunit 15	Med15
9	9.6	Mediator of RNA polymerase II transcription subunit 14	Med14
10	6.2	Mediator of RNA polymerase II transcription subunit 12	Med12
1	10.7	Mediator of RNA polymerase II transcription subunit 22	Med22
10	8.8	Mediator of RNA polymerase II transcription subunit 23	Med23
4	6.6	Mediator of RNA polymerase II transcription subunit 16	Med16
3	2.6	Mediator of RNA polymerase II transcription subunit 13	Med13
2	20.5	Mediator of RNA polymerase II transcription subunit 19	Med19
8	16.8	Mediator of RNA polymerase II transcription subunit 17	Med17
2	6.5	Mediator of RNA polymerase II transcription subunit 6	Med6
8	6.4	Mediator of RNA polymerase II transcription subunit 1	Med1
11	15.1	Mediator of RNA polymerase II transcription subunit 24	Med24
2	23.6	Mediator of RNA polymerase II transcription subunit 21	Med21
4	18.5	Mediator of RNA polymerase II transcription subunit 4	Med4
2	9	Mediator of RNA polymerase II transcription subunit 30	Med30
2	15.4	Mediator of RNA polymerase II transcription subunit 8	Med8
2	21.4	Mediator of RNA polymerase II transcription subunit 11	Med11
3	11.3	Mediator of RNA polymerase II transcription subunit 27	Med27
2	9.9	Mediator of RNA polymerase II transcription subunit 20	Med20;Gm20517
3	7.6	Peroxisome proliferator-activated receptor gamma	Pparg
1	16	NAD-dependent protein deacetylase sirtuin-3	Sirt3
1	3.4	NAD-dependent protein deacetylase sirtuin-6	Sirt6
1	12.4	NAD-dependent protein deacetylase sirtuin-1;SirtT1 75 kDa fragment	Sirt1
1	3	NAD-dependent protein deacetylase sirtuin-4	Sirt4
5	4.2	Nuclear receptor coactivator 1	Ncoa1
2	1.6	Nuclear receptor corepressor 1	Ncor1
11	6.9	Nuclear receptor corepressor 2	Ncor2
12	31.6	Nuclear receptor coactivator 5	Ncoa5
8	7.4	CREB-binding protein	Crebbp
3	17.6	Cyclic AMP-responsive element-binding protein 1	Creb1;CREB
1	3.7	Cyclin-dependent kinase 8;Cyclin-dependent kinase 19	Cdk8;Cdk19
4	9.2	Retinoic acid receptor RXR-alpha;Retinoic acid receptor RXR-beta;Retinoic acid receptor RXR-gamma	Rxra;Rxrb;Rxrg
2	6.9	Steroid hormone receptor ERR1	Esrra

Table 6: MS analysis of the tryptic and LysC digest of 3T3-L1 nuclear extract, repeat 3. The different protein subgroups are highlighted: green: the mediator complex, blue: sirtuins, orange: nuclear receptor corepressors and coactivators, purple: CREB and CREBBP, blue: retinoic acid receptor and related, grey: other nuclear hormone receptors.

3 unique peptides for PPARγ were found, giving a sequence coverage of 7.6%. In addition, the average sequence coverage for the PPAR interactors was 10.95%. Comparison of the 3 different repeats utilising the trypsin and Lys C combination (Figure 90) revealed an overlap of 27 proteins, with a further 14 proteins appearing in at least two datasets. However, the overall sequence coverage was low: in the first repeat, merely 12 out of 36 (33.3%) proteins identified had a sequence coverage greater than 10%, in the second it was 37 out of 53 (69.8%), and in the third it was 14 out of 37 (37.8%). This, coupled with the fact that the highest sequence coverage of PPARγ reported was 9.9%, meant that the chance of detecting PPARγ via MS spectrometry in an MS-CETSA experiment was low.



Names	total	elements
Repeat 1 Repeat 2 Repeat 3	27	Ncor2 Med13 Sirt3 Med19 Ncoa5 Med17 Med1 Med25 Med22 Med11 Med14 Ncoa1 Rxrb Esrra Rxra Med24 Med8 Ncor1 Med23 Sirt4 Med6 Med15 Med21 Med12 Crebbp Med4 Med16
Repeat 1 Repeat 2	4	Rarg Ncoa3 Ncoa2 Sirt2
Repeat 1 Repeat 3	2	Cdk8;Cdk19 Pparg
Repeat 2 Repeat 3	8	Med10 Sirt6 Creb1;CREB Sirt1 Med27 Med20 Rxrg Med30
Repeat 1	3	Rara Vdr Creb1
Repeat 2	12	Med29 Med9 Ncoa6;Rap250 Cdk8 Med31 Med28 Med18 Med26 Sirt7 Ncoa4 Med13l Med7

Figure 90: The overlap between the nuclear factors involved in NHR transcription detected between the three replicates. In each experiment, a different fresh batch of differentiated 3T3-L1 cells was used. Nuclear extraction was performed according to established protocols, followed by peptide digestion with trypsin and LysC combination. In each case, the peptides were high-pH fractionated and analysed via HPLC-MS.

6.3 Thermal Profiling of Rosiglitazone in 3T3-L1 cells

6.3.1 Design of the experiment

With the above in mind, it was reasoned that the chance of detecting PPARγ or the interacting nuclear factors in a thermal profiling experiment on a 3T3-L1 nuclear extract is small, and the chance of finding sufficient quantities of peptides to be able to construct accurate 2D melting surface plots is likewise small. As a result, the 2D-TPP strategy would focus on investigating possible off-target interactions of rosiglitazone, or perhaps understand its MoA beyond modulation of PPARγ to potentially explain some of the more interesting phenotypes it produces. The side effects associated with TZD treatment largely fall into two camps: the first one revolves around cardiovascular side effects and ultimately an increased risk of cardiotoxicity and heart failure[281]; the second one is the increasing amount of evidence that rosiglitazone and other TZDs impair bone regeneration and reduce bone mineral density, as well as increasing the risk of fractures[282,283]. Whether those side effects are due to on-target, or off-target effects is currently unknown. A recent chemoproteomic analysis of rosiglitazone, pioglitazone, and the TZD scaffold using compound immobilisation and protein pulldown from rat tissue via affinity chromatography followed by MS analysis revealed that the compounds bind a number of dehydrogenases, mitochondrial enzymes, ion channels and related proteins, which could explain the cardiovascular risk associated with TZD treatment[86], however, nothing in the analysis points to proteins associated with negative side effects on bone mineral density (BMD); it's also important to point out that PPARγ was not detected in rat tissue using this technique, and repeating

the experiment in rat liver resulted in the detection of only one PPARγ peptide across 4 scans.

The deleterious effects TZD treatment has on osteogenesis is more likely to be a feature of PPARγ signalling. Initially, an analysis of single nucleotide polymorphisms (SNPs) in the gene encoding PPARγ and associated effects on BMD found that, indeed, there are a number of SNPs that result in population-wide effects on BMD[284]. Subsequently, it was revealed that mice fed a high-fat diet had increased levels of bone resorption genes, however, the diet also resulted in decreased levels of PPARγ[285]. Meanwhile, lower PPARγ levels were found to increase osteogenesis in stem cells whilst decreasing adipocyte differentiation, an effect which was rescued by PPARγ restoration, suggesting that PPARγ might act as a switch between osteogenic and adipogenic differentiation[286].

The seminal discovery came when it was found through genetic mouse models that PPARγ enacts its negative effects on BMD together with the nuclear coactivator PGC1b, and stimulates expression of the estrogen-related receptor alpha protein ERRa, the homolog of murine Esrra[287]. PGC1b knockout mice are protected from the deleterious effects of rosiglitazone on bone[288]. Incidentally, in our analyses Esrra was detected in all three analyses of 3T3-L1 nuclear extract.

It was decided to perform the 2D-TPP experiment using rosiglitazone in live 3T3-L1 cells, with the aim of the experiment being to elucidate either rosiglitazone off-

target interactors, or proteins that interact with PPARγ to facilitate gene expression to perhaps try to investigate some of the phenotypic effects of rosiglitazone (however, as the 3T3-L1 cells are adipose cells, any results that would point towards effects on bone tissue would have to be validated in a more appropriate cell line). Similarly to the immunoblot format, 4 concentrations of rosiglitazone were chosen (0.8 µM, 4 µM, 20 µM and 100 µM), with 12 temperatures ranging from 37 to 59 °C. 2D-TPP was performed according to the established protocol, with the following layout for TMT-labelling (Figure 91).

Temp (°C)	126	127L	127H	128L	128H	129L	129H	130L	130H	131	RefCol	
37	100	20	4	0.8	0	-	-	-	-	-	128H	F1
57	-	-	-	-	-	100	20	4	0.8	0	131	
39	100	20	4	0.8	0	-	-	-	-	-	128H	F2
59	-	-	-	-	-	100	20	4	0.8	0	131	
41	100	20	4	0.8	0	-	-	-	-	-	128H	F3
53	-	-	-	-	-	100	20	4	0.8	0	131	
43	100	20	4	0.8	0	-	-	-	-	-	128H	F4
55	-	-	-	-	-	100	20	4	0.8	0	131	
45	100	20	4	0.8	0	-	-	-	-	-	128H	F5
49	-	-	-	-	-	100	20	4	0.8	0	131	
47	100	20	4	0.8	0	-	-	-	-	-	128H	F6
51	-	-	-	-	-	100	20	4	0.8	0	131	

Figure 91: The TMT labelling layout for the quantitative proteomics of the rosiglitazone dataset. F1-F6 denote the pooled fractions of TMT-labelled samples.

6.3.2 Results

Overall, 6765 proteins were detected, with 6126 identified with high confidence. The efficiency of TMT-labelling was found to be lower than usual, at 84%. PPARγ was not detected in the dataset. On the other hand, 22 members of the mediator complex, as well as 3 sirtuins and Cdk8 were successfully identified.

Initially, the results were analysed using the TPP R script. Overall, 109 proteins were found to meet the criteria established by Becher et al[109], namely fold change cutoff for stabilisation at each temperature being at least 50%, sigmoidal dose-response curves plotted, minimum $R^2 > 0.8$ and minimum of two adjacent temperatures at which stabilisation occurs (Figure 92).

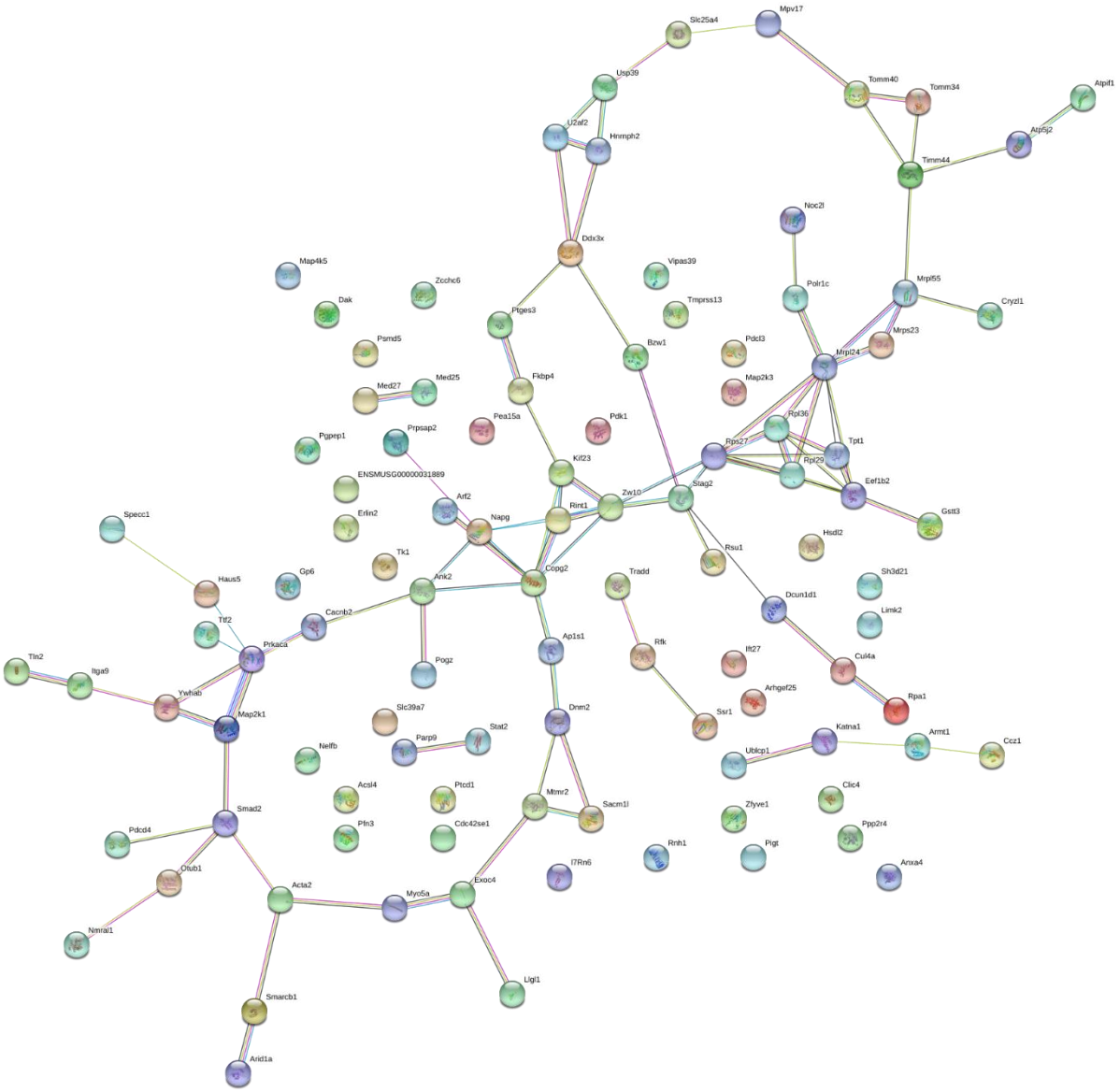


Figure 92: STRING analysis of the proteins obtained as hits from the TPP R script.

Notably, the dataset appears to be enriched in proteins involved in RNA binding, ribosomal components and mRNA proteins. Moreover, a number of commonly observed false positive heat maps appear in the dataset (Figure 93). As a result, the dataset was also analysed by the MATLAB algorithm described in chapter 3.

Calmodulin-2

37	1.00	1.29	2.36	1.95	1.95
39	1.00	1.13	1.76	1.72	1.68
41	1.00	0.98	1.14	1.28	1.48
43	1.00	0.90	1.58	1.46	1.45
45	1.00	0.80	1.39	0.61	1.36
47	1.00	1.25	1.12	1.19	1.60
49	1.00	0.47	1.33	1.13	0.65
51	1.00	0.66	1.89	1.46	3.95
53	1.00	1.44	2.04	1.91	1.70
55	1.00	1.28	2.39	0.90	0.92
57	1.00	0.73	1.41	1.34	1.97
59	1.00	0.44	1.45	2.42	1.62

ADP-Ribosylation factor 2

37	1.00	1.58	1.60	1.53	2.36
39	1.00	1.19	1.83	2.44	1.56
41	1.00	1.75	0.63	2.10	1.85
43	1.00	0.46	2.37	2.09	2.02
45	1.00	1.95	1.16	0.55	3.41
47	1.00	2.26	0.62	3.07	1.33
49	1.00	0.51	1.84	2.90	0.76
51	1.00	0.85	4.25	1.28	1.27
53	1.00	1.51	2.34	3.57	3.74
55	1.00	1.68	4.03	2.67	1.37
57	1.00	0.92	2.21	1.86	4.25
59	1.00	1.81	2.97	4.03	7.06

Figure 93: Potentially spurious results appearing as a result of analysis with the TPP R script. Both proteins meet the criteria set by Becher et al, however, by inspection the heat maps do not resemble the typical heat maps associated with hits.

As described earlier, the MATLAB algorithm in contrast to the TPP R script looks at each matrix holistically, and tries to fit a surface equation that describes previously-validated heat maps, giving both a measure of stabilisation (integral volume under the surface) and a measure of confidence (R^2) value. By setting the fit cut off value at 0.8, the following proteins appear to be most strongly stabilised and de-stabilised (Figure 94).

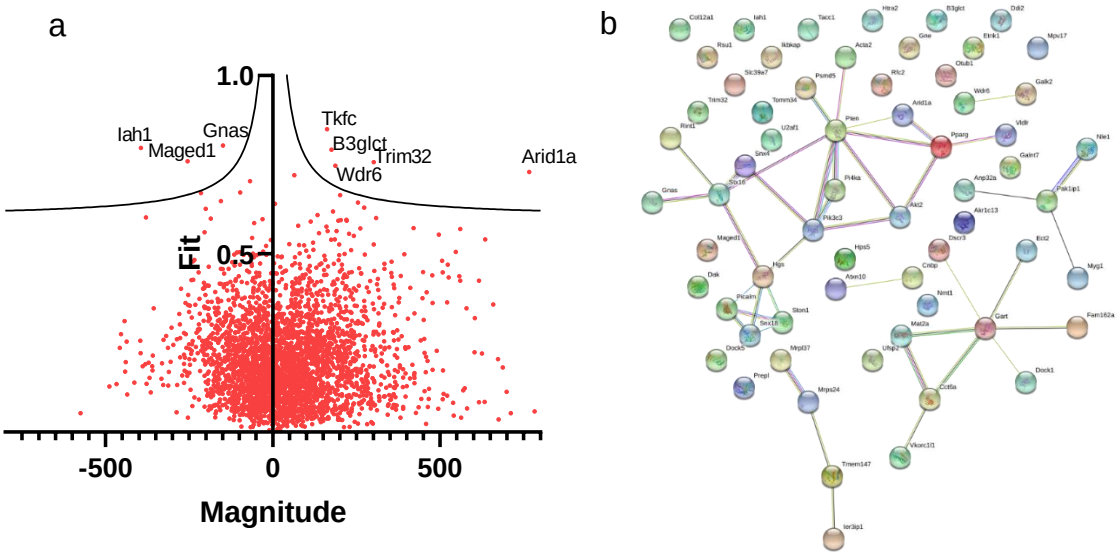


Figure 94: Hits from the dataset, as analysed by the MATLAB algorithm. (a) Pseudo-volcano plot showing the top proteins by magnitude and fit. (b) STRING analysis of the top 50 stabilised and destabilised proteins, including the PPI analysis.

Interestingly, the hit dataset is no longer enriched in ribosomal and mRNA-processing proteins. In general, ribonucleoproteins and ribosomal components are frequently enriched in proteomic experiments[205], meaning it is likely they were false positives successfully separated out by the algorithm. In turn, the dataset is functionally enriched in regulators of catalytic activity; moreover, 15 out of the 50 proteins fall into the category of small molecule binders (15/50). In addition, the hits lack the 'un-hit-like' heat maps from the TPP R script analysis; for instance Calmodulin-2 was rejected with an R^2 value of 0.198 (3 s.f.)

Isoamyl acetate-hydrolyzing esterase1 homolog (Iah1) is a protein with no known function in mice – its yeast homolog is a homodimer with esterase activity and a preference for isoamyl acetates[289], however, its function has not been characterised

in other species. In a recent analysis of gene loci possibly implicated in fatty liver disease, Iah1 was identified and, interestingly, overexpression in hepatocytes caused a downregulation in the expression of a number of genes, including CD36 and PPARγ itself, as well an increase in SREBP1, a gene heavily contributing to fatty liver disease[290].

Melanoma-associated antigen D1 (Maged1) is a poorly-characterised, but ubiquitously-expressed protein that appears to be involved in intellectual and neural development[291]. Recently, Maged1 has been shown to act as an inhibitor of PPARγ – in cellular assays, Maged1 expression inhibited adipocyte differentiation by suppressing PPARγ transcriptional activity, and in IP-WB studies, the two proteins coelute, suggesting Maged1 binds PPARγ[292]. In the 2D-TPP dataset, Maged1 appears to be heavily destabilised by rosiglitazone treatment (Figure 95) – this could imply that the compound binding to PPARγ disrupts the PPARγ-Maged1 complex, both stabilising PPARγ and destabilising Maged1. Further experiments and validation are needed, such as an immunoprecipitation of Maged1 with PPARγ in the presence and absence of rosiglitazone.

	Maged1				
37	1.00	0.90	0.95	0.91	1.02
39	1.00	0.84	0.87	1.08	0.95
41	1.00	0.86	1.14	1.06	0.97
43	1.00	0.84	0.92	0.99	1.00
45	1.00	0.77	0.93	0.97	1.00
47	1.00	1.09	0.99	1.34	1.05
49	1.00	1.20	1.08	1.08	1.17
51	1.00	0.86	0.99	1.02	0.90
53	1.00	1.16	1.16	0.96	0.81
55	1.00	1.09	0.64	0.67	0.68
57	1.00	0.45	0.39	0.32	0.28
59	1.00	0.36	0.27	0.15	0.12

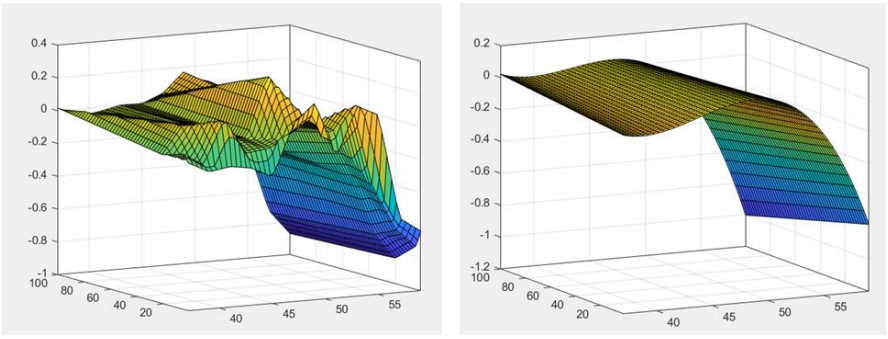


Figure 95: Maged1 has a strongly thermally-destabilised matrix. The surface plot of Maged1 using the MATLAB algorithm and the fitted surface for Maged1, with R^2 of 0.8259.

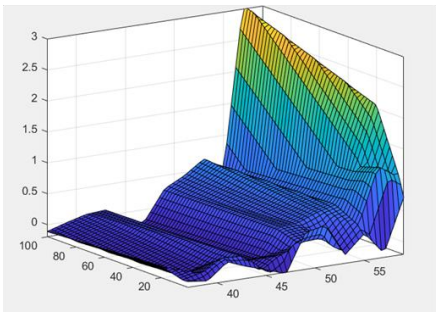
The Gnas gene produces numerous transcripts encoding the various forms of the Gs-alpha protein, which is a key mediator of GPCR signal transduction[293]. There is a strong link between Gnas downregulation/impairment and increased ossification[294], as well as decreased adipogenesis[295]. Nonetheless, given that there is no evidence on a mechanistic level of PPARγ binding to Gs-alpha, its seeming destabilisation by rosiglitazone could be indicative of a number of possible effects, such as the compound disrupting a PPI between Gnas and another protein.

Arid1a is a member of SWI/SNF chromatin remodelling complex and appears to be one of the most strongly-stabilised proteins in the dataset with a hit-like heat map (Figure 96). This is particularly interesting, as Arid1a has been recently implicated in the expression of brown fat adipose genes in response to stimuli. A recent analysis has shown that jumonji-family member Jmjd1a, upon phosphorylation by Pka in response to GPCR signalling, acts as a scaffold capable of binding both the SWI/SNF complex and DNA-bound PPARγ, resulting in the

remodelling of chromatin that leads to increased expression of brown adipose genes including Ucp1[296]. Perhaps even more interesting is the fact that, when Jmjd1a was immunoprecipitated, Arid1a and PPARγ were co-purified, suggesting a strong interaction. This means that it is possible for Arid1a and PPARγ to exist in a complex, with rosiglitazone-mediated stabilisation of PPARγ conferring residual stabilisation onto Arid1a. Moreover, whilst unfortunately Jmjd1a was not detected in the 2D-TPP dataset, it would be pertinent to investigate the link between the three proteins further, and how rosiglitazone affects it.

Arid1a

37	1.00	0.90	0.89	0.99	0.89
39	1.00	0.86	0.96	0.77	0.98
41	1.00	1.12	1.16	0.89	1.07
43	1.00	1.00	1.14	1.12	1.09
45	1.00	0.89	0.84	0.87	0.69
47	1.00	0.78	1.06	0.88	0.82
49	1.00	1.40	1.20	1.31	1.29
51	1.00	1.46	1.22	1.34	1.45
53	1.00	0.94	1.02	1.46	1.67
55	1.00	1.24	1.35	1.54	1.42
57	1.00	0.87	2.24	2.12	4.07
59	1.00	1.72	2.03	3.05	3.73



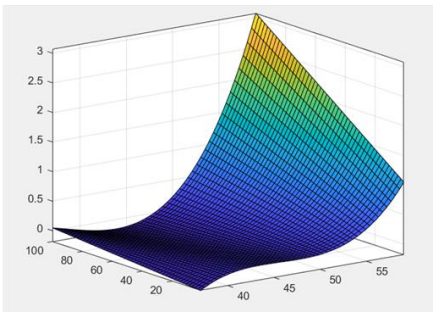


Figure 96: Arid1a as the most hit-like protein from the dataset. The surface plot of Arid1a using the MATLAB algorithm and the fitted surface for Arid1a, with R^2 of 0.8137.

Out of the top 8 hits, 3 (Tkfc, Wdr6, Trim32) have been predicted, but not validated, to be PPARγ-target genes, from the PPARGene database[297]. Trim32 is a recently-characterised member of the ubiquitin ligase family whose deficiency has been shown to contribute to muscular dystrophy[298]. Tkfc (triokinase) is an enzyme that catalyses the phosphorylation of dihydroxyacetone and triokinase, whereas Wdr6 belongs to the ubiquitously-expressed WD-repeat family of proteins. Whilst their presence as some of the top hits is certainly interesting and they are hits in TPP R

script (with strong stabilisation at 2 adjacent temperatures), it has to be stressed that the MATLAB algorithm tends to bias in favour of strong fold changes at the final two temperatures, therefore caution is advised in interpreting the results (Fig. 97).

Trim32

37	1.00	1.13	1.04	0.90	1.00
39	1.00	1.33	1.11	1.16	0.98
41	1.00	0.90	0.89	1.09	0.84
43	1.00	0.94	0.98	0.98	0.95
45	1.00	0.95	0.93	0.98	0.86
47	1.00	0.95	1.01	0.93	0.85
49	1.00	1.10	0.90	0.97	1.01
51	1.00	1.11	0.94	0.99	0.99
53	1.00	1.42	1.18	1.17	1.03
55	1.00	1.10	0.94	1.21	1.10
57	1.00	1.53	1.38	1.59	2.41
59	1.00	2.57	1.80	2.23	2.28

Tkfc

37	1.00	0.97	0.91	0.97	1.04
39	1.00	0.88	0.95	1.01	0.95
41	1.00	0.95	1.00	1.05	0.98
43	1.00	0.94	1.01	1.02	1.01
45	1.00	1.05	1.06	1.08	1.05
47	1.00	0.90	0.93	1.03	0.87
49	1.00	0.95	0.93	0.99	0.93
51	1.00	1.00	0.98	1.00	0.89
53	1.00	0.90	0.82	0.89	0.81
55	1.00	0.99	0.93	1.14	1.21
57	1.00	0.89	0.93	1.40	2.25
59	1.00	1.28	1.28	1.29	2.56

Wdr6

37	1.00	1.18	0.99	1.05	1.13
39	1.00	0.96	0.99	1.09	1.05
41	1.00	1.02	0.99	1.05	1.05
43	1.00	0.97	1.04	1.06	1.06
45	1.00	1.03	0.97	0.99	1.02
47	1.00	1.01	0.96	1.03	1.01
49	1.00	0.91	1.00	1.01	0.88
51	1.00	0.99	0.99	0.89	0.83
53	1.00	0.78	0.97	0.96	0.94
55	1.00	0.90	1.01	1.04	1.15
57	1.00	1.32	1.36	1.70	1.86
59	1.00	1.63	1.77	1.88	1.60

Figure 97: Three additional hits from the MATLAB algorithm. All three proteins are strongly-stabilised at the final two adjacent temperatures, and although the TPP R script also classifies them as hits, it is possible that they are nonetheless false positives due to MATLAB's bias towards large fold changes at the final two temperatures.

6.4 Discussion

Overall, the hits from the MATLAB algorithm tend to meet the criteria for hit selection with the TPP R script. However, there are a number of key differences and potential drawbacks. Firstly, the MATLAB algorithm, whilst excellent at rejecting 'un-hit-like' matrices, tends to heavily penalise outliers and missing values. As a result, it may have a higher false negative rate than TPP. Secondly, as mentioned before, it biases in favour of matrices with large fold shifts in the final two temperatures – as a result, if the temperature range is large enough and the protein unfolding occurs in the middle of the matrix, rather than at the end, the algorithm could potentially reject it. Thus, it must be stressed that the MATLAB program was primarily designed as a complement of the TPP R script analysis, and

as a coarse screen that accepts a small number of matrices that most resemble hit-like matrices.

Following the promising results from the initial 2D TPP experiment, a number of future CETSA experiments are envisioned as a follow-up to these results. Firstly, it would be potentially interesting to perform cellular fractionation and nuclear extraction following live-cell CETSA, possibly even followed by MS analysis of both fractions, though this will by necessity double the resource cost and instrument time. Whilst the process of nuclear extraction might disrupt some of the protein complexes due to the harsh detergent present in the nuclear extraction buffer, this is done after the thermal pulse, thus secondary thermal stabilisation effects are preserved. The advantage would be greater proteome coverage and the detection of a greater number of nuclear proteins, possibly even PPARγ.

Conversely, when a fold change increase or decrease is suspected to have arisen from gene expression changes due to compound presence, rather than thermal stabilisation as a result of binding, performing the CETSA assay on a lysate instead of live cells enables to effectively act as a counter-screen. Because the lysate is static (no new protein synthesis or degradation) and, depending on the strength of the detergent, PPIs are potentially disrupted, lysate CETSA in principle only detects primary stabilisation events (and secondary, if PPIs are not disrupted), and the two are often combined[109], if resources and instrument time permit. In the case of PPARγ, it would also be possible to run a CETSA on a nuclear extract, instead of

lysate, to assay the stabilisation of nuclear components and CETSA coactivators. However, previous AlphaScren and WB data shows that there is a notable discrepancy between the PPARγ melting temperature in live cell and lysate CETSA, possibly as a consequence of other stabilisation events (metabolites or detergents). This could also skew what secondary effects are observed.

Lastly, as mentioned earlier, 3T3-L1 is not a bone cell line, therefore it makes for a poor model to study the effects of PPARγ agonism on bone. As a result, it would be interesting to try TPP using rosiglitazone on a cell line, such as the osteosarcoma cell line U2OS.

6.5 Conclusions

To conclude, PPARγ, and related NHRs make for notoriously difficult proteins to detect via MS, despite adequate detection on immunoblot. A number of methods to increase the chance of detection have been presented, and it appears that immunoprecipitation is not a valid one; by contrast, nuclear extraction followed by deep fractionation will result in some PPARγ unique peptides showing in the dataset, however, the sequence coverage never crossed the threshold of 10%. 2D-TPP was instead performed using a standard protocol, on live 3T3-L1 mouse adipocyte cells. A number of proteins were identified as possible hits, however, it looks like those proteins are more likely to be indirect stabilisers of even downstream effectors of PPARγ; nonetheless it is interesting to note that one potential hit is involved in brown fat adipogenesis, namely ARID1A.

7. Closing Remarks

The aim of this work was to investigate, evaluate and improve upon various orthogonal approaches assessing binding affinity and protein thermal stability with respect to their ability to characterise potential tool compounds and drugs. Out of the biological areas chosen for study, the first involved protein-protein interactions (PPIs), which, though previously thought "undruggable", have recently seen an uptick in the number of small molecules targeting them[299]. However, due to PPI interfaces being shallower and more featureless than ligand binding sites[300], such compounds require increased scrutiny to ensure they selectively engage their targets in a physiologically-relevant environment, rather than just being non-specific binders.

SJ-172550, described in chapter 2, is an example of a compound, which initially sparked a lot of interest due to being a first-in-class inhibitor of the MDMX-p53 interaction, and as such being potentially complementary to the MDM2-p53 inhibition that is already relatively well-established in literature and in the clinic[301]. However, subsequent analysis indicated that the compound's Michael acceptor moiety can indiscriminately covalently bind a number of nucleophilic species, including cysteine thiols, and its specificity was called into question when it was shown to label a significant portion of the proteome in an in-gel click fluorescence assay. Moreover, cellular thermal shift assay (CETSA), which was previously validated in the context of peptide-based MDMX inhibitors[100] indicated that the compound does not engage MDMX in a physiological context. This underscores

the importance of early-stage cellular target engagement assays as methods to validate tool compound candidates and, coupled with unfavourable physicochemical data that indicated SJ-172550 decomposition in basic aqueous buffers ultimately disqualified it as a potential chemical probe[184].

Chapter 3 described the development of a novel MATLAB algorithm to analyse MS output from 2D CETSA experiments, where thermal stability data is a function of both compound concentration and temperature, and acts as a proxy for compound binding. Such experiments can provide data on thousands of proteins and as a result, require post-processing to separate the true hits from the non-responders, or potential false positives. Current data post-processing involves looking at each protein as a series of 1D isothermal experiments rather than a 2D matrix, and as a result, can produce false positives. Examining hit-like matrices from public datasets, such as the 2D TPP panobinostat experiment[109], as well as the dataset obtained from looking at the cellular targets of the PRMT5 inhibitor GSK3326595, revealed that they have a number of features, such as a non-uniform increase in abundance over the temperature range dependent on compound concentration, which were used to build the algorithm. The program fits a surface, providing both a measure of stabilisation calculated as the integrated volume under the surface, as well as a measure of confidence in the form of the goodness-of-fit, and was used to successfully detect a protein stabilised by GSK3326595, which was subsequently validated by CETSA-WB. The downsides, however, include heavy penalties for outliers or bias towards surfaces with high abundance towards the end of the

temperature range and as a result, the next step in the development of the algorithm would be to refine the surface fitting model. Nonetheless, it can be used to complement current 2D TPP data analysis.

The second half of the thesis deals with the development of methods to annotate small molecules targeting the nuclear hormone receptor PPARγ. The phenotypes associated with some of these compounds include the morphological conversion of white fat to beige fat, with a concomitant increase in the expression of the uncoupling protein UCP1, making them potentially therapeutically-relevant. However, as the exact MoA of these compounds is unknown, MS-based proteomic techniques, such as CETSA would be primed towards elucidating potential off-target interactions or the formation of key PPIs as a result of compound treatment. Initially, CETSA-WB data indicated that, for a number of PPARγ agonists and antagonists, there is indeed thermal stabilisation of PPARγ in a cellular context, signifying target engagement. However, due to the general unreliability of WB for high-throughput and quantitative experiments, it was decided to develop an AlphaScreen-based dual antibody recognition readout system. Following a series of optimisation experiments, a novel approach was developed, where instead of using secondary antibodies conjugated to beads, as seen in literature[302], one antibody would be directly conjugated to the acceptor beads, whereas another would be biotinylated, to interact with donor beads conjugated to streptavidin. Initial promising data using recombinant PPARγ showed a wide assay window between heat-denatured and native protein, which was successfully replicated using

lysate from an appropriate cell model. Subsequently, the experiment was translated to live cells, where quantitative thermal stabilisation data was obtained using a number of compounds. This led to the development of a HT-CETSA screening platform, where multiple compounds could be tested at once in a microplate format. Although initially, the screen had issues pertaining to low signal to background ratio and noisy data, the next optimisation steps will focus on increasing the assay window and reducing noise by altering cell number, compound incubation and heating pulse strategies, as well as introduction of automated steps using liquid handlers to minimise human error.

Rosiglitazone, a well-studied UCP1 inducer[303] shown to stabilise PPARγ in both CETSA-WB and AlphaScreen-based CETSA, was subsequently carried forward to MS analysis via 2D TPP. Given the difficulty in detecting NHR in MS analyses, a number of strategies were put forward to try to increase PPARγ sequence coverage, including immunoprecipitation and cellular fractionation. However, in neither case were the results satisfactory, shifting the focus from PPARγ to potential off-target binders of rosiglitazone. Moreover, as formation or breaking of PPIs as a result of rosiglitazone treatment can manifest itself as apparent thermal stabilisation and destabilisation, TPP can also be used to annotate compounds in terms of their ability to alter the cellular interactome. Indeed, the appearance of Arid1a, a PPARγ interactor intimately involved in brown fat adipogenesis[296] as a hit in the 2D-CETSA indicates that rosiglitazone-induced PPARγ activation can result in the formation of PPIs that confer thermal stability onto both interacting partners.

Conversely, the destabilisation of a PPARγ repressor Maged1[292] could be indicative of a disruption of an inhibitory PPI as part of PPARγ activation. Potential future experiments to validate these hits include immunoprecipitation in the presence and absence of rosiglitazone, as well as biophysical techniques, such as BLI, on recombinant proteins to study complex formation. In addition, a number of other MS-based CETSA experiments can be delineated, such as CETSA followed by cellular fractionation to deepen the proteome pool that is explored, or CETSA on a bone cell line to explore the effects of rosiglitazone treatment on bone[283]. Taken together, these results underscore the importance of CETSA in annotating small molecules in terms of their MoA.

References

(1) Mullard, A. 2018 FDA Drug Approvals. *Nat. Rev. Drug Discov.* **2019**, *18* (2), 85–89.

(2) Hay, M.; Thomas, D. W.; Craighead, J. L.; Economides, C.; Rosenthal, J. Clinical Development Success Rates for Investigational Drugs. *Nat. Biotechnol.* **2014**, *32* (1), 40–51.

(3) Paul, S. M.; Mytelka, D. S.; Dunwiddie, C. T.; Persinger, C. C.; Munos, B. H.; Lindborg, S. R.; Schacht, A. L. How to Improve R&D Productivity: The Pharmaceutical Industry's Grand Challenge. *Nat. Rev. Drug Discov.* **2010**, *9* (3), 203–214.

(4) Arrowsmith, J. Phase II Failures: 2008–2010. *Nat. Rev. Drug Discov.* **2011**, *10* (5), 328–329.

(5) Kola, I.; Landis, J. Can the Pharmaceutical Industry Reduce Attrition Rates? *Nat. Rev. Drug Discov.* **2004**, *3* (8), 711–716.

(6) Cummings, J. L.; Morstorf, T.; Zhong, K. Alzheimer's Disease Drug-Development Pipeline: Few Candidates, Frequent Failures. *Alzheimers. Res. Ther.* **2014**, *6* (4), 37.

(7) Moellering, R. E.; Cravatt, B. F. How Chemoproteomics Can Enable Drug Discovery and Development. *Chem. Biol.* **2012**, *19* (1), 11–22.

(8) Scannell, J. W.; Bosley, J. When Quality Beats Quantity: Decision Theory, Drug Discovery, and the Reproducibility Crisis. *PLoS One* **2016**, *11* (2), e0147215.

(9) Lewis, K. Drug Tolerance, Persister Cells and Drug Discovery. In

Antimicrobial Drug Discovery: Emerging Strategies; 2012; pp 101–114.

(10) Macarron, R.; Banks, M. N.; Bojanic, D.; Burns, D. J.; Cirovic, D. A.; Garyantes, T.; S Green, D. V; Hertzberg, R. P.; Janzen, W. P.; Paslay, J. W.; Schopfer, U.; Sitta Sittampalam, G. *Impact of High-Throughput Screening in Biomedical Research*; 2011; Vol. 10.

(11) Cook, D.; Brown, D.; Alexander, R.; March, R.; Morgan, P.; Satterthwaite, G.; Pangalos, M. N. Lessons Learned from the Fate of AstraZeneca's Drug Pipeline: A Five-Dimensional Framework. *Nat. Rev. Drug Discov.* **2014**, *13* (6), 419–431.

(12) Shih, H.-P.; Zhang, X.; Aronov, A. M. Drug Discovery Effectiveness from the Standpoint of Therapeutic Mechanisms and Indications. *Nat. Publ. Gr.* **2017**.

(13) Kametani, F.; Hasegawa, M. Reconsideration of Amyloid Hypothesis and Tau Hypothesis in Alzheimer's Disease. *Front. Neurosci.* **2018**, *12* (JAN).

(14) Farese, R. V. The Nine Lives of ACAT Inhibitors. *Arterioscler. Thromb. Vasc. Biol.* **2006**, *26* (8), 1684–1686.

(15) Edwards, A. M.; Isserlin, R.; Bader, G. D.; Frye, S. V; Willson, T. M.; Yu, F. H. Too Many Roads Not Taken. *Nature* **2011**, *470* (7333), 163–165.

(16) Bunnage, M. E. Getting Pharmaceutical R&D Back on Target. *Nat. Chem. Biol.* **2011**, *7* (6), 335–339.

(17) Morgan, P.; Van Der Graaf, P. H.; Arrowsmith, J.; Feltner, D. E.; Drummond, K. S.; Wegner, C. D.; Street, S. D. A. Can the Flow of Medicines Be Improved? Fundamental Pharmacokinetic and

Pharmacological Principles toward Improving Phase II Survival. *Drug Discov. Today* **2012**, *17* (9–10), 419–424.

(18) Malyuchenko, N. V; Kotova, E. Y.; Kulaeva, O. I.; Kirpichnikov, M. P.; Studitskiy, V. M. PARP1 Inhibitors: Antitumor Drug Design. *Acta Naturae* **2015**, *7* (3), 27–37.

(19) Mateo, J.; Ong, M.; Tan, D. S. P.; Gonzalez, M. A.; de Bono, J. S. Appraising Iniparib, the PARP Inhibitor That Never Was—What Must We Learn? *Nat. Rev. Clin. Oncol.* **2013**, *10* (12), 688–696.

(20) Waring, M. J.; Arrowsmith, J.; Leach, A. R.; Leeson, P. D.; Mandrell, S.; Owen, R. M.; Pairaudeau, G.; Pennie, W. D.; Pickett, S. D.; Wang, J.; Wallace, O.; Weir, A. An Analysis of the Attrition of Drug Candidates from Four Major Pharmaceutical Companies. *Nat. Rev. Drug Discov.* **2015**, *14* (7), 475–486.

(21) Kaur, R.; Sidhu, P.; Singh, S. What Failed BIA 10-2474 Phase I Clinical Trial? Global Speculations and Recommendations for Future Phase I Trials. *J. Pharmacol. Pharmacother.* **2016**, *7* (3), 120.

(22) van Esbroeck, A. C. M.; Janssen, A. P. A.; Cognetta, A. B.; Ogasawara, D.; Shpak, G.; van der Kroeg, M.; Kantae, V.; Baggelaar, M. P.; de Vrij, F. M. S.; Deng, H.; Allarà, M.; Fezza, F.; Lin, Z.; van der Wel, T.; Soethoudt, M.; Mock, E. D.; den Dulk, H.; Baak, I. L.; Florea, B. I.; Hendriks, G.; De Petrocellis, L.; Overkleeft, H. S.; Hankemeier, T.; De Zeeuw, C. I.; Di Marzo, V.; Maccarrone, M.; Cravatt, B. F.; Kushner, S. A.; van der Stelt, M. Activity-Based Protein Profiling Reveals off-Target Proteins of the

FAAH Inhibitor BIA 10-2474. *Science* **2017**, *356* (6342), 1084–1087.

(23) Huang, Z.; Ogasawara, D.; Seneviratne, U. I.; Cognetta, A. B.; am Ende, C. W.; Nason, D. M.; Lapham, K.; Litchfield, J.; Johnson, D. S.; Cravatt, B. F. Global Portrait of Protein Targets of Metabolites of the Neurotoxic Compound BIA 10–2474. *ACS Chem. Biol.* **2019**, *14* (2), 192–197.

(24) Lin, A.; Giuliano, C. J.; Palladino, A.; John, K. M.; Abramowicz, C.; Yuan, M. Lou; Sausville, E. L.; Lukow, D. A.; Liu, L.; Chait, A. R.; Galluzzo, Z. C.; Tucker, C.; Sheltzer, J. M. Off-Target Toxicity Is a Common Mechanism of Action of Cancer Drugs Undergoing Clinical Trials. *Sci. Transl. Med.* **2019**, *11* (509), eaaw8412.

(25) Vangamudi, B.; Paul, T. A.; Shah, P. K.; Kost-Alimova, M.; Nottebaum, L.; Shi, X.; Zhan, Y.; Leo, E.; Mahadeshwar, H. S.; Protopopov, A.; Futreal, A.; Tieu, T. N.; Peoples, M.; Heffernan, T. P.; Marszalek, J. R.; Toniatti, C.; Petrocchi, A.; Verhelle, D.; Owen, D. R.; Draetta, G.; Jones, P.; Palmer, W. S.; Sharma, S.; Andersen, J. N. The SMARCA2/4 ATPase Domain Surpasses the Bromodomain as a Drug Target in SWI/SNF-Mutant Cancers: Insights from CDNA Rescue and PFI-3 Inhibitor Studies. *Cancer Res.* **2015**, *75* (18), 3865–3878.

(26) Filippakopoulos, P.; Qi, J.; Picaud, S.; Shen, Y.; Smith, W. B.; Fedorov, O.; Morse, E. M.; Keates, T.; Hickman, T. T.; Felletar, I.; Philpott, M.; Munro, S.; McKeown, M. R.; Wang, Y.; Christie, A. L.; West, N.; Cameron, M. J.; Schwartz, B.; Heightman, T. D.; La Thangue, N.; French, C. A.; Wiest, O.; Kung, A. L.; Knapp, S.; Bradner, J. E. Selective

Inhibition of BET Bromodomains. *Nature* **2010**, *468* (7327), 1067–1073.

(27) Alqahtani, A.; Choucair, K.; Ashraf, M.; Hammouda, D. M.; Alloghbi, A.; Khan, T.; Senzer, N.; Nemunaitis, J. Bromodomain and Extra-Terminal Motif Inhibitors: A Review of Preclinical and Clinical Advances in Cancer Therapy. *Futur. Sci. OA* **2019**, *5* (3), FSO372.

(28) Arrowsmith, C. H.; Audia, J. E.; Austin, C.; Baell, J.; Bennett, J.; Blagg, J.; Bountra, C.; Brennan, P. E.; Brown, P. J.; Bunnage, M. E.; Buser-Doepner, C.; Campbell, R. M.; Carter, A. J.; Cohen, P.; Copeland, R. a; Cravatt, B.; Dahlin, J. L.; Dhanak, D.; Edwards, A. M.; Frederiksen, M.; Frye, S. V; Gray, N.; Grimshaw, C. E.; Hepworth, D.; Howe, T.; Huber, K. V. M.; Jin, J.; Knapp, S.; Kotz, J. D.; Kruger, R. G.; Lowe, D.; Mader, M. M.; Marsden, B.; Mueller-Fahrnow, A.; Müller, S.; O'Hagan, R. C.; Overington, J. P.; Owen, D. R.; Rosenberg, S. H.; Roth, B.; Roth, B.; Ross, R.; Schapira, M.; Schreiber, S. L.; Shoichet, B.; Sundström, M.; Superti-Furga, G.; Taunton, J.; Toledo-Sherman, L.; Walpole, C.; Walters, M. a; Willson, T. M.; Workman, P.; Young, R. N.; Zuercher, W. J. The Promise and Peril of Chemical Probes. *Nat. Chem. Biol.* **2015**, *11* (8), 536–541.

(29) Baell, J.; Walters, M. A. Chemistry: Chemical Con Artists Foil Drug Discovery. *Nature* **2014**, *513* (7519), 481–483.

(30) Blagg, J.; Workman, P. Choose and Use Your Chemical Probe Wisely to Explore Cancer Biology. *Cancer Cell* **2017**, *32* (1), 9–25.

(31) Nelson, K. M.; Dahlin, J. L.; Bisson, J.; Graham, J.; Pauli, G. F.; Walters, M. A. The Essential Medicinal Chemistry of Curcumin. *J. Med. Chem.*

2017, *60* (5), 1620–1637.

(32) Saqib, U.; Kelley, T. T.; Panguluri, S. K.; Liu, D.; Savai, R.; Baig, M. S.; Schürer, S. C. Polypharmacology or Promiscuity? Structural Interactions of Resveratrol With Its Bandwagon of Targets. *Front. Pharmacol.* **2018**, *9*, 1201.

(33) Bhandarkar, S. S.; Bromberg, J.; Carrillo, C.; Selvakumar, P.; Sharma, R. K.; Perry, B. N.; Govindarajan, B.; Fried, L.; Sohn, A.; Reddy, K.; Arbiser, J. L. Tris (Dibenzylideneacetone) Dipalladium, a N-Myristoyltransferase-1 Inhibitor, Is Effective against Melanoma Growth In Vitro and In Vivo. *Clin. Cancer Res.* **2008**, *14* (18), 5743–5748.

(34) Kallemeijn, W. W.; Lueg, G. A.; Faronato, M.; Hadavizadeh, K.; Goya Grocin, A.; Song, O.-R.; Howell, M.; Calado, D. P.; Tate, E. W. Validation and Invalidation of Chemical Probes for the Human N-Myristoyltransferases. *Cell Chem. Biol.* **2019**, *26* (6), 892-900.e4.

(35) Kruidenier, L.; Chung, C.; Cheng, Z.; Liddle, J.; Che, K.; Joberty, G.; Bantscheff, M.; Bountra, C.; Bridges, A.; Diallo, H.; Eberhard, D.; Hutchinson, S.; Jones, E.; Katso, R.; Leveridge, M.; Mander, P. K.; Mosley, J.; Ramirez-Molina, C.; Rowland, P.; Schofield, C. J.; Sheppard, R. J.; Smith, J. E.; Swales, C.; Tanner, R.; Thomas, P.; Tumber, A.; Drewes, G.; Oppermann, U.; Patel, D. J.; Lee, K.; Wilson, D. M. A Selective Jumonji H3K27 Demethylase Inhibitor Modulates the Proinflammatory Macrophage Response. *Nature* **2012**, *488* (7411), 404–408.

(36) Niesen, F. H.; Berglund, H.; Vedadi, M. The Use of Differential Scanning Fluorimetry to Detect Ligand Interactions That Promote Protein Stability. *Nat. Protoc.* **2007**, *2* (9), 2212–2221.

(37) Alexandrov, A. I.; Mileni, M.; Chien, E. Y. T.; Hanson, M. A.; Stevens, R. C. Microscale Fluorescent Thermal Stability Assay for Membrane Proteins. *Structure* **2008**, *16* (3), 351–359.

(38) Saini, S. K.; Abualrous, E. T.; Tigan, A.-S.; Covella, K.; Wellbrock, U.; Springer, S. Not All Empty MHC Class I Molecules Are Molten Globules: Tryptophan Fluorescence Reveals a Two-Step Mechanism of Thermal Denaturation. *Mol. Immunol.* **2013**, *54* (3–4), 386–396.

(39) Ireland, S. M.; Sula, A.; Wallace, B. A. Thermal Melt Circular Dichroism Spectroscopic Studies for Identifying Stabilising Amphipathic Molecules for the Voltage-Gated Sodium Channel NavMs. *Biopolymers* **2018**, *109* (8), e23067.

(40) Desroses, M.; Busker, S.; Astorga-Wells, J.; Attarha, S.; Kolosenko, I.; Zubarev, R. A.; Helleday, T.; Grandér, D.; Page, B. D. G. STAT3 Differential Scanning Fluorimetry and Differential Scanning Light Scattering Assays: Addressing a Missing Link in the Characterization of STAT3 Inhibitor Interactions. *J. Pharm. Biomed. Anal.* **2018**, *160*, 80–88.

(41) Kroeger, T.; Frieg, B.; Zhang, T.; Hansen, F. K.; Marmann, A.; Proksch, P.; Nagel-Steger, L.; Groth, G.; Smits, S. H. J.; Gohlke, H. EDTA Aggregates Induce SYPRO Orange-Based Fluorescence in Thermal Shift Assay. *PLoS One* **2017**, *12* (5), e0177024.

(42) Basse, N.; Kaar, J. L.; Settanni, G.; Joerger, A. C.; Rutherford, T. J.; Fersht, A. R. Toward the Rational Design of P53-Stabilizing Drugs: Probing the Surface of the Oncogenic Y220C Mutant. *Chem. Biol.* **2010**, *17* (1), 46–56.

(43) Silin, V.; Plant, A. Biotechnological Applications of Surface Plasmon Resonance. *Trends Biotechnol.* **1997**, *15* (9), 353–359.

(44) Fee, C. J. Label-Free, Real-Time Interaction and Adsorption Analysis 1: Surface Plasmon Resonance; 2013; pp 287–312.

(45) Vashist, S. K.; Dixit, C. K.; MacCraith, B. D.; O'Kennedy, R. Effect of Antibody Immobilization Strategies on the Analytical Performance of a Surface Plasmon Resonance-Based Immunoassay. *Analyst* **2011**, *136* (21), 4431.

(46) Shuker, S. B.; Hajduk, P. J.; Meadows, R. P.; Fesik, S. W. Discovering High-Affinity Ligands for Proteins: SAR by NMR. *Science (80-.).* **1996**, *274* (5292), 1531–1534.

(47) Mayer, M.; Meyer, B. Characterization of Ligand Binding by Saturation Transfer Difference NMR Spectroscopy. *Angew. Chemie Int. Ed.* **1999**, *38* (12), 1784–1788.

(48) Adams, R. W.; Holroyd, C. M.; Aguilar, J. A.; Nilsson, M.; Morris, G. A. "Perfecting" WATERGATE: Clean Proton NMR Spectra from Aqueous Solution. *Chem. Commun.* **2013**, *49* (4), 358–360.

(49) Zhang, H.; Wu, Q.; Berezin, M. Y. Fluorescence Anisotropy (Polarization): From Drug Screening to Precision Medicine. *Expert Opin. Drug Discov.* **2015**, *10* (11), 1145–1161.

(50) Lea, W. A.; Simeonov, A. Fluorescence Polarization Assays in Small Molecule Screening. *Expert Opin. Drug Discov.* **2011**, *6* (1), 17–32.

(51) Lebakken, C. S.; Riddle, S. M.; Singh, U.; Frazee, W. J.; Eliason, H. C.; Gao, Y.; Reichling, L. J.; Marks, B. D.; Vogel, K. W. Development and Applications of a Broad-Coverage, TR-FRET-Based Kinase Binding Assay Platform. *J. Biomol. Screen.* **2009**, *14* (8), 924–935.

(52) Guhathakurta, P.; Prochniewicz, E.; Grant, B. D.; Peterson, K. C.; Thomas, D. D. High-Throughput Screen, Using Time-Resolved FRET, Yields Actin-Binding Compounds That Modulate Actin–Myosin Structure and Function. *J. Biol. Chem.* **2018**, *293* (31), 12288–12298.

(53) Gulick, A. M.; Bauer, C. B.; Thoden, J. B.; Rayment, I. *X-Ray Structures of the MgADP, MgATPγS, and MgAMPPNP Complexes of the Dictyostelium Discoideum Myosin Motor Domain †, ‡*; 1997.

(54) Danley, D. E. Crystallization to Obtain Protein–Ligand Complexes for Structure-Aided Drug Design. *Acta Crystallogr. Sect. D Biol. Crystallogr.* **2006**, *62* (6), 569–575.

(55) Hassell, A. M.; An, G.; Bledsoe, R. K.; Bynum, J. M.; Carter, H. L.; Deng, S.-J. J.; Gampe, R. T.; Grisard, T. E.; Madauss, K. P.; Nolte, R. T.; Rocque, W. J.; Wang, L.; Weaver, K. L.; Williams, S. P.; Wisely, G. B.; Xu, R.; Shewchuk, L. M. Crystallization of Protein-Ligand Complexes. *Acta Crystallogr. D. Biol. Crystallogr.* **2007**, *63* (Pt 1), 72–79.

(56) Swinney, D. C.; Anthony, J. How Were New Medicines Discovered? *Nat. Rev. Drug Discov.* **2011**, *10* (7), 507–519.

(57) Dubach, J. M.; Vinegoni, C.; Mazitschek, R.; Fumene Feruglio, P.; Cameron, L. A.; Weissleder, R. In Vivo Imaging of Specific Drug–Target Binding at Subcellular Resolution. *Nat. Commun.* **2014**, *5* (1), 3946.

(58) Dubach, J. M.; Kim, E.; Yang, K.; Cuccarese, M.; Giedt, R. J.; Meimetis, L. G.; Vinegoni, C.; Weissleder, R. Quantitating Drug-Target Engagement in Single Cells in Vitro and in Vivo. *Nat. Chem. Biol.* **2017**, *13* (2), 168–173.

(59) England, C. G.; Ehlerding, E. B.; Cai, W. NanoLuc: A Small Luciferase Is Brightening Up the Field of Bioluminescence. *Bioconjug. Chem.* **2016**, *27* (5), 1175–1187.

(60) Machleidt, T.; Woodroofe, C. C.; Schwinn, M. K.; Méndez, J.; Robers, M. B.; Zimmerman, K.; Otto, P.; Daniels, D. L.; Kirkland, T. A.; Wood, K. V. NanoBRET—A Novel BRET Platform for the Analysis of Protein–Protein Interactions. *ACS Chem. Biol.* **2015**, *10* (8), 1797–1804.

(61) Robers, M. B.; Dart, M. L.; Woodroofe, C. C.; Zimprich, C. A.; Kirkland, T. A.; Machleidt, T.; Kupcho, K. R.; Levin, S.; Hartnett, J. R.; Zimmerman, K.; Niles, A. L.; Ohana, R. F.; Daniels, D. L.; Slater, M.; Wood, M. G.; Cong, M.; Cheng, Y.-Q.; Wood, K. V. Target Engagement and Drug Residence Time Can Be Observed in Living Cells with BRET. *Nat. Commun.* **2015**, *6* (1), 10091.

(62) Vasta, J. D.; Corona, C. R.; Wilkinson, J.; Zimprich, C. A.; Hartnett, J. R.; Ingold, M. R.; Zimmerman, K.; Machleidt, T.; Kirkland, T. A.; Huwiler, K. G.; Ohana, R. F.; Slater, M.; Otto, P.; Cong, M.; Wells, C. I.; Berger, B.-T.;

Hanke, T.; Glas, C.; Ding, K.; Drewry, D. H.; Huber, K. V. M.; Willson, T. M.; Knapp, S.; Müller, S.; Meisenheimer, P. L.; Fan, F.; Wood, K. V.; Robers, M. B. Quantitative, Wide-Spectrum Kinase Profiling in Live Cells for Assessing the Effect of Cellular ATP on Target Engagement. *Cell Chem. Biol.* **2018**, *25* (2), 206-214.e11.

(63) Eder, J.; Sedrani, R.; Wiesmann, C. The Discovery of First-in-Class Drugs: Origins and Evolution. *Nat. Rev. Drug Discov.* **2014**, *13* (8), 577–587.

(64) Bickle, M. The Beautiful Cell: High-Content Screening in Drug Discovery. *Anal. Bioanal. Chem.* **2010**, *398* (1), 219–226.

(65) Bray, M.-A.; Singh, S.; Han, H.; Davis, C. T.; Borgeson, B.; Hartland, C.; Kost-Alimova, M.; Gustafsdottir, S. M.; Gibson, C. C.; Carpenter, A. E. Cell Painting, a High-Content Image-Based Assay for Morphological Profiling Using Multiplexed Fluorescent Dyes. *Nat. Protoc.* **2016**, *11* (9), 1757–1774.

(66) Kolla, L.; Heo, D. S.; Rosenberg, D. P.; Barlow, S. A.; Maximova, A. A.; Cassio, E. E.; Buchser, W. J. High Content Screen for Identifying Small-Molecule LC3B-Localization Modulators in a Renal Cancer Cell Line. *Sci. Data* **2018**, *5* (1), 180116.

(67) Martin, D. D. O.; Kanuparthi, P. S.; Holland, S. M.; Sanders, S. S.; Jeong, H.-K.; Einarson, M. B.; Jacobson, M. A.; Thomas, G. M. Identification of Novel Inhibitors of DLK Palmitoylation and Signaling by High Content Screening. *Sci. Rep.* **2019**, *9* (1), 3632.

(68) Reggio, A.; Spada, F.; Rosina, M.; Massacci, G.; Zuccotti, A.; Fuoco, C.;

Gargioli, C.; Castagnoli, L.; Cesareni, G. The Immunosuppressant Drug Azathioprine Restrains Adipogenesis of Muscle Fibro/Adipogenic Progenitors from Dystrophic Mice by Affecting AKT Signaling. *Sci. Rep.* **2019**, *9* (1), 4360.

(69) Tolosa, L.; Gómez-Lechón, M. J.; Donato, M. T. High-Content Screening Technology for Studying Drug-Induced Hepatotoxicity in Cell Models. *Arch. Toxicol.* **2015**, *89* (7), 1007–1022.

(70) Fenn, J. B. Electrospray Wings for Molecular Elephants (Nobel Lecture). *Angew. Chemie Int. Ed.* **2003**, *42* (33), 3871–3894.

(71) Wilm, M.; Shevchenko, A.; Houthaeve, T.; Breit, S.; Schweigerer, L.; Fotsis, T.; Mann, M. Femtomole Sequencing of Proteins from Polyacrylamide Gels by Nano-Electrospray Mass Spectrometry. *Nature* **1996**, *379* (6564), 466–469.

(72) Henderson, R.; Michel, H.; Sakaguchi, K.; Shabanowitz, J.; Appella, E.; Hunt, D.; Engelhard, V. HLA-A2.1-Associated Peptides from a Mutant Cell Line: A Second Pathway of Antigen Presentation. *Science (80-.).* **1992**, *255* (5049), 1264–1266.

(73) Henzel, W. J.; Billeci, T. M.; Stults, J. T.; Wong, S. C.; Grimley, C.; Watanabe, C. Identifying Proteins from Two-Dimensional Gels by Molecular Mass Searching of Peptide Fragments in Protein Sequence Databases. *Proc. Natl. Acad. Sci.* **1993**, *90* (11), 5011–5015.

(74) Yates, J. R.; Eng, J. K.; McCormack, A. L.; Schieltz, D. Method to Correlate Tandem Mass Spectra of Modified Peptides to Amino Acid

Sequences in the Protein Database. *Anal. Chem.* **1995**, *67* (8), 1426–1436.

(75) Yates, J. R.; Eng, J. K.; Clauser, K. R.; Burlingame, A. L. Search of Sequence Databases with Uninterpreted High-Energy Collision-Induced Dissociation Spectra of Peptides. *J. Am. Soc. Mass Spectrom.* **1996**, *7* (11), 1089–1098.

(76) Jonscher, K. R.; Yates, J. R. The Quadrupole Ion Trap Mass Spectrometer—A Small Solution to a Big Challenge. *Anal. Biochem.* **1997**, *244* (1), 1–15.

(77) Ducret, A.; Oostveen, I. Van; Eng, J. K.; Yates, J. R.; Aebersold, R. High Throughput Protein Characterization by Automated Reverse-Phase Chromatography/Electrospray Tandem Mass Spectrometry. *Protein Sci.* **1998**, *7* (3), 706–719.

(78) Hebert, A. S.; Richards, A. L.; Bailey, D. J.; Ulbrich, A.; Coughlin, E. E.; Westphall, M. S.; Coon, J. J. The One Hour Yeast Proteome. *Mol. Cell. Proteomics* **2014**, *13* (1), 339–347.

(79) Wilhelm, M.; Schlegl, J.; Hahne, H.; Gholami, A. M.; Lieberenz, M.; Savitski, M. M.; Ziegler, E.; Butzmann, L.; Gessulat, S.; Marx, H.; Mathieson, T.; Lemeer, S.; Schnatbaum, K.; Reimer, U.; Wenschuh, H.; Mollenhauer, M.; Slotta-Huspenina, J.; Boese, J.-H.; Bantscheff, M.; Gerstmair, A.; Faerber, F.; Kuster, B. Mass-Spectrometry-Based Draft of the Human Proteome. *Nature* **2014**, *509* (7502), 582–587.

(80) Ong, S.-E.; Blagoev, B.; Kratchmarova, I.; Kristensen, D. B.; Steen, H.; Pandey, A.; Mann, M. Stable Isotope Labeling by Amino Acids in Cell

Culture, SILAC, as a Simple and Accurate Approach to Expression Proteomics. *Mol. Cell. Proteomics* **2002**, *1* (5), 376–386.

(81) Rauniyar, N.; Yates, J. R. Isobaric Labeling-Based Relative Quantification in Shotgun Proteomics. *J. Proteome Res.* **2014**, *13* (12), 5293–5309.

(82) Song, D.; Chaerkady, R.; Tan, A. C.; García-García, E.; Nalli, A.; Suárez-Gauthier, A.; López-Ríos, F.; Zhang, X. F.; Solomon, A.; Tong, J.; Read, M.; Fritz, C.; Jimeno, A.; Pandey, A.; Hidalgo, M. Antitumor Activity and Molecular Effects of the Novel Heat Shock Protein 90 Inhibitor, IPI-504, in Pancreatic Cancer. *Mol. Cancer Ther.* **2008**, *7* (10), 3275–3284.

(83) Zhang, J.; Sui, J.; Ching, C. B.; Chen, W. N. Protein Profile in Neuroblastoma Cells Incubated WithS- AndR-Enantiomers of Ibuprofen by ITRAQ-Coupled 2-D LC-MS/MS Analysis: Possible Action of Induced Proteins on Alzheimer's Disease. *Proteomics* **2008**, *8* (8), 1595–1607.

(84) Bermúdez, V.; Finol, F.; Parra, N.; Parra, M.; Pérez, A.; Peñaranda, L.; Vílchez, D.; Rojas, J.; Arráiz, N.; Velasco, M. PPAR-γ Agonists and Their Role in Type 2 Diabetes Mellitus Management. *Am. J. Ther.* **2010**, *17* (3), 274–283.

(85) Nissen, S. E.; Wolski, K. Effect of Rosiglitazone on the Risk of Myocardial Infarction and Death from Cardiovascular Causes. *N. Engl. J. Med.* **2007**, *356* (24), 2457–2471.

(86) Hoffmann, B. R.; El-Mansy, M. F.; Sem, D. S.; Greene, A. S. Chemical Proteomics-Based Analysis of off-Target Binding Profiles for Rosiglitazone and Pioglitazone: Clues for Assessing Potential for

Cardiotoxicity. *J. Med. Chem.* **2012**, *55* (19), 8260–8271.

(87) Ito, T.; Ando, H.; Suzuki, T.; Ogura, T.; Hotta, K.; Imamura, Y.; Yamaguchi, Y.; Handa, H. Identification of a Primary Target of Thalidomide Teratogenicity. *Science* **2010**, *327* (5971), 1345–1350.

(88) Bantscheff, M.; Eberhard, D.; Abraham, Y.; Bastuck, S.; Boesche, M.; Hobson, S.; Mathieson, T.; Perrin, J.; Raida, M.; Rau, C.; Reader, V.; Sweetman, G.; Bauer, A.; Bouwmeester, T.; Hopf, C.; Kruse, U.; Neubauer, G.; Ramsden, N.; Rick, J.; Kuster, B.; Drewes, G. Quantitative Chemical Proteomics Reveals Mechanisms of Action of Clinical ABL Kinase Inhibitors. *Nat. Biotechnol.* **2007**, *25* (9), 1035–1044.

(89) Médard, G.; Pachl, F.; Ruprecht, B.; Klaeger, S.; Heinzlmeir, S.; Helm, D.; Qiao, H.; Ku, X.; Wilhelm, M.; Kuehne, T.; Wu, Z.; Dittmann, A.; Hopf, C.; Kramer, K.; Kuster, B. Optimized Chemical Proteomics Assay for Kinase Inhibitor Profiling. *J. Proteome Res.* **2015**, *14* (3), 1574–1586.

(90) Liang, L.; Astruc, D. The Copper(I)-Catalyzed Alkyne-Azide Cycloaddition (CuAAC) “Click” Reaction and Its Applications. An Overview. *Coord. Chem. Rev.* **2011**, *255* (23–24), 2933–2945.

(91) Presolski, S. I.; Hong, V. P.; Finn, M. G. Copper-Catalyzed Azide-Alkyne Click Chemistry for Bioconjugation. *Curr. Protoc. Chem. Biol.* **2011**, *3* (4), 153–162.

(92) Ward, J. A.; McLellan, L.; Stockley, M.; Gibson, K. R.; Whitlock, G. A.; Knights, C.; Harrigan, J. A.; Jacq, X.; Tate, E. W. Quantitative Chemical Proteomic Profiling of Ubiquitin Specific Proteases in Intact Cancer Cells.

ACS Chem. Biol. **2016**, *11* (12), 3268–3272.

(93) Shi, H.; Cheng, X.; Sze, S. K.; Yao, S. Q. Proteome Profiling Reveals Potential Cellular Targets of Staurosporine Using a Clickable Cell-Permeable Probe. *Chem. Commun.* **2011**, *47* (40), 11306.

(94) Shi, H.; Zhang, C.-J.; Chen, G. Y. J.; Yao, S. Q. Cell-Based Proteome Profiling of Potential Dasatinib Targets by Use of Affinity-Based Probes. *J. Am. Chem. Soc.* **2012**, *134* (6), 3001–3014.

(95) Li, Z.; Hao, P.; Li, L.; Tan, C. Y. J.; Cheng, X.; Chen, G. Y. J.; Sze, S. K.; Shen, H.-M.; Yao, S. Q. Design and Synthesis of Minimalist Terminal Alkyne-Containing Diazirine Photo-Crosslinkers and Their Incorporation into Kinase Inhibitors for Cell- and Tissue-Based Proteome Profiling. *Angew. Chemie Int. Ed.* **2013**, *52* (33), 8551–8556.

(96) Guo, C.; Chang, Y.; Wang, X.; Zhang, C.; Hao, P.; Ding, K.; Li, Z. Minimalist Linkers Suitable for Irreversible Inhibitors in Simultaneous Proteome Profiling, Live-Cell Imaging and Drug Screening. *Chem. Commun.* **2019**, *55* (6), 834–837.

(97) Shrimp, J. H.; Sorum, A. W.; Garlick, J. M.; Guasch, L.; Nicklaus, M. C.; Meier, J. L. Characterizing the Covalent Targets of a Small Molecule Inhibitor of the Lysine Acetyltransferase P300. *ACS Med. Chem. Lett.* **2016**, *7* (2), 151–155.

(98) Jafari, R.; Almqvist, H.; Axelsson, H.; Ignatushchenko, M.; Lundbäck, T.; Nordlund, P.; Molina, D. M. The Cellular Thermal Shift Assay for Evaluating Drug Target Interactions in Cells. *Nat. Protoc.* **2014**, *9* (9),

2100–2122.

(99) Molina, D. M.; Jafari, R.; Ignatushchenko, M.; Seki, T.; Larsson, E. A.; Dan, C.; Sreekumar, L.; Cao, Y.; Nordlund, P. Monitoring Drug Target Engagement in Cells and Tissues Using the Cellular Thermal Shift Assay. *Science (80-.).* **2013**, *341* (6141), 84–87.

(100) Tan, B. X.; Brown, C. J.; Ferrer, F. J.; Yuen, T. Y.; Quah, S. T.; Chan, B. H.; Jansson, A. E.; Teo, H. L.; Nordlund, P.; Lane, D. P. Assessing the Efficacy of Mdm2/Mdm4-Inhibiting Stapled Peptides Using Cellular Thermal Shift Assays. *Sci. Rep.* **2015**, *5* (1), 12116.

(101) Alshareef, A.; Zhang, H.-F.; Huang, Y.-H.; Wu, C.; Zhang, J. D.; Wang, P.; El-Sehemy, A.; Fares, M.; Lai, R. The Use of Cellular Thermal Shift Assay (CETSA) to Study Crizotinib Resistance in ALK-Expressing Human Cancers. *Sci. Rep.* **2016**, *6* (1), 33710.

(102) Bai, L.; Chen, J.; McEachern, D.; Liu, L.; Zhou, H.; Aguilar, A.; Wang, S. BM-1197: A Novel and Specific Bcl-2/Bcl-XL Inhibitor Inducing Complete and Long-Lasting Tumor Regression in Vivo. *PLoS One* **2014**, *9* (6), e99404.

(103) Zhu, D.; Guo, H.; Chang, Y.; Ni, Y.; Li, L.; Zhang, Z.-M.; Hao, P.; Xu, Y.; Ding, K.; Li, Z. Cell- and Tissue-Based Proteome Profiling and Dual Imaging of Apoptosis Markers with Probes Derived from Venetoclax and Idasanutlin. *Angew. Chemie Int. Ed.* **2018**, *57* (30), 9284–9289.

(104) Savitski, M. M.; Reinhard, F. B. M.; Franken, H.; Werner, T.; Savitski, M. F.; Eberhard, D.; Molina, D. M.; Jafari, R.; Dovega, R. B.; Klaeger, S.;

Kuster, B.; Nordlund, P.; Bantscheff, M.; Drewes, G. Tracking Cancer Drugs in Living Cells by Thermal Profiling of the Proteome. *Science (80-.).* **2014**, *346* (6205), 1255784.

(105) Huber, K. V. M.; Olek, K. M.; Müller, A. C.; Tan, C. S. H.; Bennett, K. L.; Colinge, J.; Superti-Furga, G. Proteome-Wide Drug and Metabolite Interaction Mapping by Thermal-Stability Profiling. *Nat. Methods* **2015**, *12* (11), 1055–1057.

(106) Dziekan, J. M.; Yu, H.; Chen, D.; Dai, L.; Wirjanata, G.; Larsson, A.; Prabhu, N.; Sobota, R. M.; Bozdech, Z.; Nordlund, P. Identifying Purine Nucleoside Phosphorylase as the Target of Quinine Using Cellular Thermal Shift Assay. *Sci. Transl. Med.* **2019**, *11* (473), eaau3174.

(107) Franken, H.; Mathieson, T.; Childs, D.; Sweetman, G. M. A.; Werner, T.; Tögel, I.; Doce, C.; Gade, S.; Bantscheff, M.; Drewes, G.; Reinhard, F. B. M.; Huber, W.; Savitski, M. M. Thermal Proteome Profiling for Unbiased Identification of Direct and Indirect Drug Targets Using Multiplexed Quantitative Mass Spectrometry. *Nat. Protoc.* **2015**, *10* (10), 1567–1593.

(108) Miettinen, T. P.; Peltier, J.; Härtlova, A.; Gierliński, M.; Jansen, V. M.; Trost, M.; Björklund, M. Thermal Proteome Profiling of Breast Cancer Cells Reveals Proteasomal Activation by CDK4/6 Inhibitor Palbociclib. *EMBO J.* **2018**, *37* (10), 8–10.

(109) Becher, I.; Werner, T.; Doce, C.; Zaal, E. A.; Tögel, I.; Khan, C. A.; Rueger, A.; Muelbaier, M.; Salzer, E.; Berkers, C. R.; Fitzpatrick, P. F.; Bantscheff, M.; Savitski, M. M. Thermal Profiling Reveals Phenylalanine

Hydroxylase as an Off-Target of Panobinostat. *Nat. Chem. Biol.* **2016**, *12* (11), 908–910.

(110) Gilda, J. E.; Ghosh, R.; Cheah, J. X.; West, T. M.; Bodine, S. C.; Gomes, A. V. Western Blotting Inaccuracies with Unverified Antibodies: Need for a Western Blotting Minimal Reporting Standard (WBMRS). *PLoS One* **2015**, *10* (8), e0135392.

(111) Butler, T. A. J.; Paul, J. W.; Chan, E.-C.; Smith, R.; Tolosa, J. M. Misleading Westerns: Common Quantification Mistakes in Western Blot Densitometry and Proposed Corrective Measures. *Biomed Res. Int.* **2019**, *2019*, 1–15.

(112) McNulty, D. E.; Bonnette, W. G.; Qi, H.; Wang, L.; Ho, T. F.; Waszkiewicz, A.; Kallal, L. A.; Nagarajan, R. P.; Stern, M.; Quinn, A. M.; Creasy, C. L.; Su, D.-S.; Graves, A. P.; Annan, R. S.; Sweitzer, S. M.; Holbert, M. A. A High-Throughput Dose-Response Cellular Thermal Shift Assay for Rapid Screening of Drug Target Engagement in Living Cells, Exemplified Using SMYD3 and IDO1. *SLAS Discov. Adv. Life Sci. R&D* **2018**, *23* (1), 34–46.

(113) Martinez, N. J.; Asawa, R. R.; Cyr, M. G.; Zakharov, A.; Urban, D. J.; Roth, J. S.; Wallgren, E.; Klumpp-Thomas, C.; Coussens, N. P.; Rai, G.; Yang, S.-M.; Hall, M. D.; Marugan, J. J.; Simeonov, A.; Henderson, M. J. A Widely-Applicable High-Throughput Cellular Thermal Shift Assay (CETSA) Using Split Nano Luciferase. *Sci. Rep.* **2018**, *8* (1), 9472.

(114) Ullman, E. F.; Kirakossian, H.; Singh, S.; Wu, Z. P.; Irvin, B. R.; Pease, J.

S.; Switchenko, A. C.; Irvine, J. D.; Dafforn, A.; Skold, C. N. Luminescent Oxygen Channeling Immunoassay: Measurement of Particle Binding Kinetics by Chemiluminescence. *Proc. Natl. Acad. Sci.* **1994**, *91* (12), 5426–5430.

(115) Almqvist, H.; Axelsson, H.; Jafari, R.; Dan, C.; Mateus, A.; Haraldsson, M.; Larsson, A.; Molina, D. M.; Artursson, P.; Lundbäck, T.; Nordlund, P. CETSA Screening Identifies Known and Novel Thymidylate Synthase Inhibitors and Slow Intracellular Activation of 5-Fluorouracil. *Nat. Commun.* **2016**, *7*.

(116) Shaw, J.; Leveridge, M.; Norling, C.; Karén, J.; Molina, D. M.; O'Neill, D.; Dowling, J. E.; Davey, P.; Cowan, S.; Dabrowski, M.; Main, M.; Gianni, D. Determining Direct Binders of the Androgen Receptor Using a High-Throughput Cellular Thermal Shift Assay. *Sci. Rep.* **2018**, *8* (1), 163.

(117) Linzer, D. I. H.; Levine, A. J. Characterization of a 54K Dalton Cellular SV40 Tumor Antigen Present in SV40-Transformed Cells and Uninfected Embryonal Carcinoma Cells. *Cell* **1979**, *17* (1), 43–52.

(118) Lane, D. P.; Crawford, L. V. T Antigen Is Bound to a Host Protein in SV40-Transformed Cells. *Nature* **1979**, *278* (5701), 261–263.

(119) Lane, D. P. P53, Guardian of the Genome. *Nature* **1992**, *358* (6381), 15–16.

(120) Kubbutat, M. H. G.; Jones, S. N.; Vousden, K. H. Regulation of P53 Stability by Mdm2. *Nature* **1997**, *387* (6630), 299–303.

(121) Maltzman, W.; Czyzyk, L. UV Irradiation Stimulates Levels of P53

Cellular Tumor Antigen in Nontransformed Mouse Cells. *Mol. Cell. Biol.* **1984**, *4* (9), 1689–1694.

(122) Zhang, Y.; Lu, H. Signaling to P53: Ribosomal Proteins Find Their Way. *Cancer Cell* **2009**, *16* (5), 369–377.

(123) Koumenis, C.; Alarcon, R.; Hammond, E.; Sutphin, P.; Hoffman, W.; Murphy, M.; Derr, J.; Taya, Y.; Lowe, S. W.; Kastan, M.; Giaccia, A. Regulation of P53 by Hypoxia: Dissociation of Transcriptional Repression and Apoptosis from P53-Dependent Transactivation. *Mol. Cell. Biol.* **2001**, *21* (4), 1297–1310.

(124) Imamura, K.; Ogura, T.; Kishimoto, A.; Kaminishi, M.; Esumi, H. Cell Cycle Regulation via P53 Phosphorylation by a 5′-AMP Activated Protein Kinase Activator, 5-Aminoimidazole-4-Carboxamide-1-β-D-Ribofuranoside, in a Human Hepatocellular Carcinoma Cell Line. *Biochem. Biophys. Res. Commun.* **2001**, *287* (2), 562–567.

(125) El-Deiry, W. S.; Kern, S. E.; Pietenpol, J. A.; Kinzler, K. W.; Vogelstein, B. Definition of a Consensus Binding Site for P53. *Nat. Genet.* **1992**, *1* (1), 45–49.

(126) Farmer, G.; Bargonetti, J.; Zhu, H.; Friedman, P.; Prywes, R.; Prives, C. Wild-Type P53 Activates Transcription in Vitro. *Nature* **1992**, *358* (6381), 83–86.

(127) El-Deiry, W. WAF1, a Potential Mediator of P53 Tumor Suppression. *Cell* **1993**, *75* (4), 817–825.

(128) Bunz, F.; Dutriaux, A.; Lengauer, C.; Waldman, T.; Zhou, S.; Brown, J. P.;

Sedivy, J. M.; Kinzler, K. W.; Vogelstein, B. Requirement for P53 and P21 to Sustain G2 Arrest after DNA Damage. *Science (80-.).* **1998**, *282* (5393), 1497–1501.

(129) Fei, P.; Bernhard, E. J.; El-Deiry, W. S. Tissue-Specific Induction of P53 Targets in Vivo. *Cancer Res.* **2002**, *62* (24), 7316–7327.

(130) Ventura, A.; Kirsch, D. G.; McLaughlin, M. E.; Tuveson, D. A.; Grimm, J.; Lintault, L.; Newman, J.; Reczek, E. E.; Weissleder, R.; Jacks, T. Restoration of P53 Function Leads to Tumour Regression in Vivo. *Nature* **2007**, *445* (7128), 661–665.

(131) Williams, A. B.; Schumacher, B. P53 in the DNA-Damage-Repair Process. *Cold Spring Harb. Perspect. Med.* **2016**, *6* (5), a026070.

(132) Tan, M.; Li, S.; Swaroop, M.; Guan, K.; Oberley, L. W.; Sun, Y. Transcriptional Activation of the Human Glutathione Peroxidase Promoter by P53. *J. Biol. Chem.* **1999**, *274* (17), 12061–12066.

(133) Schwartzenberg-Bar-Yoseph, F.; Armoni, M.; Karnieli, E. The Tumor Suppressor P53 Down-Regulates Glucose Transporters GLUT1 and GLUT4 Gene Expression. *Cancer Res.* **2004**, *64* (7), 2627–2633.

(134) Feng, Z.; Levine, A. J. The Regulation of Energy Metabolism and the IGF-1/MTOR Pathways by the P53 Protein. *Trends Cell Biol.* **2010**, *20* (7), 427–434.

(135) Cho, Y.; Gorina, S.; Jeffrey, P.; Pavletich, N. Crystal Structure of a P53 Tumor Suppressor-DNA Complex: Understanding Tumorigenic Mutations. *Science (80-.).* **1994**, *265* (5170), 346–355.

(136) Soussi, T.; Lozano, G. P53 Mutation Heterogeneity in Cancer. *Biochem. Biophys. Res. Commun.* **2005**, *331* (3), 834–842.

(137) Dittmer, D.; Pati, S.; Zambetti, G.; Chu, S.; Teresky, A. K.; Moore, M.; Finlay, C.; Levine, A. J. Gain of Function Mutations in P53. *Nat. Genet.* **1993**, *4* (1), 42–46.

(138) Chan, W. M.; Siu, W. Y.; Lau, A.; Poon, R. Y. C. How Many Mutant P53 Molecules Are Needed To Inactivate a Tetramer? *Mol. Cell. Biol.* **2004**, *24* (8), 3536–3551.

(139) Sabapathy, K. The Contrived Mutant P53 Oncogene – Beyond Loss of Functions. *Front. Oncol.* **2015**, *5* (DEC).

(140) Kim, M. P.; Lozano, G. Mutant P53 Partners in Crime. *Cell Death Differ.* **2018**, *25* (1), 161–168.

(141) Momand, J.; Zambetti, G. P.; Olson, D. C.; George, D.; Levine, A. J. The Mdm-2 Oncogene Product Forms a Complex with the P53 Protein and Inhibits P53-Mediated Transactivation. *Cell* **1992**, *69* (7), 1237–1245.

(142) Fang, S.; Jensen, J. P.; Ludwig, R. L.; Vousden, K. H.; Weissman, A. M. Mdm2 Is a RING Finger-Dependent Ubiquitin Protein Ligase for Itself and P53. *J. Biol. Chem.* **2000**, *275* (12), 8945–8951.

(143) Haupt, Y.; Maya, R.; Kazaz, A.; Oren, M. Mdm2 Promotes the Rapid Degradation of P53. *Nature* **1997**, *387* (6630), 296–299.

(144) Momand, J. The MDM2 Gene Amplification Database. *Nucleic Acids Res.* **1998**, *26* (15), 3453–3459.

(145) Florenes, V. A.; Maelandsmo, G. M.; Forus, A.; Andreassen, A.;

Myklebost, O.; Fodstad, O. MDM2 Gene Amplification and Transcript Levels in Human Sarcomas: Relationship to TP53 Gene Status. *JNCI J. Natl. Cancer Inst.* **1994**, *86* (17), 1297–1302.

(146) Bond, G. L.; Hirshfield, K. M.; Kirchhoff, T.; Alexe, G.; Bond, E. E.; Robins, H.; Bartel, F.; Taubert, H.; Wuerl, P.; Hait, W.; Toppmeyer, D.; Offit, K.; Levine, A. J. MDM2 SNP309 Accelerates Tumor Formation in a Gender-Specific and Hormone-Dependent Manner. *Cancer Res.* **2006**, *66* (10), 5104–5110.

(147) Araki, S.; Eitel, J. A.; Batuello, C. N.; Bijangi-Vishehsaraei, K.; Xie, X.-J.; Danielpour, D.; Pollok, K. E.; Boothman, D. A.; Mayo, L. D. TGF-B1–Induced Expression of Human Mdm2 Correlates with Late-Stage Metastatic Breast Cancer. *J. Clin. Invest.* **2010**, *120* (1), 290–302.

(148) Shvarts, A.; Steegenga, W. T.; Riteco, N.; Van Laar, T.; Dekker, P.; Bazuine, M.; Van Ham, R. C. A.; Van Der Houven Van Oordt, W.; Hateboer, G.; Van Der Eb, A. J.; Jochemsen, A. G. MDMX: A Novel P53-Binding Protein with Some Functional Properties of MDM2. **1996**, *15* (19), 5349–5357.

(149) Momand, J.; Villegas, A.; Belyi, V. A. The Evolution of MDM2 Family Genes. *Gene* **2011**, *486* (1–2), 23–30.

(150) Tanimura, S.; Ohtsuka, S.; Mitsui, K.; Shirouzu, K.; Yoshimura, A.; Ohtsubo, M. MDM2 Interacts with MDMX through Their RING Finger Domains. *FEBS Lett.* **1999**, *447* (1), 5–9.

(151) Linares, L. K.; Hengstermann, A.; Ciechanover, A.; Muller, S.; Scheffner,

M. HdmX Stimulates Hdm2-Mediated Ubiquitination and Degradation of P53. *Proc. Natl. Acad. Sci.* **2003**, *100* (21), 12009–12014.

(152) Riemenschneider, M. J.; Büschges, R.; Wolter, M.; Reifenberger, J.; Boström, J.; Kraus, J. A.; Schlegel, U.; Reifenberger, G. Amplification and Overexpression of the MDM4 (MDMX) Gene from 1q32 in a Subset of Malignant Gliomas without TP53 Mutation or MDM2 Amplification. *Cancer Res.* **1999**, *59* (24), 6091–6096.

(153) Liang, M.; Han, X.; Vadhan-Raj, S.; Nguyen, M.; Zhang, Y. H.; Fernandez, M.; Drakos, E.; Konoplev, S. N.; Yin, C. C.; Miranda, R. N.; McDonnell, T. J.; Medeiros, L. J.; Bueso-Ramos, C. E. HDM4 Is Overexpressed in Mantle Cell Lymphoma and Its Inhibition Induces P21 Expression and Apoptosis. *Mod. Pathol.* **2010**, *23* (3), 381–391.

(154) Böttger, V.; Böttger, A.; Garcia-Echeverria, C.; Ramos, Y. F.; van der Eb, A. J.; Jochemsen, A. G.; Lane, D. P. Comparative Study of the P53-Mdm2 and P53-MDMX Interfaces. *Oncogene* **1999**, *18* (1), 189–199.

(155) Kussie, P. H.; Gorina, S.; Marechal, V.; Elenbaas, B.; Moreau, J.; Levine, A. J.; Pavletich, N. P. Structure of the MDM2 Oncoprotein Bound to the P53 Tumor Suppressor Transactivation Domain. *Science (80-.).* **1996**, *274* (5289), 948–953.

(156) Borcherds, W.; Theillet, F.-X.; Katzer, A.; Finzel, A.; Mishall, K. M.; Powell, A. T.; Wu, H.; Manieri, W.; Dieterich, C.; Selenko, P.; Loewer, A.; Daughdrill, G. W. Disorder and Residual Helicity Alter P53-Mdm2 Binding Affinity and Signaling in Cells. *Nat. Chem. Biol.* **2014**, *10* (12),

1000–1002.

(157) Wasylyk, C.; Salvi, R.; Argentini, M.; Dureuil, C.; Delumeau, I.; Abecassis, J.; Debussche, L.; Wasylyk, B. P53 Mediated Death of Cells Overexpressing MDM2 by an Inhibitor of MDM2 Interaction with P53. *Oncogene* **1999**, *18* (11), 1921–1934.

(158) Chène, P.; Fuchs, J.; Carena, I.; Furet, P.; García-Echeverría, C. Study of the Cytotoxic Effect of a Peptidic Inhibitor of the P53-Hdm2 Interaction in Tumor Cells. *FEBS Lett.* **2002**, *529* (2–3), 293–297.

(159) Hardcastle, I. R.; Ahmed, S. U.; Atkins, H.; Farnie, G.; Golding, B. T.; Griffin, R. J.; Guyenne, S.; Hutton, C.; Källblad, P.; Kemp, S. J.; Kitching, M. S.; Newell, D. R.; Norbedo, S.; Northen, J. S.; Reid, R. J.; Saravanan, K.; Willems, H. M. G.; Lunec, J. Small-Molecule Inhibitors of the MDM2-P53 Protein-Protein Interaction Based on an Isoindolinone Scaffold. *J. Med. Chem.* **2006**, *49* (21), 6209–6221.

(160) Ding, Q.; Zhang, Z.; Liu, J.; Jiang, N.; Zhang, J.; Ross, T. M.; Chu, X.; Bartkovitz, D.; Podlaski, F.; Janson, C.; Tovar, C.; Filipovic, Z. M.; Higgins, B.; Glenn, K.; Packman, K.; Vassilev, L. T.; Graves, B. Discovery of RG7388, a Potent and Selective P53–MDM2 Inhibitor in Clinical Development. *J. Med. Chem.* **2013**, *56* (14), 5979–5983.

(161) Sun, D.; Li, Z.; Rew, Y.; Gribble, M.; Bartberger, M. D.; Beck, H. P.; Canon, J.; Chen, A.; Chen, X.; Chow, D.; Deignan, J.; Duquette, J.; Eksterowicz, J.; Fisher, B.; Fox, B. M.; Fu, J.; Gonzalez, A. Z.; Gonzalez-Lopez De Turiso, F.; Houze, J. B.; Huang, X.; Jiang, M.; Jin, L.; Kayser,

F.; Liu, J. J.; Lo, M.; Long, A. M.; Lucas, B.; McGee, L. R.; McIntosh, J.; Mihalic, J.; Oliner, J. D.; Osgood, T.; Peterson, M. L.; Roveto, P.; Saiki, A. Y.; Shaffer, P.; Toteva, M.; Wang, Y.; Wang, Y. C.; Wortman, S.; Yakowec, P.; Yan, X.; Ye, Q.; Yu, D.; Yu, M.; Zhao, X.; Zhou, J.; Zhu, J.; Olson, S. H.; Medina, J. C. Discovery of AMG 232, a Potent, Selective, and Orally Bioavailable MDM2–P53 Inhibitor in Clinical Development. *J. Med. Chem.* **2014**, *57* (4), 1454–1472.

(162) Vassilev, L. T. In Vivo Activation of the P53 Pathway by Small-Molecule Antagonists of MDM2. *Science (80-.).* **2004**, *303* (5659), 844–848.

(163) Popowicz, G. M.; Czarna, A.; Holak, T. A. Structure of the Human Mdmx Protein Bound to the P53 Tumor Suppressor Transactivation Domain. *Cell Cycle* **2008**, *7* (15), 2441–2443.

(164) Joseph, T. L.; Madhumalar, A.; Brown, C. J.; Lane, D. P.; Verma, C. S. Differential Binding of P53 and Nutlin to MDM2 and MDMX: Computational Studies. *Cell Cycle* **2010**, *9* (6), 1167–1181.

(165) Burgess, A.; Chia, K. M.; Haupt, S.; Thomas, D.; Haupt, Y.; Lim, E. Clinical Overview of MDM2/X-Targeted Therapies. *Front. Oncol.* **2016**, *6* (January), 1–7.

(166) Marine, J.-C.; Francoz, S.; Maetens, M.; Wahl, G.; Toledo, F.; Lozano, G. Keeping P53 in Check: Essential and Synergistic Functions of Mdm2 and Mdm4. *Cell Death Differ* **2006**, *13* (6), 927–934.

(167) Hu, B.; Gilkes, D. M.; Farooqi, B.; Sebti, S. M.; Chen, J. MDMX Overexpression Prevents P53 Activation by the MDM2 Inhibitor Nutlin. *J.*

Biol. Chem. **2006**, *281* (44), 33030–33035.

(168) Reed, D.; Shen, Y.; Shelat, A. A.; Arnold, L. A.; Ferreira, A. M.; Zhu, F.; Mills, N.; Smithson, D. C.; Regni, C. A.; Bashford, D.; Cicero, S. A.; Schulman, B. A.; Jochemsen, A. G.; Guy, R. K.; Dyer, M. A. Identification and Characterization of the First Small Molecule Inhibitor of MDMX. *J. Biol. Chem.* **2010**, *285* (14), 10786–10796.

(169) Bista, M.; Smithson, D.; Pecak, A.; Salinas, G.; Pustelny, K.; Min, J.; Pirog, A.; Finch, K.; Zdzalik, M.; Waddell, B.; Wladyka, B.; Kedracka-Krok, S.; Dyer, M. A.; Dubin, G.; Guy, R. K. On the Mechanism of Action of SJ-172550 in Inhibiting the Interaction of MDM4 and P53. *PLoS One* **2012**, *7* (6), e37518.

(170) Chen, R.; Zhou, J.; Qin, L.; Chen, Y.; Huang, Y.; Liu, H.; Su, Z. A Fusion Protein of the P53 Transaction Domain and the P53-Binding Domain of the Oncoprotein MdmX as an Efficient System for High-Throughput Screening of MdmX Inhibitors. *Biochemistry* **2017**, *56* (25), 3273–3282.

(171) Soares, J.; Raimundo, L.; Pereira, N. A. L. L.; dos Santos, D. J. V. A. V. A.; Pérez, M.; Queiroz, G.; Leão, M.; Santos, M. M. M. M.; Saraiva, L. A Tryptophanol-Derived Oxazolopiperidone Lactam Is Cytotoxic against Tumors via Inhibition of P53 Interaction with Murine Double Minute Proteins. *Pharmacol. Res.* **2015**, *95–96* (May-Jun), 42–52.

(172) Leão, M.; Gomes, S.; Bessa, C.; Soares, J.; Raimundo, L.; Monti, P.; Fronza, G.; Pereira, C.; Saraiva, L. Studying P53 Family Proteins in Yeast: Induction of Autophagic Cell Death and Modulation by Interactors and

Small Molecules. *Exp. Cell Res.* **2015**, *330* (1), 164–177.

(173) Baell, J. B.; Holloway, G. A. New Substructure Filters for Removal of Pan Assay Interference Compounds (PAINS) from Screening Libraries and for Their Exclusion in Bioassays. *J. Med. Chem* **2010**, *53*, 2719–2740.

(174) Irwin, J. J.; Duan, D.; Torosyan, H.; Doak, A. K.; Ziebart, K. T.; Sterling, T.; Tumanian, G.; Shoichet, B. K. An Aggregation Advisor for Ligand Discovery. *J. Med. Chem.* **2015**, *58* (17), 7076–7087.

(175) Yang, J. J.; Ursu, O.; Lipinski, C. A.; Sklar, L. A.; Oprea, T. I.; Bologa, C. G. Badapple: Promiscuity Patterns from Noisy Evidence. *J. Cheminform.* **2016**, *8* (1), 29.

(176) Amani, P.; Sneyd, T.; Preston, S.; Young, N. D.; Mason, L.; Bailey, U.-M.; Baell, J.; Camp, D.; Gasser, R. B.; Gorse, A.-D.; Taylor, P.; Hofmann, A. A Practical Java Tool for Small-Molecule Compound Appraisal. *J. Cheminform.* **2015**, *7*, 28.

(177) Tomašić, T.; Peterlin Mašič, L. Rhodanine as a Scaffold in Drug Discovery: A Critical Review of Its Biological Activities and Mechanisms of Target Modulation. *Expert Opin. Drug Discov.* **2012**, *7* (7), 549–560.

(178) Du, X.; Li, Y.; Xia, Y.-L.; Ai, S.-M.; Liang, J.; Sang, P.; Ji, X.-L.; Liu, S.-Q. Insights into Protein-Ligand Interactions: Mechanisms, Models, and Methods. *Int. J. Mol. Sci.* **2016**, *17* (2).

(179) Garcia-Fuentes, L.; Ramiro; Sanz, T.; Quesada-Soriano, I.; Baro, C. Thermodynamics of Molecular Recognition by Calorimetry. In *Thermodynamics - Physical Chemistry of Aqueous Systems*; Pesek, K., Ed.;

InTech, 2011.

(180) Montero, D.; Tachibana, C.; Rahr Winther, J.; Appenzeller-Herzog, C. Intracellular Glutathione Pools Are Heterogeneously Concentrated. *Redox Biol.* **2013**, *1* (1), 508–513.

(181) Enders, D.; Saint-Dizier, A.; Lannou, M.-I.; Lenzen, A. The Phospha-Michael Addition in Organic Synthesis. *European J. Org. Chem.* **2006**, *2006* (1), 29–49.

(182) Fanghänel, E.; Akhlaq, M. S.; Grossmann, N. Untersuchungen Zur Hydrolysestabilität von 4-Arylmethyliden-2-Pyrazolin-5-Onen. *J. für Prakt. Chemie* **1985**, *327* (2), 209–219.

(183) Singh, D.; Singh, D. Syntheses of 1,3-Disubstituted 4-Arylidenepyrazolin-5-Ones and the Keto and Enol Forms of 4,4'-Arylidenebis(1,3-Disubstituted Pyrazolin-5-Ones). *J. Chem. Eng. Data* **1984**, *29* (3), 355–356.

(184) Stefaniak, J.; Lewis, A. M.; Conole, D.; Galan, S. R. G.; Bataille, C. J. R.; Wynne, G. M.; Castaldi, M. P.; Lundbäck, T.; Russell, A. J.; Huber, K. V. M. Chemical Instability and Promiscuity of Arylmethylidenepyrazolinone-Based MDMX Inhibitors. *ACS Chem. Biol.* **2018**, *13* (10).

(185) Mann, M.; Wilm, M. Electrospray Mass Spectrometry for Protein Characterization. *Trends Biochem. Sci.* **1995**, *20* (6), 219–224.

(186) Karas, M.; Bahr, U. Laser Desorption Ionization Mass Spectrometry of Large Biomolecules. *TrAC Trends Anal. Chem.* **1990**, *9* (10), 321–325.

(187) Miladinović, S. M.; Kozhinov, A. N.; Gorshkov, M. V.; Tsybin, Y. O. On

the Utility of Isotopic Fine Structure Mass Spectrometry in Protein Identification. *Anal. Chem.* **2012**, *84* (9), 4042–4051.

(188) Senko, M. W.; Beu, S. C.; McLaffertycor, F. W. Determination of Monoisotopic Masses and Ion Populations for Large Biomolecules from Resolved Isotopic Distributions. *J. Am. Soc. Mass Spectrom.* **1995**, *6* (4), 229–233.

(189) Perkins, D. N.; Pappin, D. J. C.; Creasy, D. M.; Cottrell, J. S. Probability-Based Protein Identification by Searching Sequence Databases Using Mass Spectrometry Data. *Electrophoresis* **1999**, *20* (18), 3551–3567.

(190) Geer, L. Y.; Markey, S. P.; Kowalak, J. A.; Wagner, L.; Xu, M.; Maynard, D. M.; Yang, X.; Shi, W.; Bryant, S. H. Open Mass Spectrometry Search Algorithm. *J. Proteome Res.* **2004**, *3* (5), 958–964.

(191) Cox, J.; Mann, M. MaxQuant Enables High Peptide Identification Rates, Individualized p.p.b.-Range Mass Accuracies and Proteome-Wide Protein Quantification. *Nat. Biotechnol.* **2008**, *26* (12), 1367–1372.

(192) Cox, J.; Neuhauser, N.; Michalski, A.; Scheltema, R. A.; Olsen, J. V.; Mann, M. Andromeda: A Peptide Search Engine Integrated into the MaxQuant Environment. *J. Proteome Res.* **2011**, *10* (4), 1794–1805.

(193) Gowd, K. H.; Krishnan, K. S.; Balaram, P. Identification of Conus Amadis Disulfide Isomerase: Minimum Sequence Length of Peptide Fragments Necessary for Protein Annotation. *Mol. Biosyst.* **2007**, *3* (8), 554.

(194) Ma, Z.-Q.; Dasari, S.; Chambers, M. C.; Litton, M. D.; Sobecki, S. M.; Zimmerman, L. J.; Halvey, P. J.; Schilling, B.; Drake, P. M.; Gibson, B.

W.; Tabb, D. L. IDPicker 2.0: Improved Protein Assembly with High Discrimination Peptide Identification Filtering. *J. Proteome Res.* **2009**, *8* (8), 3872–3881.

(195) Nesvizhskii, A. I.; Keller, A.; Kolker, E.; Aebersold, R. A Statistical Model for Identifying Proteins by Tandem Mass Spectrometry. *Anal. Chem.* **2003**, *75* (17), 4646–4658.

(196) Lai, X.; Wang, L.; Witzmann, F. A. Issues and Applications in Label-Free Quantitative Mass Spectrometry. *Int. J. Proteomics* **2013**, *2013*, 1–13.

(197) Thompson, A.; Schäfer, J.; Kuhn, K.; Kienle, S.; Schwarz, J.; Schmidt, G.; Neumann, T.; Hamon, C. Tandem Mass Tags: A Novel Quantification Strategy for Comparative Analysis of Complex Protein Mixtures by MS/MS. *Anal. Chem.* **2003**, *75* (8), 1895–1904.

(198) Erdjument-Bromage, H.; Huang, F.-K.; Neubert, T. A. Sample Preparation for Relative Quantitation of Proteins Using Tandem Mass Tags (TMT) and Mass Spectrometry (MS). *Methods Mol. Biol.* **2018**, *1741*, 135–149.

(199) Xiao, W.; Chen, X.; Liu, L.; Shu, Y.; Zhang, M.; Zhong, Y. Role of Protein Arginine Methyltransferase 5 in Human Cancers. *Biomed. Pharmacother.* **2019**, *114*, 108790.

(200) Jansson, M.; Durant, S. T.; Cho, E.-C.; Sheahan, S.; Edelmann, M.; Kessler, B.; La Thangue, N. B. Arginine Methylation Regulates the P53 Response. *Nat. Cell Biol.* **2008**, *10* (12), 1431–1439.

(201) Powers, M. A.; Fay, M. M.; Factor, R. E.; Welm, A. L.; Ullman, K. S. Protein Arginine Methyltransferase 5 Accelerates Tumor Growth by

Arginine Methylation of the Tumor Suppressor Programmed Cell Death 4. *Cancer Res.* **2011**, *71* (16), 5579–5587.

(202) Wei, T.-Y. W.; Juan, C.-C.; Hisa, J.-Y.; Su, L.-J.; Lee, Y.-C. G.; Chou, H.-Y.; Chen, J.-M. M.; Wu, Y.-C.; Chiu, S.-C.; Hsu, C.-P.; Liu, K.-L.; Yu, C.-T. R. Protein Arginine Methyltransferase 5 Is a Potential Oncoprotein That Upregulates G1 Cyclins/Cyclin-Dependent Kinases and the Phosphoinositide 3-Kinase/AKT Signaling Cascade. *Cancer Sci.* **2012**, *103* (9), 1640–1650.

(203) Gerhart, S. V.; Kellner, W. A.; Thompson, C.; Pappalardi, M. B.; Zhang, X.-P.; Montes de Oca, R.; Penebre, E.; Duncan, K.; Boriack-Sjodin, A.; Le, B.; Majer, C.; McCabe, M. T.; Carpenter, C.; Johnson, N.; Kruger, R. G.; Barbash, O. Activation of the P53-MDM4 Regulatory Axis Defines the Anti-Tumour Response to PRMT5 Inhibition through Its Role in Regulating Cellular Splicing. *Sci. Rep.* **2018**, *8* (1), 9711.

(204) Gaetani, M.; Sabatier, P.; Saei, A. A.; Beusch, C.; Yang, Z.; Lundström, S.; Zubarev, R. A. Proteome Integral Stability Alteration Assay Dramatically Increases Throughput and Sensitivity in Profiling Factor-Induced Proteome Changes. *bioRxiv* **2018**, 496398.

(205) Mellacheruvu, D.; Wright, Z.; Couzens, A. L.; Lambert, J.-P.; St-Denis, N. A.; Li, T.; Miteva, Y. V; Hauri, S.; Sardiu, M. E.; Low, T. Y.; Halim, V. A.; Bagshaw, R. D.; Hubner, N. C.; Al-Hakim, A.; Bouchard, A.; Faubert, D.; Fermin, D.; Dunham, W. H.; Goudreault, M.; Lin, Z.-Y.; Badillo, B. G.; Pawson, T.; Durocher, D.; Coulombe, B.; Aebersold, R.; Superti-Furga, G.;

Colinge, J.; Heck, A. J. R.; Choi, H.; Gstaiger, M.; Mohammed, S.; Cristea, I. M.; Bennett, K. L.; Washburn, M. P.; Raught, B.; Ewing, R. M.; Gingras, A.-C.; Nesvizhskii, A. I. The CRAPome: A Contaminant Repository for Affinity Purification–Mass Spectrometry Data. *Nat. Methods* **2013**, *10* (8), 730–736.

(206) Friesen, W. J.; Wyce, A.; Paushkin, S.; Abel, L.; Rappsilber, J.; Mann, M.; Dreyfuss, G. A Novel WD Repeat Protein Component of the Methylosome Binds Sm Proteins. *J. Biol. Chem.* **2002**, *277* (10), 8243–8247.

(207) Antonysamy, S.; Bonday, Z.; Campbell, R. M.; Doyle, B.; Druzina, Z.; Gheyi, T.; Han, B.; Jungheim, L. N.; Qian, Y.; Rauch, C.; Russell, M.; Sauder, J. M.; Wasserman, S. R.; Weichert, K.; Willard, F. S.; Zhang, A.; Emtage, S. Crystal Structure of the Human PRMT5:MEP50 Complex. *Proc. Natl. Acad. Sci.* **2012**, *109* (44), 17960–17965.

(208) Hashimoto, M.; Girardi, E.; Eichner, R.; Superti-Furga, G. Detection of Chemical Engagement of Solute Carrier Proteins by a Cellular Thermal Shift Assay. *ACS Chem. Biol.* **2018**, *13* (6), 1480–1486.

(209) Rengasamy, M.; Zhang, F.; Vashisht, A.; Song, W.-M.; Aguilo, F.; Sun, Y.; Li, S.; Zhang, W.; Zhang, B.; Wohlschlegel, J. A.; Walsh, M. J. The PRMT5/WDR77 Complex Regulates Alternative Splicing through ZNF326 in Breast Cancer. *Nucleic Acids Res.* **2017**, *45* (19), 11106–11120.

(210) Hu, D.; Gur, M.; Zhou, Z.; Gamper, A.; Hung, M.-C.; Fujita, N.; Lan, L.; Bahar, I.; Wan, Y. Interplay between Arginine Methylation and Ubiquitylation Regulates KLF4-Mediated Genome Stability and

Carcinogenesis. *Nat. Commun.* **2015**, *6*, 8419.

(211) Ribeiro, R. C.; Kushner, P. J.; Baxter, J. D. The Nuclear Hormone Receptor Gene Superfamily. *Annu. Rev. Med.* **1995**, *46* (1), 443–453.

(212) Zhu, Y.; Alvares, K.; Huang, Q.; Rao, M. S.; Reddy, J. K. Cloning of a New Member of the Peroxisome Proliferator-Activated Receptor Gene Family from Mouse Liver. *J. Biol. Chem.* **1993**, *268* (36), 26817–26820.

(213) Tontonoz, P.; Hu, E.; Spiegelman, B. M. Stimulation of Adipogenesis in Fibroblasts by PPARγ2, a Lipid-Activated Transcription Factor. *Cell* **1994**, *79* (7), 1147–1156.

(214) Tontonoz, P.; Hu, E.; Graves, R. A.; Budavari, A. I.; Spiegelman, B. M. MPPAR Gamma 2: Tissue-Specific Regulator of an Adipocyte Enhancer. *Genes Dev.* **1994**, *8* (10), 1224–1234.

(215) Escher, P.; Braissant, O.; Basu-Modak, S.; Michalik, L.; Wahli, W.; Desvergne, B. Rat PPARs: Quantitative Analysis in Adult Rat Tissues and Regulation in Fasting and Refeeding. *Endocrinology* **2001**, *142* (10), 4195–4202.

(216) Gerhold, D. L.; Liu, F.; Jiang, G.; Li, Z.; Xu, J.; Lu, M.; Sachs, J. R.; Bagchi, A.; Fridman, A.; Holder, D. J.; Doebber, T. W.; Berger, J.; Elbrecht, A.; Moller, D. E.; Zhang, B. B. Gene Expression Profile of Adipocyte Differentiation and Its Regulation by Peroxisome Proliferator-Activated Receptor-γ Agonists. *Endocrinology* **2002**, *143* (6), 2106–2118.

(217) Rosen, E. D.; Sarraf, P.; Troy, A. E.; Bradwin, G.; Moore, K.; Milstone, D. S.; Spiegelman, B. M.; Mortensen, R. M. PPARγ Is Required for the

Differentiation of Adipose Tissue In Vivo and In Vitro. *Mol. Cell* **1999**, *4* (4), 611–617.

(218) Hosono, T.; Mizuguchi, H.; Katayama, K.; Koizumi, N.; Kawabata, K.; Yamaguchi, T.; Nakagawa, S.; Watanabe, Y.; Mayumi, T.; Hayakawa, T. RNA Interference of PPARgamma Using Fiber-Modified Adenovirus Vector Efficiently Suppresses Preadipocyte-to-Adipocyte Differentiation in 3T3-L1 Cells. *Gene* **2005**, *348*, 157–165.

(219) Way, J. M.; Harrington, W. W.; Brown, K. K.; Gottschalk, W. K.; Sundseth, S. S.; Mansfield, T. A.; Ramachandran, R. K.; Willson, T. M.; Kliewer, S. A. Comprehensive Messenger Ribonucleic Acid Profiling Reveals That Peroxisome Proliferator-Activated Receptor γ Activation Has Coordinate Effects on Gene Expression in Multiple Insulin-Sensitive Tissues. *Endocrinology* **2001**, *142* (3), 1269–1277.

(220) Schoonjans, K.; Peinado-Onsurbe, J.; Lefebvre, A. M.; Heyman, R. A.; Briggs, M.; Deeb, S.; Staels, B.; Auwerx, J. PPARalpha and PPARgamma Activators Direct a Distinct Tissue-Specific Transcriptional Response via a PPRE in the Lipoprotein Lipase Gene. *EMBO J.* **1996**, *15* (19), 5336–5348.

(221) Avallone, R.; Demers, A.; Rodrigue-Way, A.; Bujold, K.; Harb, D.; Anghel, S.; Wahli, W.; Marleau, S.; Ong, H.; Tremblay, A. A Growth Hormone-Releasing Peptide That Binds Scavenger Receptor CD36 and Ghrelin Receptor Up-Regulates Sterol Transporters and Cholesterol Efflux in Macrophages through a Peroxisome Proliferator-Activated Receptor γ-Dependent Pathway. *Mol. Endocrinol.* **2006**, *20* (12), 3165–3178.

(222) Laplante, M.; Festuccia, W. T.; Soucy, G.; Gelinas, Y.; Lalonde, J.; Berger, J. P.; Deshaies, Y. Mechanisms of the Depot Specificity of Peroxisome Proliferator-Activated Receptor Action on Adipose Tissue Metabolism. *Diabetes* **2006**, *55* (10), 2771–2778.

(223) Bogacka, I.; Xie, H.; Bray, G. A.; Smith, S. R. The Effect of Pioglitazone on Peroxisome Proliferator-Activated Receptor- Target Genes Related to Lipid Storage In Vivo. *Diabetes Care* **2004**, *27* (7), 1660–1667.

(224) Girnun, G. D.; Domann, F. E.; Moore, S. A.; Robbins, M. E. C. Identification of a Functional Peroxisome Proliferator-Activated Receptor Response Element in the Rat Catalase Promoter. *Mol. Endocrinol.* **2002**, *16* (12), 2793–2801.

(225) Tontonoz, P.; Hu, E.; Devine, J.; Beale, E. G.; Spiegelman, B. M. PPAR Gamma 2 Regulates Adipose Expression of the Phosphoenolpyruvate Carboxykinase Gene. *Mol. Cell. Biol.* **1995**, *15* (1), 351–357.

(226) Hu, E.; Kim, J. B.; Sarraf, P.; Spiegelman, B. M. Inhibition of Adipogenesis Through MAP Kinase-Mediated Phosphorylation of PPAR. *Science (80-.).* **1996**, *274* (5295), 2100–2103.

(227) Ristow, M.; Müller-Wieland, D.; Pfeiffer, A.; Krone, W.; Kahn, C. R. Obesity Associated with a Mutation in a Genetic Regulator of Adipocyte Differentiation. *N. Engl. J. Med.* **1998**, *339* (14), 953–959.

(228) Rangwala, S. M.; Rhoades, B.; Shapiro, J. S.; Rich, A. S.; Kim, J. K.; Shulman, G. I.; Kaestner, K. H.; Lazar, M. A. Genetic Modulation of PPARgamma Phosphorylation Regulates Insulin Sensitivity. *Dev. Cell*

2003, *5* (4), 657–663.

(229) Hiragun, A.; Sato, M.; Mitsui, H. Preadipocyte Differentiation in Vitro: Identification of a Highly Active Adipogenic Agent. *J. Cell. Physiol.* **1988**, *134* (1), 124–130.

(230) Fujita, T.; Sugiyama, Y.; Taketomi, S.; Sohda, T.; Kawamatsu, Y.; Iwatsuka, H.; Suzuoki, Z. Reduction of Insulin Resistance in Obese and/or Diabetic Animals by 5-[4-(1-Methylcyclohexylmethoxy)Benzyl]-Thiazolidine-2,4-Dione (ADD-3878, U-63,287, Ciglitazone), a New Antidiabetic Agent. *Diabetes* **1983**, *32* (9), 804–810.

(231) Lehmann, J. M.; Moore, L. B.; Smith-Oliver, T. A.; Wilkison, W. O.; Willson, T. M.; Kliewer, S. A. An Antidiabetic Thiazolidinedione Is a High Affinity Ligand for Peroxisome Proliferator-Activated Receptor γ (PPARγ). *J. Biol. Chem.* **1995**, *270* (22), 12953–12956.

(232) Ye, J.-M.; Dzamko, N.; Cleasby, M. E.; Hegarty, B. D.; Furler, S. M.; Cooney, G. J.; Kraegen, E. W. Direct Demonstration of Lipid Sequestration as a Mechanism by Which Rosiglitazone Prevents Fatty-Acid-Induced Insulin Resistance in the Rat: Comparison with Metformin. *Diabetologia* **2004**, *47* (7), 1306–1313.

(233) Boden, G.; Homko, C.; Mozzoli, M.; Showe, L. C.; Nichols, C.; Cheung, P. Thiazolidinediones Upregulate Fatty Acid Uptake and Oxidation in Adipose Tissue of Diabetic Patients. *Diabetes* **2005**, *54* (3), 880–885.

(234) Steppan, C. M.; Bailey, S. T.; Bhat, S.; Brown, E. J.; Banerjee, R. R.; Wright, C. M.; Patel, H. R.; Ahima, R. S.; Lazar, M. A. The Hormone

Resistin Links Obesity to Diabetes. *Nature* **2001**, *409* (6818), 307–312.

(235) Nesto, R. W.; Bell, D.; Bonow, R. O.; Fonseca, V.; Grundy, S. M.; Horton, E. S.; Le Winter, M.; Porte, D.; Semenkovich, C. F.; Smith, S.; Young, L. H.; Kahn, R. Thiazolidinedione Use, Fluid Retention, and Congestive Heart Failure: A Consensus Statement from the American Heart Association and American Diabetes Association. *Diabetes Care* **2004**, *27* (1), 256–263.

(236) Yamauchi, T.; Kamon, J.; Waki, H.; Murakami, K.; Motojima, K.; Komeda, K.; Ide, T.; Kubota, N.; Terauchi, Y.; Tobe, K.; Miki, H.; Tsuchida, A.; Akanuma, Y.; Nagai, R.; Kimura, S.; Kadowaki, T. The Mechanisms by Which Both Heterozygous Peroxisome Proliferator-Activated Receptor Gamma (PPARgamma) Deficiency and PPARgamma Agonist Improve Insulin Resistance. *J. Biol. Chem.* **2001**, *276* (44), 41245–41254.

(237) Barroso, I.; Gurnell, M.; Crowley, V. E. F.; Agostini, M.; Schwabe, J. W.; Soos, M. A.; Maslen, G. L.; Williams, T. D. M.; Lewis, H.; Schafer, A. J.; Chatterjee, V. K. K.; O'Rahilly, S. Dominant Negative Mutations in Human PPARγ Associated with Severe Insulin Resistance, Diabetes Mellitus and Hypertension. *Nature* **1999**, *402* (6764), 880–883.

(238) Nakano, R.; Kurosaki, E.; Yoshida, S.; Yokono, M.; Shimaya, A.; Maruyama, T.; Shibasaki, M. Antagonism of Peroxisome Proliferator-Activated Receptor Gamma Prevents High-Fat Diet-Induced Obesity in Vivo. *Biochem. Pharmacol.* **2006**, *72* (1), 42–52.

(239) Rieusset, J.; Touri, F.; Michalik, L.; Escher, P.; Desvergne, B.; Niesor, E.;

Wahli, W. A New Selective Peroxisome Proliferator-Activated Receptor Gamma Antagonist with Antiobesity and Antidiabetic Activity. *Mol. Endocrinol.* **2002**, *16* (11), 2628–2644.

(240) Wright, H. M.; Clish, C. B.; Mikami, T.; Hauser, S.; Yanagi, K.; Hiramatsu, R.; Serhan, C. N.; Spiegelman, B. M. A Synthetic Antagonist for the Peroxisome Proliferator-Activated Receptor Gamma Inhibits Adipocyte Differentiation. *J. Biol. Chem.* **2000**, *275* (3), 1873–1877.

(241) Yamauchi, T.; Waki, H.; Kamon, J.; Murakami, K.; Motojima, K.; Komeda, K.; Miki, H.; Kubota, N.; Terauchi, Y.; Tsuchida, A.; Tsuboyama-Kasaoka, N.; Yamauchi, N.; Ide, T.; Hori, W.; Kato, S.; Fukayama, M.; Akanuma, Y.; Ezaki, O.; Itai, A.; Nagai, R.; Kimura, S.; Tobe, K.; Kagechika, H.; Shudo, K.; Kadowaki, T. Inhibition of RXR and PPARgamma Ameliorates Diet-Induced Obesity and Type 2 Diabetes. *J. Clin. Invest.* **2001**, *108* (7), 1001–1013.

(242) Ma, X.; Wang, D.; Zhao, W.; Xu, L. Deciphering the Roles of PPARγ in Adipocytes via Dynamic Change of Transcription Complex. *Front. Endocrinol. (Lausanne).* **2018**, *9*, 473.

(243) Cohen, R. N. Nuclear Receptor Corepressors and PPARgamma. *Nucl. Recept. Signal.* **2006**, *4*, e003.

(244) Puigserver, P.; Wu, Z.; Park, C. W.; Graves, R.; Wright, M.; Spiegelman, B. M. A Cold-Inducible Coactivator of Nuclear Receptors Linked to Adaptive Thermogenesis. *Cell* **1998**, *92* (6), 829–839.

(245) Kajimura, S.; Saito, M. A New Era in Brown Adipose Tissue Biology:

Molecular Control of Brown Fat Development and Energy Homeostasis. *Annu. Rev. Physiol.* **2014**, *76* (1), 225–249.

(246) Arechaga, I.; Ledesma, A.; Rial, E. The Mitochondrial Uncoupling Protein UCP1: A Gated Pore. *IUBMB Life* **2001**, *52* (3–5), 165–173.

(247) Ukropec, J.; Anunciado, R. P.; Ravussin, Y.; Hulver, M. W.; Kozak, L. P. UCP1-Independent Thermogenesis in White Adipose Tissue of Cold-Acclimated Ucp1-/- Mice. *J. Biol. Chem.* **2006**, *281* (42), 31894–31908.

(248) Liu, X.; Rossmeisl, M.; McClaine, J.; Riachi, M.; Harper, M.-E.; Kozak, L. P. Paradoxical Resistance to Diet-Induced Obesity in UCP1-Deficient Mice. *J. Clin. Invest.* **2003**, *111* (3), 399–407.

(249) Kopecky, J.; Clarke, G.; Enerbäck, S.; Spiegelman, B.; Kozak, L. P. Expression of the Mitochondrial Uncoupling Protein Gene from the AP2 Gene Promoter Prevents Genetic Obesity. *J. Clin. Invest.* **1995**, *96* (6), 2914–2923.

(250) Lean, M. E. Brown Adipose Tissue in Humans. *Proc. Nutr. Soc.* **1989**, *48* (2), 243–256.

(251) Soloveva, V.; Graves, R. A.; Rasenick, M. M.; Spiegelman, B. M.; Ross, S. R. Transgenic Mice Overexpressing the Beta 1-Adrenergic Receptor in Adipose Tissue Are Resistant to Obesity. *Mol. Endocrinol.* **1997**, *11* (1), 27–38.

(252) Cummings, D. E.; Brandon, E. P.; Planas, J. V.; Motamed, K.; Idzerda, R. L.; McKnight, G. S. Genetically Lean Mice Result from Targeted Disruption of the RII Beta Subunit of Protein Kinase A. *Nature* **1996**, *382*

(6592), 622–626.

(253) Kozak, U. C.; Kopecky, J.; Teisinger, J.; Enerbäck, S.; Boyer, B.; Kozak, L. P. An Upstream Enhancer Regulating Brown-Fat-Specific Expression of the Mitochondrial Uncoupling Protein Gene. *Mol. Cell. Biol.* **1994**, *14* (1), 59–67.

(254) Sears, I. B.; MacGinnitie, M. A.; Kovacs, L. G.; Graves, R. A. Differentiation-Dependent Expression of the Brown Adipocyte Uncoupling Protein Gene: Regulation by Peroxisome Proliferator-Activated Receptor Gamma. *Mol. Cell. Biol.* **1996**, *16* (7), 3410–3419.

(255) Pardo, R.; Enguix, N.; Lasheras, J.; Feliu, J. E.; Kralli, A.; Villena, J. A. Rosiglitazone-Induced Mitochondrial Biogenesis in White Adipose Tissue Is Independent of Peroxisome Proliferator-Activated Receptor γ Coactivator-1α. *PLoS One* **2011**, *6* (11), e26989.

(256) Fukui, Y.; Masui, S.; Osada, S.; Umesono, K.; Motojima, K. A New Thiazolidinedione, NC-2100, Which Is a Weak PPAR-Gamma Activator, Exhibits Potent Antidiabetic Effects and Induces Uncoupling Protein 1 in White Adipose Tissue of KKAy Obese Mice. *Diabetes* **2000**, *49* (5), 759–767.

(257) Choi, S.-S.; Kim, E.-S.; Jung, J.-E.; Marciano, D. P.; Jo, A.; Koo, J. Y.; Choi, S. Y.; Yang, Y. R.; Jang, H.-J.; Kim, E.-K.; Park, J.; Kwon, H. M.; Lee, I. H.; Park, S. B.; Myung, K.-J.; Suh, P.-G.; Griffin, P. R.; Choi, J. H. PPARγ Antagonist Gleevec Improves Insulin Sensitivity and Promotes the Browning of White Adipose Tissue. *Diabetes* **2016**, *65* (4), 829–839.

(258) Moon, C. M.; Kwon, J.-H.; Kim, J. S.; Oh, S.-H.; Jin Lee, K.; Park, J. J.; Pil Hong, S.; Cheon, J. H.; Kim, T. Il; Kim, W. H. Nonsteroidal Anti-Inflammatory Drugs Suppress Cancer Stem Cells via Inhibiting PTGS2 (Cyclooxygenase 2) and NOTCH/HES1 and Activating PPARG in Colorectal Cancer. *Int. J. Cancer* **2014**, *134* (3), 519–529.

(259) Keshamouni, V. G.; Reddy, R. C.; Arenberg, D. A.; Joel, B.; Thannickal, V. J.; Kalemkerian, G. P.; Standiford, T. J. Peroxisome Proliferator-Activated Receptor-γ Activation Inhibits Tumor Progression in Non-Small-Cell Lung Cancer. *Oncogene* **2004**, *23* (1), 100–108.

(260) Liu, K. G.; Lambert, M. H.; Ayscue, A. H.; Henke, B. R.; Leesnitzer, L. M.; Oliver, Jr., W. R.; Plunket, K. D.; Xu, H. E.; Sternbach, D. D.; Willson, T. M. Synthesis and Biological Activity of L-Tyrosine-Based PPARγ Agonists with Reduced Molecular Weight. *Bioorg. Med. Chem. Lett.* **2001**, *11* (24), 3111–3113.

(261) Sohn, K.-A. K.; Cruciani-Guglielmacci, C.; Kassis, N.; Clément, L.; Ouali, F.; Caüzac, M.; Lebègue, N.; Berthelot, P.; Caignard, D.-H.; Pégorier, J.-P.; Renard, P.; Dacquet, C.; Ktorza, A.; Magnan, C.; Consortium of the French Ministry of Research and Technology. S26948, a New Specific Peroxisome Proliferator Activated Receptor Gamma Modulator Improved in Vivo Hepatic Insulin Sensitivity in 48 h Lipid Infused Rats. *Eur. J. Pharmacol.* **2009**, *608* (1–3), 104–111.

(262) Carmona, M. C.; Louche, K.; Lefebvre, B.; Pilon, A.; Hennuyer, N.; Audinot-Bouchez, V.; Fievet, C.; Torpier, G.; Formstecher, P.; Renard, P.;

Lefebvre, P.; Dacquet, C.; Staels, B.; Casteilla, L.; Pénicaud, L.; Consortium of the French Ministry of Research and Technology. S 26948: A New Specific Peroxisome Proliferator Activated Receptor Gamma Modulator with Potent Antidiabetes and Antiatherogenic Effects. *Diabetes* **2007**, *56* (11), 2797–2808.

(263) Liu, S.; Ogilvie, K. M.; Klausing, K.; Lawson, M. A.; Jolley, D.; Li, D.; Bilakovics, J.; Pascual, B.; Hein, N.; Urcan, M.; Leibowitz, M. D. Mechanism of Selective Retinoid X Receptor Agonist-Induced Hypothyroidism in the Rat. *Endocrinology* **2002**, *143* (8), 2880–2885.

(264) Eglen, R. M.; Reisine, T.; Roby, P.; Rouleau, N.; Illy, C.; Bossé, R.; Bielefeld, M. The Use of AlphaScreen Technology in HTS: Current Status. *Curr. Chem. Genomics* **2008**, *1*, 2–10.

(265) Voloshin, A. I.; Shavaleev, N. M.; Kazakov, V. P. Water Enhances Photoluminescence Intensity of Europium (III), Terbium (III) and Samarium (III) Tris-β-Diketonates in Toluene Solutions and Chemiluminescence Intensity of Europium (III) and Samarium (III) Tris-β-Diketonates in the Reaction with Dioxetane. *J. Photochem. Photobiol. A Chem.* **2000**, *136* (3), 203–208.

(266) Axelsson, H.; Almqvist, H.; Otrocka, M.; Vallin, M.; Lundqvist, S.; Hansson, P.; Karlsson, U.; Lundbäck, T.; Seashore-Ludlow, B. In Situ Target Engagement Studies in Adherent Cells. *ACS Chem. Biol.* **2018**, *13* (4), 942–950.

(267) Umemoto, T.; Fujiki, Y. Ligand-Dependent Nucleo-Cytoplasmic Shuttling

of Peroxisome Proliferator-Activated Receptors, PPARα and PPARγ. *Genes Cells* **2012**, *17* (7), 576–596.

(268) Atanasov, A. G.; Wang, J. N.; Gu, S. P.; Bu, J.; Kramer, M. P.; Baumgartner, L.; Fakhrudin, N.; Ladurner, A.; Malainer, C.; Vuorinen, A.; Noha, S. M.; Schwaiger, S.; Rollinger, J. M.; Schuster, D.; Stuppner, H.; Dirsch, V. M.; Heiss, E. H. Honokiol: A Non-Adipogenic PPARγ Agonist from Nature. *Biochim. Biophys. Acta* **2013**, *1830* (10), 4813–4819.

(269) Kim, E.-K.; Lee, S. H.; Lee, S.-Y.; Kim, J.; Jhun, J. Y.; Na, H. S.; Kim, S.-Y.; Choi, J. Y.; Yang, C. W.; Park, S.-H.; Cho, M.-L. Metformin Ameliorates Experimental-Obesity-Associated Autoimmune Arthritis by Inducing FGF21 Expression and Brown Adipocyte Differentiation. *Exp. Mol. Med.* **2018**, *50* (1), e432–e432.

(270) Overington, J. P.; Al-Lazikani, B.; Hopkins, A. L. How Many Drug Targets Are There? *Nat. Rev. Drug Discov.* **2006**, *5* (12), 993–996.

(271) Liu, Q.; Ding, C.; Liu, W.; Song, L.; Liu, M.; Qi, L.; Fu, T.; Malovannaya, A.; Wang, Y.; Qin, J.; Zhen, B. In-Depth Proteomic Characterization of Endogenous Nuclear Receptors in Mouse Liver. *Mol. Cell. Proteomics* **2013**, *12* (2), 473–484.

(272) Williams, K. E.; Lemieux, G. A.; Hassis, M. E.; Olshen, A. B.; Fisher, S. J.; Werb, Z. Quantitative Proteomic Analyses of Mammary Organoids Reveals Distinct Signatures after Exposure to Environmental Chemicals. *Proc. Natl. Acad. Sci.* **2016**, *113* (10), E1343–E1351.

(273) Kim, M.-S.; Pinto, S. M.; Getnet, D.; Nirujogi, R. S.; Manda, S. S.;

Chaerkady, R.; Madugundu, A. K.; Kelkar, D. S.; Isserlin, R.; Jain, S.; Thomas, J. K.; Muthusamy, B.; Leal-Rojas, P.; Kumar, P.; Sahasrabuddhe, N. A.; Balakrishnan, L.; Advani, J.; George, B.; Renuse, S.; Selvan, L. D. N.; Patil, A. H.; Nanjappa, V.; Radhakrishnan, A.; Prasad, S.; Subbannayya, T.; Raju, R.; Kumar, M.; Sreenivasamurthy, S. K.; Marimuthu, A.; Sathe, G. J.; Chavan, S.; Datta, K. K.; Subbannayya, Y.; Sahu, A.; Yelamanchi, S. D.; Jayaram, S.; Rajagopalan, P.; Sharma, J.; Murthy, K. R.; Syed, N.; Goel, R.; Khan, A. A.; Ahmad, S.; Dey, G.; Mudgal, K.; Chatterjee, A.; Huang, T.-C.; Zhong, J.; Wu, X.; Shaw, P. G.; Freed, D.; Zahari, M. S.; Mukherjee, K. K.; Shankar, S.; Mahadevan, A.; Lam, H.; Mitchell, C. J.; Shankar, S. K.; Satishchandra, P.; Schroeder, J. T.; Sirdeshmukh, R.; Maitra, A.; Leach, S. D.; Drake, C. G.; Halushka, M. K.; Prasad, T. S. K.; Hruban, R. H.; Kerr, C. L.; Bader, G. D.; Iacobuzio-Donahue, C. A.; Gowda, H.; Pandey, A. A Draft Map of the Human Proteome. *Nature* **2014**, *509* (7502), 575–581.

(274) Johansson, H. J.; Socciarelli, F.; Vacanti, N. M.; Haugen, M. H.; Zhu, Y.; Siavelis, I.; Fernandez-Woodbridge, A.; Aure, M. R.; Sennblad, B.; Vesterlund, M.; Branca, R. M.; Orre, L. M.; Huss, M.; Fredlund, E.; Beraki, E.; Garred, Ø.; Boekel, J.; Sauer, T.; Zhao, W.; Nord, S.; Höglander, E. K.; Jans, D. C.; Brismar, H.; Haukaas, T. H.; Bathen, T. F.; Schlichting, E.; Naume, B.; Luders, T.; Borgen, E.; Kristensen, V. N.; Russnes, H. G.; Lingjærde, O. C.; Mills, G. B.; Sahlberg, K. K.; Børresen-Dale, A.-L.; Lehtiö, J. Breast Cancer Quantitative Proteome and

Proteogenomic Landscape. *Nat. Commun.* **2019**, *10* (1), 1600.

(275) Malovannaya, A.; Lanz, R. B.; Jung, S. Y.; Bulynko, Y.; Le, N. T.; Chan, D. W.; Ding, C.; Shi, Y.; Yucer, N.; Krenciute, G.; Kim, B.-J.; Li, C.; Chen, R.; Li, W.; Wang, Y.; O'Malley, B. W.; Qin, J. Analysis of the Human Endogenous Coregulator Complexome. *Cell* **2011**, *145* (5), 787–799.

(276) Edvardsson, M. A Comparative Study of QPCR , Western Blot and Mass Spectrometry for the Estimation of Protein Concentrations. 2016.

(277) Lefterova, M. I.; Haakonsson, A. K.; Lazar, M. A.; Mandrup, S. PPARγ and the Global Map of Adipogenesis and Beyond. *Trends Endocrinol. Metab.* **2014**, *25* (6), 293–302.

(278) Lam, V. Q.; Zheng, J.; Griffin, P. R. Unique Interactome Network Signatures for Peroxisome Proliferator-Activated Receptor Gamma (PPARγ) Modulation by Functional Selective Ligands. *Mol. Cell. Proteomics* **2017**, *16* (12), 2098–2110.

(279) DeCaprio, J.; Kohl, T. O. Cross-Linking Antibodies to Beads Using Dimethyl Pimelimidate (DMP). *Cold Spring Harb. Protoc.* **2019**, *2019* (2), pdb.prot098624.

(280) Yang, F.; Shen, Y.; Camp, D. G.; Smith, R. D. High-PH Reversed-Phase Chromatography with Fraction Concatenation for 2D Proteomic Analysis. *Expert Rev. Proteomics* **2012**, *9* (2), 129–134.

(281) Nissen, S. E. The Rise and Fall of Rosiglitazone. *Eur. Heart J.* **2010**, *31* (7), 773–776.

(282) Berberoglu, Z.; Yazici, A. C.; Demirag, N. G. Effects of Rosiglitazone on Bone Mineral Density and Remodelling Parameters in Postmenopausal Diabetic Women: A 2-Year Follow-up Study. *Clin. Endocrinol. (Oxf).* **2010**, *73* (3), 305–312.

(283) Liu, L.; Aronson, J.; Huang, S.; Lu, Y.; Czernik, P.; Rahman, S.; Kolli, V.; Suva, L. J.; Lecka-Czernik, B. Rosiglitazone Inhibits Bone Regeneration and Causes Significant Accumulation of Fat at Sites of New Bone Formation. *Calcif. Tissue Int.* **2012**, *91* (2), 139–148.

(284) Ackert-Bicknell, C.; Rosen, C. The Genetics of PPARG and the Skeleton. *PPAR Res.* **2006**, *2006*, 93258.

(285) Xiao, Y.; Cui, J.; Li, Y.-X.; Shi, Y.-H.; Le, G.-W. Expression of Genes Associated with Bone Resorption Is Increased and Bone Formation Is Decreased in Mice Fed a High-Fat Diet. *Lipids* **2010**, *45* (4), 345–355.

(286) Akune, T.; Ohba, S.; Kamekura, S.; Yamaguchi, M.; Chung, U.; Kubota, N.; Terauchi, Y.; Harada, Y.; Azuma, Y.; Nakamura, K.; Kadowaki, T.; Kawaguchi, H. PPARgamma Insufficiency Enhances Osteogenesis through Osteoblast Formation from Bone Marrow Progenitors. *J. Clin. Invest.* **2004**, *113* (6), 846–855.

(287) Wan, Y. PPARγ in Bone Homeostasis. *Trends Endocrinol. Metab.* **2010**, *21* (12), 722–728.

(288) Wei, W.; Wang, X.; Yang, M.; Smith, L. C.; Dechow, P. C.; Sonoda, J.; Evans, R. M.; Wan, Y. PGC1beta Mediates PPARgamma Activation of Osteoclastogenesis and Rosiglitazone-Induced Bone Loss. *Cell Metab.*

2010, *11* (6), 503–516.

(289) Fukuda, K.; Kiyokawa, Y.; Yanagiuchi, T.; Wakai, Y.; Kitamoto, K.; Inoue, Y.; Kimura, A. Purification and Characterization of Isoamyl Acetate-Hydrolyzing Esterase Encoded by the IAH1 Gene of Saccharomyces Cerevisiae from a Recombinant Escherichia Coli. *Appl. Microbiol. Biotechnol.* **2000**, *53* (5), 596–600.

(290) Kobayashi, M.; Suzuki, M.; Ohno, T.; Tsuzuki, K.; Taguchi, C.; Tateishi, S.; Kawada, T.; Kim, Y.; Murai, A.; Horio, F. Detection of Differentially Expressed Candidate Genes for a Fatty Liver QTL on Mouse Chromosome 12. *BMC Genet.* **2016**, *17* (1), 73.

(291) Grau, C.; Starkovich, M.; Azamian, M. S.; Xia, F.; Cheung, S. W.; Evans, P.; Henderson, A.; Lalani, S. R.; Scott, D. A. Xp11.22 Deletions Encompassing CENPVL1, CENPVL2, MAGED1 and GSPT2 as a Cause of Syndromic X-Linked Intellectual Disability. *PLoS One* **2017**, *12* (4), e0175962.

(292) Wang, Q.; Tang, J.; Jiang, S.; Huang, Z.; Song, A.; Hou, S.; Gao, X.; Ruan, H.-B. Inhibition of PPARγ, Adipogenesis and Insulin Sensitivity by MAGED1. *J. Endocrinol.* **2018**, *239* (2), 167–180.

(293) Turan, S.; Bastepe, M. The GNAS Complex Locus and Human Diseases Associated with Loss-of-Function Mutations or Epimutations within This Imprinted Gene. *Horm. Res. Paediatr.* **2013**, *80* (4), 229–241.

(294) Pignolo, R. J.; Xu, M.; Russell, E.; Richardson, A.; Kaplan, J.; Billings, P. C.; Kaplan, F. S.; Shore, E. M. Heterozygous Inactivation of Gnas in

Adipose-Derived Mesenchymal Progenitor Cells Enhances Osteoblast Differentiation and Promotes Heterotopic Ossification. *J. Bone Miner. Res.* **2011**, *26* (11), 2647–2655.

(295) Liu, J.; Russell, E.; Zhang, D.; Kaplan, F. S.; Pignolo, R. J.; Shore, E. M. Paternally Inherited Gsα Mutation Impairs Adipogenesis and Potentiates a Lean Phenotype in Vivo. *Stem Cells* **2012**, *30* (7), 1477–1485.

(296) Abe, Y.; Rozqie, R.; Matsumura, Y.; Kawamura, T.; Nakaki, R.; Tsurutani, Y.; Tanimura-Inagaki, K.; Shiono, A.; Magoori, K.; Nakamura, K.; Ogi, S.; Kajimura, S.; Kimura, H.; Tanaka, T.; Fukami, K.; Osborne, T. F.; Kodama, T.; Aburatani, H.; Inagaki, T.; Sakai, J. JMJD1A Is a Signal-Sensing Scaffold That Regulates Acute Chromatin Dynamics via SWI/SNF Association for Thermogenesis. *Nat. Commun.* **2015**, *6* (1), 7052.

(297) Fang, L.; Zhang, M.; Li, Y.; Liu, Y.; Cui, Q.; Wang, N. PPARgene: A Database of Experimentally Verified and Computationally Predicted PPAR Target Genes. *PPAR Res.* **2016**, *2016*, 1–6.

(298) Kudryashova, E.; Kudryashov, D.; Kramerova, I.; Spencer, M. J. Trim32 Is a Ubiquitin Ligase Mutated in Limb Girdle Muscular Dystrophy Type 2H That Binds to Skeletal Muscle Myosin and Ubiquitinates Actin. *J. Mol. Biol.* **2005**, *354* (2), 413–424.

(299) Ran, X.; Gestwicki, J. E. Inhibitors of Protein-Protein Interactions (PPIs): An Analysis of Scaffold Choices and Buried Surface Area. *Curr. Opin. Chem. Biol.* **2018**, *44*, 75–86.

(300) Scott, D. E.; Bayly, A. R.; Abell, C.; Skidmore, J. Small Molecules, Big

Targets: Drug Discovery Faces the Protein-Protein Interaction Challenge. *Nat. Rev. Drug Discov.* **2016**, *15* (8), 533–550.

(301) Her, N.-G.; Oh, J.-W.; Oh, Y. J.; Han, S.; Cho, H. J.; Lee, Y.; Ryu, G. H.; Nam, D.-H. Potent Effect of the MDM2 Inhibitor AMG232 on Suppression of Glioblastoma Stem Cells. *Cell Death Dis.* **2018**, *9* (8), 792.

(302) Axelsson, H.; Almqvist, H.; Seashore-Ludlow, B.; Lundbäck, T. *Screening for Target Engagement Using the Cellular Thermal Shift Assay - CETSA*; Eli Lilly & Company and the National Center for Advancing Translational Sciences, 2016.

(303) Teruel, T.; Hernandez, R.; Benito, M.; Lorenzo, M. Rosiglitazone and Retinoic Acid Induce Uncoupling Protein-1 (UCP-1) in a P38 Mitogen-Activated Protein Kinase-Dependent Manner in Fetal Primary Brown Adipocytes. *J. Biol. Chem.* **2003**, *278* (1), 263–269.

(304) Mougin, C. Identification, Synthesis and Screening of the Properties of New Modulating Agents for Radical Polymerization., Ecole Polytechnique X, 2006.

(305) Cohen, J. B. *A Class-Book of Organic Chemistry*; Macmillan and Co., limited: London, 1920.

(306) Coutts, R. T.; El-Hawari, A.-M. Derivatives of 2-Pyrazolin-5-One. II. Catalyzed Sodium Borohydride Reduction of Some 4–(2-Nitrobenzylidene)-2-Pyrazolin-5-Ones. A Reappraisal. *Can. J. Chem.* **1975**, *53* (23), 3637–3644.

(307) Warpman Berglund, U.; Sanjiv, K.; Gad, H.; Kalderén, C.; Koolmeister, T.;

Pham, T.; Gokturk, C.; Jafari, R.; Maddalo, G.; Seashore-Ludlow, B.; Chernobrovkin, A.; Manoilov, A.; Pateras, I. S.; Rasti, A.; Jemth, A.-S.; Almlöf, I.; Loseva, O.; Visnes, T.; Einarsdottir, B. O.; Gaugaz, F. Z.; Saleh, A.; Platzack, B.; Wallner, O. A.; Vallin, K. S. A.; Henriksson, M.; Wakchaure, P.; Borhade, S.; Herr, P.; Kallberg, Y.; Baranczewski, P.; Homan, E. J.; Wiita, E.; Nagpal, V.; Meijer, T.; Schipper, N.; Rudd, S. G.; Bräutigam, L.; Lindqvist, A.; Filppula, A.; Lee, T.-C.; Artursson, P.; Nilsson, J. A.; Gorgoulis, V. G.; Lehtiö, J.; Zubarev, R. A.; Scobie, M.; Helleday, T. Validation and Development of MTH1 Inhibitors for Treatment of Cancer. *Ann. Oncol. Off. J. Eur. Soc. Med. Oncol.* **2016**, *27* (12), 2275–2283.

(308) Zebisch, K.; Voigt, V.; Wabitsch, M.; Brandsch, M. Protocol for Effective Differentiation of 3T3-L1 Cells to Adipocytes. *Anal. Biochem.* **2012**, *425* (1), 88–90.

Appendix A: Materials and Methods

For reader convenience, methods are arranged by chapter.

Chapter 2

Chemistry General Comments

All commercial reagents, reactants and solvents were purchased from Sigma and used without prior purification. Compounds were purified using flash chromatography, using a glass column and Geduran SI 60, 0.063-0.200 mm silica gel (EMD Millipore). Solutions were concentrated and dried on a rotavapor (Büchi) under reduced pressure. All reactions were monitored by TLC (Merck silica gel 60 F254 glass plates) under UV light (254 nm), as well as low resolution mass spectrometry (Waters Micromass LCT Premier Mass Spectrometer, ESI-TOF). Routine ^{1}H NMR measurements were performed on a Bruker AVIII HD 400 Nanobay spectrometer. Accurate ^{1}H and ^{13}C spectra were obtained on Bruker AVIIIHD 600 spectrometer. ^{1}H and ^{13}C NMR chemical shifts are reported in ppm (δ) relative to the ^{1}H and ^{13}C signals of the solvent ($CDCl_3$: δ 7.26). Coupling constants (*J*) are reported in Hz. Accurate compound mass analysis was performed on a Bruker µTOF ESI-TOF mass spectrometer. Melting points were determined using a Kofler hot stage microscope and are uncorrected. High Performance Liquid Chromatography-MS measurements were carried out using a Waters Autopurification System equipped with Waters 2489 UV/Vis detector, Waters 2424 ELS detector and SQ Detector 2. Chromolith Performance RP-18e, 3 × 100 mm and Phenomenex Kinetex 5µ EVO C18 100A, 3×100 mm columns were used for the analytical measurements using a gradient program; Chromolith

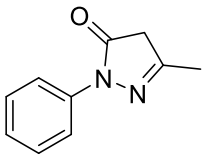
SemiPrep RP18-e 10×100 mm and Phenomenex 5µm EVO C18 100A 21.2 × 150 mm columns were used for the preparative HPLC purifications using a gradient program described below; Eluent A: MeCN/water = 1:19 with 20 mM ammonium acetate buffer, pH 6.0, Eluent B: MeCN/water = 4:1 with 20 mM ammonium acetate buffer, pH 6.0. IR measurements were obtained on a Bruker Tensor 27 open-access FTIR spectrometer and are rounded to the nearest cm^{-1}.

Step lenght (min)	Elapsed time (min)	%A	%B
1	1	100	0
10	11	0	100
3	14	0	100
1	15	100	0
5	20	100	0

Table 1: HPLC Conditions

Experimental Data

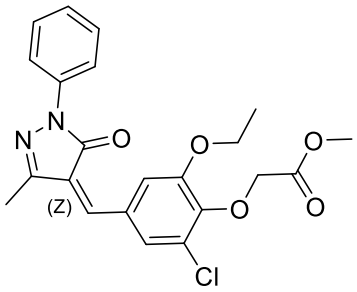
3-Methyl-1-phenyl-2-pyrazoline-5-one[304,305]



To a solution of phenylhydrazine (2.60 mL, 25.0 mmol, 1 eq.) in glacial AcOH (10 mL) was added ethylacetoacetate (3.20 mL, 25.0 mmol, 1 eq.) and the resulting solution was heated at 130 °C for 3 h. The mixture was cooled down to room temperature and partitioned between water and EtOAc. The organic layer was separated, dried (Na_2SO_4) and evaporated under reduced pressure. The residue was purified using flash chromatography (10% to 100% EtOAc in pentane) to afford the compound (2.50 g, 57%) as a light yellow crystalline solid.

^{1}H NMR (400 MHz, $CDCl_3$) δ 7.79 (d, *J* = 7.8 Hz, 2H), 7.32 (t, *J* = 8.0 Hz, 2H), 7.12 (t, *J* = 7.4 Hz, 1H), 3.37 (s, 2H), 2.14 (s, 3H); LRMS ESI^{+} found MS *m/*z 175 for $[M+H]^{+}$. The data were in accordance with those of the literature.

Methyl (*Z*)-2-(2-chloro-6-ethoxy-4-((3-methyl-5-oxo-1-phenyl-1,5-dihydro-4H-pyrazol-4-ylidene)methyl)phenoxy)acetate; SJ-172550[304]

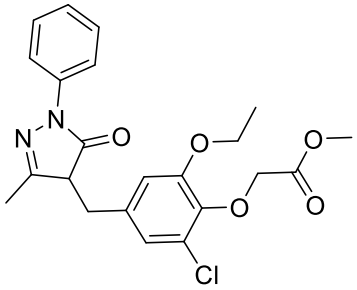


A solution of compound **1** (65 mg, 0.374 mmol, 1 eq.) in iPrOH (1.12 mL) was added slowly (1.5 mL/h) to a solution of methyl 2-(2-chloro-6-ethoxy-4-formylphenoxy)acetate (102 mg, 0.374 mmol, 1 eq.) in iPrOH (1.12 mL) before addition of catalytic piperidine (2 drops) and the resulting mixture was heated at 60 °C for 18 h. The mixture was then cooled down to room temperature and concentrated under reduced pressure. The product was purified using flash chromatography (50% to 100% CH_2Cl_2 in pentane) to afford the compound (40 mg, 25%) as an orange solid.

^{1}H NMR (500 MHz, $CDCl_3$) δ 8.95 (d, *J* = 2.0 Hz, 1H), 7.92 (d, *J* = 7.5 Hz, 2H), 7.60 (d, *J* = 2.0 Hz, 1H), 7.41 (t, *J* = 8.6, 7.3 Hz, 2H), 7.23–7.16 (m, 2H), 4.86 (s, 2H), 4.24 (q, *J* = 7.0 Hz, 2H), 3.82 (s, 3H), 2.32 (s, 3H), 1.47 (t, *J* = 7.0 Hz, 3H); ^{13}C NMR (126 MHz, $CDCl_3$) δ 169.4, 162.0, 151.6, 150.8, 147.4, 145.3, 138.4, 129.4, 129.0, 129.0 (2C), 127.5, 127.3, 125.2, 119.5 (2C), 116.4, 69.4, 65.3, 52.3,

14.7, 13.4; LRMS ESI^+ found MS *m/*z 429 for $[M+H]^+$. The data were in accordance with those of the literature.

Methyl 2-(2-chloro-6-ethoxy-4-((3-methyl-5-oxo-1-phenyl-4,5-dihydro-1H-pyrazol-4-yl)methyl)phenoxy)acetate; SJ-Reduced[306]

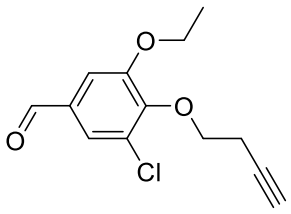


A solution of $NaBH_4$ (3.9 mg, 0.100 mmol, 2 eq.) in 50% aqueous 1,4-dioxane (1.2 mL) was added dropwise to a solution of compound **2** (22 mg, 0.050 mmol, 1 eq.) in 1,4-dioxane (2 mL). The mixture was stirred at 0 °C for 1 h (until the complete disappearance of colour). The reaction was then was partitioned between water and EtOAc, the organic layer was separated, dried (Na_2SO_4) and evaporated under reduced pressure. The product was purified using flash chromatography (50% EtOAc in pentane) to afford the compound (14 mg, 67% yield) as a crystalline white solid.

m.p.=145-150 °C (EtOAc), by comparison, 3-methyl-4-(2-nitrobenzyl)-1-phenyl-2-pyrazolin-5-one: m.p. of 168-169 °C;[306] ν_{max} (film)/cm^{-1} = 3313 (O-H) 2919 (C=C-H) 2850 (C-C-H) 1762 (C=O) 1696 (C=O) 1220 (C-O) 1202 (C-O) 1148 (C-O); ^1H NMR (600 MHz, $CDCl_3$) δ 7.65 (d, *J* = 9.8 Hz, 2H), 7.35 (t, *J* = 8.3, 7.6 Hz, 2H), 7.17 (t, *J* = 7.4 Hz, 1H), 6.77 (d, *J* = 2.0 Hz, 1H), 6.53 (d, *J* = 2.0 Hz, 1H), 4.54 (s, 2H), 3.85 (td, *J* = 7.0, 2.2 Hz, 1H), 3.78 (s, 3H), 3.64 (q, *J* = 9.1, 6.9 Hz, 2H), 3.13 (d, *J* = 13.3 Hz, 1H), 3.01 (d, *J* = 13.3 Hz, 1H), 2.17 (s, 3H), 1.24 (t,

J = 7.5 Hz, 3H); ^{13}C NMR (151 MHz, $CDCl_3$) δ 173.1, 169.5, 160.9, 152.2, 143.4, 137.3, 129.0 (3C), 127.7, 125.7, 123.0, 119.0 (2C), 113.3, 80.5, 69.4, 64.9, 52.2, 42.5, 14.7, 13.7; LC/MS retention time 1.53 min and 1.61 min for the tautomers, 100% UV254, 431 $[M+H]^+$; HRMS ESI$^+$ calculated for $C_{22}H_{24}O_5N_2{}^{35}Cl$: 431.13683; found MS *m/*z 431.13658 for $[M+H]^+$

4-(But-3-yn-1-yloxy)-3-chloro-5-ethoxybenzaldehyde

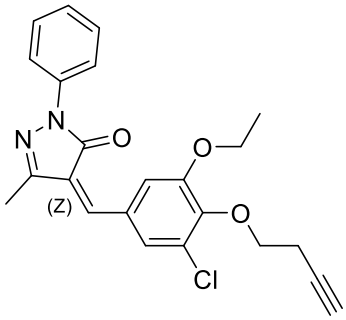


4-Bromo-1-butyne (338 µL, 3.75 mmol, 3 eq.) and K_2CO_3 (259 mg, 1.87 mmol, 1.5 eq.) were sequentially added to a solution of 3-chloro-5-ethoxy-4-hydroxybenzaldehyde (250 mg, 1.25 mmol, 1 eq.) in DMF (10 mL) and the mixture stirred at 80 °C for 3 h. The mixture was subsequently partitioned between water and EtOAc, the aqueous layer extracted three times with EtOAc, and the combined organic layers washed five times with brine. The organic layer was then dried (Na_2SO_4) and evaporated under reduced pressure. The product was purified using flash chromatography (20% to 100% EtOAc in pentane) to afford the compound (220 mg, 70%) as a crystalline white solid.

m.p. = 77-79 °C (EtOAc); ν_{max} (film)/cm^{-1} = 3273 (C≡C-H) 2979 (C=C-H) 2936 (C=C-H) 2827 (C-C-H) 1695 (C=O) 1137 (C-O); ^{1}H NMR (600 MHz, $CDCl_3$) δ 9.84 (s, 1H), 7.48 (d, *J* = 1.8 Hz, 1H), 7.33 (d, *J* = 1.8 Hz, 1H), 4.26 (t, *J* = 7.2 Hz, 2H), 4.15 (q, *J* = 7.0 Hz, 2H), 2.73 (td, *J* = 7.2, 2.7 Hz, 2H), 2.01 (t, *J* = 2.7 Hz, 1H), 1.49 (t, *J* = 7.0 Hz, 3H); ^{13}C NMR (151 MHz, $CDCl_3$) δ 190.1, 153.6, 149.7,

132.7, 129.2, 125.7, 110.5, 80.3, 71.4, 70.1, 65.1, 20.5, 14.8; LC/MS retention time 2.5 min, 100% UV254, 253 $[M+H]^+$; HRMS ESI+ calculated for $C_{13}H_{14}O_3{}^{35}Cl$: 253.0626; found MS *m/z* 253.0627 for $[M+H]^+$

(*Z*)-4-(4-(But-3-yn-1-yloxy)-3-chloro-5-ethoxybenzylidene)-5-methyl-2-phenyl-2,4-dihydro-3H-pyrazol-3-one; SJ-Alkyne

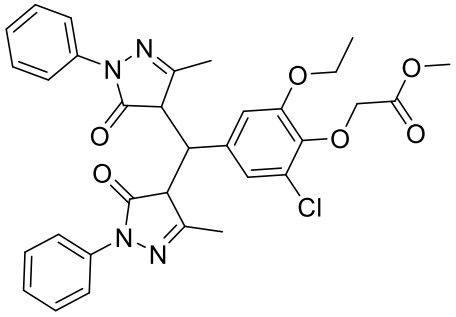


Title product **5** was prepared following the procedure described for compound **2**. Compound **1** (65 mg, 0.374 mmol, 1 eq.) afforded after purification using flash chromatography (50% to 100% CH_2Cl_2 in pentane) the compound (27 mg, 18%) as an orange solid.

m.p. = 128-132 °C (CH_2Cl_2); ν_{max} (film)/cm^{-1} = 3282 (C≡C-H) 3074 (C=C-H) 2921 (C-C-H) 2852 (C-C-H) 2120 (C≡C) 1676 (C=O) 1614 (C=N) 1137 (C-O); ^{1}H NMR (600 MHz, $CDCl_3$) δ 8.89 (d, *J* = 2.0 Hz, 1H), 7.93 (d, *J* = 8.8 Hz, 2H), 7.64 (d, *J* = 2.0 Hz, 1H), 7.42 (t, *J* = 8.1, 7.6 Hz, 2H), 7.23–7.17 (m, 2H), 4.33–4.23 (m, 4H), 2.73 (td, *J* = 7.3, 2.7 Hz, 2H), 2.33 (s, 3H), 2.02 (t, *J* = 2.6 Hz, 1H), 1.52 (t, *J* = 7.0 Hz, 3H); ^{13}C NMR (151 MHz, $CDCl_3$) δ 162.0, 152.8, 150.8, 148.4, 145.4, 138.4, 129.6, 129.0 (2C), 128.8, 128.1, 127.6, 125.2, 119.6 (2C), 116.3, 80.4, 71.4, 70.1, 65.2, 20.5, 14.9, 13.5; LC/MS retention time 2.21 min,

100% UV254, 409 $[M+H]^+$; HRMS ESI^+ calculated for $C_{23}H_{22}O_3N_2{}^{35}Cl$: 409.1314; found MS *m/*z 409.1309 for $[M+H]^+$

Methyl 2-(4-(*bis*(3-methyl-5-oxo-1-phenyl-4,5-dihydro-1H-pyrazol-4-yl)methyl)-2-chloro -6-ethoxyphenoxy)acetate; SJ-Bis



A solution of compound **1** (130 mg, 0.748 mmol, 2 eq.) in iPrOH (2.25 mL) was added slowly (1.5 mL/h over 1 h) to a solution of methyl 2-(2-chloro-6-ethoxy-4-formylphenoxy)acetate (102 mg, 0.374 mmol, 1 eq.) in iPrOH (1.12 mL) with catalytic piperidine (2 drops), at 60 °C. When the addition was complete, the mixture was subsequently cooled to room temperature and concentrated under reduced pressure. The product was purified using flash chromatography (4% MeOH in CH_2Cl_2) to afford the title product (48 mg, 21%) as a crystalline white solid.

m.p. = 131-133 °C (CH_2Cl_2); ν_{max} (film)/cm^{-1} = 3066 (C=C-H) 2921 (C-C-H) 2358 1762 (C=O) 1740 (C=O) 1596 (C=N) 1577 (C=N) 1130 (C-O); ^{1}H NMR (600 MHz, $CDCl_3$) δ 7.60 (d, *J* = 7.9 Hz, 4H), 7.30 (t, *J* = 8.0 Hz, 4H), 7.14 (t, *J* = 7.4 Hz, 2H), 6.84 – 6.75 (m, 2H), 4.71 (s, 1H), 4.58 (s, 2H), 3.87 (q, *J* = 7.0 Hz, 2H), 3.79 (s, 3H), 2.19 (s, 6H), 1.29 (t, *J* = 7.0 Hz, 3H) (note that this reflects the enol, rather than the keto form of the compound); ^{13}C NMR (151 MHz, $CDCl_3$) δ

170.1, 157.8 (2C), 152.1, 146.7 (2C), 141.8, 138.2, 137.3 (2C), 129.1 (4C), 127.3, 126.3 (2C), 121.4 (4C), 120.6, 111.8, 105.3 (2C), 69.3, 64.7, 52.3, 33.7, 14.7, 12.0 (2C); LC/MS retention time 1.57 min, 100% UV254, 603 $[M+H]^+$; HRMS ESI^+ calculated for $C_{32}H_{32}O_6N_4{}^{35}Cl$: 603.2005; found MS *m/*z 603.2002 for $[M+H]^+$.

Protein Expression and Purification

Plasmids containing the p53-binding region of human MDMX (pGEX6P2-*MDMX* (1-120)) were obtained from Addgene (plasmid #62063 and #62065)[156]. Proteins were expressed in BL21(DE3) RIL competent cells by transformation of the plasmid DNA (100 ng). Following transformation, cells were grown overnight on ampicillin-positive agar plates. Individual colonies were grown in TB medium at 37 °C and induced with 1mM IPTG at OD_{600} of 0.8, at which point the temperature was shifted to 20 °C and the cells grown overnight in the incubator. Cultures were the centrifuged at 5,000 × g for 45 min at 4 °C and the pellets frozen at –20 °C. The following day, the pellets were resuspended in GST binding buffer (150 mM NaCl, 3 mM KCl, 10 mM Na_2HPO_4, 2 mM KH_2HPO_4, pH 7.3) and lysed with a French press. The lysate was clarified by centrifugation at 24,000 × g for 1 h at 4 °C and the supernatant was purified by GST-affinity chromatography (AktaPrime Plus) at 4 °C. Fractions containing the fusion protein were collected, and the GST tag was cleaved using Precision Protease (GE Healthcare) according to the manufacturer's specifications. Upon further purification using sise-exclusion chromatography the protein was concentrated and frozen at –80 °C. Protein identity and purity were confirmed by SDS-PAGE and MALDI-TOF. (NuPAGE Bis-Tris Gel, ThermoFisher).

Sequence of the MDMX construct used in the study:

```
        10         20         30         40         50         60
GPLGSMTSFS TSAQCSTSDS ACRISPGQIN QVRPKLPLLK ILHAAGAQGE MFTVKEVMHY

        70         80         90        100        110        120
LGQYIMVKQL YDQQEQHMVY CGGDLLGELL GRQSFSVKDP SPLYDMLRKN LVTLATATTD


AAQTL
```

The 3 cysteines are highlighted. Predicted MW is 13640

Differential Scanning Fluorimetry

The thermal shift assay (DSF) was performed according to previously-established protocols[36]. Briefly, MDMX was diluted to a final concentration of 2 µM in HEPES-NaCl buffer (20 mM HEPES, 150 mM NaCl, pH 7.5) in a 384-well PCR assay plate (PerkinElmer). SJ-172550 was dispensed across the wells, in triplicates, to a final concentration of 20 µM (or equivalent DMSO volume). Stock SYPRO Orange (LifeTechnologies) was added at 1:1000 dilution to a final volume of 20 µL per well. MDMX was melted in an RT-PCR (MX3005p, Agilent) instrument at 0.19 °C s^{-1}, 20 to 95 °C, with three acquisitions of fluorescence intensity per cycle. The melting temperature (T_M) was calculated as the mid-point on the sigmoidal curve fitted between the onset and endpoint of unfolding.

Isothermal Titration Calorimetry

All experiments were done at 15 °C using an ITC buffer containing 20 mM HEPES, pH 7.5 and 150 mM NaCl. The protein was dialysed overnight at 4 °C into ITC buffer. MDMX concentration was 200 μM (loaded in the syringe), and the compound concentration 20 μM (cell). The titrations were conducted using an initial injection of 0.2 μL followed by 19 injections of 4 μL. The dilution heats were determined in separate experiments and subtracted from the titration data. Thermodynamic parameters were calculated using $\Delta G = \Delta H - T\Delta S = RT \ln K_D$, where ΔG, ΔH, and ΔS are the changes in free energy, enthalpy, and entropy of binding, respectively. In all cases, a single binding site model was employed.

Protein Mass Spectrometry

To a 100 μL solution of MDMX in a 20 mM HEPES 150 mM NaCl buffer (pH 7.5) at 1 mg/mL was added each compound to a final concentration of 100 μM, and the mixture was incubated at RT for 1 hour. Reversed-phase chromatography was performed in-line prior to mass spectrometry using an Agilent 1290 μHPLC system (solvent A 0.1% HCOOH in ultra-high purity water, solvent B 0.1% HCOOH in MeOH). 1 μL of each mixture was added to 59 μL of solvent A and 50 μL of the resulting mixture was injected onto a 2.1 mm × 12.5 mm *Zorbax* 5um 300SB-C3 guard column housed in a column oven set at 40 ºC. Chromatography was performed with a flow rate of 1.0 ml/min and a linear gradient 10 % → 80 % solvent B in solvent A over 35 seconds. Elution then proceeded isocratically at 95 % B for 40 seconds followed by equilibration at 10 % solvent B in solvent A for a further 15 seconds. Compound mass was determined using a 6530 electrospray ionisation quadrupole time-of-flight mass

spectrometer (Agilent). The instrument was configured with the standard ESI source and operated in positive ion mode. The ion source was operated with the capillary voltage at 4000 V, nebuliser pressure at 60 psig, drying gas at 350ºC and drying gas flow rate at 12 L/min. The instrument ion optic voltages were as follows: fragmentor 250 V, skimmer 60 V and octopole RF 250 V.

Cell Culture and Viability Testing

U2OS cells were obtained from ATCC and cultured in McCoy's 5A medium supplemented with 10% v/v FCS and 1% v/v GlutaMAX (Gibco) at 37 °C and 5% CO_2. All compounds were dissolved in DMSO and kept as 10 mM stock solutions at –20 °C, with routine quality control via LC/MS. For viability testing, a 96-well tissue culture plate (Corning) was seeded with 5,000 cells per well; serial dilutions of compounds were added 24 hours later with bortezomib serving as a positive control. DMSO was kept constant at 1% v/v. Following 72 h of incubation, the plate was assayed with the Cell-Titer Glo Luminescent Cell Viability Assay (Promega), according to manufacturer's specifications.

Western Blotting

Following SDS-PAGE, transfer to nitrocellulose blotting membrane was performed for 30 minutes at 100 V (Amersham, GE healthcare). Subsequently, membranes were blocked with blocking buffer (2.5% (m/v) BLOT-QuickBlocker (Merck) in PBST (Phosphate-buffered saline with 0.05% (v/v) Tween 20) for 1 hour at RT before probing with primary antibodies (4 °C, overnight). Blots were then washed 3 times in PBST, then probed for 1 hour with secondary antibodies, then washed 3 times again. Blots were imaged on an Odyssey CLx imager (LI-

COR), with quantitative analysis performed using Image Studio Lite 5.2 and GraphPad Prism 7 software. Antibodies: Primary Bethyl A300-287A 1:1000, Secondary: Alexa Fluor Goat anti-rabbit (ThermoFisher), 1:10 000

Cellular Thermal Shift Assay (CETSA)

The CETSA assay was performed according to previously-reported procedures[100]. U2OS cells were pre-treated with 10 µM MG-132 for one hour. Subsequently, one flask was treated with 100 µM SJ-172550 in DMSO, whereas the control flask was treated with an equivalent volume of DMSO for one hour. The cells were then harvested and aliquoted for heating to different temperatures for 3 minutes, followed by snap-freezing and lysis in liquid nitrogen with the addition of a RIPA buffer supplemented with protease and phosphatase inhibitors (Sigma). The insoluble fraction was removed by centrifugation at 17,000 × g for 20 minutes. BCA assay was performed on the soluble fraction, and 45 µg of protein was used for SDS-PAGE and Western Blotting.

Activity-Based Protein Profiling (ABPP) and Affinity Pulldown

The bioconjugation assay was performed according to previously reported procedures[91]. To a solution of 200 µL of U2OS lysate at 5 mg/mL (1 mg total protein per pulldown) was added SJ-Alkyne in DMSO to achieve a final concentration of 100 µM (or equivalent volume of DMSO in the control group), and the lysate was incubated for 1 hour at 4 °C (the temperature was deliberately chosen to prevent degradation of SJ-Alkyne). Subsequently, $CuSO_4$, THPTA, sodium ascorbate and biotin azide (Sigma) were added to a final concentration of 100 µM, 500 µM, 2.5 mM and 100 µM, respectively, and the lysates were

incubated for another 2 hours at 4 °C. Afterwards, the lysates were added onto Streptavidin Sepharose High Performance resin (Sigma/GE Healthcare) and incubated for a further 2 hours at 4 °C. The supernatant was eluted, and the resin washed with PBS, followed by elution with Laemmli Buffer, and separated SDS-PAGE, followed by either Coomassie staining and imaging or Western Blot, as described above.

Lysate Binding In-gel Fluorescence Assay

The assay was performed similarly to as described above. Briefly, to a solution of 200 µL of U2OS lysate at 2 mg/mL was added 1 µL of SJ-Alkyne solution in DMSO at varying concentrations to achieve final concentrations ranging from 1 to 100 µM, and the lysates were incubated for 1 hour at 4 °C (the temperature was deliberately chosen to prevent degradation of SJ-Alkyne). Subsequently, $CuSO_4$, THPTA, sodium ascorbate and cyanine-5.5-azide (Lumiprobe) were added to a final concentration of 100 µM, 500 µM, 2.5 mM and 100 µM, respectively, and the lysates were incubated for another 2 hours at 4 °C. The proteins were extracted and cleaned using a mixture of chloroform and methanol, and subsequently separated by SDS-PAGE, following by fluorescence imaging on the Odyssey CLx imager (LI-COR) system.

Compound Degradation Assay

SJ-172550, C646 and SJ-Bis were dissolved in HEPES buffer (20 mM HEPES, pH 7.5 and 200 mM NaCl) to make stock solutions ranging from 1 µM to 200 µM in concentration in order to create a standard curve of concentrations. Subsequently, each compound was added to HEPES buffer to a final

concentration of 100 µM, and incubated at 37 °C. LC/MS measurements of samples were taken as described above at T=0, 1, 2, 3 and 4 hours and compound concentration at each time point was determined using the standard curve.

Measuring TCEP/Glutathione Reactivity via MS

To a solution of 100 µM GSH in water was added equimolar SJ-172550 to a final volume of 100 µL, and the mixture was incubated at RT for 1 hour. To a 100 µM SJ-172550 or C646 in DMSO was added equimolar TCEP to a final volume of 100 µL, and the mixture was incubated for 10 minutes, with color change occurring instantly. Reversed-phase chromatography was performed in-line prior to mass spectrometry using an Agilent 1290 µHPLC system (solvent A 0.1% HCOOH in ultra-high purity water, solvent B 0.1% HCOOH in MeOH). 1 µL of each mixture was added to 59 µL of solvent A and 50 µL of the resulting mixture was injected onto a 2.1 mm × 12.5 mm *Zorbax* 5um 300SB-C3 guard column housed in a column oven set at 40 ^{o}C. Chromatography was performed with a flow rate of 1.0 ml/min and a linear gradient 10 % → 80 % solvent B in solvent A over 35 seconds. Elution then proceeded isocratically at 95 % B for 40 seconds followed by equilibration at 10 % solvent B in solvent A for a further 15 seconds. Compound mass was determined using a 6530 electrospray ionisation quadrupole time-of-flight mass spectrometer (Agilent). The instrument was configured with the standard ESI source and operated in positive ion mode. The ion source was operated with the capillary voltage at 4000 V, nebuliser pressure at 60 psig, drying gas at 350^{o}C and drying gas flow rate at 12 L/min. The instrument ion

optic voltages were as follows: fragmentor 250 V, skimmer 60 V and octopole RF 250 V.

Chapter 3

Cell culture and General Remarks

KMS11 cells were obtained from ATCC and cultured in RPMI-1640 medium supplemented with 10% v/v FCS and 1% v/v GlutaMAX (Gibco) at 37 °C and 5% CO_2. GSK3326595 was purchased from MedChemExpress and dissolved in DMSO and kept as 10 mM stock solutions at –20 °C, with routine quality control via LC/MS.

Western Blotting

Western blotting was performed as outlined earlier. Antibodies used: anti-PRMT5: ab109451 (abcam), 1:1000, anti-CAP1: ab88446 (abcam) 1:1000, anti MEP50: 2823 (Cell Signalling), 1:1000.

CETSA

CETSA-WB was performed as described earlier.

2D MS-CETSA was performed according to previously-described protocols[307]. 5 flasks of confluent KMS-11 cells were treated with the following concentrations of GSK33265905: 5, 1, 0.2, 0.04 µM or equivalent volume of DMSO for one hour. The cells were then harvested and aliquoted for heating to different temperatures for 3 minutes, followed by snap-freezing and lysis in liquid nitrogen with the addition of an NP-40 lysis buffer supplemented with protease and

phosphatase inhibitors (Sigma). The insoluble fraction was removed by centrifugation at 17,000 × g for 20 minutes. BCA assay was performed on the soluble fraction, and 100 µg of protein was taken for MS analysis. Protein reduction was performed by addition of DTT up to a final concentration of 5 mM, followed by a 60 min incubation at RT. Alkylation was performed by addition of iodoacetamide to final concentration 20 mM and incubating for 60 minutes at RT. Afterwards, the protein content was precipitated by the addition of cold (–20 °C) acetone and overnight precipitation at –20°C. Samples were then centrifuged at 8,000 x g for 10 minutes at 4 °C and acetone decanted carefully, leaving the pellet to dry for 10 minutes. Dry pellets were resuspended in 100 µL of 50 mM TEAB, followed by vortexing and sonication. Digestion was performed by the addition of 2.5 µg of Trypsin/Lys C solution (Promega) and overnight incubation at 37 °C, with shaking. TMT label reagents (ThermoFisher) were equilibrated at RT, then dissolved in 90 µL anhydrous acetonitrile. 27 µL of the label was then added to the peptides as per the following layout:

Temp (°C)	126	127L	127H	128L	128H	129L	129H	130L	130H	131	RefCol	
42	5	1	0.2	0.04	0	-	-	-	-	-	128H	F1
62	-	-	-	-	-	5	1	0.2	0.04	0	131	
44	5	1	0.2	0.04	0	-	-	-	-	-	128H	F2
64	-	-	-	-	-	5	1	0.2	0.04	0	131	
46	5	1	0.2	0.04	0	-	-	-	-	-	128H	F3
58	-	-	-	-	-	5	1	0.2	0.04	0	131	
48	5	1	0.2	0.04	0	-	-	-	-	-	128H	F4
60	-	-	-	-	-	5	1	0.2	0.04	0	131	
50	5	1	0.2	0.04	0	-	-	-	-	-	128H	F5
54	-	-	-	-	-	5	1	0.2	0.04	0	131	
52	5	1	0.2	0.04	0	-	-	-	-	-	128H	F6
56	-	-	-	-	-	5	1	0.2	0.04	0	131	

The reaction was incubated for 1 hour at RT, followed by quenching for 15 minutes by the addition of 8 µL of 5% hydroxylamine. Samples were pooled

according to the above figure and desalted using C18 spin tips (Pierce), followed by solvent removal under reduced pressure in a SpeedVac Vacuum concentrator. Samples were then resuspended in 120 µL Buffer A (v/v 98% MilliQ-H_2O, 2% CH_3CN, 0.1% FA) and fractionated at pH 10 with concatenation into 10 fractions on a UltiMate 3000 HPLC system (Thermo) using a 60 minute gradient of 0% to 90% CH_3CN in H_2O. Fractions were dried under reduced pressure in a SpeedVac Vacuum concentrator and resuspended in 100 µL Buffer A. Subsequently they were analysed by nano-HPLC–MS/MS using a Dionex Ultimate 3000 nano HPLC with EASY spray column (75 µm × 500 mm, 2 µm particle sise, Thermo Scientific) with a 60 min gradient of 2% to 35% (v/v) CH_3CN in H_2O with 5% (v/v) DMSO and 0.1% (v/v) HCOOH at a flow rate of approximately 250 nL/min (600 bar per 40 °C column temperature). Measurements were performed using the Q Exactive™ HF Hybrid Quadrupole-Orbitrap™ Mass Spectrometer (Thermo Fisher). MS1 survey scans were acquired at a resolution of 60,000 at 375-1500 m/z and the 20 most abundant precursors were selected for CID fragmentation in a HCD cell. MS2 data were analysed in Thermo Proteome Discoverer 2.1 according to the manufacturer's protocol.

Chapter 4

Cell culture and General Remarks

A549 and SW620 cells were obtained from ATCC and cultured in Dulbecco's modified Eagle medium supplemented with 10% v/v FCS and 1% v/v GlutaMAX (Gibco) at 37 °C and 5% CO_2. Mouse 3T3-L1 preadipocytes were obtained from Zen-Bio and cultured in Dulbecco's modified Eagle medium supplemented with

10% v/v FCS, 1% v/v GlutaMAX (Gibco), 33 µM biotin (MP Biomedicals UK), 17 µM pantothenic acid (MP Biomedicals UK). 3T3-L1 cells were differentiated according to previously-described protocols[308]. Rosiglitazone and Pioglitazone were purchased from Sigma. Metformin was purchased from Cayman Chemical Company. S26948 and LG100268 were purchased from Tocris. Saroglitazar, Honokiol and Magnolol were purchased from MedChem Express. GW7647 was purchased from Cambridge Bioscience. GW9662 was purchased from Stratech Scientific.

Western Blotting and CETSA

Western blotting was performed as outlined earlier. Antibodies used: anti- PPARγ (81B8), Cell Signalling, 1:1000. CETSA-WB experiments were performed as described earlier.

Chapter 5

Double-Antibody Pulldown

Firstly, antibody buffer exchange was performed using the Amicom ultra centrifugal filters according to the manufacturer's protocol to place it in borate buffer pH 8.5 at 4°C. NHS-activated Sepharose 4 Fast Flow (GE Healthcare) was pipetted was washed in 500 µL ice-cold PBS pH 7.0; the antibody solution was then added to the beads with 0.75 µL TEA to initiate the conjugation to the resin. The mixture was incubated on roto-shaker overnight (later reduced to 1 hour). The conjugation was quenched with 2.5 µL ethanolamine and a further 2 hour incubation on roto-shaker at 4 °C, followed by centrifugation at 1000 rpm for 3

minutes and removal of the supernatant. For the second-antibody pulldown, at the same time, 500 µL of fresh A549 or SW620 lysate at 4 µg/µl (2 mg total protein) was allowed to incubate with the second antibody for 2 hours at 4 °C on a roto-shaker and subsequently added to the resin. After gentle resuspension, the resin was incubated for 2 hours at 4 °C on a roto-shaker, followed by removal of the supernatant, washing with PBS and elution with Laemmli Buffer and analysis by SDS-PAGE and WB.

Biolayer-Interferometry Assay (BLI)

Firstly, antibodies were conjugated to biotin using the Chromalink kit according to manufacturer's specifications. BLI was performed using a BLI Octet RED384 (FortéBio Inc). Superstreptavidin biosensors (FortéBio Inc.) were coated in a solution containing 50 µg/mL of biotinylated antibody for 5 min at 25 °C. Recombinant full-length PPARγ was kindly donated from AstraZeneca. PPARγ-binding assays were performed at 25°C in a volume of 60 µL PBS at 1 µM PPARγ. A duplicate set of sensors without protein was used as a background binding control. Association of PPARγ was measured over 60 seconds and dissociation over 120. Data analysis was performed using GraphPad Prism.

Optimisation of the AlphaScreen-based CETSA Readout

Initially, antibodies were conjugated to the AlphaScreen acceptor beads (PerkinElmer) according to the manufacturer's protocol. Subsequently, optimisation of the AlphaScreen protocol was performed as previously-reported[115]. Initial antibody pair selection experiments were performed on recombinant protein. Four different conditions were tested, namely presence and

absence of recombinant PPARγ, presence of heat-denatured PPARγ, as well recombinant PPARγ in the presence of 50 µM rosiglitazone. All conditions were diluted in 1 x AlphaLISA buffer (AL000F, PerkinElmer) and the concentrations of each reagent were as follows: Strep-Donor Beads 17 µg/ml, antibody-acceptor beads 8 µg/ml, recombinant PPARγ 10 nM, biotin-Ab 1 nM to a total volume of 30 µL in an AlphaPlate (PerkinElmer). Although the manufacturer's protocol recommends adding the antibodies first, followed by the beads, in our experience the order of addition did not affect the signal. All the additions were performed under subdued light and the plates were allowed to incubate at room temperature for 2 h to overnight before reading in a PheraSTAR plate reader (BMG Labtech). Titrations were later performed with respect to biotinylated antibody and recombinant PPARγ concentration to ensure hook effect does not occur. The data were analysed using Microsoft Excel and GraphPad Prism.

The antibody pairs were then selected from the screen to study the recognition of PPARγ in 3T3-L1 lysate. Fresh 3T3-L1 cells were lysed using the AlphaLISA lysis buffer (PerkinElmer) and the lysate was used at 2 mg/ml in place of recombinant PPARγ. The remainder of the reagents was added as above and the plates were allowed to incubate at room temperature for 2 h to overnight before reading in a Pherastar plate reader (BMG Labtech). Titrations were later performed with respect to biotinylated antibody and 3T3-L1 lysate concentration. For experiments with spiked-in PPARγ, recombinant PPARγ was added in at concentrations ranging from 120 nM down to 0.23 nM.

One antibody pair was selected for live-cell experiments. Two batches of confluent 3T3-L1 cells in supplemented cell culture medium were prepared to serve as max and min controls. The cells were harvested and aliquoted in a 384-well hard-shell PCR plate (BioRad) at varying concentrations. One plate was kept at room temperature and the other was heated to 60 ° C for 3 min in a C1000 PCR machine (Biorad). Both batches of cells were then lysed by the addition of AlphaLISA lysis buffer. After thorough mixing, the plates were spun down and 10 µL aliquots of the lysates were transferred to a ProxiPlate and detected, followed by the addition of 10 µL of the antibody and bead mix, to the same final concentrations as described above.

Thermal Aggregation Experiments Using AlphaScreen

Rosiglitazone was added to a 3T3-L1 cell suspension at a density of 10 million cells per mL to a final concentration of 50 µM, and the suspension was aliquoted at 100 µL per well to a skirted Twin.tec PCR 96-wellplate (0030 128 672, Eppendorf). The PCR plates containing the compounds and cells were sealed with a breathable plate seal (3345, Corning) and incubated for 30 minutes in a humidified incubator at 37 °C and 5% CO_2. The cells were then transiently centrifuged for 3 min at 300 x g, the supernatant removed and the pellets heated to different temperatures ranging from 37 °C to 51 °C for 3 min, followed by a controlled cooling to 20 °C for 1 min using a real-time PCR machine (VWR). After the heating step the pellets were lysed with AlphaLISA lysis buffer (PerkinElmer). To ensure sufficient lysis the cell lysates were mixed by 10 repetitive aspiration and dispensing cycles using a multi-channel pipette. The

lysates (10 µL) were then transferred to 384-well ProxiPlates followed by the addition of 10 µL of a mix of antibodies and AlphaScreen acceptor and donor beads in AlphaLISA buffer under subdued light to the concentrations above. The plates were sealed with TopSeal-A PLUS and incubated over night at room temperature prior to detection in a PheraSTAR plate reader. The data were analysed using Microsoft Excel and GraphPad Prism 6. In ITDRF experiments, different concentrations of rosiglitazone were added at a volume of 1 µL per well to 100 µL per well of the cell suspension. In the screening format experiment, 1 µL of different compounds were added.

Chapter 6

General remarks

Cell culture performed as described earlier.

Immunoprecipitation and MS Analysis

Firstly, antibody buffer exchange was performed using the Amicom ultra centrifugal filters according to the manufacturer's protocol to place it in borate buffer pH 8.5 at 4 °C. NHS-activated Sepharose 4 Fast Flow (GE Healthcare) was pipetted was washed in 500 µL ice-cold PBS pH 7.0; the antibody solution was then added to the beads with 0.75 µL TEA to initiate the conjugation to the resin. The mixture was incubated on roto-shaker overnight (later reduced to 1 hour). The conjugation was quenched with 2.5 µL ethanolamine and a further 2 hour incubation on roto-shaker at 4 °C, followed by centrifugation at 1000 x *g* for 3 minutes and removal of the supernatant. Subsequently, 500 µL of fresh A549 or SW620 lysate at 4 µg/µL (2 mg total protein) was added to the resin. After gentle

resuspension, the resin was incubated for 2 hours at 4 °C on a roto-shaker, followed by removal of the supernatant, washing with PBS and elution with Laemmli Buffer. 10 µL of the eluant was taken for SDS-PAGE, and the rest for MS analysis. To reduce the sample, DTT was added to a final concentration 5 mM and the sample incubated at RT for 1 hour, followed by alkylation with iodoacetamide (final concentration 20 mM) and incubation for an additional 1 hour at RT. Protein content was precipitated via Methanol/Chloroform extraction and the pellet was resuspended in 50 µL 6 M urea with vortexing and sonication. Urea was diluted to <1 M with the addition of 250 µL MilliQ-H_2O. Digestion was performed with 2 µg of either trypsin or a trypsin-LysC combination (Promega) overnight at 37 ºC followed by purification and desalting using C18 spin tips (Pierce), followed by solvent removal under reduced pressure in a SpeedVac Vacuum concentrator. The pellet was then dissolved in 98% MilliQ-H20 2% CH_3CN 0.1% and injected into a Dionex Ultimate 3000 nano-HPLC coupled to a QExactive HF mass spectrometer (Thermo Scientific). Data was analysed using MaxQuant 1.6.2.10 software.

Lysate MS Analysis

Lysate from 3T3-L1 cells totalling 100 µg protein was reduced, alkylated, extracted, digested and desalted as described above. The peptides were then fractionated via reversed-phase high pH fractionation on the Bravo AssayMAP (Agilent), before MS analysis as described above.

CETSA

CETSA-WB and 2D MS-CETSA experiments were performed as described earlier.

Appendix B: Source Code for the MATLAB Algorithm

```
Unique_Accession_Codes = unique(input(:,1)); %get
the total number of different proteins (assumes
first column in the table)
fprintf("\nDetected %d unique accession
codes...\n\n", height(Unique_Accession_Codes))
%print the total number of different protein
for i = 1:height(Unique_Accession_Codes) %for
every protein:
    fprintf("Accession Code: %s\n",
Unique_Accession_Codes{i,:})  %display its
accession code
    output{i,1}=char(Unique_Accession_Codes{i,:});
%write its name to the output table

Protein_Name_ID=min(find(input{:,1}==Unique_Access
ion_Codes{i,:})); %find the index of the protein
name
    fprintf("Protein Name: %s\n",
input{Protein_Name_ID,4}) %display its name
(assumes fourth column in the table, change
accordingly)
    output{i,2}=char(input{Protein_Name_ID,4});
%write protein name to the output table
    if sum(input{:,2} == input{Protein_Name_ID,2})
~= 12 %assuming 12 temperatures, if there aren't
12 entires, skip
        fprintf("Number of occurences unequal to
12, skipping\n\n")
            for j = 3:7
                output{i,j}=NaN;
            end
    elseif sum(input{:,2} ==
input{Protein_Name_ID,2}) == 12
        fprintf("Number of occurences equal to 12,
proceeding\n")
        Values =
input{Protein_Name_ID:(Protein_Name_ID+11),15:18};
%create a 12x4 heat map for every protein
```

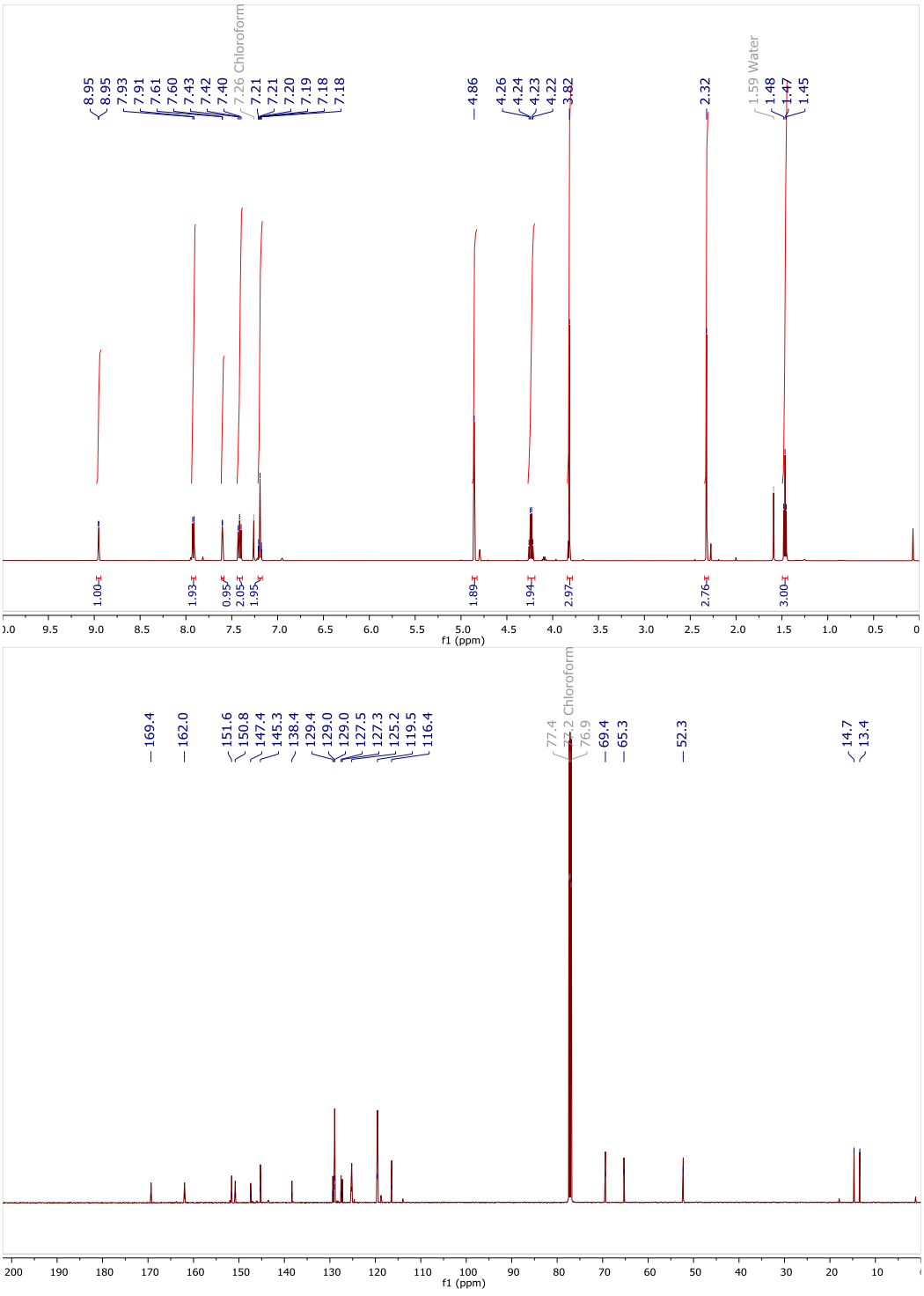
```
        Values = Values-1; %baseline correction
        concentrations= [0.04 0.2 1 5];
%concentrations of the compound - change
accordingly
        temperatures= [42:2:64]; %temperatures -
change accordingly
        if sum(isnan(Values),'all') >= 1
            fprintf("NaN values detected \n\n")
            output{i,3}=sum(isnan(Values),'all');
%if there are missing values, write how many
            for ii = 0:11 %trim the matrix to
remove missing values
                if (sum(isnan(Values(12-ii,1:4)))
>= 1)
                    Values(12-ii,:) = [];
                    temperatures(12-ii) = [];
                end
            end
        elseif sum(isnan(Values),'all') == 0 %if
no missing values, proceed
            fprintf("No NaN values detected \n")
            output{i,3}=0;
        end


[C,D]=meshgrid(concentrations,temperatures);
%create a meshgrid of temperatures and
concentrations
        try
        sf = fit( [D(:), C(:)], Values(:),
'linearinterp' ); %create a 3D surface based on
the values
        vol = quad2d( sf,
min(temperatures),max(temperatures),min(concentrat
ions),max(concentrations),'MaxFunEvals', 10000);
        output{i,4}=vol; %calculate the volume of
the 3d mesh without surface equation fitting
        catch
        output{i,4}=NaN;
        end
        try
        [f3, gof3] = fit( [D(:), C(:)], Values(:),
'poly31' ); %fit a surface to the heat map
```

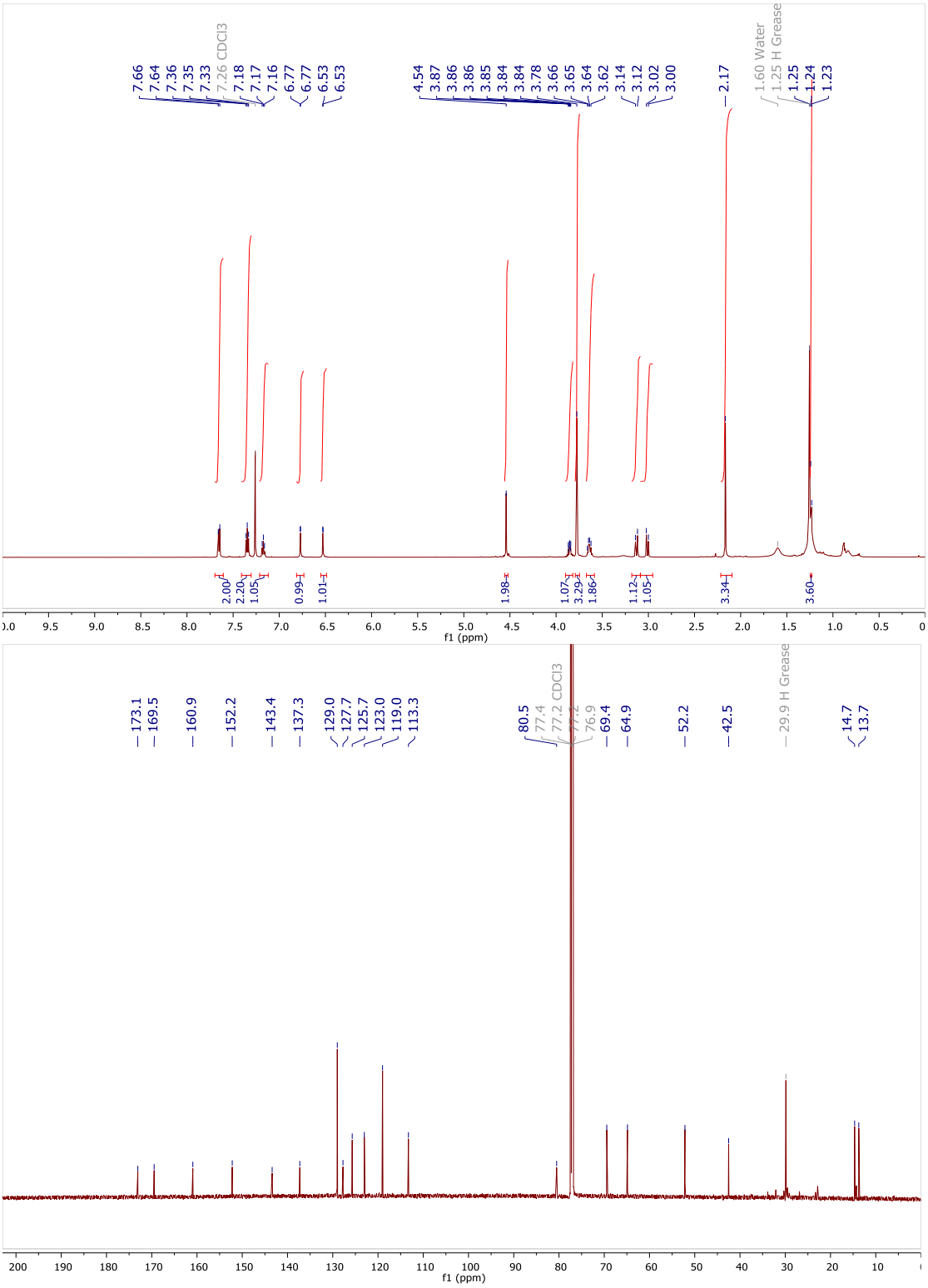
```
        adjvol3 = quad2d( f3,
min(temperatures),max(temperatures),min(concentrat
ions),max(concentrations),'MaxFunEvals', 10000);
        output{i,5}=adjvol3; %calculate its volume
and write to output
        output{i,6}=gof3.rsquare; %write goodness
of fit (R2) to the output
        output{i,7}=gof3.adjrsquare; %write
adjusted goodness of fit (R2) to the output
        catch
        output{i,5}=NaN;
        output{i,6}=NaN;
        output{i,7}=NaN;
        end
    end
end
```

Appendix C: Compound NMR Spectra

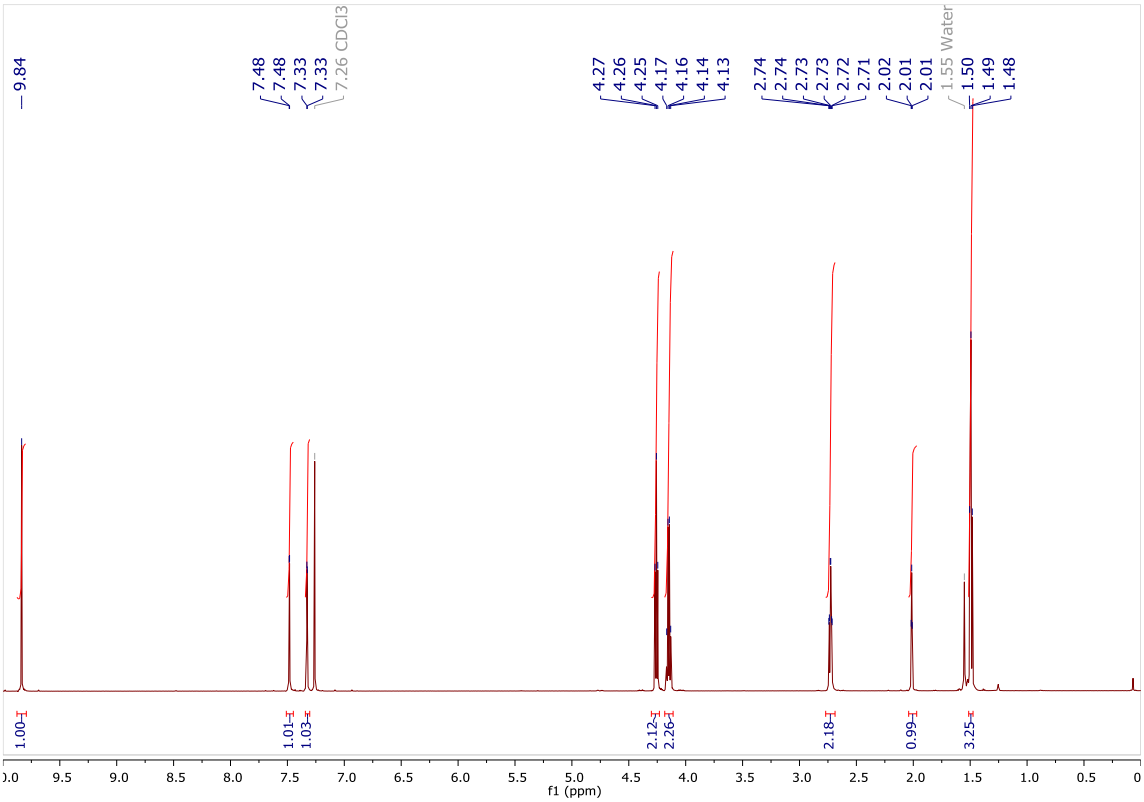
SJ-172550

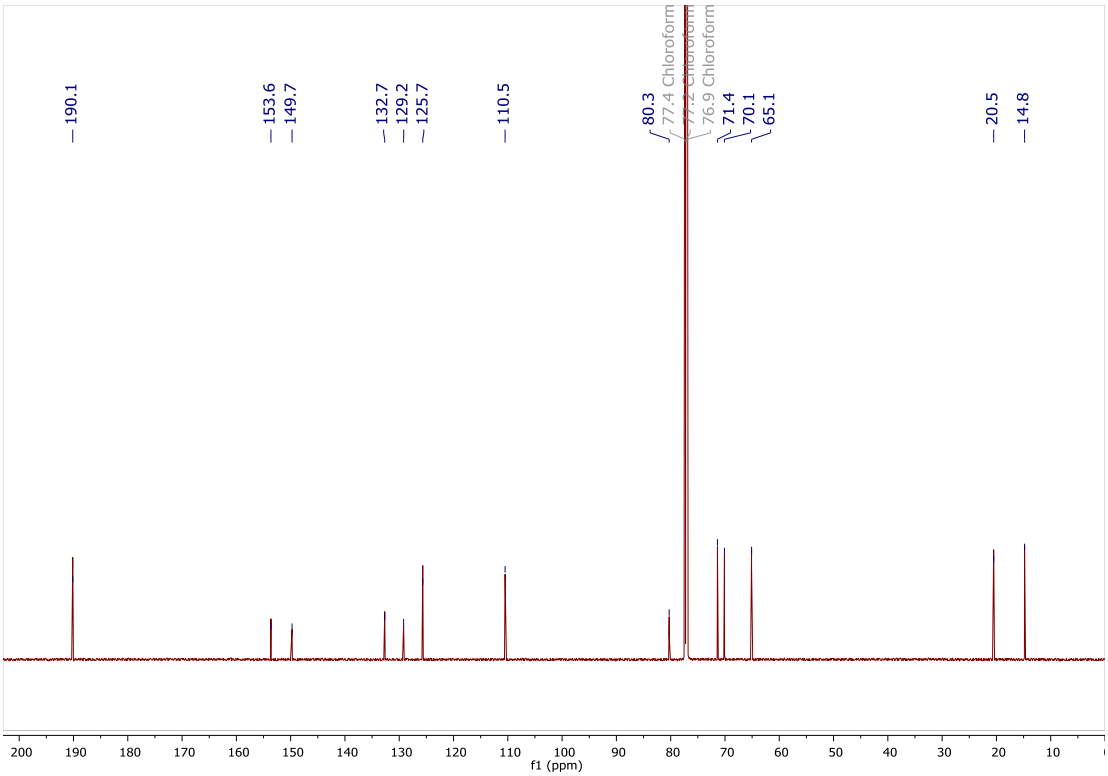


SJ-Reduced

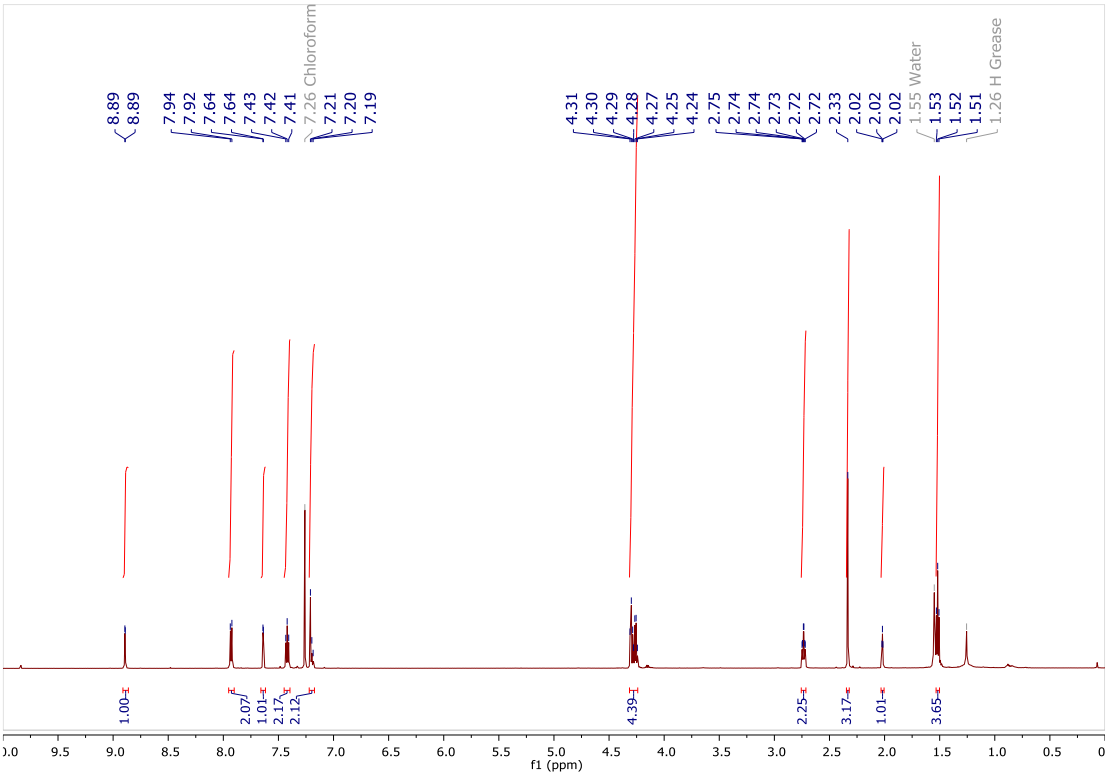

7.66
7.64
7.36
7.35
7.33
7.26 CDCl3
7.18
7.17
7.16
6.77
6.77
6.53
6.53
4.54
3.87
3.86
3.86
3.85
3.84
3.84
3.78
3.66
3.65
3.64
3.62
3.14
3.12
3.02
3.00
2.17
1.60 Water
1.25 H Grease
1.25
1.24
1.23
2.00
2.20
1.05
0.99
1.01
1.98
1.07
3.29
1.86
1.12
1.05
3.34
3.60
f1 (ppm)
173.1
169.5
160.9
152.2
143.4
137.3
129.0
127.7
125.7
123.0
119.0
113.3
80.5
77.4
77.2 CDCl3
76.9
69.4
64.9
52.2
42.5
29.9 H Grease
14.7
13.7
f1 (ppm)

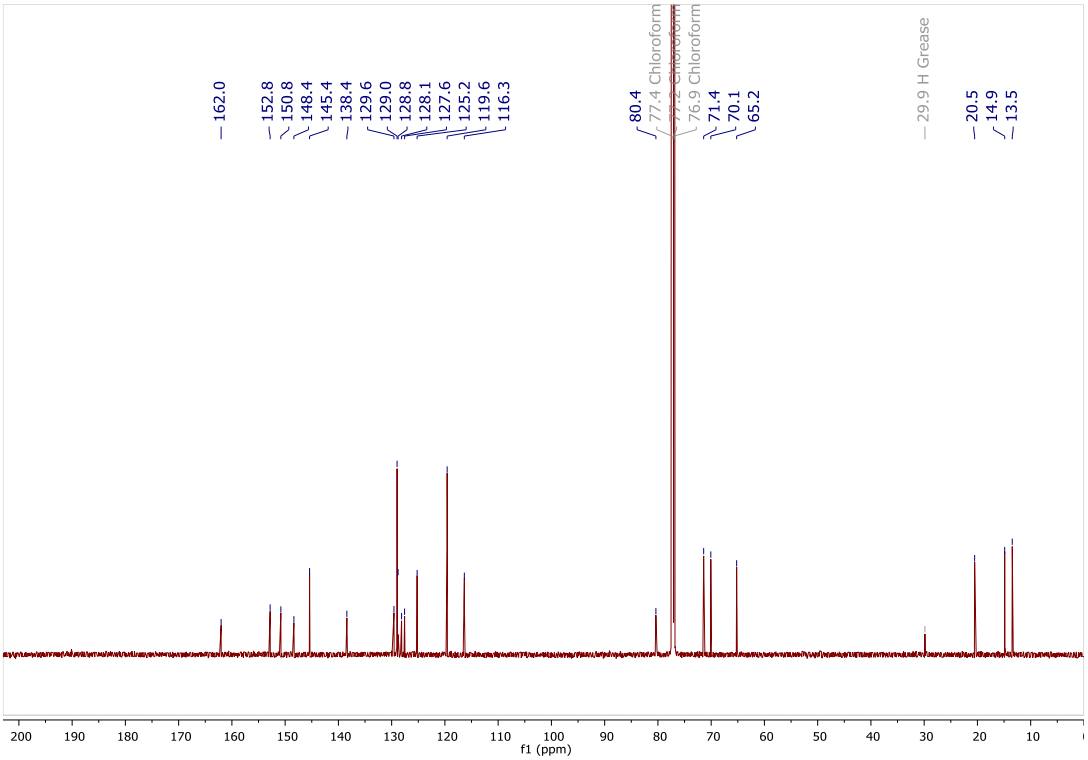
4-(but-3-yn-1-yloxy)-3-chloro-5-ethoxybenzaldehyde



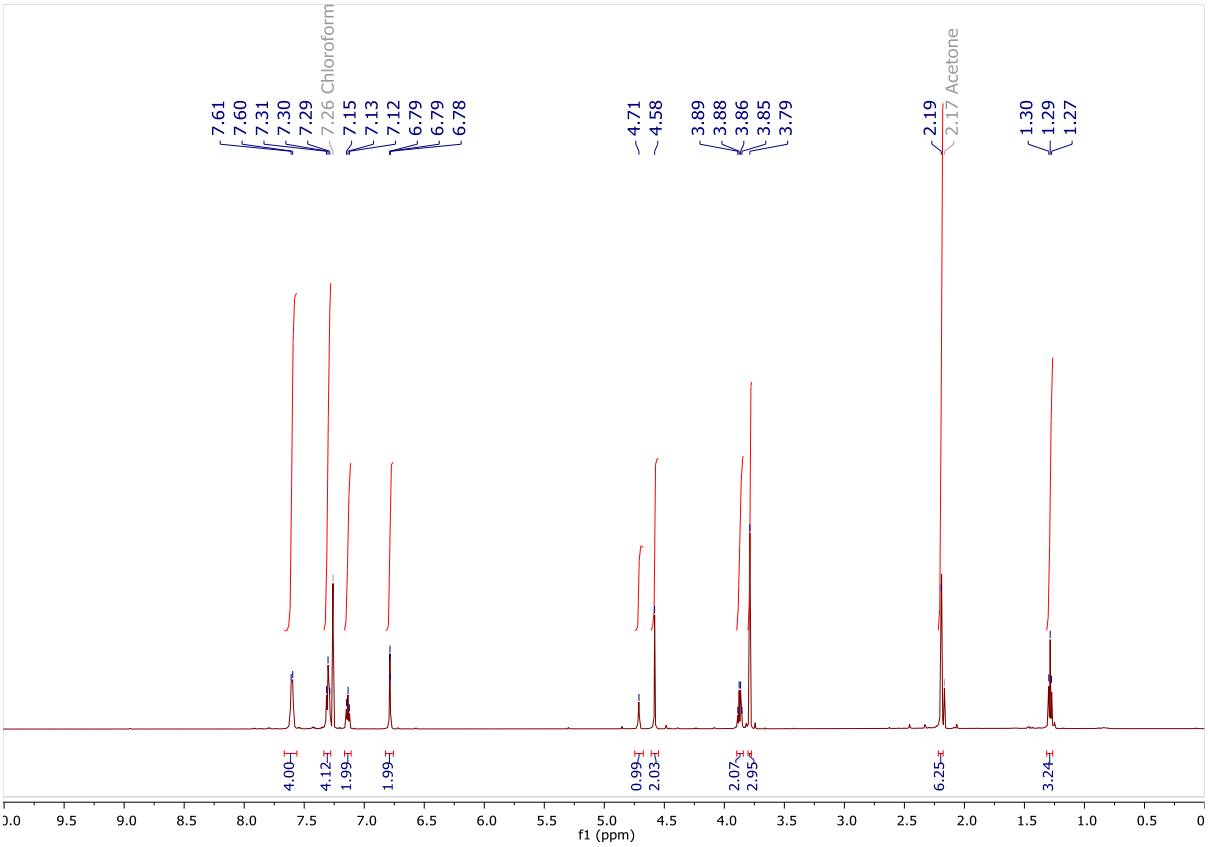


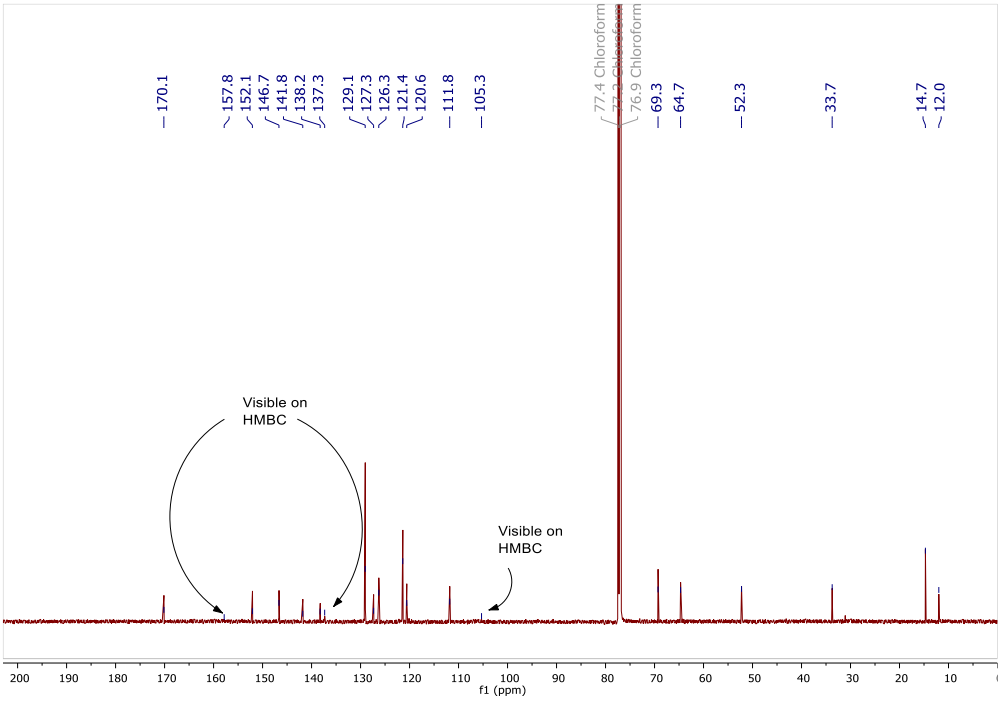
SJ-Alkyne

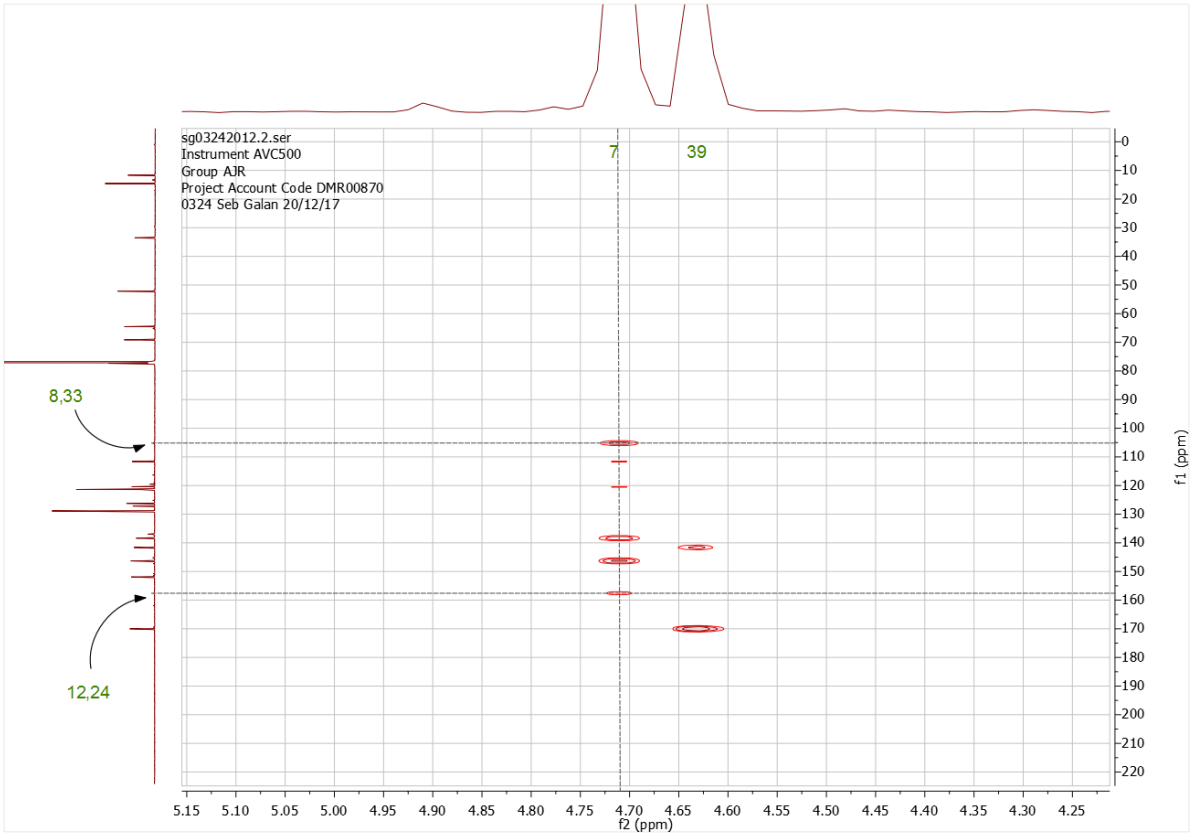

8.89
8.89
7.94
7.92
7.64
7.64
7.43
7.42
7.41
7.26 Chloroform
7.21
7.20
7.19
4.31
4.30
4.29
4.28
4.27
4.25
4.24
2.75
2.74
2.74
2.73
2.72
2.72
2.33
2.02
2.02
2.02
1.55 Water
1.53
1.52
1.51
1.26 H Grease
1.00
2.07
1.01
2.17
2.12
4.39
2.25
3.17
1.01
3.65
f1 (ppm)

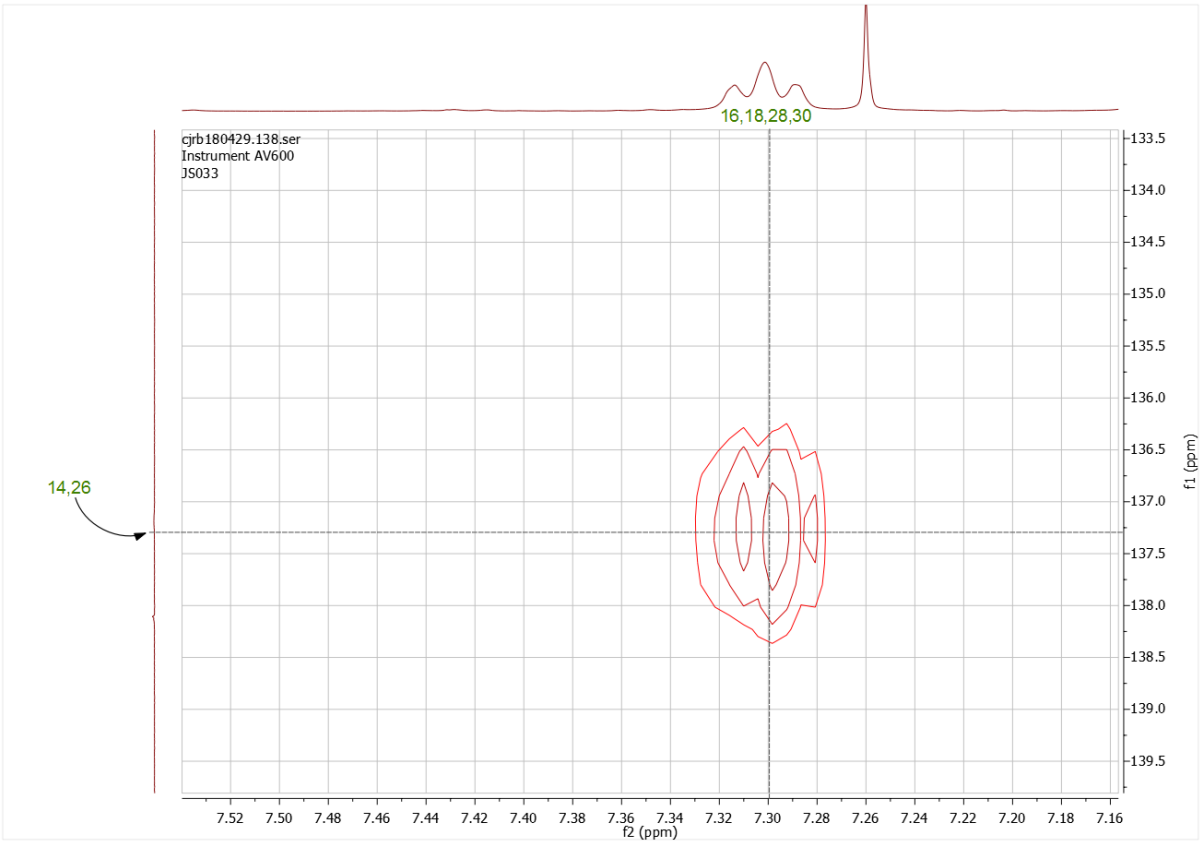

162.0
152.8
150.8
148.4
145.4
138.4
129.6
129.0
128.8
128.1
127.6
125.2
119.6
116.3
80.4
77.4 Chloroform
77.2 Chloroform
76.9 Chloroform
71.4
70.1
65.2
29.9 H Grease
20.5
14.9
13.5
f1 (ppm)

SJ-Bis


7.61
7.60
7.31
7.30
7.29
7.26 Chloroform
7.15
7.13
7.12
6.79
6.79
6.78
4.71
4.58
3.89
3.88
3.86
3.85
3.79
2.19
2.17 Acetone
1.30
1.29
1.27
4.00
4.12
1.99
1.99
0.99
2.03
2.07
2.95
6.25
3.24
f1 (ppm)


170.1
157.8
152.1
146.7
141.8
138.2
137.3
129.1
127.3
126.3
121.4
120.6
111.8
105.3
77.4 Chloroform
76.9 Chloroform
69.3
64.7
52.3
33.7
14.7
12.0
Visible on HMBC
Visible on HMBC
f1 (ppm)


sg03242012.2.ser
Instrument AVC500
Group AJR
Project Account Code DMR00870
0324 Seb Galan 20/12/17
7
39
8,33
12,24
f2 (ppm)
f1 (ppm)


16,18,28,30
cjrb180429.138.ser
Instrument AV600
JS033
14,26
f2 (ppm)
f1 (ppm)